Aerosol distribution above Munich using remote sensing techniques

Franziska Ingrid Josefine Schnell

München 2014

Aerosol distribution above Munich using remote sensing techniques

Franziska Ingrid Josefine Schnell

Dissertation
an der Fakultät für Physik
der Ludwig–Maximilians–Universität
München

vorgelegt von
Franziska Ingrid Josefine Schnell
aus Freising

München, den 21. Februar 2014

Erstgutachter: Prof. Dr. Bernadett Weinzierl
Zweitgutachter: Prof. Dr. Markus Rapp
Tag der mündlichen Prüfung: 21. Juli 2014

Contents

Zusammenfassung **ix**

Abstract **xi**

1 Introduction **1**
1.1 Aerosol classification . . . 1
1.2 The influence of aerosols on our climate . . . 2
1.3 Measurement of aerosols . . . 5
1.4 Aerosols above Europe . . . 5
1.5 Aerosol studies with CALIPSO . . . 7
1.6 Objective and outline . . . 8
1.7 External data . . . 9

2 Theory **11**
2.1 Interaction of light and particles in the atmosphere . . . 11
2.1.1 Electromagnetic waves . . . 11
2.1.2 Scattering and absorption . . . 12
2.1.3 Optical properties of aerosols . . . 13
2.2 Passive Remote Sensing . . . 16
2.2.1 Sun photometer measurements from ground . . . 16
2.2.2 Space borne spectroradiometer measurements . . . 16
2.3 Active Remote Sensing . . . 17
2.3.1 Backscatter lidar . . . 18
2.3.2 Raman lidar . . . 25
2.3.3 Depolarization lidar . . . 26
2.3.4 Multi wavelength measurements . . . 28
2.4 Summary . . . 28

3 Instrumentation, data and methods **31**
3.1 Definition of the Munich region . . . 31
3.2 AERONET-Cimel Sunphotometer . . . 31
3.2.1 Instrument . . . 33
3.2.2 Used data . . . 33

3.3 MODIS . . . 34
3.3.1 Instrument . . . 35
3.3.2 Aerosol retrieval over land . . . 35
3.3.3 Used data . . . 35
3.4 MULIS . . . 36
3.4.1 Instrument . . . 37
3.4.2 Description of the measurements . . . 37
3.4.3 Description of analysis method . . . 40
3.4.4 Data handling in this study . . . 41
3.5 CALIOP (Space lidar on-board CALIPSO) . . . 42
3.5.1 Instrument . . . 42
3.5.2 Regular data from NASA . . . 43
3.5.3 Data handling in this study . . . 53
3.6 Comparison of MULIS and CALIPSO profiles . . . 56
3.6.1 Data used for intercomparison . . . 56
3.6.2 Attenuated backscatter . . . 56
3.6.3 Limitations in the CALIPSO extinction profiles . . . 59
3.6.4 Meteorological conditions studied with HYSPLIT measurements . . . 63
3.7 Summary . . . 66

4 Aerosol distribution above Munich 67
4.1 AERONET . . . 68
4.2 MODIS . . . 71
4.3 MULIS . . . 72
4.3.1 Variation of the optical depth . . . 73
4.3.2 Seasonal variation of extinction profiles . . . 77
4.3.3 Seasonal variation of depolarization ratio and Ångström exponent . . . 77
4.3.4 Profile of the convective PBL . . . 79
4.4 CALIPSO . . . 81
4.4.1 Variation of the optical depth . . . 82
4.4.2 Occurrences of aerosol types . . . 82
4.4.3 Optical properties of aerosol types . . . 90
4.5 Summary . . . 91

5 Discussion 93
5.1 Monthly and seasonal comparison of all four datasets . . . 93
5.1.1 Comparison of AODs . . . 94
5.1.2 Comparison of Ångström exponents . . . 96
5.2 Direct comparison of AOD from AERONET with MULIS and CALIPSO . . . 97
5.3 Comparison of profiles CALIPSO / MULIS . . . 101
5.3.1 Comparison of AODs . . . 101
5.3.2 Causes for deviation of AOD . . . 103
5.3.3 Comparison of layer mean values of MULIS and CALIPSO . . . 112

5.3.4 Calculation of extinction coefficients from CALIPSO L1B data . . . 114
5.4 Identification of aerosol type . . . 116
5.4.1 Saharan dust . . . 117
5.4.2 Smoke . . . 119
5.4.3 Marine aerosol . . . 123
5.5 Aerosol studies in Central Europe . . . 123
5.6 Influence on radiative forcing . . . 128

6 Summary and Outlook **131**
6.1 Summary of results . . . 131
6.2 Open scientific questions and outlook . . . 134

A Overview of MULIS / CALIPSO comparison **137**

B Monthly and seasonal values **139**

C Error calculation of Ångström exponent **145**

Acknowledgments **160**

Zusammenfassung

Aerosole sind ein wichtiger Bestandteil unserer Atmosphäre. Da Aerosole sowohl zeitlich wie auch räumlich sehr inhomogen verteilt sind, ist es sehr schwierig, ihren Einfluss auf das Klima abzuschätzen. Daher ist es wichtig, unser Wissen über die Verteilung von Aerosolen zu verbessern. In dieser Arbeit werden mit Hilfe von Fernerkundungs-Instrumenten Aerosole über der Region München, Deutschland, für die Zeitdauer von 2007 bis 2010 untersucht. Der Schwerpunkt ist dabei auf die Lidardaten des Bodenlidars MULIS des Meteorologischen Instituts München und des Weltraum-Lidars CALIOP an Bord des Satelliten CALIPSO gesetzt, die beide höhenaufgelöste Informationen liefern. Als Ergänzung und im Rahmen einer besseren Vergleichbarkeit mit vorangegangenen Studien werden zusätzlich Aerosol-Informationen vom AERONET Sonnenphotometer in München und dem Satelliten-Spektroradiometer MODIS verwendet.

Mit Hilfe dieser vier Datensätze können verschiedene Größen bestimmt werden: die Durchschnittswerte der Aerosol optischen Dicke (AOD) über München liegen bei 0.05 - 0.06 für 1064 nm, 0.12 - 0.17 für 532 nm und 0.22-0.28 für 355 nm. Die Höhe der Grenzschicht variiert von durchschnittlich 1.68 km im Frühling zu 0.73 km im Winter. Dagegen ist die geometrische Dicke von abgehobenen Schichten deutlich stabiler (Frühling: 1.43 km, Winter: 1.02 km). Abgehobene Schichten treten am häufigsten im Frühjahr auf (in 75 % aller Messungen), im Winter sind sie relativ selten (36 %). Messungen des linearen Partikeldepolarisationsverhältnisses und des Ångström-Exponenten zeigen, dass sich die Aerosol-Typen in abgehobenen Schichten deutlich von denen in der Grenzschicht unterscheiden. Besonders im Frühling ist die Depolarisation in den abgehobenen Schichten sehr hoch (25 %), was darauf hinweist, dass stark depolarisierende Aerosol-Typen wie beispielsweise Wüstenstaub aus der Sahara bis nach München transportiert wurde. Der vorherrschende Aerosol-Typ in der Region München ist Brand-Aerosol ('Smoke'), auch verschmutztes kontinentales Aerosol ('polluted continental') kann in hohen Konzentrationen vor allem im Sommer auftreten. Wüstenstaub kommt nur selten vor, meist vermischt mit anderen Aerosol-Typen ('polluted dust').

Ein wichtiges Ergebnis des Vergleiches der vier Datensätze ist, dass CALIPSO die AOD stark unterschätzt. Um die Gründe dafür zu finden, wurden Profile des Extinktionskoeffizienten von CALIPSO mit zeitgleichen Messungen von MULIS verglichen: die Unterschätzung der AOD kommt vor allem durch das Übersehen von Schichten zustande. Dieser Effekt führt in der Münchner Region zu einer Unterschätzung um ca. 36 %. Auch ein falsch gewähltes Lidarverhältnis steuert dazu, allerdings in geringerem Maße von etwa 5

%. Der Einfluss von Wolken in der näheren Umgebung auf die AOD ist nicht direkt quantifizierbar, allerdings zeigt eine Analyse, dass Wolken zu einer Überschätzung der AOD führen können. Es konnte gezeigt werden, dass es –zumindest für Fallstudien– sehr gut möglich ist, die Extinktionskoeffizienten direkt aus den Rohdaten (L1B) zu berechnen, um diese Probleme zu kompensieren und detaillierte Profile von CALIPSO zu erhalten.

Abstract

Aerosols are an important part of our atmosphere. As they are very inhomogenously distributed both in time and space the estimation of their influence on the climate is very complex. So it is important to improve the knowledge about the aerosol distribution. In this study the distribution of aerosols above the region around Munich, Germany in the time period 2007 to 2010 is studied with measurements from remote sensing instruments. Thereby the main focus is set on the lidar data from the ground based lidar system MULIS of the Meteorological Institute Munich and the space lidar CALIOP onboard the satellite CALIPSO which both deliver aerosol information height resolved. As an addition and for a better comparison with previous studies, aerosol information from the AERONET Sunphotometer in Munich and the satellite spectroradiometer MODIS are used.

With help of these four datasets several aerosol parameters could be studied: on average the aerosol optical depth (AOD) above the Munich region is at 1064 nm about 0.05 to 0.06, at 532 nm about 0.12 to 0.17, and at 355 nm about 0.22 to 0.28. The height of the boundary layer top decreases from 1.68 km in spring to 0.73 km in winter, while the thickness of the elevated layers is more stable (spring: 1.43 km, winter: 1.02 km). The occurrence of ELs is highest in spring (in 75 % of all measurements), and lowest in winter (36 %). Measurements of the particle linear depolarization ratio and the Ångström exponent show that the aerosols in elevated layers clearly differ from the aerosols in the PBL. Especially in spring the average EL depolarization is large (25 %) indicating transportation of strongly depolarizing aerosols like Saharan dust in the free troposphere. The dominant aerosol type in the Munich region is smoke (also called biomass burning), polluted continental can occur in high concentrations especially during summer time. Dust occurs only in rare occasions, mainly mixed with other aerosol types (polluted dust).

One important finding from the comparison of the four datasets is that CALIPSO strongly underestimates the AOD. To study the significances of different causes for this, the CALIPSO extinction coefficient profiles are compared with coincidentally performed measurements of MULIS. The underestimation of the AOD above Munich by CALIPSO is mainly found to be due to the failure of the layer detection: its effect on the AOD underestimation is about 36 %. Also the wrong assumption of the lidar ratio contributes to the underestimation, though on a smaller account of about 5 %. The influence of clouds in the surroundings on the AOD is not quantifiable, but the analysis shows that clouds lead to an overestimation of the AOD. To compensate these reasons and to get detailed profiles from CALIPSO, it could be shown that –for case studies– it is very efficient to

calculate the extinction coefficients from CALIPSO raw data (L1B) manually.

Chapter 1

Introduction

Atmospheric aerosols affect our life in various aspects. They impact the climate by interactions with radiation and by influencing cloud development and properties [Stocker et al., 2013]. They also play an important role for our health; for example the air quality is directly linked with the concentration of aerosols [Brunekreef and Holgate, 2002]. Especially in urban regions with high industrial background the pollution can be so strong that due to smog, being outdoors can lead to severe health problems and the daily routine in the whole region can collapse. Additionally, traffic can also be affected by aerosols: for example in April 2010 the Iceland volcano Eyjafjallajökull erupted and spread huge amounts of volcanic ash above Europe. Due to air safety, international travel, too, was severely restricted; airports in Europe were closed for several days, also international travel was strongly degraded. These examples stress the importance of studying aerosols, their properties and their spatial and temporal distribution.

In this study the aerosol distribution in the troposphere above the region around Munich, Germany in the time period from 2007 to 2010 is studied with measurements from remote sensing instruments. Thereby the main focus is set on the lidar data from the ground based lidar system MULIS of the Meteorological Institute Munich and the space lidar CALIOP onboard the satellite CALIPSO[1]. These two systems deliver aerosol information height resolved. As an addition and for a better comparison with previous studies, aerosol information from the AERONET Sunphotometer in Munich and the satellite spectroradiometer MODIS are used.

1.1 Aerosol classification

Aerosols are small solid or liquid particles (excluding cloud droplets and ice crystals) in air. The microphysical properties of aerosols like their chemical composition, their size, or their shape vary strongly depending on their sources [Wallace and Hobbs, 2006]. They can differ in shape from spherical to complex irregular structures; the size typically varies from

[1] In this thesis, the satellite lidar data is referred to being from CALIPSO as usually done in literature, while it would be more correct to say that the data are from the instrument CALIOP.

10 nm to 10 μm. Their sources can have natural origins like soil and dust from deserts, organic material from pollen, or sea salt from the oceans, as well as anthropogenic origins like sulphate aerosols from industrial emissions or soot particles from fuel. To describe aerosols in atmospheric research, they are classified into types which have a similar chemical composition because they originate from the same or similar sources, like the type 'mineral dust' from the deserts or 'carbon' from biomass burning. But there exists no standardized classification of aerosol types, the definition of an aerosol type can vary from study to study. Aerosol particles occur mostly in the troposphere and have in general a residence time of a few days to several weeks [Haywood and Boucher, 2000]. As their distribution is highly inhomogeneous both temporally and spatially, it is a very complex challenge to quantify their influence on the atmosphere.

1.2 The influence of aerosols on our climate

The understanding of climate change, its impact on the atmospheric conditions, and in particular the anthropogenic influence on climate has become the main task of atmospheric physics during the last decades. The influences of several components of the atmosphere like the greenhouse gas CO_2 on the radiative budget of the Earth are by now well understood and quantifiable [IPCC report, Stocker et al., 2013]. However, this is not the case for all atmospheric components: especially the influence of the aerosols on atmospheric processes is still not well determined.

Aerosols influence the radiative budget of the Earth by direct interaction with the radiation via scattering and absorption of solar and terrestrial radiation [McCormick and Ludwig, 1967, Satheesh and Moorthy, 2005] as well as indirectly by the modification of cloud properties [Twomey, 1991, Lohmann and Feichter, 2005]. Even small amounts of aerosol may have a significant contribution to the radiative budget. However, our knowledge about this influence is at the moment still sparse: in the last report of the Intergovernmental Panel on Climate Change (IPCC 2013, Fig. 1.1) the contribution of the direct aerosol effect to the global mean radiative forcing is assumed to be somewhere around -0.27 Wm^{-2} but with possible values varying from -0.77 $Wm^{-2}$to +0.24 Wm^{-2}. The negative or positive influence on the radiative forcing is thereby itemized for five aerosol types: while mineral dust, sulphates, nitrates and organic carbon lead to cooling, the impact of black carbon is strongly positive. The direct aerosol effect is by now well understood, however the absolute uncertainties are still high and for the indirect effects even more so: the effect via cloud alteration is assumed to be around -0.55 Wm^{-2} with an even larger range between -1.33 Wm^{-2} and -0.06 Wm^{-2}.

The main reason for the high uncertainty of the aerosol effects lies in the very variable distribution of aerosols in space and time. Also, aerosols can be altered during their transportation through the atmosphere due to chemical processes and mixing with other aerosol types. It is the lack of knowledge of the atmospheric aerosol abundance and mixing processes that makes it complicated to determine how much of an effect aerosols have on the climate and especially to identify the anthropogenic influence.

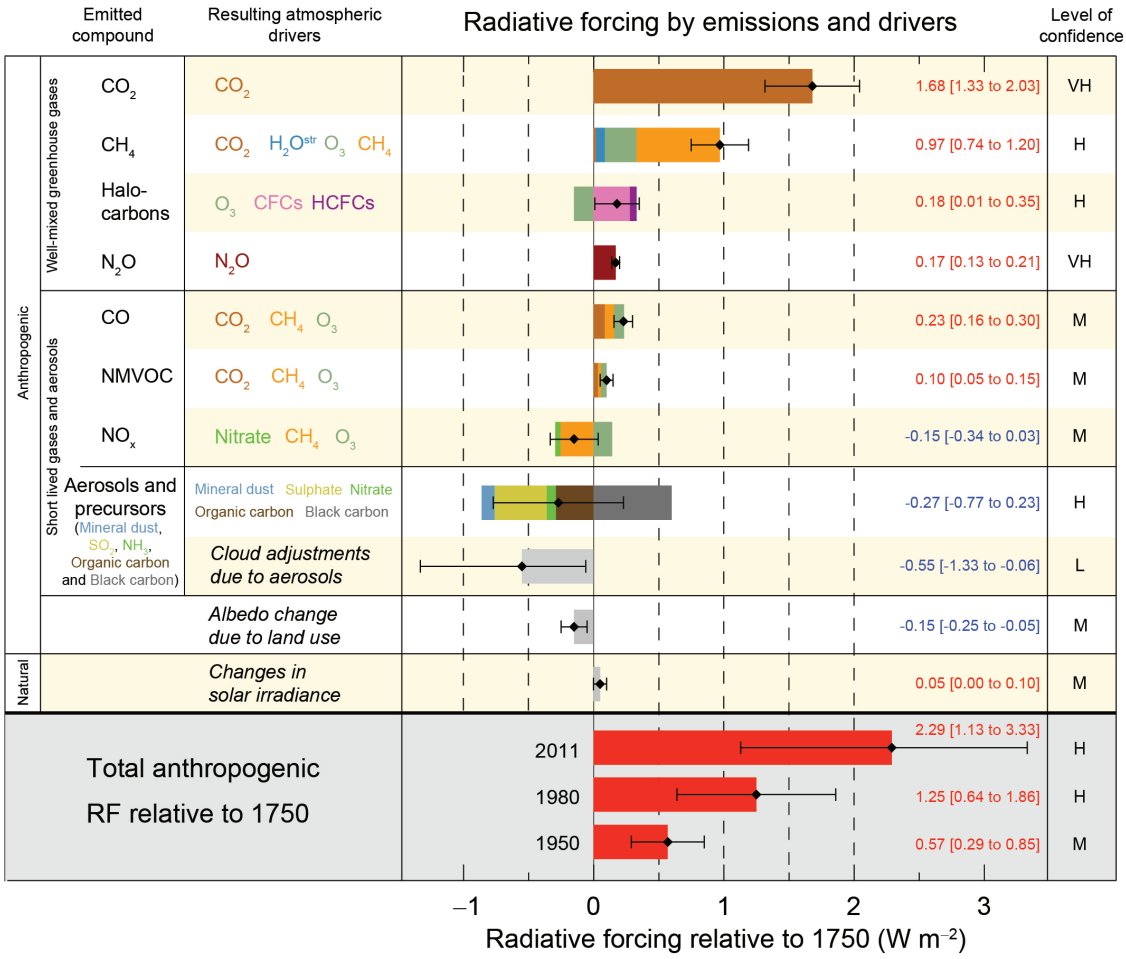

Figure 1.1: Radiative Forcing relative to the year 1750, dissected into various emission components, IPCC 2013. Source: http://www.ipcc.ch/

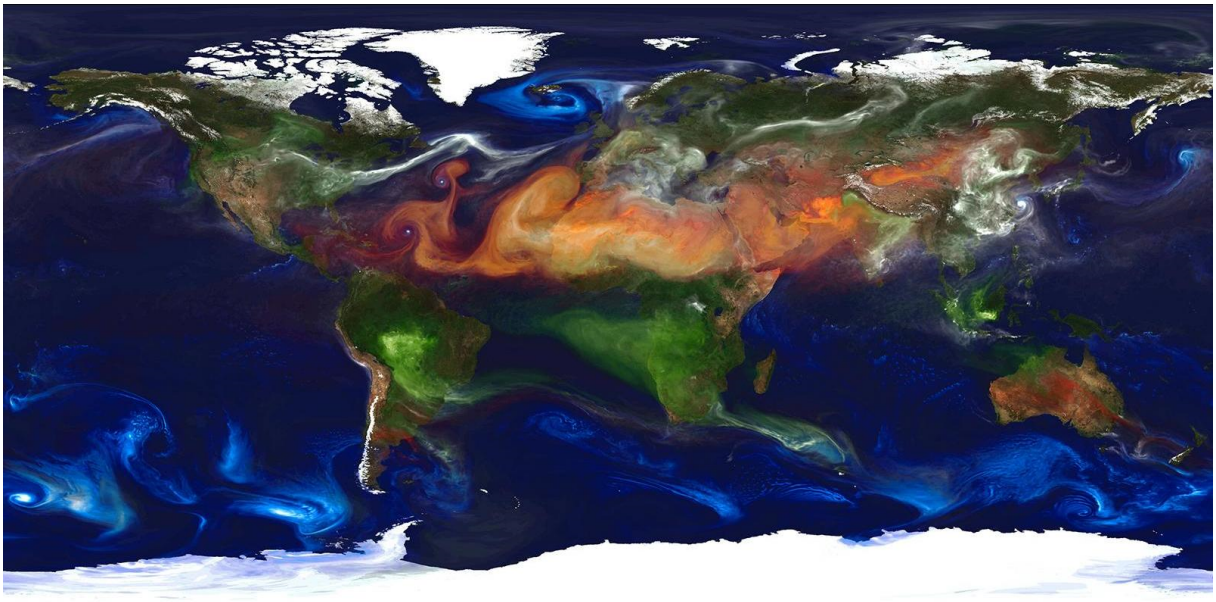

Figure 1.2: Global portrait of aerosols: GEOS-5 simulation of NASA with dust (red), sea salt (blue) smoke (green), and sulfate particles (white), excerpt (13. September 2006) of a model run of from 1. September 2006 through 17. April 2007. Source: William Putman, NASA/Goddard.

To quantify the aerosol influence on the climate, models are developed to simulate their transport and mixing and so to gain their horizontal and vertical distribution in the atmosphere. An example for the complexity of aerosols is shown in Fig. 1.2. This figure illustrates the very variable global distribution of four aerosol types calculated with the GEOS-5 model of NASA [Molod et al., 2012]: dust (red), sea salt (blue), black and organic carbon mainly from biomass burning (green), and sulphate from fossil fuel and volcanic emissions (white) for one model step (13. September 2006). All four aerosol types have typical areas of occurrences – e.g. sea salt can mostly be detected above the oceans – but due to the global circulations they can be widely distributed and may also mix.

There exist various other aerosol models running on different time scales, taking into account different sources, aerosol types, and mixing algorithms like the ECHAM4 [Roeckner, 1996], the Flexpart [Stohl et al., 2005], or the GOCART model [Chin et al., 2002]. Their different input parameters lead to different distributions and amounts of aerosols and hence different influence on the climate [Kinne et al., 2003]. As a consequence, the calculated radiative influence of aerosols may differ significantly depending on the used model. The reliability of aerosol models and therefore the right estimation of the aerosol impact is dependent on the right estimation of the location and strength of the sources of these aerosols, the microphysical properties of the aerosols, the weather conditions which drive the transport, as well as the correct implementation of aerosol interactions during transport. Accordingly, the models require measured aerosol data for input, in order to derive correct parametrizations as well as for validation.

1.3 Measurement of aerosols

There are several possibilities to gain aerosol data by using in-situ and remote sensing measurements. Often these measurements are collected in networks, e.g., AERONET [Holben et al., 1998], SKYNET [Takamura and Nakajima, 2004], MPLNET [Welton et al., 2006], or EARLINET [Boesenberg, 2003], the latter being the European Lidar Network which gains vertically resolved information about aerosols. These networks are used to monitor the atmosphere for long term studies. In contrast, field campaigns are generally used to intensely study a special aerosol type or a special region with a multitude of instruments: the properties of Saharan dust and its alteration during transport were studied in the two SAMUM campaigns 2006 at Morocco [Heintzenberg, 2009] and 2008 at Cape Verdi [Ansmann et al., 2009], while in the ACE-Asia campaign several aerosol types above the Asian continent were studied with main focus on Asian dust [Arimoto et al., 2006]. But all these measurements are spatially or temporally limited: the network instruments are in general sparsely distributed at permanent locations on land, the coverage of ground based aerosol instruments above the oceans is very poor. Also field campaigns are only realized for short periods from weeks to months and as such they cannot be used to study the annual or seasonal variation. A global coverage of aerosol data over several years can only be obtained by satellite measurements.

Passive satellite measurements are by now well established. There is a whole set of instruments in space to gain aerosol information, like MODIS (Moderate-Resolution Imaging Spectroradiometer, Remer et al., 2005), MISR (Multiangle Imaging Spectroradiometer, Diner et al., 1998), POLDER (Polarization and Directionality of Earth's Reflectances, Deschamps et al., 1994), or OMI (Ozone Monitoring Instrument, Levelt et al., 2006).

These instruments have different advantages; some observe the atmosphere from different viewing angles, others at many spectral channels, some have both advantages. Nevertheless, as passive remote sensing instruments, the measurements depend on the radiation source (be it sun, atmosphere, or surface) and on a multitude of other atmospheric conditions such as clouds and especially the surface albedo. Obtaining aerosol information with these instruments requires very sophisticated retrievals and aerosol models. Consequently, these instruments deliver mostly column integrated aerosol properties.

1.4 Aerosols above Europe

With all the instruments mentioned above, it is possible to describe the aerosol distribution in the atmosphere. For Europe, there exist several studies based on satellite measurements of the aerosol optical depth (AOD) – a column value to estimate the aerosol concentration. Chubarova [2009] studied the seasonal distribution of aerosol properties over Europe and their impact on UV irradiance by using the MODIS AOD for the time period 2000-2008. A case study on biomass burning aerosols above Finland transported from Eastern Europe was done by Arola et al. [2007], which shows that single events of transported aerosol can bring a sudden change in the AOD at 550 nm from nearly zero to values as high as 1.2.

This transportation of biomass burning aerosols was also studied in detail by Barnaba et al. [2011] who used MODIS and MISR data to detect fires in Eastern Europe and Russia and calculated the contribution of these wildfires to the AOD above all Europe. Bovchaliuk et al. [2013] used AOD and Ångström exponent data from POLDER combined with ground based Sunphotometer measurements from AERONET to study the aerosol variation above Eastern Europe and to identify the different aerosol sources. The AOD can also help to improve the knowledge about the air quality: Koelemeijer et al. [2006] studied the correlation between the AOD measured by MODIS and the in-situ measurements of PM10/PM2.5 of the AIRBASE database [Buijsman and De Leeuw, 2004]. Thereby the correlation improves when the AOD is divided by the height of the planetary boundary layer (PBL), showing that the structural distribution of the aerosol concentration also matters.

For a more detailed analysis of the atmosphere, it is very useful to use lidar measurements. With these, it is possible to analyze not only the AOD, but layer heights or optical properties of the aerosols like the extinction coefficient or the particle depolarization ratio. Especially Saharan dust is an aerosol type which can be identified well by using depolarization measurements: most frequently, dust occurs above Southern Europe [Papayannis et al., 2008], e.g. in Greece [Balis et al., 2004], in Italy [Mona et al., 2009], Spain [Perez et al., 2006], or Portugal [Preißler et al., 2011], but on rare occasions large amounts of Saharan dust can be detected above Central Europe [Wiegner et al., 2011]. Also the optical properties of biomass burning aerosols and their alteration depending on the transportation time can be studied [e.g. Amiridis et al., 2009, Wandinger et al., 2002, Balis et al., 2003]. The outbreak of the Iceland volcano Eyjafjallajökull and its influence on the air traffic in large parts of Europe in April 2010 triggered a series of measurements to track the propagation of its ash plume [Mattis et al., 2010, Groß et al., 2010, Wiegner et al., 2012, Ansmann et al., 2010]. It was even possible to estimate the mass concentration from ground-based lidar measurements [Gasteiger et al., 2011] which was urgently needed to reduce air safety risks. Due to the collaboration of several lidar stations of EARLINET, a four dimensional distribution of the ash cloud above Europe could be provided for the time period from 15th April to 26th May 2010 [Pappalardo et al., 2013]. This can be used to improve chemical models which calculate the propagation of aerosols.

While there are a lot of lidar studies on single aerosol types, there exist only few on the typical values above a lidar site. Therefor the members of the EARLINET lidar network, including Munich, decided to perform routine measurements on a weekly schedule [Pappalardo, 2007] to build a database of aerosol profiles for Europe. Thereby parameters like the height of the PBL, the occurrence of elevated layers, or the most frequent aerosol type can be determined. First results on PBL top and AOD were presented by Matthias et al. [2004]. In contrast, Preißler et al. [2013] and Mattis et al. [2004] studied aerosol layers in the free troposphere (elevated layers) above Evora, Portugal and Leipzig, Germany, respectively: due to the calculation of the lidar ratio at two wavelengths, the Ångström exponent, and the particle linear depolarization, several aerosol types could be distinguished and classified. Ten years of measurement provided typical values for the boundary layer above Leipzig [Mattis et al., 2008]: the PBL top is decreasing from ca. 2.35 km in summer

to 1.30 km in winter with AOD values of 0.38 ± 0.23 and 0.18 ± 0.11 at 355 nm and 532 nm, respectively. Nevertheless, these analyses have so far only been performed for few EARLINET sites.

1.5 Aerosol studies with CALIPSO

As explained in the last section, lidar systems are a great source for height resolved information on aerosols. The main disadvantage of these systems is that they are normally fixed to one location and sparsely distributed over Europe and even more so worldwide. Also – in contrast to AERONET– only few instruments are identical in construction; most are individually built by different lidar groups. Accordingly, a comparison between these instruments is a complex challenge

At the moment, the best source for height resolved aerosol information around the globe is the Cloud-Aerosol Lidar with Orthogonal Polarization (CALIOP) on board the Cloud-Aerosol Lidar and Infrared Pathfinder Satellite Observations (CALIPSO). It was launched as part of the A-Train of NASA in April 2006 and offers a unique possibility to get vertically resolved optical properties of aerosols and clouds [Winker et al., 2009]. With CALIPSO, a multitude of different aerosol studies is possible, for example to examine the air quality above polluted areas like Bangkok [Bridhikitti, 2013] or the transportation of the Eyjafjallajökull ash plume [Winker et al., 2012], or to determine the distribution of aerosols in the arctic [Di Pierro et al., 2013]. Huang et al. [2013] derived the seasonal and diurnal variations of aerosol extinction profiles and analyzed the aerosol types from CALIPSO 5-year observations. With CALIPSO it is possible to study the aerosol distribution above any region, like the variation of the aerosol optical depth (AOD) along the flight path. Additionally, CALIPSO can also be used to describe the variation of the PBL [McGrath-Spangler and Denning, 2013]. Also the aerosol interaction with clouds is an important topic, for which CALIPSO data – mostly in combination with passive remote sensing instruments– can be a great advantage [e.g. Costantino and Bréon, 2013, Várnai and Marshak, 2011].

But the CALIPSO lidar also has limitations when very low signal-to-noise ratios prevent a quantitative retrieval or a definite discrimination between aerosols and clouds. Also the data analysis is very complex and demands several assumptions. These limitations need to be explored, as seen in several validation studies in the last years: as a first step, Mona et al. [2009] and Wu et al. [2011] compared the raw data (attenuated backscatter) of CALIPSO with coincident measurements of ground based Raman lidar systems and both found good agreement of the profiles above the boundary layer. Most of the time, however, comparisons of the AOD with other instruments like MODIS or AERONET show an underestimation of the AOD by CALIPSO [Redemann et al., 2012, Omar et al., 2013]. In case studies, some reasons for this underestimation were found: for example a comparison with ground based and airborne lidar systems indicated that the lidar ratio chosen by the CALIPSO algorithms is not always valid [Chazette et al., 2010]. Underflights with a lidar mounted on an airplane in Illinois, US, generally show a good agreement of the extinction

coefficient profiles [Sheridan et al., 2012]. However, while the extinction coefficient was underestimated in the free troposphere by CALIPSO, it was overestimated in the PBL, in particular in the presence of boundary layer clouds. The latter hints to problems with the CALIPSO cloud screening methods.

The one day multi-platform study of Kacenelenbogen et al. [2011] identified several potential reasons for the underestimation of the AOD: 'CALIOP's low signal-to-noise ratio (SNR) leading to the misclassification and/or lack of aerosol layer identification; the cloud contamination of CALIOP Version 2 (V2) aerosol backscatter and extinction profiles; potentially erroneous assumptions of the aerosol lidar ratio (Sp); and calibration coefficient biases in the CALIOP daytime attenuated backscatter coefficient profiles.' The study thereby showed the improvements of the newest data version (V3) of the CALIPSO aerosol data compared with the V2 data, e.g. the better resolution of the profiles and better cloud screening processes. But as a one day study it is only possible to show potential limitations without further examination. The listed reasons still influence the Version 3 CALIPSO level 2 data and need further study.

In summary, although CALIPSO delivers global aerosol information from a single instrument, the results are based on too many assumptions and have too large uncertainties to be able to fully replace the much more precise ground based measurements; CALIPSO can only be seen as amendment and requires constant validation by ground based instruments.

1.6 Objective and outline

The aim of this thesis is to add the Munich region in Southern Germany as another site to the sparsely filled map of locations in Europe with known aerosol distribution. For this purpose, datasets are derived for the period 2007 to 2010 from four independently measuring instruments: the Sunphotometer Cimel of the network AERONET located on the roof of the Meteorological Institute Munich (MIM), the spectroradiometer MODIS onboard the TERRA satellite, the space lidar onboard CALIPSO, and the MUlti wavelength LIdar System (MULIS) of the MIM, located at Maisach (∼25 km west of Munich). Using these data sets, the following aspects can be studied:

- What are the typical values of the aerosol optical depth (AOD) above the Munich region and how does the AOD change with season?
- How is the vertical distribution of the aerosols? How often do elevated layers occur?
- What aerosol types are typical for the region?

Part of this study focuses on the comparison of the results from the different instruments. Therefore reasons for the deviation between the four instruments are identified and quantified:

- How well do the four datasets match?

- What are the reasons for discrepancies between the instruments?

One important finding is that CALIPSO strongly underestimates the AOD. This behavior has already been observed by other studies (see previous section); however the significances of the different causes for the underestimations were not assessed very thoroughly. For that purpose, the CALIPSO profiles are compared with coincidentally performed measurements of the multi-wavelength lidar MULIS. This comparison of profiles of extinction coefficients, Ångström exponents and the particle linear depolarization ratios for a time range of four years is so far unique. The comparison is further used to study how best to handle CALIPSO data:

- Under what conditions are CALIPSO data useful?
- What can be done to improve the quality of the CALIPSO data e.g. for case studies? How effective is the improvement?

The structure of this thesis is as follows:

In Chapter 2 the basic concepts of interaction of light with aerosols are presented, as well as a description of the remote sensing theory with focus on lidar retrieval.

Chapter 3 introduces the instruments and datasets of CALIPSO, MULIS, AERONET-Cimel, and MODIS. As the CALIPSO lidar retrievals are very complex, they are explained in detail. Additionally, a comparison between coincident measurements of MULIS and CALIPSO for selected cases is used to illustrate some of the limitations of the CALIPSO data and to develop a methodology with which the full datasets can be analyzed for the effect of these limitations.

In the following Chapter 4 the aerosol distribution derived independently from each of the four datasets is shown. While the datasets of AERONET and MODIS only refer to the column value AOD, the two lidar systems are additionally used to study the height distribution of the aerosols and further results such as the linear particle depolarization and detected aerosol types.

Chapter 5 then discusses these results: the different climatologies are compared to each other. Especially the day to day comparison of CALIPSO and MULIS quantifies the importance of the main reasons for the significant misestimation of the AOD by CALIPSO and gives an impression of the validity of the aerosol type classification of CALIPSO. Finally, the consequences of the underestimation of the AOD are briefly evaluated; at the same time, the aerosol type is taken into account, and the results are put into perspective with existing studies.

This thesis concludes in Chapter 6 with a synopsis of the findings and suggestions for future possibilities to extend the aerosol study.

1.7 External data

For the realization of this study, data and calculations from several external organizations were used, as are listed below:

The calculation of the radiative transfer with libRadtran was done by Robert Buras.

HYSPLIT cluster analyses above Munich were calculated by Astrid Gosewisch of the MIM as part of her bachelor thesis.

Josef Gasteiger provided calculations for the Ångström exponents for several aerosol types.

The program to calculate intersections between HYSPLIT trajectories and CALIPSO paths is based on software from Thomas Kanitz, TROPOS Leipzig.

For the analysis of the MULIS data radiosondes of the German Weather Service (DWD), launched in Oberschleißheim, were used.

The CALIPSO data were obtained from the NASA Langley Research Center Atmospheric Science Data Center.

The MODIS data used in this study were acquired as part of the NASA's Earth-Sun System Division and archived and distributed by the MODIS Adaptive Processing System (MODAPS).

Sunphotometer measurements of the CIMEL were downloaded from the AERONET web page (http://aeronet.gsfc.nasa.gov - PI: Matthias Wiegner). CIMEL Calibration was performed at the AERONET-EUROPE calibration center at GOA-UVA, supported by ACTRIS (European Union Seventh Framework Program, FP7/2007-2013) under grant agreement no. 262254.

HYSPLIT trajectories were calculated with the Hybrid Single particle Lagrangian Integrated Trajectory (HYSPLIT) transport and dispersion model on the READY website (http://ready.arl.noaa.gov/HYSPLIT.php).

The dust forecast images are from the BSC-DREAM8b (Dust REgional Atmospheric Model) model, operated by the Barcelona Supercomputing Center (http://www.bsc.es /projects/earthscience/BSC-DREAM/).

I acknowledge the use of Rapid Response imagery from the Land Atmosphere Near-real time Capability for EOS (LANCE) system operated by the NASA/GSFC/Earth Science Data and Information System (ESDIS) with funding provided by NASA/HQ.

Chapter 2

Theory

For a better understanding of the instruments used in this thesis, a short overview is given about radiative transfer, aerosol optical parameters, and the basic concepts of remote sensing instruments with focus on aerosol measurements.

2.1 Interaction of light and particles in the atmosphere

The focus of this section will be on the properties of radiation relevant for the following study. These are the properties of electromagnetic waves and the types of interactions of radiation with the atmosphere, in particular with aerosols. A thorough introduction to radiative transfer theory in the atmosphere can be found in e.g. Petty 2006.

2.1.1 Electromagnetic waves

The terms radiation and light describe electromagnetic (EM) waves which propagate through space at the speed of light c ($c = 2.99 \cdot 10^8 \frac{m}{s}$). Maxwell's equations fully describe this propagation of radiation [Petty, 2006]. Accordingly, due to the dual nature of radiation light cannot only be understood as EM waves, but also as particles called photons.

The wavelength λ which is related to the frequency $\nu = \lambda c$ can be used to calculate the energy of a photon with wavelength λ using Plank's constant $h = 6.626 \cdot 10^{-34}$ Js:

$$E = h\nu = \frac{hc}{\lambda} \tag{2.1}$$

Visible light (VIS) has wavelengths from 390 nm to 760 nm [Wallace and Hobbs, 2006], but for atmospheric remote sensing purposes, wavelengths between 200 nm (UV measurements) and 10 cm (radar applications) are used. This study also mentions the near infrared (NIR) wavelengths from 0.78 to 3 μm. Fig. 2.1 is an example of EM radiation as wave with wavelength λ. This image in particular shows the orientation of the wave in different directions in the plane perpendicular to the direction of propagation, the so-called polarization.

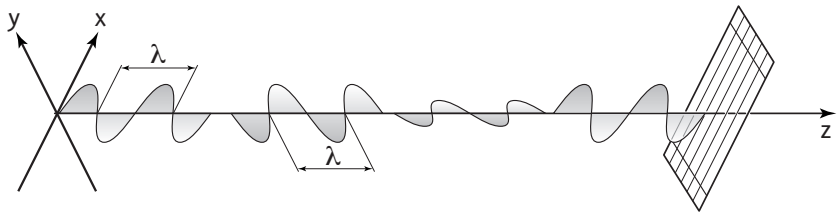

Figure 2.1: Electromagnetic radiation shown as wave with wavelength λ and statistically uniform distributed oscillation directions. [Köpke and Sachweh, 2012, Fig. 2.1]

The intensity as well as the polarization degree of an EM wave is useful information for remote sensing.

2.1.2 Scattering and absorption

The interactions of EM waves with particles can be described by two processes: scattering and absorption. The direction of light after scattering strongly depends on the ratio between the wavelength λ and the particle radius r. If the particle is small compared to the wavelength, the so called Rayleigh theory is valid and the probabilities of scattering in forward and backward direction are equal. For increasing particle size, the probability of forward scattering starts to dominate when r becomes of order of λ. Then, for spherical particles the Mie theory applies. The probability of scattering is quantified by the scattering coefficient$\alpha_{scat}(\lambda)$, which in the Rayleigh regime ($\lambda \gg r$) is roughly proportional to λ^{-4}, and in the Mie regime ($\lambda < r$) is almost constant with wavelength. The second process, absorption, describes the acquisition of the energy of the photon by the particle. The so-called absorption coefficient $\alpha_{abs}(\lambda)$ depends on the material of the particle as well as on the wavelength λ.

The absorption and scattering coefficients of the atmosphere depend on the concentration and composition of the interacting gases and particles. For most remote sensing applications, the atmosphere can be assumed to be horizontally homogeneous, hence the coefficients – in particular all those discussed in this thesis – depend only on height z.

The extinction of light through the atmosphere can be described by Beer's law (also called Lambert-Beer law or law of Beer-Lambert-Bouguer, BLB), which relates the extinction of EM radiation to the properties of a homogenous medium through which the wave is traveling [Petty, 2006]. The initial radiance $I_{\lambda,0}$ is diminished through the extinction along the way. At a distance z only the radiance $I_\lambda(z)$ remains:

$$I_\lambda(z) = I_{\lambda,0} \exp\left[-\int_{z_0}^{z} \alpha(z', \lambda) dz'\right] \tag{2.2}$$

where the extinction coefficient α is the sum of the absorption and scattering coefficients,

$$\alpha(z,\lambda) = \alpha_{scat}(z,\lambda) + \alpha_{abs}(z,\lambda) \tag{2.3}$$

Accordingly, the diminishing part of Eq. 2.2 is the transmission T which will be used in several sections of the thesis:

$$T_\lambda(z_0,z) = \exp\left[-\int_{z_0}^{z} \alpha(z',\lambda)dz'\right] \tag{2.4}$$

In the following, the dependencies on z and λ will be omitted unless relevant for the discussion.

2.1.3 Optical properties of aerosols

The strength and the direction of scattering and absorption of light on aerosol particles is influenced by their size, chemical composition and shape – all of which vary strongly between aerosols of different origin. Furthermore, as the wavelengths λ at which the instruments presented in Chap. 3 work is of the order or larger than the typical size of aerosol particles, the optical properties also depend on λ.

To study aerosols in the atmosphere, the discrimination between air molecules and the much larger aerosols is important[1] as both contribute to the extinction. So α_m is the molecular extinction coefficient, while α_p refers to the particle extinction coefficient which is dependent on the aerosol type as well as on its concentration.

$$\alpha(z,\lambda) = \alpha_m(z,\lambda) + \alpha_p(z,\lambda) \tag{2.5}$$

The integration of the particle extinction coefficient from ground to top of the atmosphere is defined as the aerosol optical depth (AOD).

$$AOD(\lambda) = \int_0^{top} \alpha_p(z,\lambda)dz \tag{2.6}$$

Both the particle extinction coefficient $\alpha_p(z)$ as well as the AOD depend not only on the microphysical properties but also on the amount of aerosols at height z. The extinction coefficient is also dependent on the wavelength. The relation between the extinction coefficients of two wavelengths ($\lambda_1 > \lambda_2$) can be described using the Ångström exponent κ:

$$\alpha_p(z,\lambda_2) = \alpha_p(z,\lambda_1)\left(\frac{\lambda_1}{\lambda_2}\right)^{\kappa} \tag{2.7}$$

In contrast to α_p, the Ångström exponent is independent of the aerosol concentration and can be used as help for the estimation of the aerosol size order. From Eq. 2.7 κ can be calculated height resolved from the extinction coefficients of two different wavelengths:

[1] In this work, the index 'm' refers to the molecular part of the optical parameters, while the index 'p' (particle) here corresponds to aerosols.

$$\kappa(z, \lambda_1, \lambda_2) = -\frac{\log \frac{\alpha_p(z, \lambda_1)}{\alpha_p(z, \lambda_2)}}{\log \frac{\lambda_1}{\lambda_2}} \tag{2.8}$$

Similarly, the Ångström exponent can also be derived as a column value from the AOD. Typical values of κ range from 0 to 3, whereby $\kappa = 0$ implies that there is no wavelength dependency and the particles are large compared to the scattered wavelengths. Increasing values of the Ångström exponent imply a decrease of the particle size. In the Rayleigh regime, the Ångström exponent reaches its limit with $\kappa = 4$.

An example for the dependency of the Ångström exponent κ on aerosol type and wavelength is shown in Fig. 2.2: the Ångström exponent for desert aerosol is clearly smaller ($\kappa \approx 0.15$) than the ones for continental average aerosol (κ ranges from $\sim$1.0 to 1.65). The relative humidity, too, influences κ: only for the continental average with 80 % relative humidity (green line) the Ångström exponent increases with increasing wavelength in the shown spectrum (near UV, VIS, NIR), while the dry continental average reaches its maximum at about 0.85 μm and decreases again with increasing wavelength.

As the Ångström exponent is an observable derived from the extinction coefficient, it is interesting to take a look at the error propagation. According to Appendix C, the error σ_κ propagated from the extinction coefficient errors, σ_α, is:

$$\frac{\sigma_\kappa}{\kappa(\lambda_1, \lambda_2)} = f(\lambda_1, \lambda_2)\frac{\sigma_\alpha}{\alpha} \tag{2.9}$$

where the factor f is defined as:

$$f(\lambda_1, \lambda_2) = \left| \frac{\sqrt{2}}{\kappa \ln \frac{\lambda_1}{\lambda_2}} \right|. \tag{2.10}$$

In other words, f can be interpreted as an error enhancement factor, i.e. if $f = 2$, then the relative error in κ is twice as large as in α_p. Assuming a value of $\kappa = 1.4$, one obtains f(1064 nm, 532 nm) $\simeq 1.4$ and f(660 nm, 470 nm) $\simeq 3.0$. For decreasing κ, the values are even higher, e.g. for $\kappa = 1$ it is f(660 nm, 470 nm) $\simeq 4.2$. Hence, an error of 10 % in the extinction coefficients can lead to up to more than 40 % error in κ. This will be considered in the later discussion of Ångström exponent.

Due to their multitude of sources, the shape, the chemical composition as well as the particle size distributions are strongly variable, leading to different optical properties for various aerosol types. Inversely, this allows the study of aerosols and their distribution in the atmosphere by measuring their optical properties.

Note that layers of mixed aerosols with different microphysical properties may occur in the atmosphere. Then $\alpha_p = \alpha_{p1} + \alpha_{p2} + ...$ Most aerosol types consist of a mixture of different particles (e.g. biomass burning contains black carbon, organic compounds, ...), also it is possible that in a layer two or more aerosol types are mixed. To distinguish between these types with remote sensing techniques is a very intricate challenge.

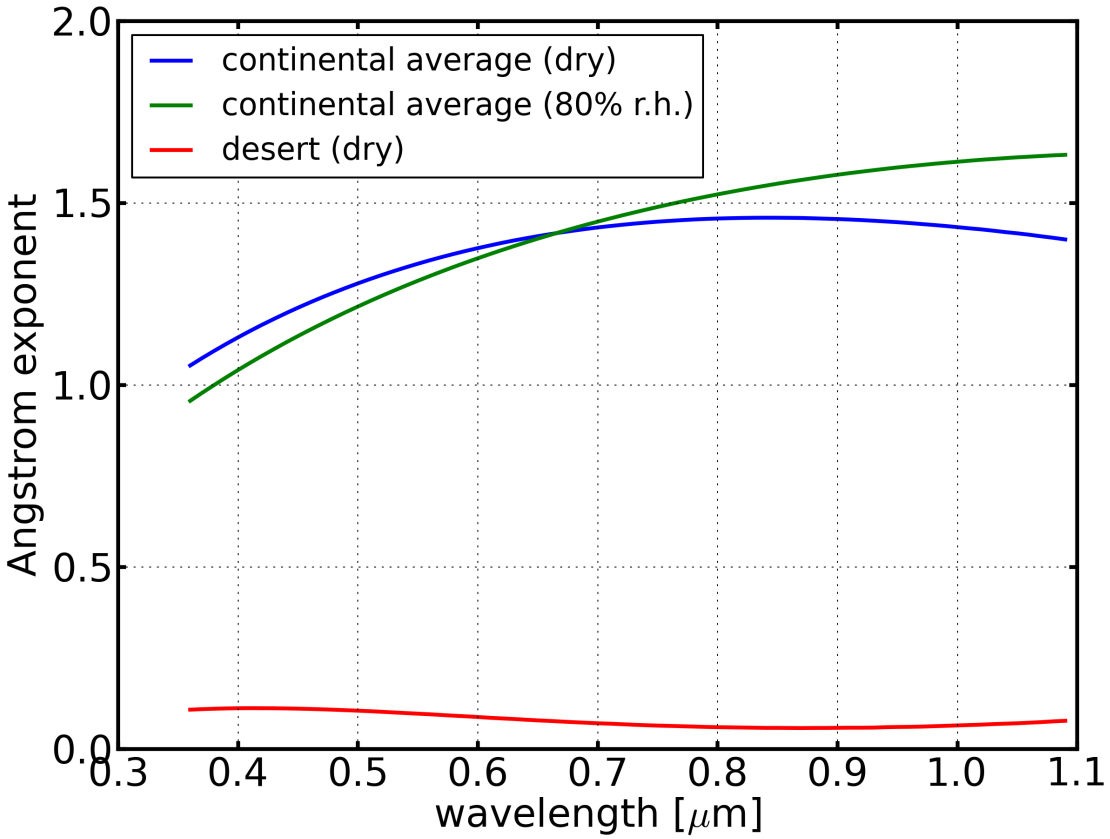

Figure 2.2: Wavelength dependency of the Ångström exponent calculated for three aerosol mixtures: continental average in dry conditions and with 80 % rel. humidity and desert of OPAC [Hess et al., 1998]. Source: J. Gasteiger, MIM.

2.2 Passive Remote Sensing

One way to gain information about the optical properties of aerosols in the atmosphere is to use passive remote sensing. In this process, the natural radiation of the Sun, the Earth, or its atmosphere is detected by the instrument after having passed the atmosphere, while no artificial radiation source is needed. By measuring the radiation at different wavelengths, various atmospheric conditions can be explored. E.g., it is possible to derive global radiation or sunshine duration from ground. Also the passive remote sensing technique is a well established technology for satellite missions to obtain a global overview of the atmosphere, e.g. to locate clouds, to distinguish between ice and water phase, or to detect aerosol sources. An overview over passive remote sensing methods can be found for example in Lillesand et al. [2007]. In the following, only the measurement techniques relevant for this thesis will be elaborated.

2.2.1 Sun photometer measurements from ground

The principle of a Sun photometer is to point a detector directly towards the Sun and to measure radiances at several wavelengths. The attenuation of the direct radiance between the Sun and the instrument is due to scattering and absorption by air molecules and particles like aerosols or water droplets in the atmosphere according to Beer's law (Eq. 2.2). With radiative transfer calculations and calibrations, the part of attenuation produced by the air molecules can be determined. This can be used to extract from the measurement the remaining attenuation caused by particles, and thus their optical depth. The attenuation by clouds is in general too strong to receive direct sun radiance, so Sun photometer measurements are mainly used to explore aerosols and trace gases. For this purpose, the data is first screened to remove cloud contaminated data, then the AOD is calculated. By comparing the AODs of the spectral channels, also the Ångström exponent κ can be calculated to gain information about the size of the particles. Thereby κ is a column value which in case of several aerosol layers of different types is a weighted mean value between the types. Then κ is of limited informational value because it cannot be used to identify the aerosol type in the single layers.

2.2.2 Space borne spectroradiometer measurements

In contrast to the spatially limited ground based Sun photometers, measurements from polar orbiting satellites deliver global coverage. However, the derivation of optical properties such as AOD is more complex: the transmission through the atmosphere in both directions as well as scattering in all of the atmosphere, ground reflection, and the viewing geometry need to be considered, see Fig. 2.3.

To derive the optical information from space borne instruments, the spectroradiometers measure incoming radiances at several wavelengths in the region of 300 nm to 2 μm. The measured radiances are compared with pre-calculated look-up tables which contain radiances for a multitude of different atmospheric scenarios and viewing geometries. In

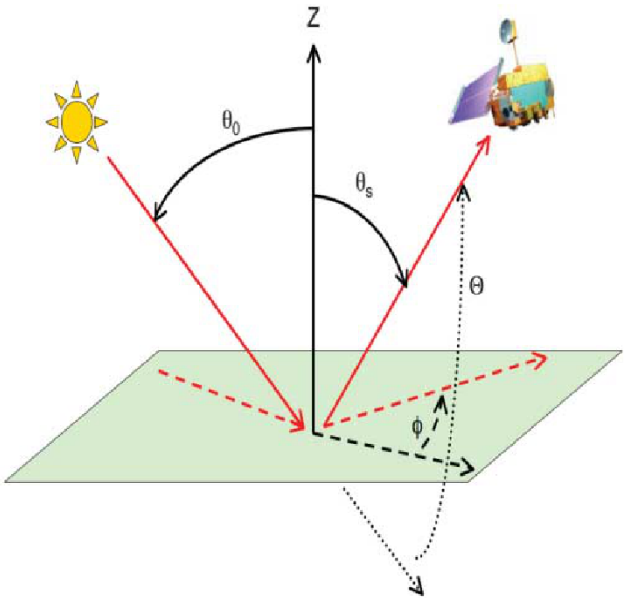

Figure 2.3: Viewing geometry for satellite remote sensing; source: Fig. 2.1 of Kokhanovsky and de Leeuw [2009].

these scenarios, several parameters like the AOD, the surface albedo, and the size distribution of the aerosol particles are varied, from which the radiances of the look-up tables are calculated using radiative transfer models. The best fitting solutions of the look-up tables are then interpolated to obtain the AOD for the measured radiance of each wavelength. Obviously the quality of the retrieved AOD depends on the capability of the models. In particular the reflectivity of the surface over land is difficult to take into account: in contrast to the ocean, the land surface is highly variable depending on the cultivation of the region. Also, the assumption of homogeneous atmospheric conditions for the two transmissions through the atmosphere is often not met, especially when the angles between the pathways are large [Kokhanovsky and de Leeuw, 2009].

The presence of clouds – as was already the case for ground based instruments – in general makes it impossible to gain information on aerosols. Newer instruments, such as e.g. POLDER, also measure the polarization of the radiance and use this additional information for an improved retrieval.

2.3 Active Remote Sensing

In contrast to passive remote sensing instruments, active systems have their own radiation source. Therefore they are independent of natural sources and their limitations (e.g. the Sun photometer can only measure during day time). The active systems are mainly composed of two parts: the emitter which repeatedly sends out short pulses of electromagnetic

waves, and the detector which measures the returning signal as a function of time. Through the time resolved measurements, it is possible to obtain height resolved information.

Depending on the size order of the meteorological parameter to be studied, suitable wavelengths of the same order are used. A radar (radio detection and ranging) system emits wavelengths in the order of 0.3 mm to 10 cm [Kollias et al., 2007]and is therefore well suited to detect particles like water droplets and ice crystals to locate clouds and precipitation. The size order of aerosol particles is smaller, from about 10 nm to 10 μm, so lidar (light detection and ranging) systems which operate at wavelengths of about 300 nm to 2 μm are more suitable for aerosol detection. The radiation source at these wavelengths is a pulsed laser. There are several kinds of lidar systems: the basic backscatter lidar, the Raman lidar, the high spectral resolution lidar (HSRL), and the differential absorption lidar (DIAL).

In the following, I will discuss the lidar systems relevant for this thesis, i.e. the backscatter and the Raman lidar. While the aerosol information from the passive instruments can be obtained directly as AOD from the corresponding platforms, the data of the ground based lidar –as well as some data of the CALIPSO lidar– had to be analyzed by myself, so a special focus of this chapter is set on the lidar data analysis.

A thorough overview of lidar measurement techniques can be found in Weitkamp [2005].

2.3.1 Backscatter lidar

A lidar system consists of two parts: the emitter and the detector. The emitter is a laser which emits pulses at one or more discrete wavelengths. As detector a telescope and photomultipliers or photo diodes are used to measure backscattered light.

The basic concept of a lidar system is the backscatter lidar. A part of the photons sent into the atmosphere are elastically backscattered on particles and molecules at a scattering angle of 180° and then detected temporally highly resolved by the lidar system at the same wavelength. The probability of the photons being scattered by 180° is given by the so called backscatter coefficient β ($= \frac{P(180^\circ)}{4\pi\alpha}$, where P is the scattering phase function).

The resolution - the so-called range bin Δr - depends on the sample rate t_s of the detector, and is given as: $\Delta r = \frac{ct_s}{2}$. The distance of the scattering particle to the lidar system is the range. In case of the lidar pointing to the zenith, the range is equivalent to the height, otherwise the range has to be corrected to height above ground by being multiplied with the cosine of the zenith angle. The received backscatter signal P is described by the lidar equation:

$$P_\lambda(r) = C_L O(r) \frac{1}{r^2} \left(\beta_m(r) + \beta_p(r)\right) \exp\left[-2 \int_0^r \left(\alpha_m(r') + \alpha_p(r')\right) dr'\right] \tag{2.11}$$

The backscatter signal $P_\lambda(r)$ at range r for wavelength λ is dependent on the backscatter coefficients of particles $\beta_p(r)$ and molecules $\beta_m(r)$ at the distance r and the transmission

(Eq. 2.4) through particles and molecules along the way between the laser, the backscatter at distance r, and the transmission on the way back, hence the factor 2 in the exponent.

The so-called lidar constant C_L combines system specific information like the energy of the outgoing laser pulse, the system efficiency, and the geometry of the telescope. These parameters are usually all constant, therefore C_L is stable. While it is therefore difficult to determine this constant, for most solutions of the lidar equation this is not necessary. The overlap function $O(r)$ describes the amount of overlap between the field of view of the telescope and the cross section of the laser beam, and is dependent on the system design. It is very difficult to obtain the function itself: $O(r)$ has a different behavior for each measured wavelength and is very sensitive to the alignment of the laser and detector. But generally it is sufficient to determine the range at which full overlap is reached ($O(r) = 1$) and to use only data above this range.

With a lidar system, a solid angle, given by the distance and the detector aperture, is analyzed, whereby the signal becomes proportional to the inverse of the squared range: $P(r) \propto \frac{1}{r^2}$. For a better detection of atmospheric structures, the signal can be 'range corrected', meaning multiplied by r^2 to get rid of this purely geometric range dependency which overlies the atmospheric structures. This range corrected signal is then used in so called 'quicklooks': images where the strength of the signal Pr^2 is color coded against time and height, with which the atmospheric conditions and their changes by time can be visualized. Fig. 2.4 shows an example of such a quicklook. The y axis shows the height of the signal from ground up to 13 km, while the x axis shows the time from 17:54 to 21:10 UTC. Several structures can be seen: due to the overlap, there is no signal from ground to ≈ 0.3 km. Above this, a strong layer can be identified in green colors up to ≈ 1.5 km. This layer is the so-called planetary boundary layer (PBL), the lowest part of the atmosphere, in which most turbulence and mixing occur. Its behavior is directly influenced by its contact with the surface, so in general the highest aerosol concentration can be measured in the PBL. In the first half hour, there are strong signals (white) from clouds on top of the PBL, which are partly so optically dense that the signal is totally attenuated and no information can be gained above (black). Also fine homogenous structures in light blue colors extend over the whole time period up to 4 km height; these are optically very thin elevated aerosol layers. In the upper atmosphere, the strong return of cirrus clouds mainly in yellow, red, and white can be seen, their base decreasing with time from 10.5 km down to 9 km. The white stripes are gaps in the measurement due to calibrations of the instrument.

For some lidar systems it is possible to obtain the lidar constant C_L via calibration. Then the range corrected signal can be normalized by dividing with the lidar constant, assuming full overlap:

$$\beta'_\lambda(r) = \frac{P_\lambda(r)r^2}{C_L} = \beta_\lambda(r)T^2 \tag{2.12}$$

β' is the attenuated backscatter, only dependent on the backscatter coefficients and the transmission.

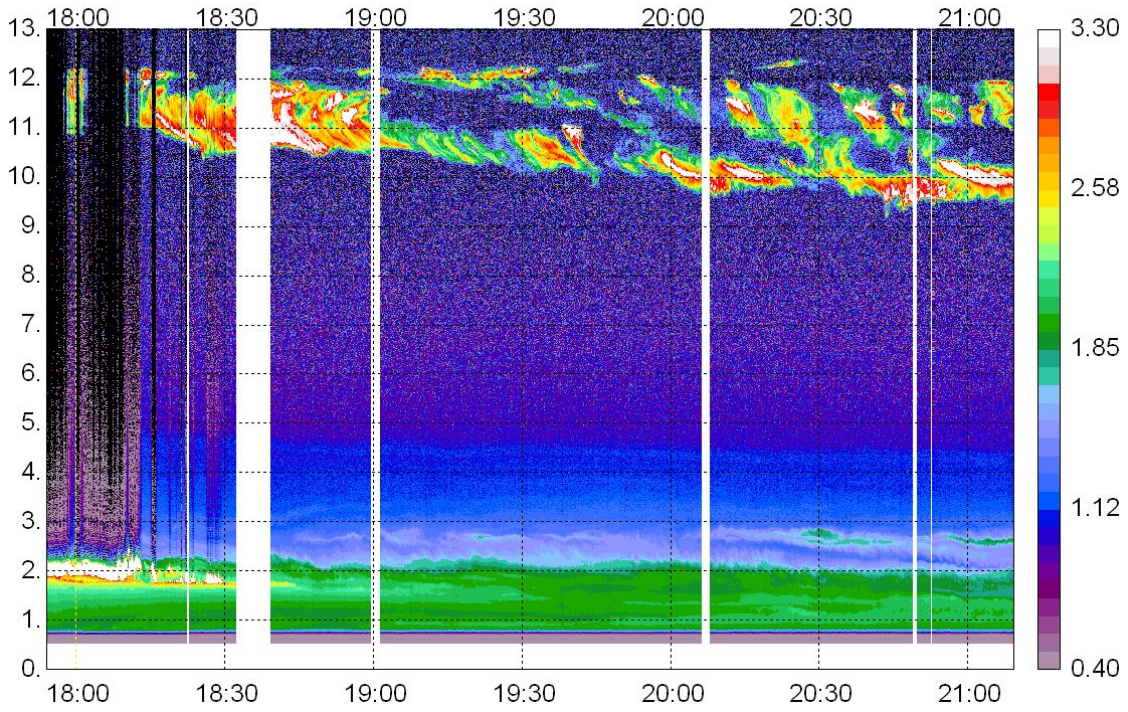

Figure 2.4: Example quicklook with range corrected backscatter signal Pr^2 of the 19th August 2010, 17:54 to 21:10 UTC. he height is given in km a.s.l. with MULIS at 0.516 km a.s.l..

Molecular part

The lidar equation 2.11 is an equation with four unknown parameters (β_m, β_p, α_m, α_p) but only one measurement for each range bin. To solve this equation and to receive the optical parameters of the particles (β_p, α_p) it is necessary to use further sources to reduce the number of unknowns. The scattering of photons on air molecules is described by the Rayleigh theory, which specifies the interaction between EM waves and particles of radius s under the condition $\lambda \gg s$. The extinction coefficient of the air molecules, α_m, can be calculated from the air density $\rho_L(r)$. The vertical profile of the air density can be obtained from several sources. The most common ones for lidar analysis are global weather models or nearby radiosonde measurements. To a very good approximation, the backscatter coefficient of air molecules β_m is proportional to the extinction coefficient and can be calculated by:

$$\beta_m(r) = \frac{3}{8\pi}\alpha_m(r) \tag{2.13}$$

Even with the determination of the molecular contribution, two unknowns for one equation are left. With a backscatter lidar it is not possible to solve this problem without further assumptions.

Lidar ratio

Without further measurements the lidar equation for a backscatter lidar is solved by presetting the (height dependent) lidar ratio, the ratio between extinction and backscatter coefficient. From Eq. 2.13 it is obvious that the molecular lidar ratio is constant and independent of the lidar wavelength:

$$S_m = \frac{\alpha_m}{\beta_m} = \frac{8\pi}{3} sr \approx 8.378 sr \tag{2.14}$$

The particle lidar ratio S_p is defined as $\frac{\alpha_p}{\beta_p}$. Because of its dependence on the microphysical properties of the particles, it can vary with height.

$$S_p(r) = \frac{\alpha_p(r)}{\beta_p(r)} \tag{2.15}$$

The lidar ratio of aerosols can vary from about 15 sr to 100 sr [Weitkamp, 2005] and is dependent on the microphysical and optical properties of the aerosol type. As examples, marine aerosols containing mainly sea salt have values of about 20 sr, while Mineral dust lidar ratios are at about 55 sr to 60 sr. For the data analysis of a backscatter lidar, the lidar ratio can be estimated by using Sun photometer data like the AOD or the Ångström exponent or by requesting additional meteorological information from atmospheric trajectory models (e.g. the HYSPLIT model [Draxler and Rolph, 2012]) to locate the source of the aerosol load and thereby make an assumption about the aerosol type, for which then a a predefined lidar ratio is used.

The lidar ratios can be derived from aerosol data bases containing optical parameters, e.g. OPAC [Hess et al., 1998]. However, in OPAC the optical properties are only calculated for spherical particles, so that calculations for Mineral dust – which has a crystalline and therefore non-spherical structure – can lead to incorrect values. It is also possible to obtain the lidar ratio through measurements with other instruments, e.g. with a Raman lidar (see Sect. 2.3.2) or in-situ measurements. Additionally, there are several field campaigns to study optical and microphysical parameters of specific aerosol types like the SAMUM campaigns to study Saharan dust [Heintzenberg, 2009] or the ACE (Aerosol Characterization Experiment) campaigns to study different aerosol types [Verver et al., 2000, Arimoto et al., 2006].

With a given particle lidar ratio, it is possible to replace the backscatter coefficient with the extinction coefficient (or vice versa) so that only one unknown is left over in the lidar equation.

Klett method

The most common method to calculate the extinction coefficient α_p is the Klett method [Klett, 1985]. It is the analytic solution of the lidar equation (Eq. 2.11) requiring the presetting of the molecular properties α_m and β_m, the particle lidar ratio $S_p(r)$ as well as the reference value $\alpha_p(r_{\text{ref}})$ at a reference range r_{ref}. The solution is:

$$\alpha_p(r) = \frac{Z_\alpha(r)}{N_\alpha(r)} - \frac{S_p(r)}{S_m}\alpha_m(r) \tag{2.16}$$

with

$$Z_\alpha(r) = S_p(r) r^2 P(r) \exp\left\{2\int_r^{r_{\text{ref}}} \left[\frac{S_p(r)}{S_m} - 1\right] \alpha_m(r')dr'\right\}$$

and

$$N_\alpha(r) = \frac{S_p(r_{\text{ref}}) r_r^2 P(r_{\text{ref}})}{S_p(r_{\text{ref}})\beta_m(r_{\text{ref}}) + \alpha_p(r_{\text{ref}})} + \int_r^{r_{\text{ref}}} Z_\alpha(r')dr'$$

The backscatter coefficient can then easily be calculated using Eq. 2.15.

For ground based lidar systems the analysis usually starts at a reference height in an aerosol free region of the atmosphere above the PBL and is calculated down to the overlap height. This Klett method with the backscatter signal $P(r)$ inversed from the reference height r_{ref} to the range r_0 near the lidar system is called 'backward'. The inversion of the lidar equation is numerically much more stable, as it is calculated from small values of α_p in direction to increasing values than the reverse. Additionally, the highest aerosol amount can normally be found in the PBL. Accordingly, the choice of r_{ref} in the aerosol free atmosphere is a benefit for the stability of the solution. There is also a forward solution which can be used for aircraft measurements. However, this solution is mathematically more unstable due to a difference in the denominator of N_α.

Reference value

The analytical solution of the lidar equation for the particle extinction coefficient is the solution of a differential equation and therefore demands a boundary condition. This boundary value is the reference value $\alpha_p(r_{\text{ref}})$ at the reference range r_{ref} and has to be estimated just as the lidar ratio S_p. If the reference value is set wrong, this can lead to severe errors in the calculation of the coefficient – depending on the numerical stability of the analytic method. Therefore it is necessary to have a good estimation of the reference value.

There are two options: for one, the reference can be chosen in the free atmosphere above the PBL in which no aerosols can be assumed. The reference value can therefore be set as $\alpha_p(r_{\text{ref}}) = 0$. The other option is to get the reference from a directly measured extinction coefficient with in-situ instruments. In case of the in-situ measurement being collocated with the lidar system (e.g. both located at the surface or at an airplane), the overlap of the lidar has to be taken into account as the lidar measurement normally does not reach the ground.

Newton Raphson

A more stable solution for forward inversion is the Newton Raphson method which is particularly suitable for aircraft and space borne measurements and which is used in the analysis of CALIPSO data [Young et al., 2008]. It is an iterative method to calculate the root of a function. The Newton Raphson method demands the same input as the Klett method, but here in contrast a bad choice of the reference value r_{ref} only leads to an increase of iteration steps, not to a wrong calculation of α_p. Therefore this solution is more tolerant to noise than the Klett method and accordingly better to handle space borne measurements. The function for which the root needs to be found is the difference between the measured signal and a modeled signal, which is calculated from the estimate of α_p:

$$f_r(\alpha_p) = \beta'(r) - M_r^n(\alpha_p(r)) \tag{2.17}$$

$\beta'(r)$ is the measured attenuated backscatter (Eq. 2.12). For each range bin the particle extinction coefficient $\alpha_p(r)$ and a corresponding modeled attenuated backscatter $M_r(\alpha_p(r))$ are alternately calculated over several iteration steps until a given criteria is reached. β' and the modeled attenuated backscatter M_r (and therewith also f_r) are dependent of the range r. In the Newton Raphson method the coefficient α_p is calculated separately for each range. In order to ensure better readability, in the following equations the notation of the range dependency is dropped for all parameters but the transmission, while all parameters refer to the same range value. The index n is the number of the iteration step. The guess value of α_p for the next iteration step is calculated using:

$$\alpha_p^{n+1} = \alpha_p^n - \frac{f(\alpha_p^n)}{f'(\alpha_p^n)} \text{ with } f'(\alpha_p) = \frac{\mathrm{d}f}{\mathrm{d}\alpha_p} \tag{2.18}$$

The modeled signal is gained directly from the lidar equation:

$$\frac{Pr^2}{C_L} = M^n(\alpha_p^n) = \left(\frac{\alpha_p^n}{S_p} + \beta_m\right) * T^2(0, r_{\text{ref}}) * T^2(r_{\text{ref}}, r) \text{ with } 0 \leq r_{\text{ref}} \leq r \tag{2.19}$$

For satellite measurements the extinction between lidar and reference height on top of a detected layer can be neglected; the transmission is assumed to be one ($T^2(0, r_{\text{ref}}) = 1$). Similar to the Klett algorithm, the meteorological conditions to calculate the molecular part of extinction and backscatter coefficient need to be known and the particle lidar ratio S_p has to be assumed. The function f is derived from Eqs. 2.17 and 2.19:

$$f(\alpha_p^n) = \beta' - M^n(\alpha_p^n) = \beta' - \left(\frac{\alpha_p^n}{S_p} + \beta_m\right) T_m^2(r_{\text{ref}}, r) T_p^2(r_{\text{ref}}, r) =$$

$$= \beta' - \left(\frac{\alpha_p^n}{S_p} + \beta_m\right) T_m^2(r_{\text{ref}}, r) T_p^2(r_{\text{ref}}, r - \Delta r) \exp\left\{-2 \int_{r-\Delta r}^{r} \alpha_p^n(r') dr'\right\} =$$

$$= \beta' - \left(\frac{\alpha_p^n}{S_p} + \beta_m\right) T_m^2(r_{\text{ref}}, r) T_p^2(r_{\text{ref}}, r - \Delta r) \exp\left\{-\left[\alpha_p(r - \Delta r) + \alpha_p^n\right] \Delta r\right\}$$

with Δr being the range resolution. Also, the transmission T is split into the molecular part, T_m, and the part induced by the aerosol particle extinction, T_p. Taking the derivative of this equation with respect to α_p results in:

$$f'(\alpha_p) = \frac{\mathrm{d}f}{\mathrm{d}\alpha_p} = T_m^2(r_{\text{ref}}, r) T_p^2(r_{\text{ref}}, r - \Delta r) \exp\left[-\alpha_p(r - \Delta r)\Delta r\right] \exp\left[-\alpha_p^n \Delta r\right] \left(\frac{\alpha_p^n}{S_p} \Delta r + \beta_m \Delta r - \frac{1}{S_p}\right)$$

Part of this equation substituted by M^nleads to

$$f'(\alpha_p) = M^n(\alpha_p^n) * \frac{1}{\frac{\alpha_p^n}{S_p} + \beta_m} \left(\frac{\alpha_p^n}{S_p} \Delta r + \beta_m \Delta r - \frac{1}{S_p}\right) =$$

$$= M^n(\alpha_p^n) \left(\Delta r - \frac{1}{\alpha_p^n + \beta_m S_p}\right)$$

Inserting this into Eq. 2.18 gives the particle extinction coefficient of the iteration step n+1:

$$\alpha_p^{n+1} = \alpha_p^n - \frac{\beta' - M^n(\alpha_p^n)}{M^n(\alpha_p^n)} \left(\Delta r - \frac{1}{\alpha_p^n + \beta_m S_p}\right)^{-1} \tag{2.20}$$

In the same way the particle backscatter coefficient can be determined:

$$\beta_p^{n+1} = \beta_p^n - \frac{\beta' - M^n(\beta_p^n)}{M^n(\beta_p^n)} \left(S_p \Delta r - \frac{1}{\beta_p^n + \beta_m}\right)^{-1} \tag{2.21}$$

One iteration is performed by successively calculating Eqs. 2.19 and 2.20 for each range bin, starting at the range bin at the reference height, and using as initial guess $\alpha_p^0(r_{\text{ref}}) = \alpha_p(r_{\text{ref}})$ and in each following range bin the solution of the previous bin, $\alpha_p^0(r) = \alpha_p^0(r - \Delta r)$. The criteria to stop the iteration can be to reach a certain amount of iteration steps ($n = N$) or the change of the coefficient within two steps being smaller then a given percentage (e.g. $\left|\frac{\alpha_p^n - \alpha_p^{n-1}}{\alpha_p^n}\right| < 1\%$). Generally the iteration converges very fast, a criterion of N = 5 is mostly sufficient.

Concluding, with the Newton Raphson method it is possible to derive the extinction coefficient profile, but it is, as with the Klett algorithm, dependent on the right choice of the particle lidar ratio.

2.3.2 Raman lidar

An alternative to estimate the lidar ratio is to actually measure it with a Raman lidar [Ansmann et al., 1992]. In this approach, a backscatter lidar is improved by adding detectors at certain wavelengths to measure inelastic backscattered photons on molecules like nitrogen N_2 or oxygen O_2. At an inelastic scattering process, a discrete part of the energy of the photon is used to change the rotational (and vibrational) state of the molecule. The discrete energy change of the photon leads to a constant in- or decrease of the wavelength. For known molecules this energy contribution and hence the shifted wavelength λ_R can be calculated accurately: e.g. for N_2, the emitted wavelength $\lambda_0 = 355$ nm shifts to 387 nm, and the wavelength 532 nm to 607 nm. As the inelastic backscattered signal is only affected by aerosol extinction and not by aerosol backscattering, it is possible to determine the aerosol extinction directly from the altered lidar equation

$$P(r, \lambda_R) = C_L^R O(r) \frac{1}{r^2} \beta^R(r) \exp\left[-\int_{r_0}^{r} \left[\alpha(r', \lambda_0) + \alpha(r', \lambda_R)\right] dr'\right] \tag{2.22}$$

Because the wavelength changes during the inelastic backscatter process, the transmission of the backscatter signal detected atλ_R between laser and backscatter event is taken at the original wavelength λ_0, while for the further transmission to the detector the transmission depends on the extinction coefficient at the shifted wavelength λ_R. The term β^R describes the Raman backscatter coefficient instead of the elastic backscatter coefficientβ_p and can be calculated from meteorological data:

$$\beta^R = n_g \frac{d\sigma^R(180°)}{d\Omega}$$

It is the differential Raman scattering cross section σ^R at 180° multiplied by the number density n_g of the Raman scattering molecules. Thereby n_g is proportional to the air density $\rho_L$which leads to $\beta^R \propto \rho_L \propto \alpha_m(\lambda_0)$.

Combined with the elastically backscattered signal $P(r, \lambda_0)$, see Eq. 2.11, it is possible to obtain the extinction coefficient α_p and the backscatter coefficient β_p separately and so to determine the lidar ratio. Solving Eq. 2.22 for $\alpha_p(r, \lambda_0)$ leads to

$$\alpha_p(r,\lambda_0) = (1+f_p)^{-1}\left[\frac{d}{dr}\ln\left(\frac{\alpha_m(r,\lambda_0)}{P(r,\lambda_R)r^2}\right) - \alpha_m(r,\lambda_0)\left[1+f_m\right]\right] \tag{2.23}$$

where f_m and f_p describe the wavelength dependencies (with the aerosol Ångström exponent κ) of the extinction and are defined as:

$$f_m = \left(\frac{\lambda_0}{\lambda_R}\right)^{4.085} \text{ and } f_p = \left(\frac{\lambda_0}{\lambda_R}\right)^{\kappa}$$

This calculation of α_p is not only independent of the choice of a lidar ratio, but also of a reference value. Only a slight dependency on the Ångström exponent κ can be observed. Fortunately, the influence of κ is very minor, so in general a value of $\kappa = 1$ can be used without causing strong errors.

In contrast, the calculation of the particle backscatter coefficient β_p needs the assumption of the reference value at reference height r_{ref}:

$$\beta_p(r,\lambda_0) = \left[\wp(r)E(r) - 1\right]\beta_m(r,\lambda_0) \tag{2.24}$$

with the signal ratio of elastic and inelastic backscatter signals:

$$\wp(r) = \frac{P(r,\lambda_0)P(r_{\text{ref}},\lambda_R)}{P(r_{\text{ref}},\lambda_0)P(r,\lambda_R)}$$

and

$$E(r) = \frac{\exp\left\{-\int_{r_0}^{r}\left[\alpha_p(\lambda_R,r') + \alpha_m(\lambda_R,r')\right]dr'\right\}}{\exp\left\{-\int_{r_0}^{r}\left[\alpha_p(\lambda_0,r') + \alpha_m(\lambda_0,r')\right]dr'\right\}}$$

The big advantage of the Raman lidar is the independent determination of α_p and β_p and therewith to gain height resolved the particle lidar ratio $S_p = \frac{\alpha_p}{\beta_p}$. A limitation of the method is that the Raman signal is several orders of magnitude lower than the elastic one because of the very small Raman backscatter coefficient β^R. The background noise has to be kept low, thus Raman measurements are mainly performed at night time conditions, while during daytime often only the elastic signals can be measured. To get a sufficiently high signal-to-noise ratio (SNR) for analysis even at night it is often necessary to average measurements over long periods of time (1-2 hours) which requires a homogenous atmosphere.

2.3.3 Depolarization lidar

In general, the emitted laser pulse is linearly or circularly polarized. Through the interaction with particles during the scattering process, the polarization direction of the EM wave can be changed. The amount of depolarization depends on the shape and size of the particles: spherical particles backscatter the emitted EM wave with the same polarization

orientation, while aspherical particles change this orientation. The EM wave is 'depolarized', i.e. part of the backscatter signal has a different polarization orientation, the degree of depolarization depending on the shape of the particles. Here only the calculations for the linearly polarized light are explained in detail, as both lidar instruments discussed in this thesis use this depolarization measurement.

To measure the degree of depolarization with a lidar system, the signal of a detected wavelength is split by cubic beam splitters into the contributions parallel ($P_\parallel$) and perpendicular ($P_\perp$) to the laser polarization. Hence

$$P_X(r) = C_{LX} O(r) \frac{1}{r^2} \beta_X(r) \exp\left[-2 \int_{r_0}^{r} \alpha(r')dr'\right] \tag{2.25}$$

where X is either $\perp$ or $\parallel$. Very important for the analysis of the signals is the determination of the calibration constant $C_\delta = \frac{C_\parallel}{C_\perp}$ which describes the ratio of the detection efficiencies of the two channels. Cross talk can be suppressed by using additional neutral filters in front of the signal detectors. For a complete description about the depolarization calibration see Freudenthaler et al. [2009]. The calibrated ratio between the perpendicular and the parallel channel is the same as the ratio between the parallel ($\beta_\parallel$) and perpendicular ($\beta_\perp$) component of the total backscatter coefficient and is called the volume linear depolarization ratio δ_v:

$$\delta_v = \frac{\beta_\perp}{\beta_\parallel} = C_\delta \frac{P_\perp}{P_\parallel} \tag{2.26}$$

It is a first indicator of the presence of non-spherical particles, but cannot be used to help identify the aerosol type, since $\beta_{p\parallel}$ and $\beta_{p\perp}$ contain the backscatter signals of both molecules and particles.

To gain the 'pure' particle information it is necessary to determine the particle linear depolarization ratio δ_p, the ratio between the parallel ($\beta_{p\parallel}$) and perpendicular ($\beta_{p\perp}$) component of the particle backscatter coefficient. For its calculation the volume linear depolarization ratio and the backscatter coefficients β_m and β_p need to be known [Biele et al., 2000]:

$$\delta_p = \frac{\beta_{p\perp}}{\beta_{p\parallel}} = (\delta_v + 1)\left(\frac{\beta_m(\delta_m - \delta_v)}{\beta_p(1 + \delta_m)} + 1\right)^{-1} - 1 \tag{2.27}$$

The depolarization ratio of air molecules δ_m calculated from the Rayleigh theory is approximately $\delta_m \approx 0.36\%$ [Behrendt and Nakamura, 2002] but a wavelength dependency needs to be considered for precise studies.

δ_p is an intensive parameter dependent on the microphysical properties of the particles but not on the particle concentration, and is therefore a suitable parameter to define aerosol types. For example, at 532 nm the strongly non-spherical Saharan dust aerosols has typical values around 0.30, while the nearly spherical marine aerosols have very small values around 0.01 to 0.02 [Groß et al., 2011].

2.3.4 Multi wavelength measurements

The laser frequency of a lidar system like the Nd:YAG can simultaneously be doubled or tripled, so that more wavelengths can be emitted. By adding corresponding detectors, it is possible to measure the signals of several wavelengths at the same time. From the backscatter signals of two wavelengths λ_1 , λ_2 the so called color ratio X can be calculated:

$$X(r) = \frac{P(\lambda_1, r)}{P(\lambda_2, r)} \tag{2.28}$$

As it is derived from the ratio of two different and uncalibrated signals, X is no intensive parameter and cannot be used directly to get information about the particle size or to identify aerosol types. However, like the volume depolarization ratio, it can be a first step towards estimating the aerosol type and by this the lidar ratio.

In contrast to this, the Ångström exponent κ (Eq. 2.8), which is dependent on the particle size, is an intensive property which can be used to distinguish different aerosol types. The left panel in Fig. 2.5 shows the particle extinction coefficients at the three wavelengths 355 nm, 532 nm, and 1064 nm. While the three lines are separate in the PBL up to 2 km, they are superposed at the elevated layer from 2.2 km to 3.2 km. This behavior can be quantified by the Ångström exponent (middle panel) which has values > 1 for all κ at the PBL and clearly smaller values in the elevated layer, which shows that the particles in the elevated layer are larger than the ones in the lower layer.

An additional parameter to distinguish between the different aerosol types is the linear particle depolarization ratio (shown in the right panel): obviously the same differentiation between the upper and lower layer can be seen. While the boundary contains aerosols with low δ_p of about 2.5 %, the elevated layer is highly depolarized $\delta_p \approx 35$ % which indicates aspherical particles.

2.4 Summary

In this chapter, the interaction between light and particles described by Beer's law is discussed as basis of remote sensing of aerosols in the atmosphere. As aerosols have different optical properties dependent on their composition, shape, size, as well as their amount, they can be distinguished by lidar and spectrometer instruments using parameters like the extinction coefficient α_p , the aerosol optical depth AOD, the Ångström exponent κ, and the particle linear depolarization ratio δ_p. Accordingly, passive remote sensing instruments in general give information about column values while lidar systems can also gain height resolved data. At the same time, it is easier for passive systems to operate continuously and provide global coverage. All instruments need assumptions like the knowledge of the meteorological conditions or a reference value. A very important presetting is also the lidar ratio S_p, which has to be assumed for backscatter lidars but can be measured directly by Raman lidars during night time.

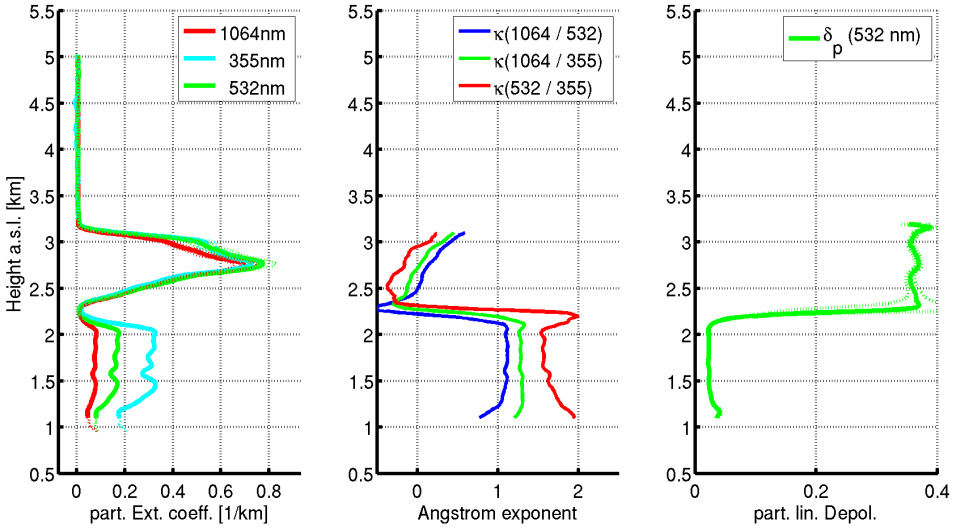

Figure 2.5: Example of particle extinction coefficient at 355 nm, 532 nm, and 1064 nm (left), the corresponding Ångström exponents (middle) and particle linear depolarization ratio at 532 nm (right); measured with the lidar system MULIS over Maisach at 6:30 UTC on 17 April 2010.

Chapter 3

Instrumentation, data and methods

This chapter describes the four instruments used in this thesis and defines the used datasets and the region of interest – the Munich region. The instruments are the Sunphotometer of AERONET, the spectroradiometer MODIS, the ground based Raman-Lidar MULIS and space lidar of the satellite CALIPSO. Special emphasis is put on the complex data retrieval of CALIPSO. In the last section, a quality analysis of the CALIPSO measurements is performed by comparing them with MULIS measurements collocated in space and time.

3.1 Definition of the Munich region

First the region to study the aerosol distribution needs to be defined. This region is further called the 'Munich region' and ranges over $\pm 1.5°$ around Maisach: 46.7°-49.7°N latitude and 9.8°-12.8°E longitude. CALIPSO overpasses this region at two nighttime and two daytime tracks, these satellite tracks have a slight variation of ± 10 km within the four years [Winker et al., 2009]. Fig. 3.1 shows the whole region including the averaged footprint paths of CALIPSO (blue); in cyan, the track of all overpasses of CALIPSO for the years 2007 to 2010 are shown to demonstrate the slight variation from track to track. Obviously, CALIPSO covers only a small part of the region; for most parts of the area no CALIPSO data is available, including Maisach with no direct overpasses. In addition to the CALIPSO footprints, the two measurement sites Maisach (MULIS) and Munich (AERONET) are shown as stars (magenta and red) in the center of the Munich region. The green rectangle in Fig. 3.1 marks the area of the used MODIS data (48°-49°N, 11°-12°E) and will here be called the 'MODIS region'.

3.2 AERONET-Cimel Sunphotometer

The sun photometer used in this study was built by the company Cimel and is part of the Aerosol Robotic Network (AERONET) [Holben et al., 1998]. For every AERONET instrument the same standardized procedures for maintenance, calibration, and data processing are operated to gain worldwide quantitatively comparable aerosol information. The

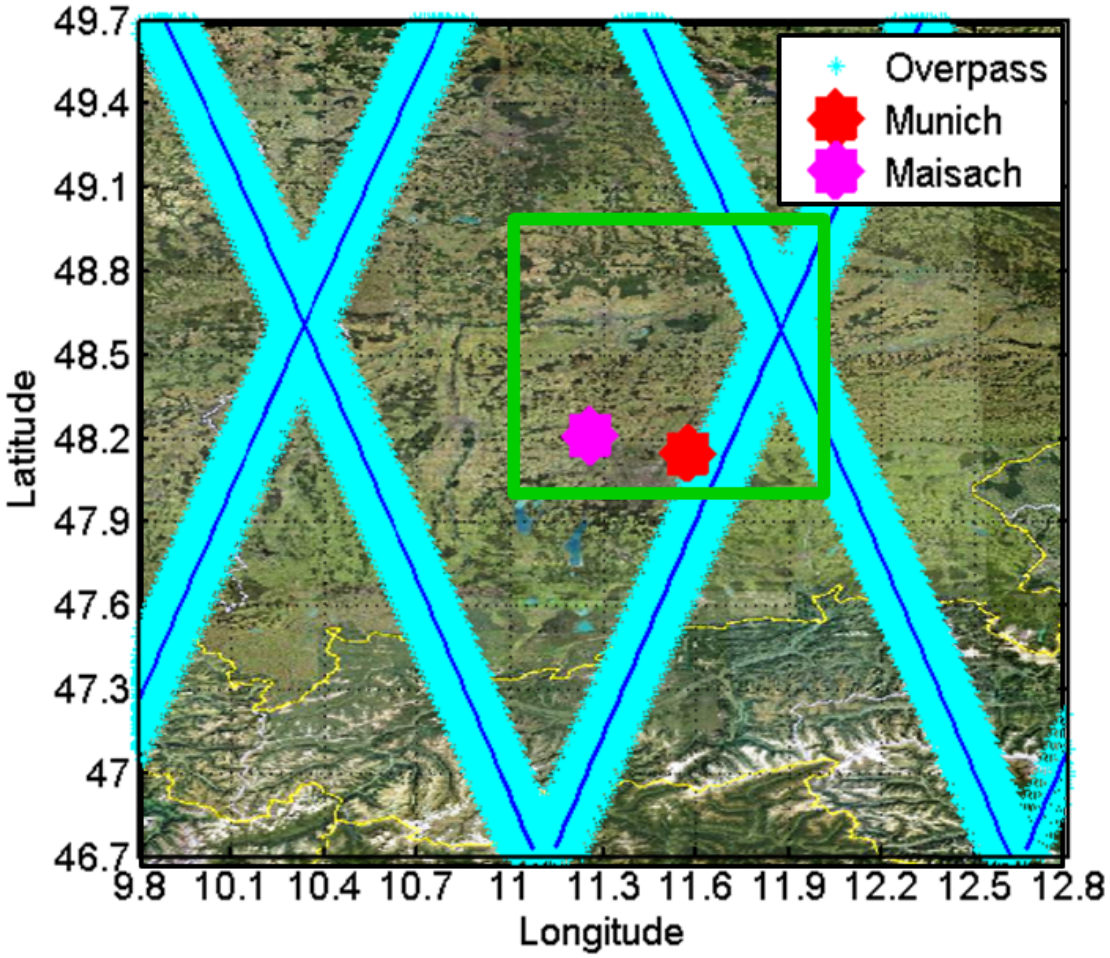

Figure 3.1: Munich region: 46.7°-49.7°N, 9.8°-12.8°E; stars mark the measurement sites for MULIS in Maisach (magenta) and for AERONET in Munich (red), while the blue lines show the averaged path of CALIPSO and the variation of this path within the years 2007 to 2010 is denoted in cyan. The green rectangle shows the used MODIS data.

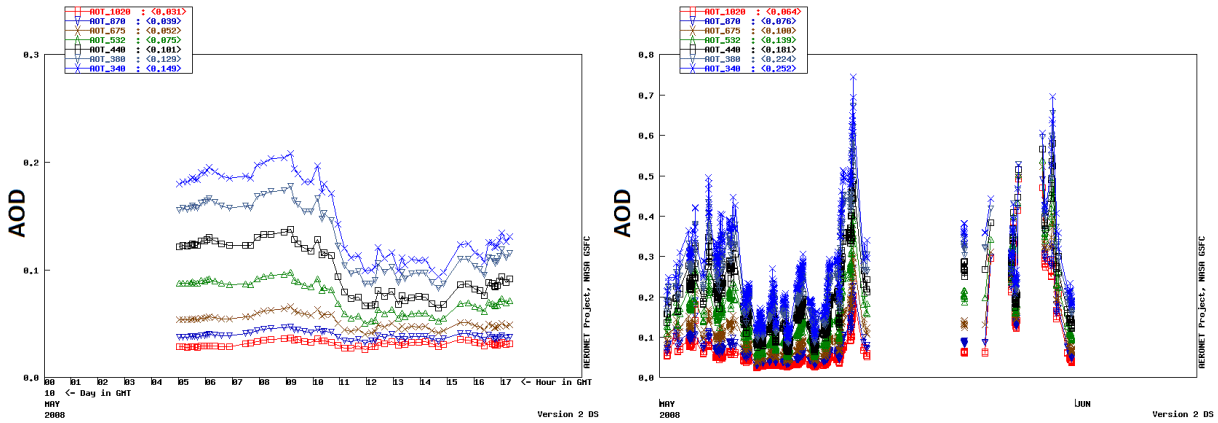

Figure 3.2: AERONET AOD for seven wavelengths over one day (left) and as monthly trend (right). Data were taken in May 2008 at the Munich station. (Source: AERONET Homepage)

instruments provide continuous measurements of the AOD at several wavelengths and as a result of these the Ångström exponents $\kappa(\lambda_1, \lambda_2)$ between these wavelengths.

3.2.1 Instrument

The Cimel Sun photometer is located at the MIM in the center of Munich (48.148°N, 11.573°E, 539 m a.s.l.). Spectral radiances at seven wavelengths (i.e. 1020 nm, 870 nm, 675 nm, 532 nm, 440 nm, 380 nm, and 340 nm) are measured. In 2011, the 532 nm filter, which was chosen for better comparability with the lidar systems of the MIM, was replaced by a 500 nm filter, which corresponds to the regular wavelength used in AERONET instrument. The direct measurements are repeated every 15 minutes. A typical measurement is shown in Fig. 3.2. In the left picture, the spectral AOD measurements over one day is shown for all seven wavelengths. The wavelength dependency is readily identifiable: the AOD increases with decreasing wavelength. At around 11 UTC, the AODs of the smaller wavelengths decrease while the ones of higher wavelengths like 1020 nm stay stable. This is a strong indication that the aerosol type has changed at this time. The daily data are averaged to get a monthly overview (right panel of Fig. 3.2). Like the lidar measurements, AERONET data are only available on cloud free conditions.

3.2.2 Used data

In the time period of 2007 to 2010, the Cimel continually collected data, only interrupted during short periods in which the instrument was not available due to calibrations and field campaigns. The number of monthly mean values is shown in Fig. 3.2 (left panel). For most months, the mean values of all four years are available. In November and December, only two monthly means can be used, while in January and August one mean is missed. This is mainly due to calibrations during the winter time and a field campaign from December to

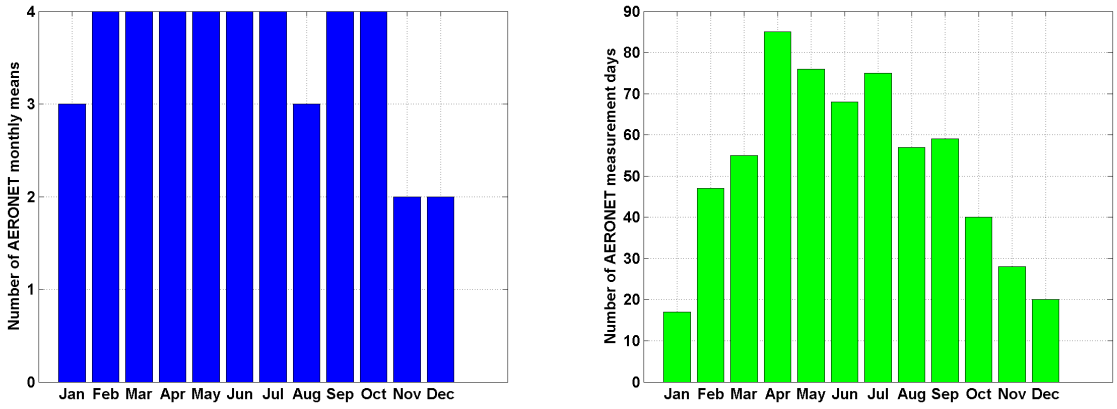

Figure 3.3: Number of used AERONET measurement for study: number of monthly means (left panel) and corresponding number of days used for the monthly data (right panel) in the time period 2007 to 2010.

February. The AERONET monthly data also contain the information about the number of measurement days used for the mean value. These values can be seen in the right panel of Fig. 3.2: In April to July, the most measurements were performed: April and August have the best measurement rate with 70 % and 72 %, respectively. In contrast, January and December in particular do not provide many measurements.

For this study, the level 2.0 AOD are used which are cloud screened and quality assured. Several types of data are available: the 'direct' point measurement every 15 min, the daily average and the monthly average. The weighted monthly mean AODs for all seven wavelengths are used to study the monthly and seasonal variation of the AOD above Munich for the time period of 2007 to 2010. Additionally to the provided Ångström exponent $\kappa(675nm/440nm)$ which matches best the MODIS wavelengths, κ is calculated for the wavelength combinations 1020 nm / 532 nm and 532 nm / 340 nm from the monthly mean AODs using Eq. 2.8 for a better comparability with CALIPSO and MULIS (1064 nm / 532 nm and 532 nm / 355 nm). Additionally, point measurements at 340 nm, 532 nm, and 1020 nm are used for the comparisons with coincident MULIS and CALIPSO measurements.

3.3 MODIS

MODIS (MOderate Resolution Imaging Spectroradiometer) instruments are on-board of the Earth Observation Systems (EOS) TERRA (since 1999) and AQUA (since 2004), satellites on an orbit height of 705 km. Both satellites are polar-orbiting, with TERRA on a descending node (southward) crossing the equator at about 10:30 local time, while AQUA is – as part of the A-Train together with CALIPSO– on an ascending node (northward) passing the equator at about 13:30 local time. Due to a $\pm$ 55° cross track scan, the MODIS swath is about 2330 km broad, so it can provide global coverage every one to two days

[Salomonson et al., 1989].

3.3.1 Instrument

MODIS is a passive remote sensing instrument with which several components of the Earth and its atmosphere are explored. It allows a determination of the spatial and pemporal distribution of the global aerosol and cloud fields as well as to detect forest fires or monitor the vegetation index. It acquires data in 36 spectral bands ranging from 0.4 μm up to 14.4 μm in – depending on the band – three different horizontal resolutions: 250m, 500 m, 1000 m.

In particular MODIS delivers optical properties such as the AOD and the Ångström coefficient, gained through complex retrieval schemes. Three different aerosol retrievals are applied depending on the surface type: for ocean, for land, and the so-called 'Deep Blue' algorithm for bright arid surfaces as for example deserts [Hsu et al., 2004]. All three aerosol retrievals make use of only a small part of the spectral channels.

3.3.2 Aerosol retrieval over land

For the Munich region, the aerosol 'land' algorithm is used. It is based on three channels: two visible (470 nm and 660 nm) and the 2.12 μm (NIR) channel. The NIR channel contains information about large particles – the so-called coarse mode. The algorithm analyzes the data of a nominal region of 10 km $\times$ 10 km (= 20 $\times$ 20 pixel at a resolution of 500 m). All pixels containing clouds, snow, ice, or water are excluded. Also the surface reflectance is taken into account: only pixels with a reflectance at 2.12 μm within the range of 0.01 and 0.25 are selected. As a further criterion, the darkest 20% and the brightest 50% in reflectance at 660 nm of the remaining pixels are discarded to eliminate pixels with possible contamination by clouds and cloud shadows. If at least 12 pixel are left, the mean reflectances of all three wavelengths are used as input parameter for a continental model look-up table of AODs. The ratio between the path radiances of 470 nm and 660 nm is used to select between different aerosol models, 'dust' if the coarse mode dominates and 'non-dust' if the fine mode dominates. These determine the AODs for the two visible wavelengths. For meteorological applications the AOD at 550 nm is often used as standard parameter: therefore it is calculated by an interpolation from the AODs at 660 nm and 470 nm regarding the Ångström law.

3.3.3 Used data

The AOD data from MODIS are available as daily, weekly and monthly averages provided for the three wavelengths 660 nm, 550 nm, and 470 nm. In this study, the monthly mean AODs with a resolution of 1°x1° are used. The dataset is based on the Collection 5.1 Level 3 monthly mean AODs (M3 data) for the years 2007 to 2010. The comparison between the monthly mean data of AQUA and TERRA (Fig. 3.4) shows that the values are very similar, especially from June to November. In January and December, no data from AQUA-MODIS

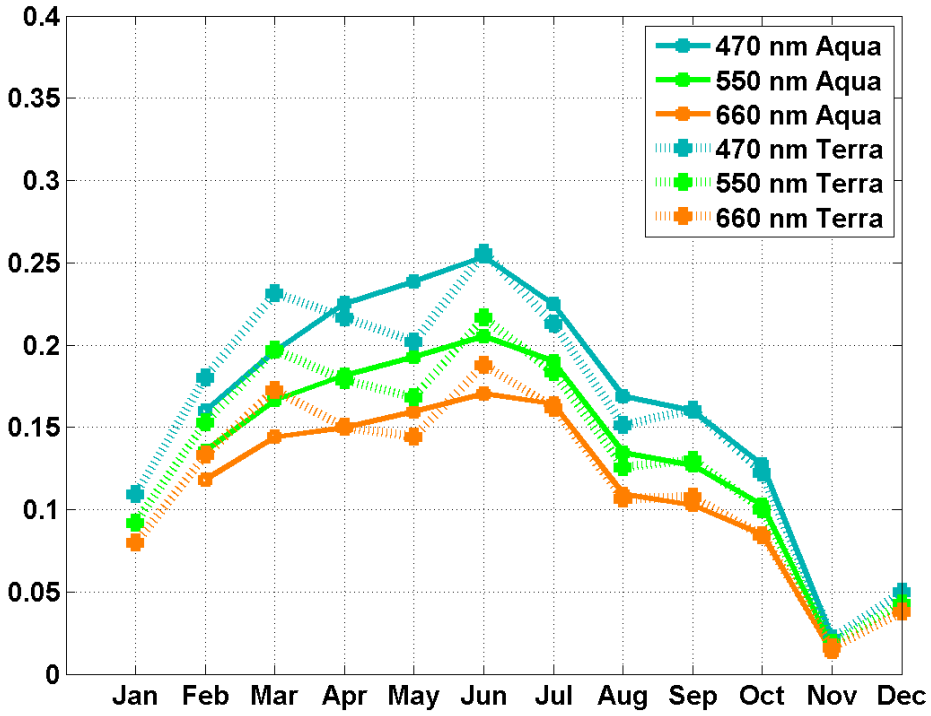

Figure 3.4: Monthly mean AODs of the MODIS instruments on-board of the AQUA (solid line) and TERRA (dotted line) satellites for 660 nm, 550 nm, and 470 nm.

are available, so for further comparison in this work, only the 48 monthly means of the TERRA-MODIS are used.

For TERRA, too, however, the number of available monthly means is not ideal for the winter months (Fig. 3.5: in January and December only for one year the mean is available, also in February and November some means are missed.

As mentioned in the last section, the AOD at 550 nm is not a measured value of MODIS but derived from the AODs at 660 nm and 470 nm. So instead of using the AOD at 550 nm, for this thesis the AOD at 532 nm is calculated to gain a better comparability with the other three instruments.

3.4 MULIS

The MUlti wavelength LIdar System (MULIS) is one of the two lidar systems of the Meteorological Institute Munich and is located at Maisach (48.209°N, 11.258°E, 516 m a.s.l,), 25 km West of Munich in a rural area [Freudenthaler et al., 2009].

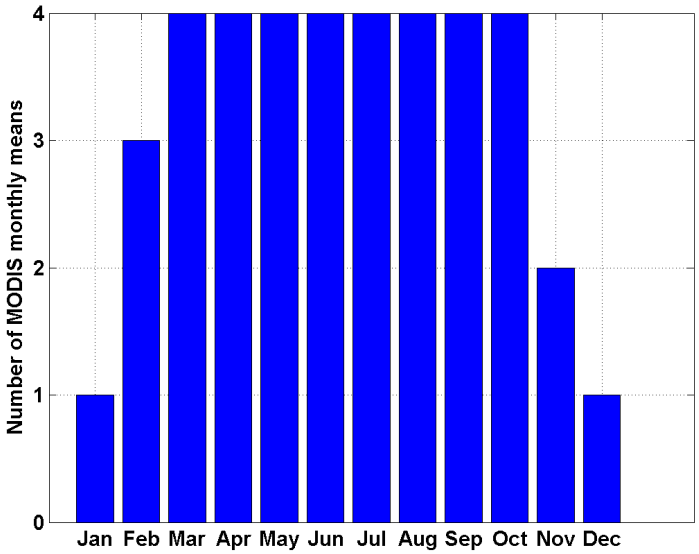

Figure 3.5: Number of available MODIS monthly means in the time period 2007 to 2010.

3.4.1 Description of instrumentation

The Nd:YAG laser of the lidar system emits linear polarized laser pulses at the three wavelengths 1064 nm, 532 nm, and 355 nm at a pulse repetition frequency of 10 Hz. The backscattered signals are detected to derive the corresponding particle backscatter coefficients β_p in a range bin resolution of 7.5 m. By measuring the parallel and the cross polarized backscattered light at 532 nm, it is possible to determine the volume and particle linear depolarization ratios (δ_v, δ_p) and therefore to gain information about the sphericity of the particles. Additionally Raman detectors at 607 nm and 387 nm allow a calculation of the extinction coefficients α_p at 532 nm and 355 nm and –combined with the backscatter coefficients– the lidar ratios S_p. However, due to the low SNR the Raman channels are only operated at night time.

A special advantage of MULIS is that the distance of full overlap is at about 250 m. As a consequence, it is possible to assess the accuracy of CALIPSO profiles for all but the lowest part of the boundary layer. Further specification can be found in Table 3.1.

3.4.2 Description of the measurements

In the framework of EARLINET-ASOS [Boesenberg, 2003], regular measurements with MULIS at Maisach started in July 2006 and are performed each Monday and Thursday evening around sunset to gain the lidar ratios, and each Monday additionally at noon when the PBL has the strongest extent in its daily development. The aim of these measurements is to gain a longterm dataset for an European aerosol climatology. Additionally in the framework of an ESA project [Mattis et al., 2007], several members of EARLINET –

Table 3.1: Characteristics of MULIS

Laser	Diode-pumped Nd:YAG
Wavelengths	1064 nm, 532 nm, 355 nm
Pulse energy	175 mJ @ 1064 nm
	50 mJ @ 532 nm
	175 mJ @ 355 nm
Repetition rate	10 Hz
Pulse length	6 ns
Nominal beam divergence	0.6 mrad
Telescope diameter	0.3 m
Field of View	0 – 3 mrad (variable)

including the lidar group of the MIM– started a validation campaign shortly after the launch of CALIPSO in 2006. Since then, validation measurements with CALIPSO are performed twice a week when the satellite overpasses Maisach at a distance of less than 100 km. The overflight times are either at noon at around 12:20 UTC, or at night time at around 01:35 UTC. Additional measurements are done during special occasions like long transport of Saharan dust [Wiegner et al., 2011] or the erruption of the Eyjafjallajökull [Groß et al., 2010, Wiegner et al., 2012]. In Fig. 3.6 the record of the measurements in Maisach is illustrated: the green area shows the fraction of performed measurements. As lidar measurements require suitable weather conditions, measurements were canceled in case of precipitation, fog, or low clouds (red areas) which is nearly the same amount as the successful days. As the MULIS instrument was also involved in dedicated field campaigns (e.g. SAMUM2 in Praia, Cape Verde [Groß et al., 2011], or EARLI09 in Leipzig, Germany), there were also 10 % interceptions in the measurements at Maisach (blue area). Only a few of the scheduled measurements could not be performed due to technical problems or upgrades of the instrument.

Even with these limitations, 339 days of measurements could be performed in the years 2007-2010 (i.e. 36% of all 940 scheduled measurements), of which about 50 % were performed by other members of the lidar group.

During daytime, measurements only the backscatter and depolarization channels can be operated, while at night the more sensitive Raman channels are activated, as well. Typical mean periods for the measurements are 1.5 hours for the regular climatological cases, while for CALIPSO overpasses the duration is 2.5 hours around the overpass time. For each measurement, a calibration between parallel and perpendicular channel at 532 nm is performed to receive the depolarization calibration factor. A second calibration, the so called 'Zero-Measurement', which helps to determine low frequency interferences of the electronics, was developed in the mid of 2007 and is therefore only available for data since August 2007. In April 2007, a roof window was added in the Maisach laboratory to improve the measurement performance. Before that it was only possible to operate the instrument

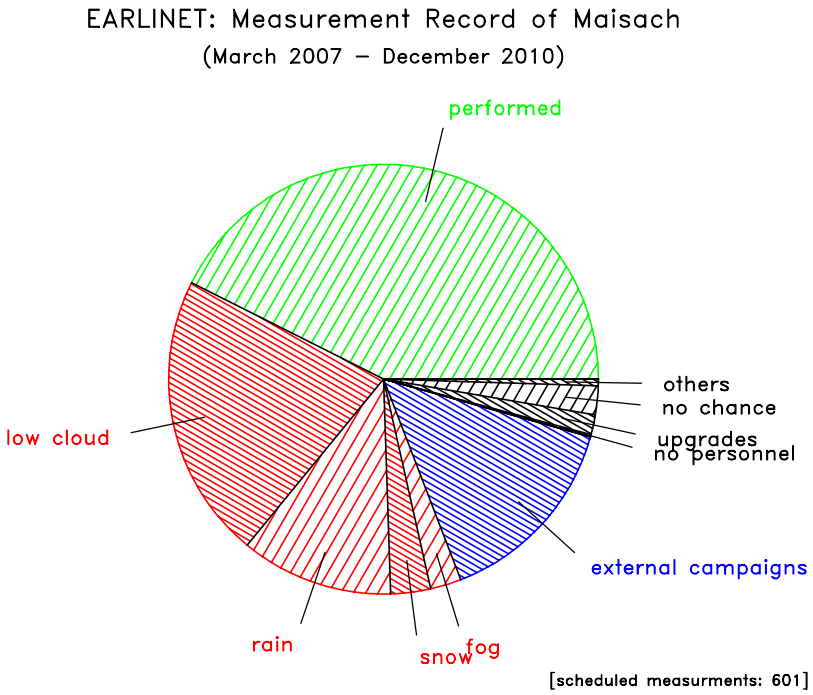

Figure 3.6: Overview over measurement performance of MULIS for EARLINET (CALIPSO overpasses not included) from 2007 to 2010, including the reasons for cancellation. Source: M. Wiegner, MIM

at a zenith angle of 45°. Since then, measurements towards the zenith are operable and thus the range of the instrument is improved. To avoid specular reflexion of ice particles in cirrus clouds the viewing angle of MULIS is tilted by 5° from the zenith. As a consequence the range bin and the effective height over ground differ slightly: as the relation between height above ground (h) and range bin (r) is described by $h = r\cos(\varphi)$, the height differs about 0.03 m / range bin for a zenith angle of $\varphi = 5°$.

The data is stored in averages over 100 laser pulses, equivalent to 10 s, to increase the SNR of the data and to reduce the amount of data. These averages are also displayed in real-time as quicklooks to see immediately the distribution of aerosols and clouds in the atmosphere during the measurement.

3.4.3 Description of analysis method

The analysis algorithms used for a manual data analysis as done for all of the MULIS data discussed here have already been described in Chap. 2: the Klett method (Sect. 2.3.1) and the Raman retrieval (Sect. 2.3.2). As the analysis of lidar data is laborious and over 200 measurements needed to be analyzed, some standard procedures in the data analysis had to be set:

First a period of about 30 minutes ($\approx$ 18000 laser shots) is selected in which the meteorological conditions have to be stable and the heights of detected layers do not vary strongly with time. If there are small scale clouds within this period, these profiles are excluded. The remaining profiles are then averaged for further analysis. As the Raman data has a very low SNR, it needs to be averaged both over a longer time period varying between 60 and 120 minutes as well as strongly smoothed over height/range. Therefore the Raman data is used only to calculate the lidar ratios S_p for the wavelengths 532 nm and 355 nm which then are used as input for the Klett analysis of the 30 minute averages. This results in resolved profiles of the extinction and backscatter coefficients for all available wavelengths (1064 nm, 532 nm, 355 nm), together with the particle linear depolarization ratio at 532 nm (Eq. 2.27). As a further product, the height dependent Ångström exponent is calculated from the extinction coefficients of the different wavelengths (see Eq. 2.8).

For daytime measurements no Raman data exists and the lidar ratio has to be estimated using other meteorological data like trajectories or by using the value derived from a measurement of the previous or following night. From the Raman analyses of 2009/2010 it turned out that a lidar ratio at 532 nm of $S_p = 55$ sr and at 355 nm of $S_p = 60$ sr is a fair approximation for the boundary layer. For the analysis of the 1064 nm channel no lidar ratio can be calculated. But the comparison of the lidar ratios of the other two wavelengths and the Ångström exponents leads to the assumption that the lidar ratio is in general smaller at 1064 nm. Also the mostly used lidar ratio in the CALIPSO data processing has a value of 40 sr. So for a better comparison of MULIS and CALIPSO data, the 1064 nm lidar ratio of MULIS is set to 40 sr.

For the CALIPSO validation measurements, an exact scheme for measurement and data analysis was operated to describe the homogeneity of the atmosphere: before and after the overpass time 1.25 h of measurement were performed. This time period is then divided

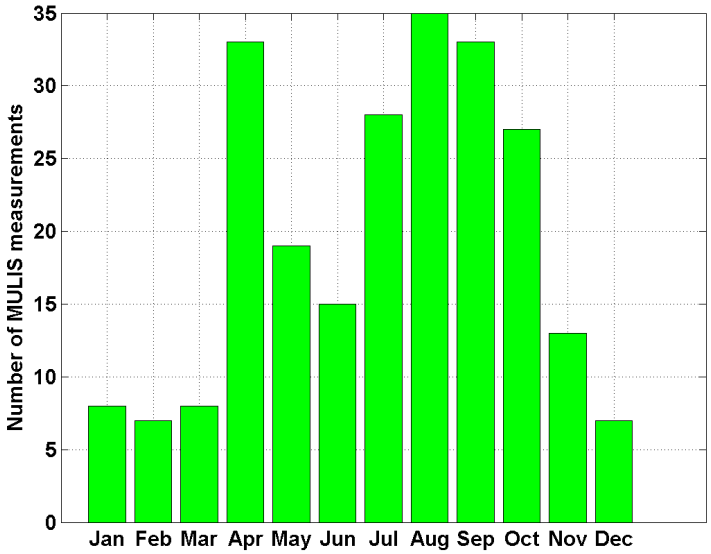

Figure 3.7: Number of used MULIS measurements for each month in the time period 2007 to 2010.

into five 30-min-averages and analyzed using the Klett method. For the Raman analysis a longer time average was used as mentioned above to calculate the lidar ratio.

3.4.4 Data handling in this study

For this thesis, the profiles of the 30-min averages of 233 measurements on 201 days are used. Measurements with strong atmospheric variations and complex cloud structures were not used for this study. Of the CALIPSO validation data, only one of the five available profiles is used, the choice depending on the weather conditions during the overpass (see also Sect. 3.6.4). Measurements at all wavelengths are not available for all days: in the beginning of 2007, the 1064 nm channel was not working properly. Due to too high SNR, single wavelengths on several days could not be analyzed, either: overall, a total of 651 extinction profiles for the three wavelengths can still be used, also depolarizations profiles of 157 measurements are available.

The measurements are dependent on the weather, so the number of measurements varies with the months. Fig. 3.7 shows this: in winter (January, February, December) and in March less than 10 measurements per month are available. The most measurements were done in August. In April 2010, additional measurements were performed to characterize diffusion of the ash from the Iceland volcano Eyjafjallajökull. Accordingly, the number of measurements in this month is increased.

As the overlap of MULIS is at about 0.25 km to 0.5 km, it is assumed that the atmosphere below the overlap is well mixed and the profile is extended to the ground as a

constant value of the lowermost calculated extinction coefficient. Otherwise the integration of the extinction profile would lack this data and the AOD would be underestimated. Also each profile set (up to 3 wavelengths for each measurement) is sub-divided into layers for each of which layer mean values are obtained for: geometric extension, optical depth, particle linear depolarization ratio, and Ångström exponent. The criteria for the layer detection are: minimum of the gradient of extinction coefficient ($\frac{d\alpha_p}{dz}$) and strong changes of δ_p and/or κ. In the further analysis, the lowest layer is defined as boundary layer (PBL), the layers above the PBL are called elevated layers (EL). A part of the measurements of MULIS are coincidental with CALIPSO overpasses and 52 of them can be used for a direct comparison.

As all profiles were carefully analyzed individually, no extra quality filtering of the data is needed except for the particle linear depolarization δ_p, for which high noise can occur, especially in optically thin layers (OD < 0.03). So δ_p cannot be provided for all detected layers.

3.5 CALIOP (Space lidar on-board CALIPSO)

On 28 April 2006 the Cloud-Aerosol Lidar and Infrared Pathfinder Satellite Observation (CALIPSO) satellite was launched. As part of the A-Train its scientific aim is to collect information about the atmospheric distribution and properties of clouds and aerosols. CALIPSO orbits the Earth 14.5 times per day and passe the same geocoordinatess every 16 days at an averaged height of 705 km a.s.l. [Winker et al., 2007]. The key instrument on board is the Cloud-Aerosol Lidar with Orthogonal Polarization (CALIOP) for continuous measurements of cloud and aerosol profiles on a global scale. The instrument and the retrieval of cloud and aerosol properties are described in detail in several CALIPSO technical reports and in a special issue [Hostetler et al., 2006, Young et al., 2008, Omar et al., 2009, Vaughan et al., 2009]. In the following sub-section only an excerpt about the relevant aspects of the lidar and its retrieved aerosol data is given.

3.5.1 Instrument

CALIOP is a space-borne dual wavelength backscatter lidar. Its most relevant technical characteristics are summarized in Table 3.2. The Nd:YAG laser of CALIOP emits linear polarized light at the two wavelengths 532 nm and 1064 nm. It measures the total backscattered signals at 1064 nm and – separately – the parallel and perpendicular polarized signals at 532 nm, using photomultiplier tubes for the two 532 nm channels and an avalanche photo diode at 1064 nm. Just like the laser of the MULIS lidar system, the CALIOP laser is tilted to avoid specular reflection by cirrus clouds containing oriented plates. Initially this angle was 0.3°; in August 2007 the angle was changed to 3.0° [Vaughan, 2008].

The vertical resolution of the raw data is 30 m. Due to the velocity of the satellite and the repetition rate of the laser the spacing of the footprint and therewith the horizontal resolution is 330 m. Calculated from the beam divergence and height of CALIPSO, the

Table 3.2: Characteristics of CALIPSO and CALIOP

Average height	705 km a.s.l.
Velocity	$\sim$ 7 km/s
Laser	Diode-pumped Nd:YAG
Wavelengths	1064 nm, 532 nm
Pulse energy	110 mJ / channel
Repetition rate	20.16 Hz
Pulse length	20 ns
Nominal beam divergence	0.1 mrad
Telescope diameter	1 m
Field of View	0.13 mrad

footprint at ground level has a diameter of about 70 m. A depolarization calibration is performed internally.

To reduce noise and also volume of the data, the backscatter signals of certain altitudes are averaged over consecutive laser shots and height bins. This effective resolution is shown in Table 3.3. The data at 532 nm is given for -2.0 to 40.0 km, while the data at 1064 nm is only available for -2.0 to 30.0 km due to too high noise in the top level. It should be mentioned at this point that the negative height as lower limit is chosen to include also the lowest land elevation, which is the shore of the Dead Sea with a depression of 392 meters below sea level. The altitude region 1 (-2.0 to -0.5 km) is provided to allow monitoring of potential delayed recovery from the surface return [Hostetler et al., 2006].

In the lower troposphere (altitude region 2, -0.5 to 8.2 km), the data of the 532 nm channels is stored as single laser shots with the original range bin length of 30 m, as the signals in this region are strong and small scale structures can be studied best. In the upper troposphere and stratosphere (altitude regions 3-5) the signals of aerosol / cloud layers (e.g. Cirrus clouds, stratospheric aerosols) are low compared to the signals of layers closer to the ground (e.g. cumulus clouds, boundary layer aerosol). To increase the SNR, in these areas the signals are averaged as described in Table 3.3.

Because of higher noise at 1064 nm, the measurements at this wavelength are already averaged vertically in the troposphere over two height bins.For the altitude region 5 data only fill values are inserted.

3.5.2 Regular data from NASA

NASA provides public access to the CALIPSO data. These can be ordered from the Langley Research Center with help of filter parameters like date or geographical region and downloaded via ftp tools. In general, the data is provided as half-orbits, but by now, subsets are available as well. Like most data of NASA's Earth Observing System, the

Table 3.3: Resolution of attenuated backscatter data (L1B data) of CALIOP

Altitude Region	**Height bin**	**Altitude Range (km)**	**Horizontal Resolution (km / shots)**	**Vertical Resolution (m) 532 nm**	**Vertical Resolution (m) 1064 nm**
5	1 - 33	30.1 to 40.0	5.00 / 15	300	-
4	34 - 88	20.2 to 30.1	1.67 / 5	180	180
3	89 - 288	8.2 to 20.2	1.00 / 3	60	60
2	289 - 578	-0.5 to 8.2	0.33 / 1	30	60
1	579 - 583	-2.0 to –0.5	0.33 / 1	300	300

CALIPSO data is stored in the hdf format (http://www.hdfgroup.org/), which makes the extraction of single parameters easy to operate. Since the launch of CALIPSO, several versions of the data have been published. The data used here is from version 3.01 and valid from 13 June 2006 to 16 February 2009 and 17 March 2009 to 31 October 2011. For more recent data, also newer versions exist: V3.02 for data from 01 November 2011 to 28 February 2013 and V3.30 from 01 March 2013 to present. For CALIOP, there are several different types of products available: level 1 (L1B) for raw data, level 2 (L2) for optical properties along the path, and level 3 (L3) for optical properties globally gridded and monthly averaged.

In this study L1 and L2 data is used, the low resolution grid of the L3 products is not suitable for this study. Also this data is still on version 1.00, and as a consequence it is not confidential.

The basic L1B data contains the attenuated backscatter β'_λ (see Eq. 2.12) for 532 nm, both for total (sum of Parallel and perpendicular signal) and perpendicular, and for 1064 nm (total), as well as information about calibration factors, orbital parameters of the satellite and the geographic location of the laser footprint, surface height, and quality flags. One profile of β'_λ is given every 330 m, partly averaged according to Table 3.3. E.g. for the altitude region 5, $\beta'_\lambda(z)$ of 15 consecutive shots contain the same averaged profile; in the altitude region 2 at 1064 nm two height bins always contain the same mean value. The vertical resolution of the height bins is the one of the 532 nm data. Additionally profiles of meteorological parameters, e.g. temperature, pressure, and relative humidity, obtained from model data of the GMAO (Global Modeling and Assimilation Office) are included which are used in the calculation of the Rayleigh backscatter coefficient β_m needed for L2 data. While the resolution of the meteorological parameters is lower than 330 m, they are given in the same horizontal resolution as the laser shot, but the vertical resolution differs: there are only 33 height bins for the altitude range from -1.8 km to 40 km, instead of the 583 bins of the β'_λ profiles.

Based on the L1B data set, three different types of products are provided for a geo-

metrical and optical characterization of significant particle layers (L2 data): the Vertical Feature Mask (VFM) for an overview over the measurement, the layer products which contain information about layer properties (e.g. base, top, optical depth of layer), and the profile products with height resolved optical properties (e.g. backscatter coefficient). The layer and the profile products are provided separately for clouds and aerosols.

The focus of this study is on the aerosol data (Aerosol Layer data: AL, Aerosol Profile data: AP) and the VFM. Therefore they are described first, then the algorithms to gain these products are explained in detail (Sect. 3.5.2.1).

The Vertical Feature Mask gives the general overview over the atmosphere. A 'feature' means any deviation of the clear atmosphere in the backscattered signal. Its type can be e.g. a cloud, an aerosol layer or the surface, but also a region with no relevant signal (only instrument noise) due to total attenuation of the laser pulse. The features are given from -0.5 km to 30.1 km (altitude regions 2-4 of Table 3.3), with the same vertical resolution as the 532 nm backscatter data. They are bundled in arrays with an horizontal span over 5 km. The VFM contains up to five parameters for each height bin: the feature type, the corresponding subtype for the features 'cloud', 'aerosol', and 'stratospheric feature', two corresponding quality flags to give an estimate for the reliability of the classification, and the horizontal averaging which was needed to detect the feature (see Sect. 3.5.2.1). The feature types and the subtypes are listed in Table 3.4. The aerosol subtypes are used in this study as part of the aerosol climatology, the other two are listed for the sake of completeness.

The subtyping is needed to estimate an initial lidar ratio for the calculation of the extinction coefficient. The six aerosol types are the result from a cluster analysis of AERONET data done by Omar et al. [2009]. They represent the main types of aerosols on a global scale. Each aerosol type is classified by specific microphysical properties, in particular the size distribution and the refractive index, with which optical properties such as the lidar ratio can be calculated. Combined with independent measurements of the lidar ratio in field campaigns, the lidar ratios for the wavelengths 532 nm and 1064 nm are prescribed.

For a better understanding of the VFM, Fig. 3.8 shows an example of a CALIPSO measurement for a 240 km path and an altitude from 0 km to 8.2 km: in the quicklook of the attenuated backscatter β' at 532 nm (panel a), the strong returns from the surface and the clouds (in red) can be seen clearly, while the aerosol layers cannot be distinguished by eye from atmospheric background. In panel b, the feature types for the same scene are shown: the main type is clear air (blue); surface (green) and clouds (cyan) agree well with the strong signals in (a), and in magenta aerosol features can be seen above the surface (0.5 - 1.5 km) and at 7 km height. The corresponding aerosol types are shown in panel c: the elevated layer from 7 km to 8 km is classified as dust, while the ground near aerosol type varies (smoke, polluted continental, clean continental, and dust). The averaging length required for the detection (panel d) is 80 km for most layers. This strong averaging is required when layers are optically thin.

While the VFM gives an overview over the atmospheric conditions, the information about the optical properties of the features is contained in the layer and profile data, separately given for clouds and aerosols with the same horizontal resolution of 5 km.

Table 3.4: VFM overview of feature types and the subtyping of Features Cloud, Aerosol, and Stratospheric Feature

	Feature Types	**Subtypes of Features 2-4:**		
		Cloud	**Aerosol**	**Stratospheric F.**
0	invalid (bad or missing data)	low overcast, transparent	not determined	not determined
1	clear air	low overcast, opaque	clean marine	non-depolarizing PSC
2	**Cloud**	transition stratocumulus	dust	depolarizing PSC
3	**Aerosol**	low, broken cumulus	polluted continental	non-depolarizing aerosol
4	**Stratospheric Feature**	altocumulus (transparent)	clean continental	depolarizing aerosol
5	surface	altostratus (opaque)	polluted dust	–
6	subsurface	cirrus (transparent)	smoke / biomass burning	–
7	no signal (totally attenuated)	deep convective (opaque)	other	other

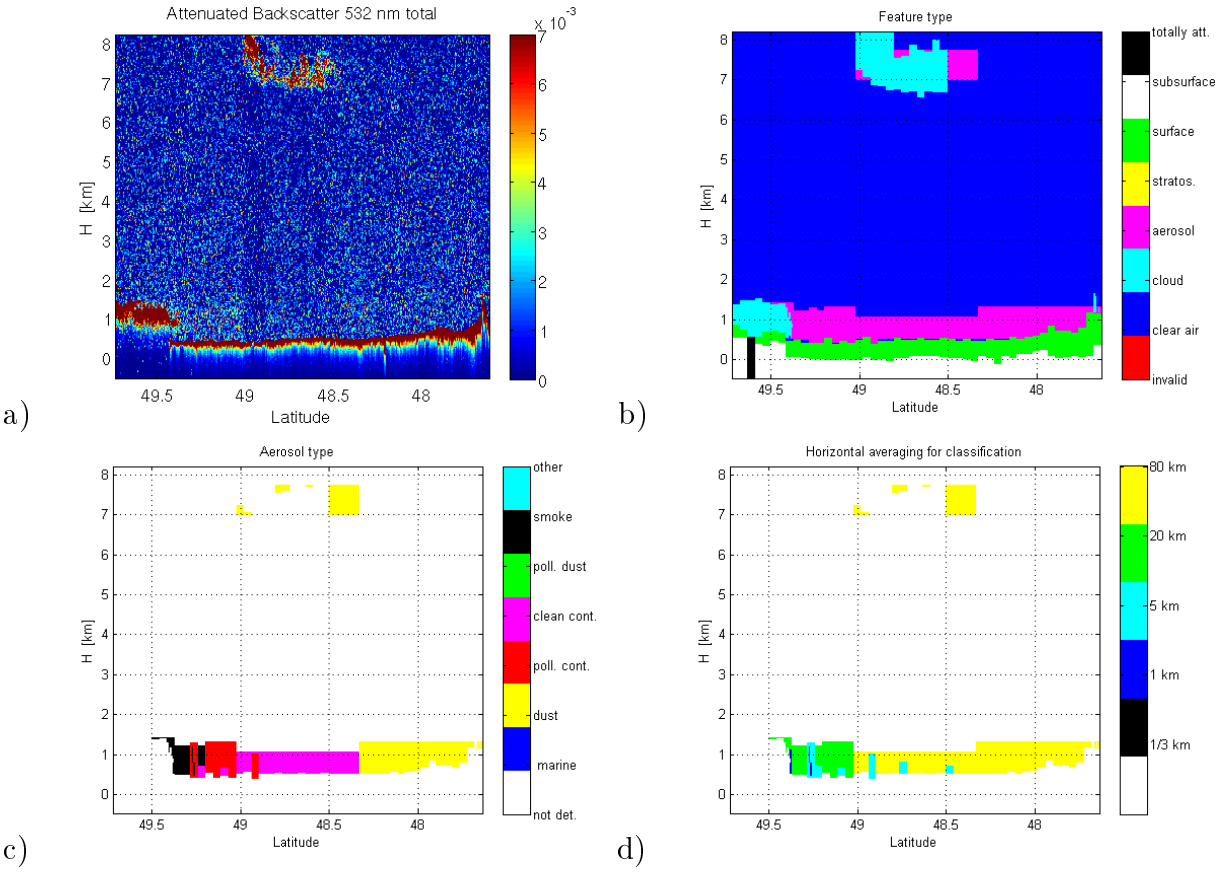

Figure 3.8: 4 representations of the same overpass region (240 km) of CALIPSO measurements: a) quicklook of attenuated backscatter 532 nm total; b) Feature type; c) Aerosol type; d) horizontal averaging for aerosol detection. All data are from the CALIPSO overpass of 08 April 2008, *V3-01.2008-04-08T01-27-43ZN.hdf (5-km-sets #497-544).

Every detected aerosol feature is represented as one layer in the AL data with its properties like the top and base heights, the assigned lidar ratio, and the optical depth of the feature (FOD = feature optical depth). For a 5 km set, a maximum of 8 layers can be recorded. Furthermore, the total number of detected layers, the cloud optical depth, and the total AOD are given. Accordingly the AOD is not always the sum of the FODs (see Sect. 3.5.2.2).

The main information in the profile products (AP) is the vertically resolved values of the aerosol backscatter and the extinction coefficient (β_p and α_p) for both wavelengths, the linear particle depolarization ratio δ_p for 532 nm and the corresponding uncertainties. These values are only given for heights where aerosol features were detected. In all other heights, only fill values are inserted. To determine the complete particle profiles in the atmosphere, aerosol and cloud profile data (AP + CP) need to be combined. The vertical resolution of the AP data is coarser than the one of the β' and VFM: 60 m for -0.5 km to 20.2 km altitude and 180 m up to 30.1 km.

3.5.2.1 Algorithms to derive L2 data

To obtain the VFM, the AL and the AP data, the lidar data needs to be analyzed to identify features and to retrieve optical properties for aerosols and clouds. This is done in three steps:

- the Selective Iterated Boundary Locator (SIBYL) searches for features in the attenuated backscatter signals $\beta'(r)$ of all three channels,
- the Scene Classification Algorithms (SCA) classifies the detected features into types and subtypes,
- and the Hybrid Extinction Retrieval Algorithms (HERA) calculates the optical parameters like β_p, α_p, and δ_p for each feature.

For a better understanding of the CALIPSO data, these algorithms are briefly explained. In this context a 'scene' is understood as a path of 80 km = 240 single profiles / laser shots, which is subdivided into 16 sets of 5 km each.

SIBYL: Selective Iterated Boundary Locator In SIBYL, the profile of the total attenuated backscatter at 532 nm, $\beta'_{532}(r)$, is screened for features. If a significant deviation from the Rayleigh profile is found, this deviation is classified as a feature. In case of no deviation it is assumed to have 'clear air' in this height.

For this analysis the attenuated scattering ratios $R'(r)$ are used instead of the attenuated backscatters β' [modified according to Vaughan et al., 2009, Eq. 2]:

$$R'(r) = \frac{\beta'_{532}(r)}{\beta'_m(r)} = \left[1 + \frac{\beta_{532,p}(r)}{\beta_{532,m}(r)}\right] T^2_{532,p}(r) \tag{3.1}$$

$\beta'_m(r)$ is the attenuated backscatter signal expected from a pure molecular atmosphere and is calculated from the meteorological data of the GMAO model. With the attenuated

scattering ratio R' it is easier to define thresholds to separate the clear air signal from feature signals: for a profile with no features (= clear air) only the air molecules contribute to the backscatter signal, $\beta'_{532}(r) = \beta'_m(r)$, and R' is therewith 1. If $R' > 1$, aerosols or clouds contribute to the signal. It is, however, not sufficient to set the threshold on $R' = 1$: due to noise from the solar background, the threshold is additionally height dependent (see Fig. 3.9 a for an example). For the detection of a feature, R' further has to exceed this threshold over several consecutive height bins to exclude noise peaks.

The backscattered signals of clouds are in general stronger than the signals of aerosols. To detect both optically thick clouds and thin aerosol layers there is an averaging scheme starting from 5 km up to 80 km horizontal average of the R' profiles. The scene (80 km) is first separated into 16 5-km-averages. Each of these 16 profiles will then be scanned from an altitude of 30 km downwards for features. After the first detection of a feature top and base, this feature is 'removed' from the profile. From Eq. 3.1 it can be seen that the attenuated scattering ratio R' only depends on the transmission of the particles, $T^2_{532,p}(r)$, not on the one of the air molecules. So the signal below a feature is normalized with the estimated T^2_p of this feature. This results in a signal R' as it would have been measured in case of the absence of the detected feature and so the efficiency of the threshold is retained.

If at least one feature (apart from the surface) is found, the so called High Resolution Cloud Screening process is applied. The 5-km-profile is separated into 1-km-averages and scanned for small scale clouds. If the (large scale) feature is below 8 km, an additional separation into into 1/3-km-profiles is performed, these single shots are then analyzed for clouds and the surface peaks. If the cloud screening process finds clouds beneath an altitude of 4 km at the 1/3-km-resolution, the 5-km profile is rejected and a new '5-km-profile' excluding the single shots with cloud peaks is used for the further search of aerosol data.

After finding all detectable features with a certain SNR, the 16 normalized 5-km-profiles are averaged into four 20-km-profiles. These four profiles are then scanned to detect weaker features which are again removed from the profiles. As a last step, the four normalized 20-km-profiles are averaged into one 80-km-profile, which is once more scanned. All detected features are stored in the VFM data. If two (or more) features are found for one height bin, only the feature detected at the smallest scale is registered.

Fig. 3.9 shows an example of a feature removal. The R' of a 5-km-profile (green line) in panel a shows strong backscatter signals at altitudes of ∼13 km to 15 km from a cirrus cloud and at ∼0 km from the surface return. Both signals clearly exceed the given threshold (blue line). In panel b the cirrus and the surface are removed. With the changed scale it is easy to see that the signal below 13 km is mostly smaller than 1 due to the attenuation of the cirrus cloud. Only noise peaks and the signal between 0 and 2 km exceed the threshold line.

Therefore R' is normalized below 12 km with the (squared) transmission of the removed feature, as shown in panel c. To detect the aerosol layer at ∼0-2 km, which has a too low SNR in panel c, four consecutive cloud screened attenuation-corrected profiles are averaged. In panel d this aerosol layer now clearly exceeds the threshold.

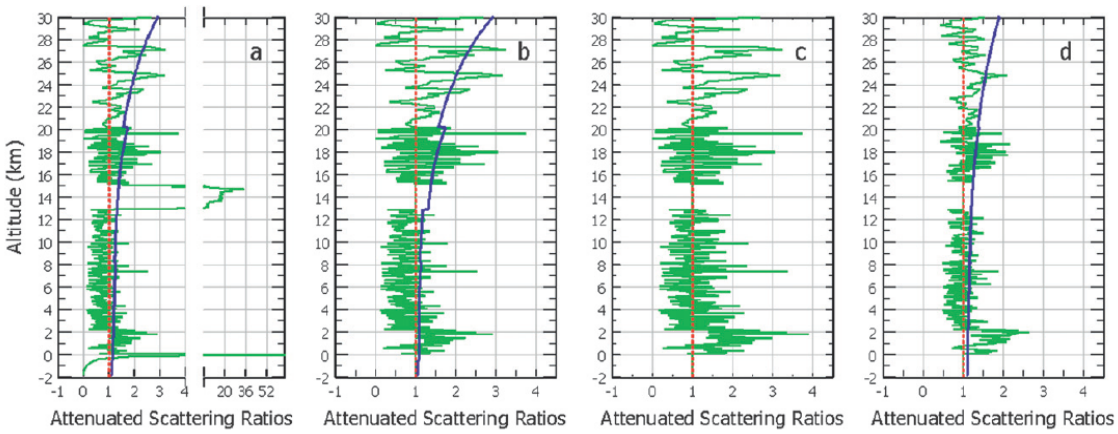

Figure 3.9: SIBYL feature removal: a) 5 km profile with cirrus over moderate aerosol (green line) and initial height dependent threshold (blue line); b) removal of surface and cirrus peaks; c) correction of the signal below the removed cirrus with its (squared) transmission; and d) averaging over four consecutive attenuation-corrected profiles to detect the aerosol layer at ∼1-3 km. The shown signal on the x-axis is the attenuated scattering ratio R' (Eq. 3.1). Source: Vaughan et al., 2009, Fig. 6.

SCA: Scene classification algorithms After detection of the features, they are classified by the SCA algorithm into types and subtypes (for a list of types see Table 3.4), as already mentioned in the description of the VFM data. For the classification several quantities are used: the mean attenuated backscatter $\overline{\beta'_{532}}$, the attenuated backscatter integrated over height at 532 nm γ'_{532}, the color ratio of the means $X = \frac{\overline{\beta'_{1064}}'}{\overline{\beta'_{532}}}$, the volume depolarization ratio $\delta_v = \frac{\overline{\beta'_{532\perp}}'}{\overline{\beta'_{532\parallel}}}$, as well as the altitude and the mean temperature of the layers.

The first step of the SCA is the discrimination between clouds and aerosols. The strongest backscatter signals in the atmosphere originate from optically dense clouds. So all features with γ'_{532} stronger than a given threshold are categorized as clouds. The mean color ratio and the volume depolarization ratio δ_v indicate the size and shape of the particles in the feature and can therefore help to distinguish between aerosols and clouds, while the temperature is used to identify ice clouds. The reliability of the discrimination between clouds and aerosols is given with the CAD (Cloud-Aerosol Discrimination) score with values between -100 and 100. The positive values belong to clouds, the negative ones to aerosols. If the absolute value of the CAD score is between 70 and 100, the cloud or aerosol discrimination is defined as highly reliable. A value of 0 means that the discrimination between aerosol and cloud is not possible. The mid-layer altitude z is used to distinguish between stratospheric and tropospheric features.

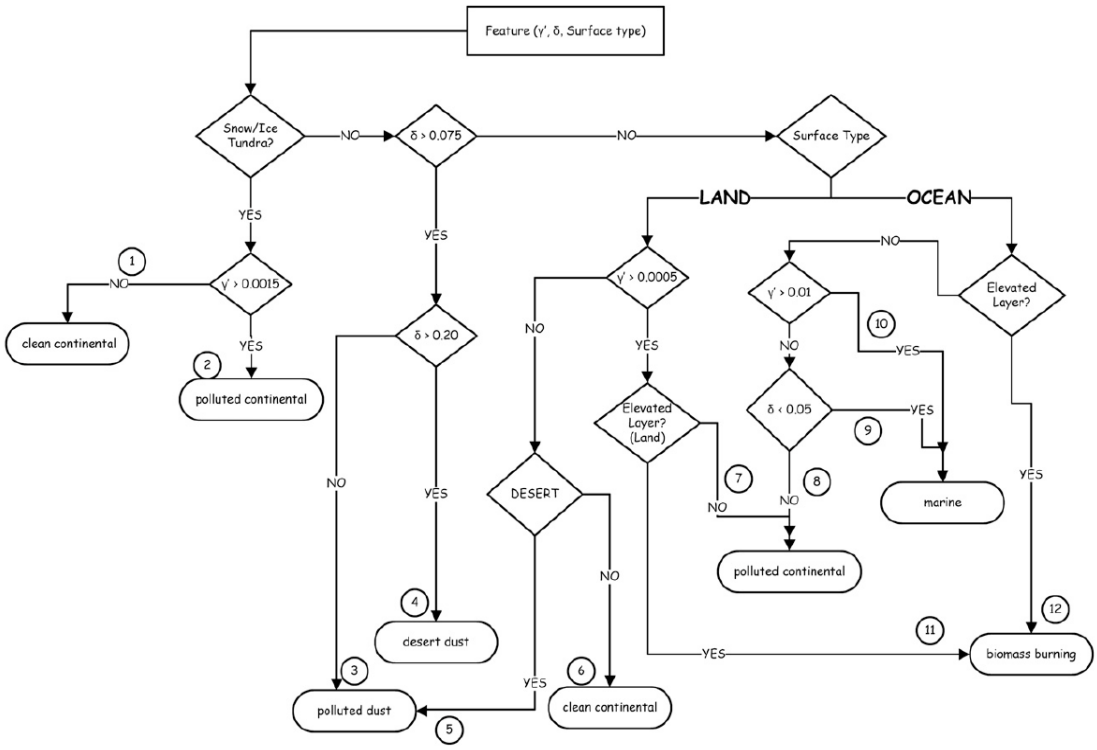

Figure 3.10: Flowchart CALIPSO selection scheme for tropospheric aerosols; from Vaughan et al., 2009, Fig. 2.

The next step in the SCA is the subtyping of clouds, aerosols and stratospheric features needed to assign estimates for the lidar ratios. Here only the classification of aerosols is described:

The six aerosol subtypes are: clean marine, dust, polluted continental, clean continental, polluted dust, and smoke/biomass burning. Fig. 3.10 shows the classification scheme for the aerosol subtypes. For the classification, not only the signal strength γ'_{532}, mean volume depolarization ratio δ and height of the aerosol feature are investigated, but also the geographical latitude and the surface properties.

E.g. the classification of a 'marine' aerosol is only possible if the geocoordinates identify the surface as ocean, and 'biomass burning' will only occur if the aerosol layer is elevated. As mentioned above, the determination of the aerosol type is mainly needed to estimate the lidar ratio needed by HERA. In Table 3.5 the lidar ratios S_p and their uncertainties of the six aerosol types are shown for both wavelengths. An incorrect classification can lead to significant differences in the lidar ratio, e.g. the 532 nm value of polluted continental is twice as high as that of clean continental aerosol. The uncertainties are used for the error calculation of the L2 data.

Table 3.5: CALIPSO lidar ratios and their uncertainties of aerosol subtypes used in the version 3.01 extinction solver.

Aerosol type	**Clean marine**	**Dust**	**Polluted dust**	**Clean continental**	**Polluted continental**	**Smoke**
$S_p(532nm)$	20 ± 6 sr	40 ± 20 sr	55 ± 22 sr	36 ± 16 sr	70 ± 25 sr	70 ± 28 sr
$S_p(1064nm)$	45 ± 23 sr	55 ± 17 sr	48 ± 24 sr	30 ± 17 sr	30 ± 14 sr	40 ± 24 sr

HERA: Hybrid Extinction Retrieval Algorithm HERA calculates the extinction and backscatter coefficient profiles (α_p and β_p) at 532 nm and 1064 nm and the particle linear depolarization ratio δ_p at 532 nm for each feature – including the features detected on larger scales – of each 5-km-profile. The horizontally averaged attenuated backscatters β' are analyzed only between top and base of the aerosol layer (found by SIBYL). These profiles are then used to calculate α_p and β_p by using iterative algorithms based on the Newton-Raphson method (see Eqs. 2.20 and 2.21) which need the lidar ratio from the SCA algorithm as further input. An important assumption is that the particles of the feature are horizontally homogeneously distributed along the averaged path [Young and Vaughan, 2009]. If the solution of the iteration is diverging due to high noise and wrong initial values, the lidar ratio is changed until convergence is successful. This change is reported in another quality flag, the Extinction QC; if the initial lidar ratio was used, the Extinction QC is set to zero.

If multiple layers are found in a profile, the extinction retrieval is executed on the uppermost layer first. As explained in the SIBYL algorithm, the β' profile below this feature is then corrected for the optical depth (FOD) of this feature. If the optical depth of the feature is significant, this correction can lead to strong uncertainties in the retrieval of the lower layers. The total optical depth (AOD) reported in the AL data is gained by the vertical integration over the 5-km-profile of the extinction coefficient assuming $\alpha_p = 0$ between the layers.

During the screening algorithm SIBYL it is possible that no aerosol data will be found, maybe because clouds attenuate the signal too strongly or an actual aerosol layer is optically too weak to be detected. In this case, the classification algorithms do not apply and the AOD is set to zero.

Since 2012 there is a new aerosol product of the CALIPSO data available: aerosol profile product (level 3 = L3) reports mean profiles of aerosol optical properties on a uniform spatial grid [Powell et al., 2013]. The resolution of these data is rather coarse with 5° longitude by 2° latitude. As the offered profiles are averages over largely varying surfaces, a lot of structures like the variation of boundary layer heights above ocean or mountains are 'smoothed' out. Accordingly, these data can be used as a good basis for global modeling, but especially for the aerosol study of a particular region – as done in this thesis – this data is not helpful.

3.5.2.2 Inconsistencies of the FODs

Within the analysis of the AL data, some inconsistencies were found concerning the aerosol optical depth (AOD) and the (feature) optical depth (FOD) of the single aerosol layers. In theory, the optical depths of all layers in a 5 km profile summed up should result in the column optical depth: $\sum FOD = AOD$. Testing this it turned out that the sum of FODs is often higher than the AOD.

The reason for this is that aerosol layers are detected at different horizontal resolutions: 5, 20, and 80 km depending on the signal strength.

However, the layer values like top, base, and FOD, which are stored on a 5km scale, are the ones obtained on the horizontal resolution at which the feature was detected. Hence, if a layer is detected at 80 km horizontal averaging, the same values for layer heights and depths be noted will be noted in all sixteen of the AL 5 km data, even if in some profiles (e.g. seen in the VFM) the layer is vertically thinner or partly covered by a cloud. On the other hand, if the layer is completely covered by a stronger feature (most time by clouds, but also by surface in mountain regions), the aerosol layer will not be stored at all. In the data represented in Fig. 3.8 panel b - d, two examples can be found: From 48.3° to 47.6° N latitude a dust (boundary) layer is visible; its base – being the surface in a mountainous region – varies significantly within the 80km path, from 0.44 km to 1.01 km a.s.l.. The aerosol layer as given in the AL data is consequently partly covered by the surface. However, as the layer was detected at an horizontal averaging over 80 km (panel d), the corresponding AL data reports the same top and base heights of 1.34 km and 0.56 km and a FOD of 0.0481 for all 16 5-km-sets. The second example is the dust layer at 7 km height which is overlapped by a cloud. From the aerosol type in panel c it can be seen that only parts of the aerosol layer are detected. However, for each 5-km-set in which aerosol occurs in this height, i.e. where the aerosol layer is not completely covered by the cirrus (6 sets in total), the same top, base and FOD are given (7.78 km, 7.03 km, 0.0111).

Because of this procedure for storage of layer information, the study of FOD in small scale regions could lead to an over-estimation of optical depths regarding the fractions of the six aerosol types. Therefore it is better to obtain the FOD by calculating them directly from the 5-km-extinction profiles so that their sum is consistent with the AOD.

3.5.3 Data handling in this study

For this thesis, several preparations needed to be done to derive information from CALIPSO measurements about the aerosol distribution above Munich. For the years 2007 - 2010 all half orbits with overpasses within the Munich region (see Sect. 3.1) were selected. For this region VFM, AL, and AP were stored for further analysis.

In principle, the AL layer information is the best basis to study the occurrence of the different layer types and their averaged optical depths. But because of the inconsistencies of the AL-FOD data (Sect. 3.5.2.2), I decided to discard the AL data and calculate the FODs in 5 km horizontal resolution directly using VFM and AP data.

In order to calculate the FODs for a 5 km data block, first the VFM is used to filter out

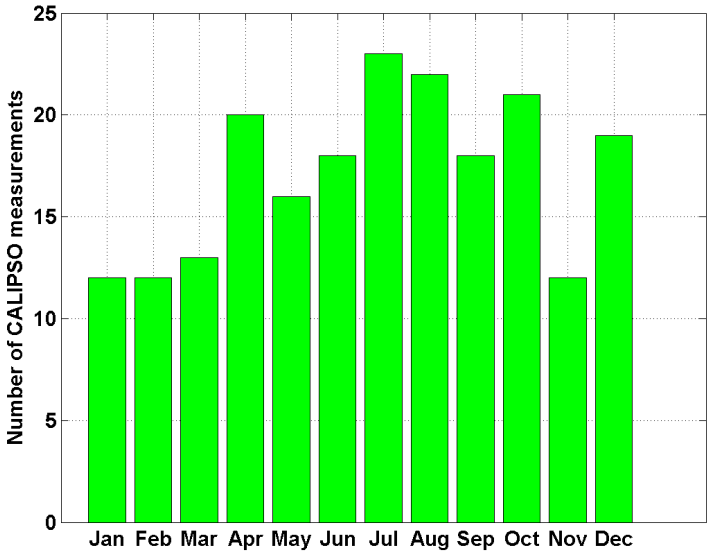

Figure 3.11: Number of used CALIPSO measurements for each month; maximal possible are ∼30 measurements / month for the time period 2007 to 2010.

any data block containing clouds. No FODs were calculated for these blocks. Also, single height bins containing more than one aerosol type according to the VFM are removed for the analysis. Although the latter should not happen according to the CALIPSO documentation, few cases were found. Next, the VFM is used to identify continuous aerosol layers of any one type, including their top and base. In case of a strong aerosol layer surrounded by a thinner layer, three succeeding layers are now noted. This is a major difference to the original AL data where layer heights can overlap. Finally the optical depths of each layer are calculated for both wavelengths by integrating the extinction coefficients of the AP data over the layer heights. The height resolutions of the VFM and the AP data are different; this can lead to minor uncertainties in the calculation of the optical depths. As a consequence of the above mentioned strategy, it is guaranteed that the comparison of the sum of the new calculated FODs with the given column AOD ($\sum FOD = AOD$) is in good agreement: small discrepancies can be explained by smaller rounding errors and filtering of height bins with more than one aerosol type. For the AOD study the AOD of one overpass in the region is averaged from all cloud free 5-km-averages.

Altogether, a number of 206 measurements could be used. The number of measurements for each month can be seen in Fig. 3.11. The most measurements are available in June, however also in winter time the number of days with usable aerosol information is quite good with more than 10 days / month. In December even 19 days (of about 30 overpasses) are used for this study. This is in contrast to the monthly frequency of usable MULIS measurements (see Fig. 3.7) which shows a much less homogeneous distribution.

As CALIPSO does not provide continuous extinction profiles but only segments, an

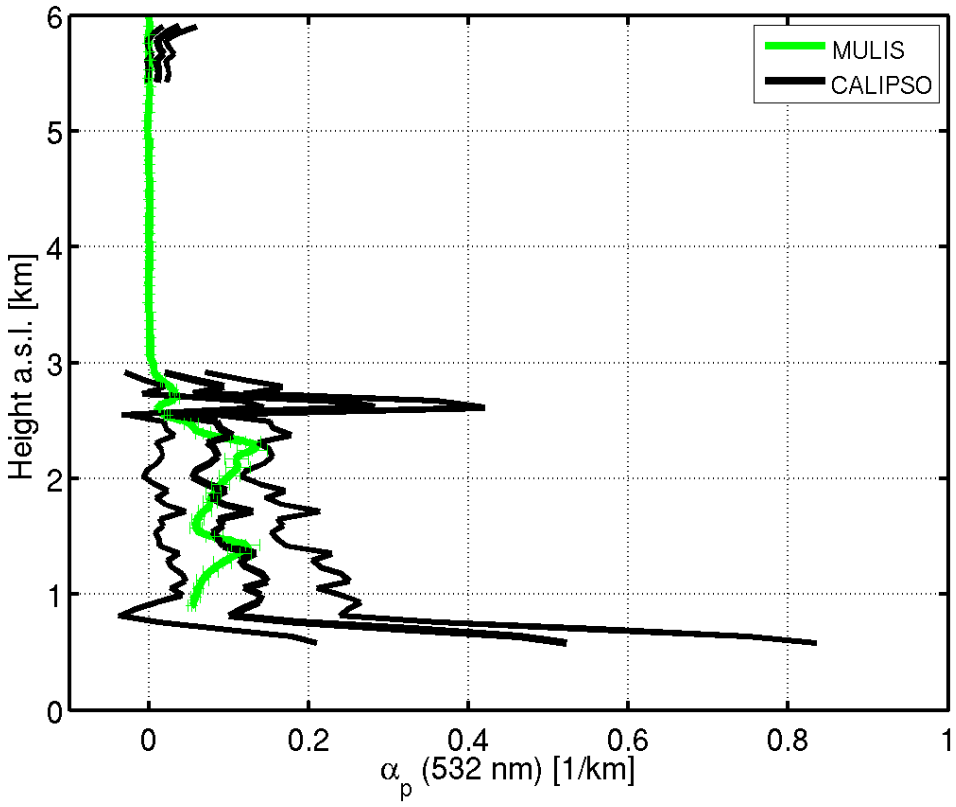

Figure 3.12: Example of extinction profiles of CALIPSO (black) and MULIS (green) including the uncertainties: thin black lines for CALIPSO and bars for MULIS.

average over all profiles is not very meaningful. More information is gained with the study of the layer averages: from the extinction coefficients at 1064 nm and 532 nm the height resolved Ångström exponent is calculated. Also the particle linear depolarization ratio is available, though the values vary strongly. As both parameters, κ(1064nm/532nm) and δ_p(532nm) have a high SNR, again layer averages are calculated. For each overpass then connected layers of identical aerosol type are located and layer averages of FOD, δ_p, and κ are built. These layer averages are the basis of the aerosol type analysis in Chap. 4.

The errors given by NASA for the extinction coefficient are not considered in this study as the values are often very high ($> 100\%$). Fig. 3.12 shows as an example extinction profiles of CALIPSO and MULIS with typical values of the uncertainty of CALIPSO often being as large as the α_p itself. Already by only considering the lidar ratio uncertainty the extinction uncertainty is always at least 40 %[1], values above 100 % are frequently observed in this study. So in comparison with CALIPSO profiles the MULIS values are nearly always within the uncertainty of CALIPSO.

[1] see http://www-calipso.larc.nasa.gov/products/

3.6 Comparison of MULIS and CALIPSO profiles

As mentioned in the last section, the CALIPSO algorithms need several assumptions and have some limitations. As a consequence, as will be shown in Chapter 5, CALIPSO measures significantly lower AODs than the other instruments and obtains different aerosol profiles than MULIS. In order to assess the reasons for these discrepancies and the limitations of the CALIPSO analysis software, a thorough analysis of coincident measurements of CALIPSO and MULIS needs to be performed.

This section first evaluates the quality of the raw data. Then it lists the reasons which were identified as possible explanations for the discrepancies and presents – illustrated by exemplary cases – the methods with which the data is evaluated for these sources of mismatch. The results of the evaluation are shown in Sect. 5.3.2.

3.6.1 Data used for intercomparison

The day to day comparison between the two lidar systems CALIPSO and MULIS is done using the MULIS profiles derived as described in Sect. 3.4.3 and the CALIPSO profiles from the L2 AP data, version 3.01. Thereby only CALIPSO profiles not contaminated by clouds ($\tau_{cloud} = 0$ and no clouds in VFM, see Sect. 3.5.3) are used, also all data with insufficient quality flags (CAD score $>$ -70 and Extinction QC > 0) is removed.

From 2007 to 2010, 97 of the 233 successful MULIS measurements (see Sect. 3.3.4) were performed simultaneously with CALIPSO overpasses. But this number of measurements has to be reduced: about a third of the CALIPSO overpasses contain clouds in all 5-km profiles of the whole path over the Munich region and can not be used. Furthermore, on several days the 30-min averages of the MULIS measurements showed a strong variation in time of the meteorological situation above Maisach, indicating small scale variability so that a comparison with the CALIPSO overpasses in at least 30km distance can not be done. All in all, the comparison is based upon 52 coincident / simultaneous measurements, whereof exactly half of the days (26) are performed during night time around 01:30 UTC, the other half at day time around 12:20 UTC. For a direct comparison between ground and spaceborn measurement, those of the seven nearest 5-km-profiles of CALIPSO were used which were not dropped due to the presence of clouds or quality screening.

3.6.2 Attenuated backscatter

Before comparing the optical parameters with regard to analysis malfunctions first the raw signals on which the algorithms operate should be compared to the MULIS raw data. It would be ideal to conduct a comparison of the backscatter signals P of both instruments. However, since the measurement geometries of the two instruments (from space / from ground) lead to completely different values of transmission, the backscatter signals are not comparable. Instead of this the attenuated backscatter of CALIPSO β' (Eq. 2.12) is compared with a 'synthetic' attenuated backscatter calculated from MULIS data which has to be 'inverted' from the ground based to the space borne configuration. For this purpose,

extinction and backscatter coefficients of the air molecules are derived from radiosonde data and the corresponding coefficients for particles from nighttime MULIS measurements (daytime MULIS measurements can not derive the lidar ratio, without which the 'inversion' is too unstable and comparison becomes difficult). Doing this, the attenuated backscatter is derived for the troposphere up to typically 5-7 km above which the weak MULIS signal lead to larger uncertainties and again to an unstable inversion. In this height, the MULIS β' profile is fitted to the CALIPSO profile, that means the transmission of the upper atmosphere is assumed to be identical in both cases. As the single β' profile of CALIPSO has a low SNR, 15 laser shots are averaged corresponding to a horizontal width of 5 km and this average afterward is smoothed vertically with a window length of 450 m (15 height bins).

As a case study, in Fig. 3.13 the attenuated backscatter signals at 532 nm (top) and their relative difference (bottom) are shown for seven nighttime measurements. The comparison demonstrates on average a good agreement of β' in the lowermost aerosol layers, indicating that the aerosol distribution is spatially very homogeneous on the scale of the distance between the MULIS site and the CALIPSO track (25-85km). Note that this large scale homogeneity is site specific; other sites such as e.g. Potenza, which is situated near the shoreline, can have strong variability in the PBL over much smaller scales [Mona et al., 2009].

In the first case (8 April) the 15 shot average of CALIPSO (red) and the 30-min average of the MULIS signal (blue) roughly follow each other (upper plot), however the CALIPSO signal shows significant small scale fluctuations, leading to a standard deviation of the relative signal difference of 15 % (lower plot). These fluctuations originate from the low signal to noise ratio of CALIPSO, and are nicely smoothed out when averaging over seven 5-km-profiles (not shown) which leads to a standard deviation of 5.3 %. This explains why the signal is averaged over 35 km for the further analysis, and can be further justified by the fact that this is on the same scale as the distance between the MULIS site and the point of nearest overpass. The second, fifth and seventh case show good absolute agreement between CALIPSO and MULIS; the larger relative differences for case five (2 November) occur because the signal is lower than usual because the atmosphere has a very low aerosol content. The third case (27 June) shows significant differences around 2km, which can be assigned to unstable and inhomogeneous conditions observed during the beginning of the ground measurement. The conditions stabilized during the progression of the measurement, and using a later MULIS 30-min average results in much better agreement (not shown) [Schnell et al., 2010]. Also case four (29 July) shows large differences due to inhomogeneous conditions, which however remained unstable during the whole measurement, which is why this case was screened. Finally, the case on 18 November contains a Cirrus above 7km, explaining the large deviations. This case was also screened. Averaged over all cases, the mean value of the relative difference is 0.2 %. Therefore it can be assumed that differences of the extinction profiles are mainly based on malfunctions of the analysis of CALIPSO after screening unstable and cloudy measurements.

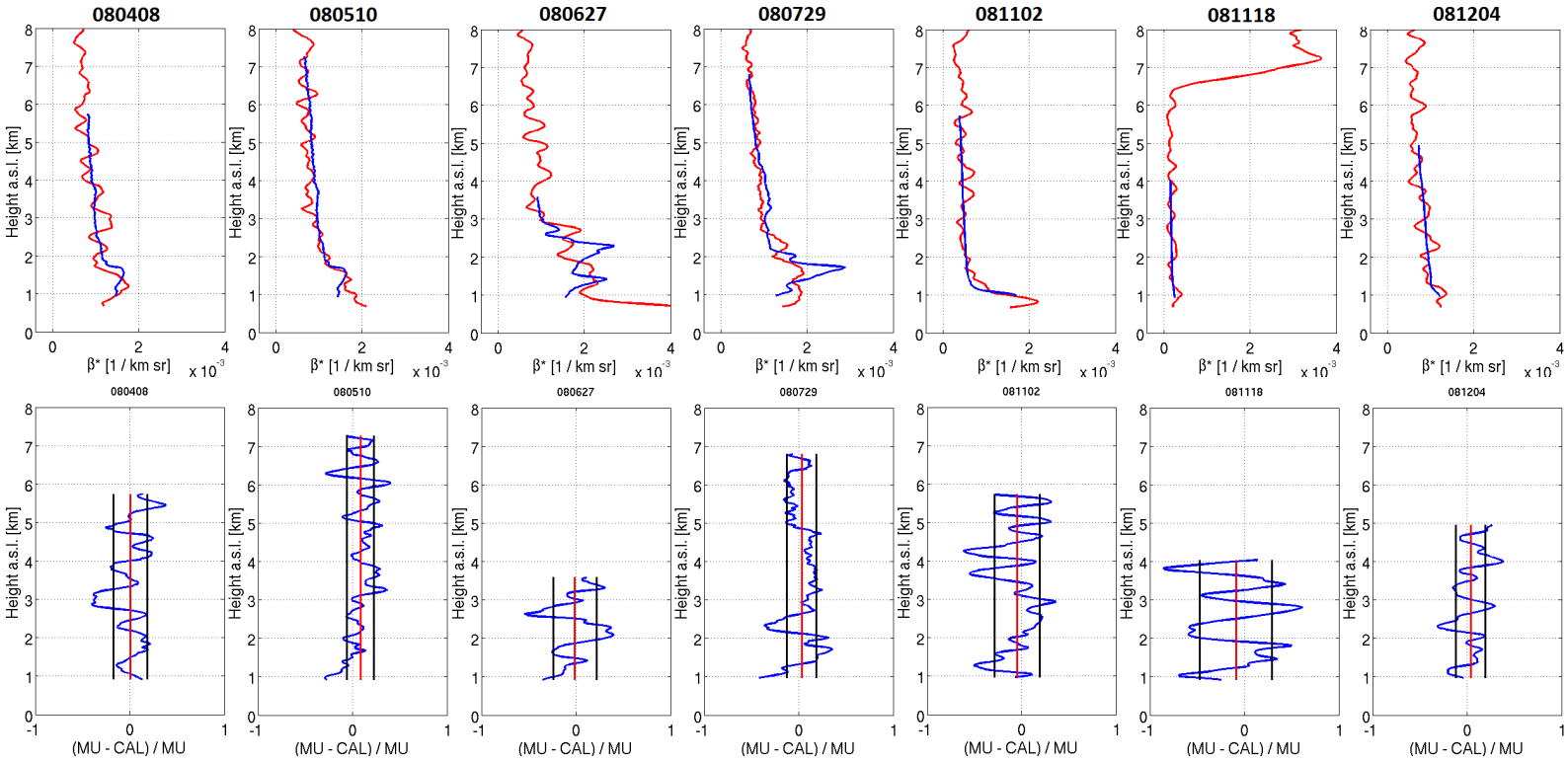

Figure 3.13: Comparison of attenuated backscatter signals β' measured by CALIPSO (red) and calculated from MULIS measurements (blue) (upper panel) and their relative differences (blue) (lower panel) for seven cases in 2008, where the red and black lines denote the mean and standard deviation, respectively. The dates are given in the format YYMMDD.

3.6.3 Limitations in the CALIPSO extinction profiles

In contrast to the attenuated backscatter profiles, the comparison of the extinction coefficient profiles of CALIPSO and MULIS shows clear differences (see e.g. Figs. 3.14, 3.15, 3.16). Several reasons originating in weaknesses of the CALIPSO algorithms were identified in this thesis: failure of layer detection, particularly in the PBL, wrong lidar ratio estimations, and insufficient cloud clearing. In the following these three error sources are illustrated by showing example cases, and the methods for analyzing the measurements with respect to the error sources are presented.

3.6.3.1 Failure of layer detection

The problem occurring most often with the CALIPSO data is that layers are overlooked. This failure can have several reasons, the most frequent of which is that the aerosol content is too small to produce backscatter signals above the detection threshold.

This happens especially when the background noise is high at daytime. Also, aerosol layers detected by CALIPSO have unnaturally sharp boundaries. Accordingly, the extinction coefficients often drop from high values to 'nothing' at the layer borders, which also leads to an underestimations of the AOD. Inhomogeneous meteorological conditions have to be taken into account, as well. Fig. 3.14 shows three examples of this detection failure: 1st May 2007 (day measurement), 5th August 2009 (day) and 20th August 2009 (night). In all three cases CALIPSO reports only part of the aerosol profile detected by MULIS. Especially on the 2nd and 3rd plot, the boundary layer is not well described, there is no aerosol information below ∼1.5 km a.s.l. (approx. 1 km above ground). Also weak layers above the PBL are not registered (e.g. 1st panel, 3.2 - 4 km a.s.l.). The regions where MULIS detects significant aerosol load not detected by CALIPSO are marked in pink, the optical depth of these regions is noted as "lost" optical depth (LOD) in the plots. The values vary from LOD = 0.042 to 0.091, which leads to a lowering of AOD in the CALIPSO data.

3.6.3.2 Incorrect assumption of lidar ratio

While the CALIPSO lidar ratios have to be assumed by a complex aerosol type classification to derive the extinction coefficients and the corresponding optical depths, these lidar ratios can be derived for 532 nm from MULIS measurements at nighttime conditions.

The effect of a wrong lidar ratio is visualized in Fig. 3.15; in the three panels, the profiles of backscatter coefficient β_p, extinction coefficient α_p, and lidar ratio S_p at 532 nm can be seen. While the backscatter coefficients of both instruments are in good agreement, the corresponding extinction coefficient of CALIPSO is clearly lower than that of MULIS. The reason is that the lidar ratios at 532 nm of MULIS and CALIPSO show a strong discrepancy; the one of MULIS is 73 sr, the S_p of CALIPSO is set to 40 sr below 1.6 km and to 55 sr above. To investigate wether the $\alpha_p's$ differ because of the different lidar ratios, the MULIS profiles are recalculated using the CALIPSO S_p instead of the measured value (red profile in Fig. 3.15). This leads to a much better agreement of the α_p profiles. As a

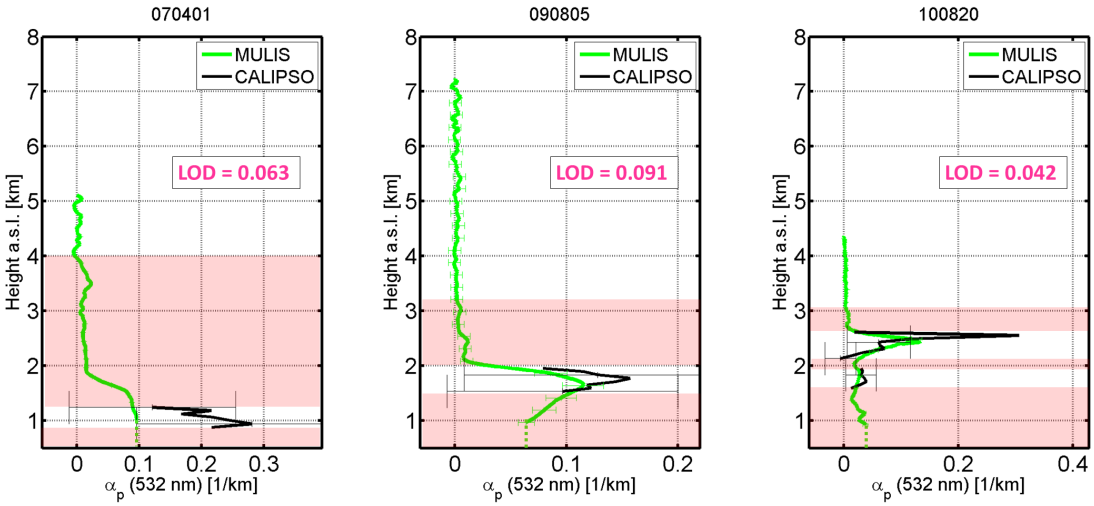

Figure 3.14: Examples of failed layer detection: extinction coefficient profiles α_p at 532 nm from MULIS (green) and CALIPSO (black) for 1st April 2007 (day), 5th August 2009 (day), and 20th August 2010 (night). The pink regions mark layers detected by MULIS but not by CALIPSO, the LOD is the optical depth integrated over these regions.

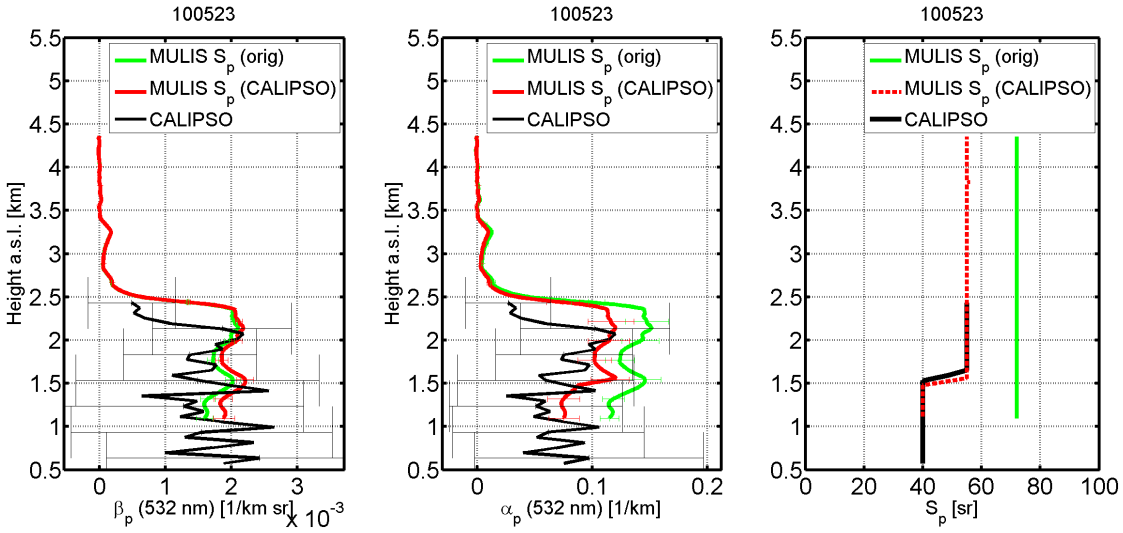

Figure 3.15: Example of incorrectly estimated lidar ratio, 23. May 2010: β_p (left), α_p (middle), and S_p (right) for 532 nm are shown for MULIS (green) and CALIPSO (black). Additionally the MULIS extinction coefficient calculated with the CALIPSO lidar ratio is shown in red.

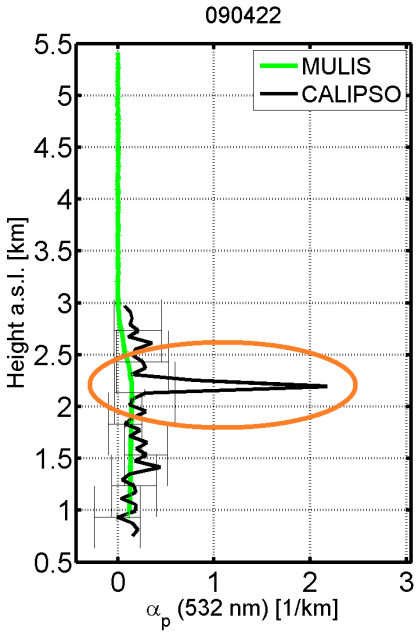

Figure 3.16: Example of an insufficient cloud clearing: 22. April 2009 (day). The diagram shows the extinction coefficients at 532 nm from MULIS (green) and CALIPSO (black).

consequence, the measured aerosol layer seems to be the same; the only difference is the used lidar ratio which also leads to a wrong calculation of the AOD. The change of the lidar ratio in the MULIS analysis produces a change of the AOD of ΔAOD = -0.083 which corresponds with an underestimation of 32 % ($AOD_{original}$= 0.260).

3.6.3.3 Clouds within analyzed scene

As mentioned above, only 5-km-profiles in which no clouds were reported and the cloud optical depth is found to be zero are used for the comparison. Nonetheless, clouds can still affect this aerosol data. In Sect. 3.5.2.1 in which the layer detection algorithm SIBYL is described, the so called 'scene' is defined for which the analysis of the CALIPSO data is done. It is a region of 80 km which is subdivided into 16 5-km sets. Detected features like clouds are removed and the underlying signals are normalized by their optical depth. Also single profiles of attenuated backscatter signals containing the signals of small scale clouds are removed. However, both of these procedures can influence cloud free signals. Most frequently there are problems with the removal of small scaled clouds at the PBL top, as can be seen in Fig. 3.16. There, one overpass 5-km-profile is shown instead of the average over all seven profiles (overpass $\pm$3). The extinction coefficient has a very strong peak at 2.2 km which is neither in agreement with the MULIS data nor meteorologically reasonable. This strong peak results from insufficient cloud clearing before the aerosol analysis: Fig. 3.17 shows the quicklook of the raw data as well as the feature type classification for the region of the overpass. Small scaled clouds can be noticed easily in the VFM (right panel) in a

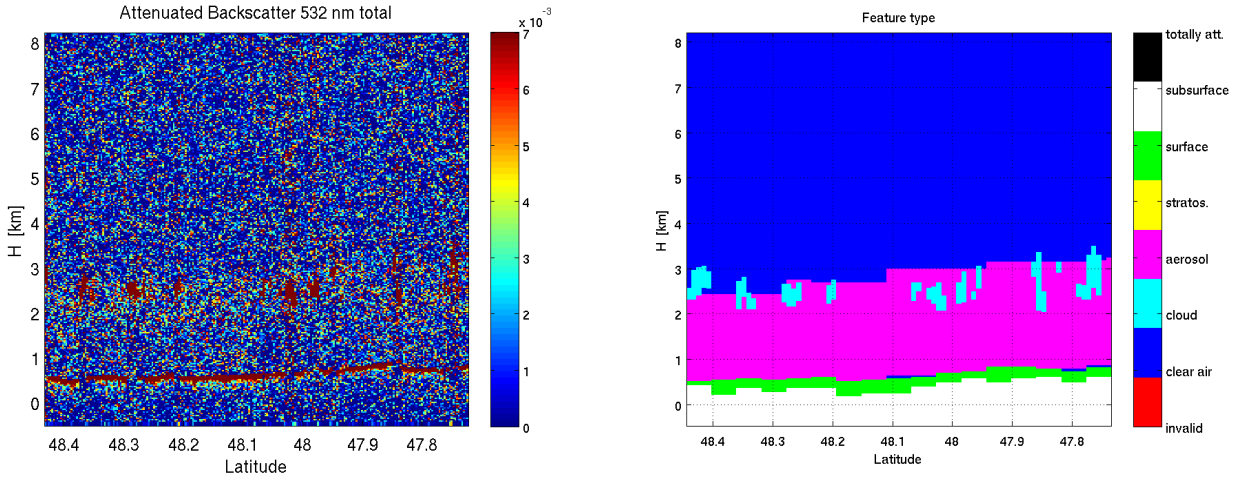

Figure 3.17: Overview of the measurement situation with quicklook (left) and VFM Feature type (right) for the overpass of 22th April 2009

height of 2 to 3.5 km above and in the upper region of the detected aerosol layer. This is not as obvious in the quicklook of the raw data: the data of this daytime measurement has a low SNR, the detection and clearing of the cloud signals is difficult and in case of Fig. 3.16 obviously failed. The average over all seven profiles used for the comparison with MULIS is therefore influenced by this peak and the extinction coefficient and the corresponding AOD is overestimated.

Another example for the influence of clouds on a profile is shown in Fig. 3.18: Regarding the feature type, the 5-km-profile of the nearest overpass of CALIPSO (between the vertical orange lines) contains no clouds. However, in the three adjoining profiles from 48.15° to 48.03° Latitude a cirrus cloud is detected at about 6 km. The four aerosol extinction profiles –marked by the green lines– consisting of these three profiles and the overpass profile have the same values above 1 km, which means that the α_p was calculated from a signal average over 20 km. Clearly, the extinction coefficients of the aerosol layer between 1 and 3 km height have much higher values than the aerosol layer detected between Latitudes 48.4° and 48.15° at approximately the same height ($\alpha_p \sim 0.1$ / km compared to $\alpha_p \sim 0.05$ / km). These values are due to a wrong transmission correction of the cirrus cloud. Further, in 2.8 km height the extinction coefficients of two height bins clearly have larger values than above and below ($\alpha_p > 0.25$ / km in this height compared to $\alpha_p < 0.1$ / km), which can be explained by a failed clearing of the small scale cloud at 48.03° at an height of 2.5 km. These analysis errors lead to an overestimation of the extinction coefficient in this profile. So also clouds which are not within the 5-km-profile but in adjacent profiles can influence the extinction and therefor the AOD calculation.

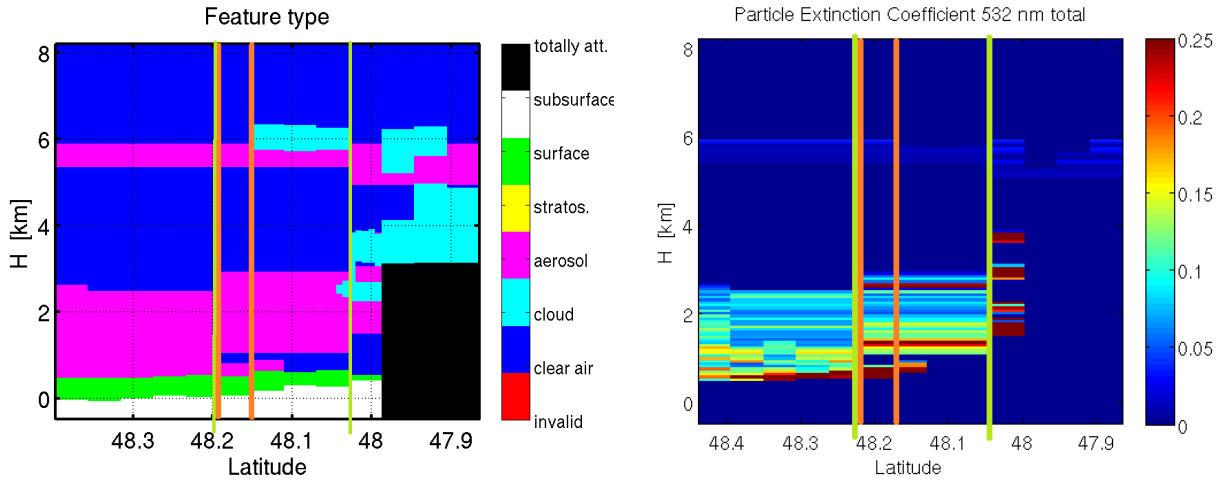

Figure 3.18: Example for clouds in scene: the left panel depicts an excerpt of the feature type (FT) from -0.5 km to 8 km for 27th June 2008 near Maisach, in the right panel the corresponding aerosol extinction coefficient color coded (in [1/km]) for the same region. The vertical orange lines mark the borders of the 5-km-profile of interest (overpass), the green lines are the borders of the 20-km-analysis containing it.

3.6.3.4 Problem criteria

In order to quantify the importance of the three different reasons for a failing CALIPSO retrieval, the following criteria are defined: A measurement is tagged to have missed layers if the LOD $>$ 0.02. Further, a measurement is defined as assuming a wrong lidar ratio if any of the aerosol layers detected by CALIPSO have been assigned a lidar ratio which differs by more than 10sr from the value that MULIS measures. This can only be done at nighttime in case MULIS is able to measure the lidar ratio. Finally, the CALIPSO scene is said to be cloud contaminated if clouds are detected anywhere within the 80 km of the scene. To this end the VFM feature types of all 52 measurements were examined.

3.6.4 Meteorological conditions studied with HYSPLIT measurements

The three above described reasons for the deviation between MULIS and CALIPSO profiles are all due to problems of the CALIPSO algorithms for layer detection, cloud clearing, and aerosol classification. However, the variability of the atmosphere has to be taken into account, as well. Accordingly, for each CALIPSO overpass air mass transportation trajectories are built from the HYSPLIT (HYbrid Single-Particle Lagrangian Integrated Trajectory, [Draxler and Rolph, 2012]) model which computes the advection of an air parcel based on an archive of gridded meteorological data (including e.g. wind speed). These trajectories start at the location of the ground based lidar MULIS in Maisach in seven heights varying from 0.5 km to 5 km a.s.l. and are calculated for 24 h. The aim is to

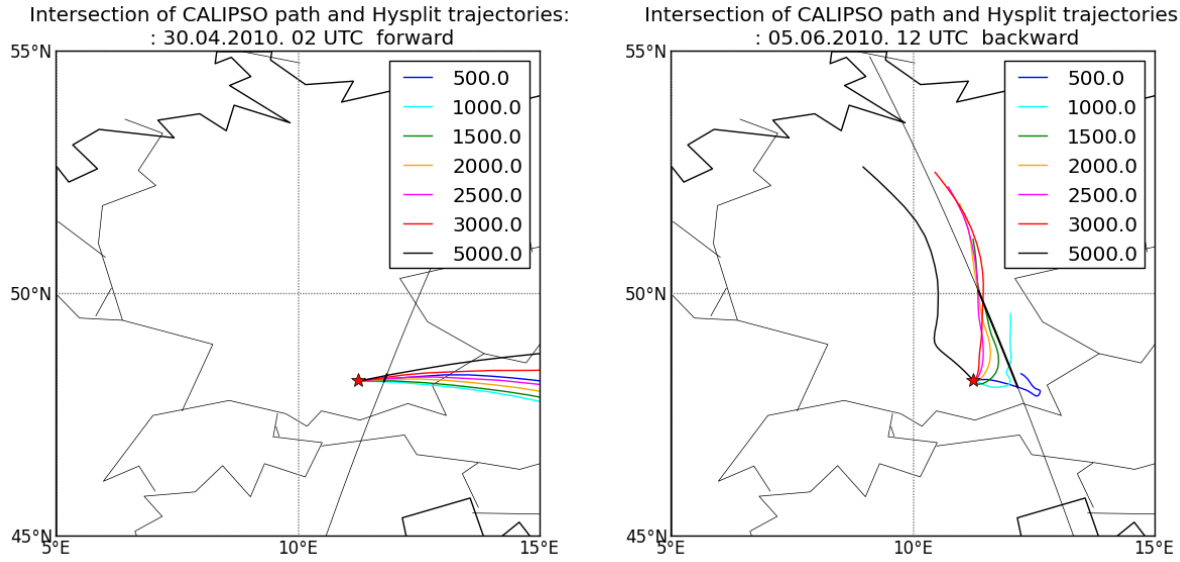

Figure 3.19: Examples of HYSPLIT trajectories starting at Maisach (48.209°N, 11.258°E) at the heights 0.5 km, 1 km, 1.5 km, 2 km, 2.5 km, 3 km, and 5 km. Additionally the CALIPSO path (black) is plotted. The diagrams show two days: the 30th April 2010 (left) with a very straight westerly wind flow and the 5th June 2010 (right) with a strong wind shear with height, the wind direction changes by ∼180° from 1 km to 5 km.

locate the intersections between the trajectories and the path of CALIPSO. Therefore the trajectories are calculated either backwards or forwards, dependent on the wind directions and the location of the CALIPSO path (overpass East or West of Maisach). For found intersections the height, the transportation time, the coordinates, and the according profile number of the CALIPSO AP data are noted. In Fig. 3.19 two examples are shown: on the left panel a very straight westerly flow can be seen, where all intersections of the trajectories with the CALIPSO path occur within the first hour of the trajectory paths and through a weak wind shear only 4 5-km-profiles are touched corresponding to a path length of 20 km. The situation in the right panel is completely different: the wind direction changes from 0.5 km to 5 km by nearly 180°, indicating a very strong wind shear. The intersections of the trajectories with the CALIPSO path are stretched over 230 km, corresponding to 46 5-km-profiles; the 5km trajectory does not even intersect within the 24h limit. Also the time from the starting point to the intersection is very long and varies from 7 h to 18 h.

For the first example, a good approach would be to take the intersection profiles when comparing with MULIS instead of the nearest overpass. In case of a CALIPSO validation measurement, the most suitable of the five MULIS 30-min-averages is chosen depending on the intersection period: In the case of 30th April 2010 the overpass of CALIPSO occurred at 01:35 UTC, the backward trajectory starting at 02 UTC intersects the satellite path within 2 hours. It is therefore reasonable to use for comparisons the first 30-min-average from 00:20 UTC to 00:50 UTC.

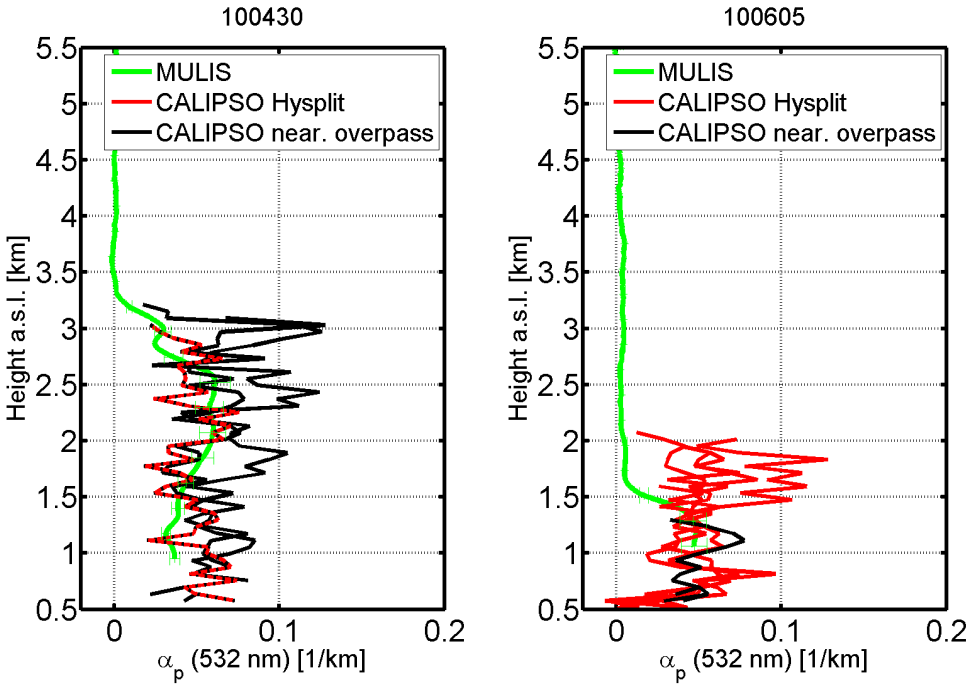

Figure 3.20: Extinction coefficient profiles for 30.04.2010 (left) and 05.06.2010 (right) of MULIS (green), CALIPSO seven profiles nearest of overpass (black) and CALIPSO profiles of HYSPLIT intersections. Note that several profiles of CALIPSO can be identical or almost so.

In contrast, in the second example the comparison with the average of the path with length 230 km is not reasonable. The best opportunity for a comparison is then the nearest overpass profile, given that the wind speeds are very low and a stationary and hopefully homogeneous aerosol distribution has to be assumed. In this case, the central 30-min-average is used for comparison. Fig. 3.20 compares the extinction coefficient profiles of MULIS (green) with CALIPSO, once showing the profiles of the nearest overpass (black) and once the profiles intersecting with the HYSPLIT-trajectories (red). On the 30th April 2010, the profiles of the intersection match the trend of the MULIS profile better than the seven profiles from nearest overpass. However, all of the intersection profiles in this example are also nearest overpass profiles, so the average over the seven overpass profiles should still be good for comparison with the MULIS extinction coefficient. On the 5th June 2010 it is obvious that the use of the nearest overpass data from CALIPSO affords better results for the comparison with MULIS than the intersection profiles. In most of these profiles, an aerosol layer from 1.5 km to 2 km with an OD of about 0.03 was recorded, which was definitely not present above the MULIS site. In contrast, the overpass value matches quiet well with the MULIS profile.

Concluding, it is sufficiently safe to compare the MULIS measurements with the seven nearest overpass profiles of CALIPSO and thereby skip the HYSPLIT analysis.

3.7 Summary

In this section the four instruments (the AERONET-Cimel, MODIS, MULIS, and CALIPSO) and their available data was described. It was also explained how the four datasets are processed in this study to receive aerosol information. Special attention was given to the complex algorithms of the CALIPSO retrievals.

As the CALIPSO results show differences compared to the results of the other instruments, a direct comparison of coincident measurements of MULIS and CALIPSO needs to be performed. It was shown that the raw signals between the two instruments are more or less in agreement, and that differences can be explained and pinpointed, the reasons being low signal to noise ratio, cloud contamination and small scale variabilities of the aerosol distribution. Further, common problems occurring in the CALIPSO aerosol algorithms, which also influences the optical depth, were determined to be the failure of layer detection, particularly in the PBL, the wrong estimation of the lidar ratio, and insufficient cloud clearing. Methods to analyze and quantify these problems were presented. Finally, a HYSPLIT analysis was performed to verify that it is safe to use the nearest CALIPSO overpass profiles for the comparison, instead of the trajectory intersections with the CALIPSO path.

Chapter 4

Aerosol distribution above Munich

After the description of the instruments and the handling of the data, the aerosol distribution above Munich can be described independently with the four instruments. Each of these instruments has its own advantages: AERONET has the most complete time coverage and – considering that it is the instrument with the most direct way of measuring the AOD – has the most precise measurements of AOD at seven wavelengths. MODIS on the other hand has global coverage and as a consequence allows to set the Munich region into perspective with Central Europe. While these two instruments only deliver AOD at daytime, the lidars measure both day and night, get better results at night when the sun does not create background noise, and in addition to the AOD and Ångström exponent obtain aerosol extinction profiles and the linear particle depolarization. While MULIS can best detect thin and dilute aerosol layers (due to a much higher signal to noise ratio) and can measure the lidar ratio at night, CALIPSO with its sophisticated aerosol type identification algorithm has the means of retrieving aerosol layers globally. By 'calibrating' CALIPSO with more precise ground based instruments such as MULIS and AERONET, it has the capability of delivering high quality aerosol profiles globally.

First the seasonal and monthly variation of the AOD is described based on AERONET and MODIS monthly averages. The studies using MULIS and CALIPSO data additionally provide height resolved information, such as a discrimination between EL and PBL, aerosol layer specific results such as e.g. optical depth and linear particle depolarization, and profiles of e.g. extinction coefficient and Ångström exponent. Please note that the four datasets will be presented here individually. The comparison of their findings will be postponed to Chap. 5.

The description of the aerosol distribution based on CALIPSO refers to the Munich region, while the later comparison with MODIS and AERONET (Chap. 5) will also include a CALIPSO dataset calculated for the smaller MODIS region. For the seasonal variation the month are summarized as follows: spring: March, April, May (MAM); summer: June, July, August (JJA); autumn: September, October, November (SON); and winter: December, January, February (DJF).

All plots showing monthly or seasonal means also depict the median and – as error bars – the *uncertainty* of the mean ($\frac{\sigma}{\sqrt{N}}$, with N being the number of data values), which is not

Table 4.1: Mean, median and uncertainty of the AERONET AOD over the time period from 2007 to 2010 for all seven wavelengths.

λ	**mean(AOD)**	**median(AOD)**	**std(AOD)**
1020 nm	0.062	0.055	0.003
870 nm	0.078	0.071	0.004
675 nm	0.108	0.098	0.006
532 nm	0.154	0.139	0.008
440 nm	0.200	0.182	0.010
380 nm	0.238	0.220	0.012
340 nm	0.269	0.251	0.014

to be confused with the *variability* of the data, σ. This also holds – unless explicitly stated otherwise – for numerary values in the text denoting the mean and uncertainty as $x \pm y$. Also note that the medians for AERONET and MODIS are based on monthly data, while those for the other two instruments is based on single measurements.

4.1 Aerosol distribution from AERONET-Cimel data

Measurements with the Sunphotometer are performed continuously at the MIM in Munich, while the only missing data is due to calibration periods. At the same time, aerosol properties can only be gained in cloud free conditions. Nevertheless, the data base presented here consists of of 627 days (43%) of measurements, all in all.

The mean AODs as well as the corresponding medians and uncertainty of the mean for the whole time period are listed in Table 4.1. These numbers point towards a wavelength dependency: with increasing wavelength the AOD decreases which is expected for aerosols. The small difference between mean and median values indicate that there are no strong outliers in the data which was expected as monthly averages were used. The fact that the median is always smaller than the mean value shows that in general smaller values of AOD than the mean were measured; only in one year the values were clearly higher than usually (not shown).

As the AERONET dataset is based on the highest number of measurements of all four datasets, it is the most suitable set to show the monthly variation of the AOD above Munich. In Fig. 4.1, the monthly means and their uncertainties for the seven wavelengths are shown. Just as on the absolute means of the AOD, the wavelength dependency can be seen clearly. Also the values from March to September (spring and summer) are significantly higher than the winter months (October to February). The lowest AOD occurs in November, while the maximum is reached in July. Only the highest wavelengths differ a bit: here the lowest values occur in December and the maximum is found in April, where the other wavelengths, too, show a local maximum. This difference indicates a change in the aerosol type, especially between May an July, where the span between the AOD at 340 nm and

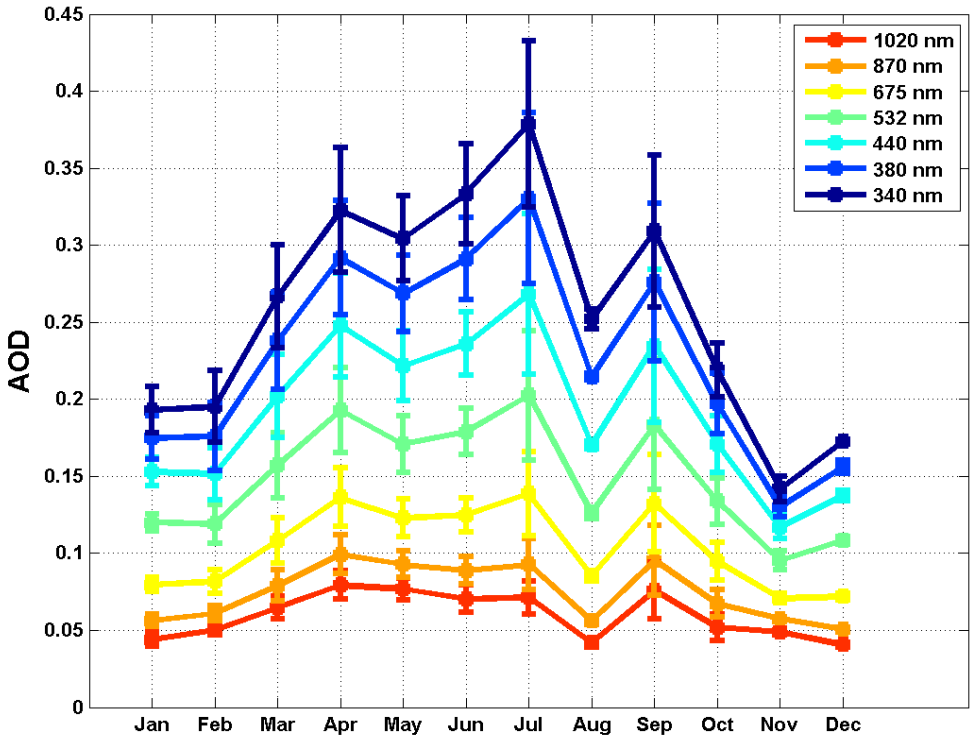

Figure 4.1: Monthly mean AOD and uncertainty at the seven wavelengths 1020 nm, 870 nm, 675 nm, 532 nm, 440 nm, 380 nm, and 340 nm derived from Cimel measurements at Munich. Used are the monthly mean values from 2007 to 2010.

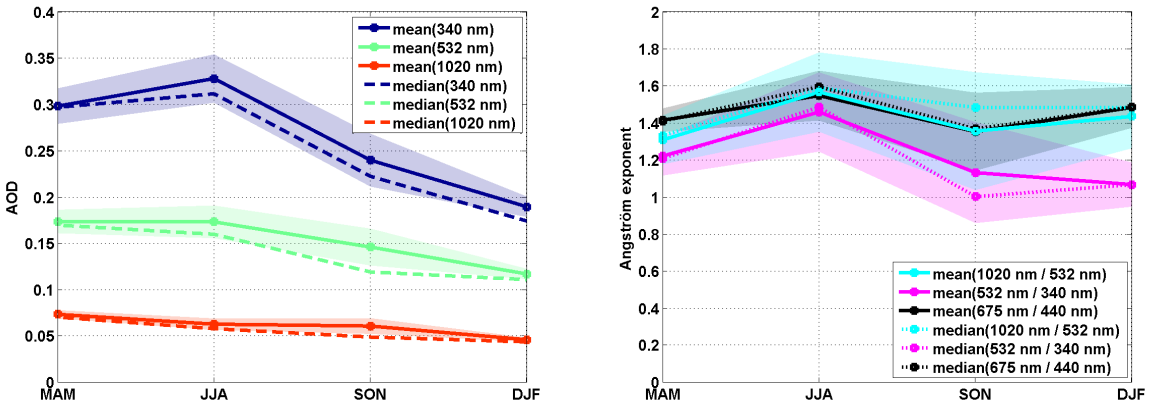

Figure 4.2: mean (solid lines), median (dashed lines), and uncertainty (shaded regions) of the AOD at 1020 nm, 532 nm, and 340 nm (left panel) and of Ångström exponents κ(1020nm/532nm) (cyan), κ(532nm/340nm) (magenta), and κ(675nm/440nm) (black) (right panel) derived from AERONET measurements at Munich. Used are the monthly means from 2007 to 2010.

at 1020 nm clearly increases. This can be explained by an increase of smaller particles on which the smaller wavelengths react more sensitively than in the near infrared (NIR).

The variation of the 1020 nm and 870 nm AODs is smaller than the one at 340 nm, the ratio between maximum and minimum is higher for the smaller wavelengths (2.67 at 340 nm, 1.95 at 1020 nm). For all seven wavelengths a local minimum in August is clearly visible; in April and September we also observe local maxima

For the further study only three wavelengths are discussed: 1020 nm in the NIR, 532 nm in the visible range, and 340 nm in the near UV. These wavelengths represent sufficiently the span of the AERONET data and best match the wavelengths of the other described instruments.

The seasonal variation (left panel of Fig. 4.2) shows that the lowest aerosol values occur in wintertime for all three wavelengths, whereas the maxima differ: for the UV the maximum is in summertime, while the AOD at 1020 nm has the highest value in spring. The green line has nearly the same values for both of these seasons. This difference indicates that the most frequent aerosol type above Munich changes between spring and summer.

This observation is also confirmed by the Ångström exponents κ (Fig. 4.2): from spring to summer κ increases which means that the particle size decreases. Regarding the κ(1020nm/532nm) and κ(532nm/340nm), the Ångström exponent increases with increasing wavelength, as expected from Fig. (2.2). However, the dependency of κ on the wavelengths is not simply linear, the (4-year) mean values of all three Ångström exponents are 1.23, 1.45, and 1.41 for κ(1020nm/532nm) κ(675nm/440nm), and κ(532nm/340nm), respectively. Thereby, κ(675nm/440nm) is covering sub-ranges of the other two Ångström exponents. This already indicates that a later comparison between the Ångström exponents

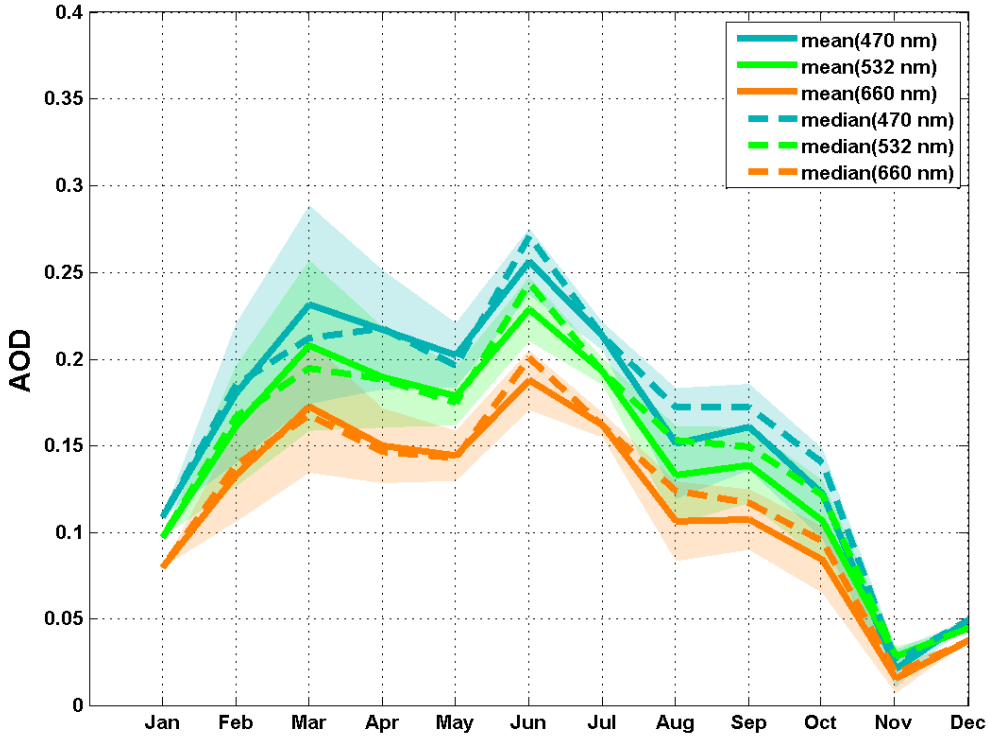

Figure 4.3: Monthly mean (solid lines), median (dashed lines), and uncertainty (shaded regions) of the AOD at the wavelengths 470 nm, 532 nm, 660 nm for MODIS region for MODIS onboard of Terra. For the months January and December only one data point for each was available.

received at different wavelength pairs due to different instruments can not be explained as simply as the comparison of a value like the AOD.

4.2 Aerosol distribution from MODIS data

In contrast to the AERONET data, the MODIS dataset covers a larger area of 1°x1° (see green rectangle in Fig. 3.1). In the MODIS region, the AOD has mean values 0.126 ± 0.009 for 660 nm, of 0.158 ± 0.011 for 532 nm, and 0.174 ± 0.013 for 470 nm. Regarding the behavior of the monthly averages (Fig. 4.3), three maxima can be identified: the strongest in June, and two local ones in March and September. The lowest AODs occur in November, while May and August values are also local minima.

The seasonal variation can be seen in Fig. 4.4; clearly the AOD in the left panel has higher values above Munich in spring and summer (0.192/0.185 at 532 nm), in autumn and winter the values are much lower (0.104 / 0.125). Unexpectedly in autumn the smallest

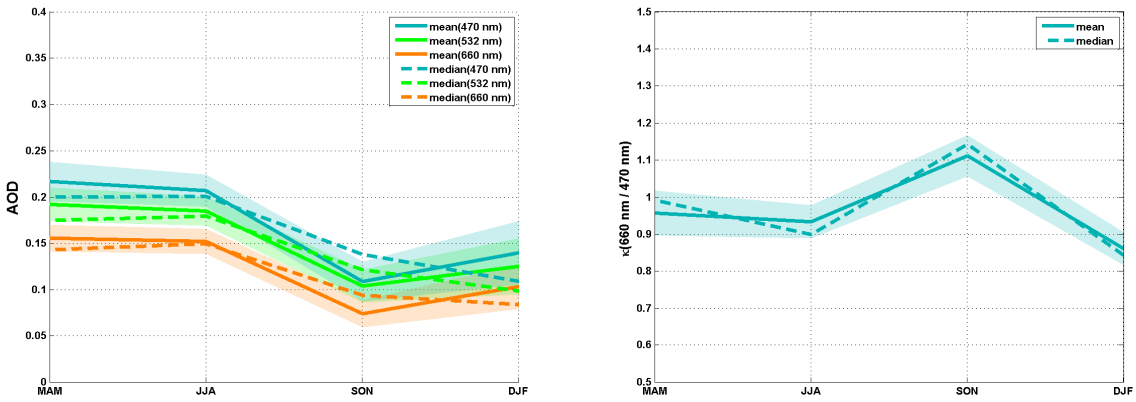

Figure 4.4: Seasonal mean (solid lines), median (dashed lines), and uncertainty (shaded regions) of the AOD at the wavelengths 660 nm, 532 nm, 470 nm (left panel) and of the Ångström exponent κ between 660 nm and 470 nm (right panel) for MODIS region for MODIS onboard of Terra and Aqua.

values occur. Additionally, the Ångström exponent in this season differs from the other three values, it is larger indicating smaller particles, and the difference between maximum and minimum of κ is 0.25. However, as in Winter there is merely a smaller amount of data available, the corresponding mean AODs and Ångström exponent need to be regarded with caution.

4.3 Aerosol distribution from MULIS data

The dataset of MULIS contains more information about aerosols than the ones of AERONET and MODIS: in addition to the total AOD and the column Ångström exponent, also layer values of optical depth, Ångström exponent κ(1064nm/532nm), and particle lin depolarization ratio δ_p can be studied. On 201 days, 233 measurements were performed. In all cases, values for the PBL are available, on 130 measurements elevated layers occurred, as well. A seasonal analysis (see Table 4.2) shows that while the most elevated layers were detected in summer, the occurrence of ELs is highest in springtime with more than three quarters of the measurements having performed elevated layers. In winter, EL are detected less frequently; in only one third of the measurements additional layers to the PBL exist. Tab. 4.2 also illustrates that the measurement conditions in winter are worse than in the other seasons. The number of PBL layers is the same as the number of measurements, so in winter significantly less measurements could be performed, mostly due to bad weather conditions.

Table 4.2: Seasonal variation of detected layers: number of PBL layers (= number of measurements), number of all elevated layers and occurrence percentage for elevated layers.

	Spring	Summer	Autumn	Winter	All
PBL layers	60	78	73	22	233
Elevated layers	45	51	43	8	147
Occurrence EL	75 %	65 %	59 %	36 %	63 %

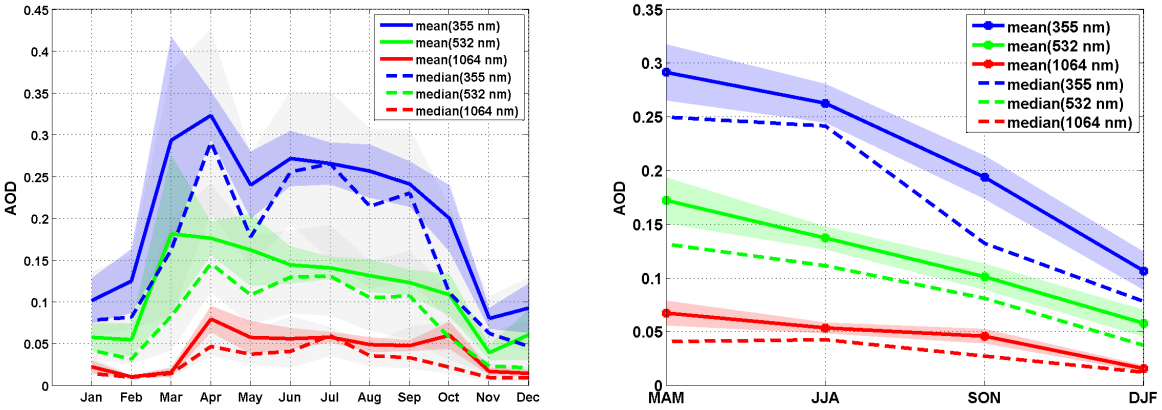

Figure 4.5: Monthly (left) and seasonal (right) mean (solid lines), median (dashed lines), and uncertainty (shaded regions) of the AOD at 1064 nm, 532 nm, and 355 nm derived from MULIS measurements in Maisach from 2007 to 2010.

4.3.1 Variation of the optical depth

Using these 233 measurements, the AOD can be studied: the wavelength dependency of the three MULIS wavelengths 1064 nm, 532 nm, and 355 nm can be seen in the average values (0.050 ± 0.004, 0.127 ± 0.008, 0.233 ± 0.011, respectively) as well as in the monthly and seasonal variation of the AOD (Fig. 4.5): the AOD decreases with increasing wavelength.

For MULIS, the largest AODs occur in March / April, the lowest in November. From May to October, the values differ only a little, no strong local maxima or minima can be found. Only a continuous slight decrease of the AOD can be seen, which is most pronounced for 532nm. Regarding the seasonal variation (Fig. 4.5, right panel) the highest aerosol load is detected in spring, while the lowest AOD values are measured in winter and are about factor 3 to 4 smaller than the spring AODs.

Note that for some measurements the extinction coefficient can not be provided for all wavelengths, resulting in differences in the datasets of the three wavelengths. Especially in wintertime only few profiles of 1064 nm exist. This also explains why the uncertainty in March is much higher for 532 nm and 355 nm than for 1064nm: on the 16th March 2007, very high AODs were measured (0.98 for 355 nm and 0.72 for 532 nm) which are explained

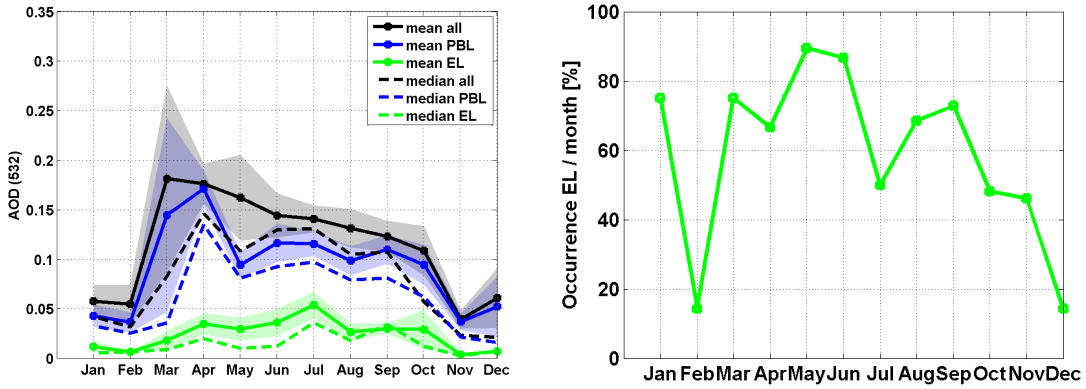

Figure 4.6: Left panel: Monthly mean mean (solid lines), median (dashed lines), and uncertainty (shaded regions) of the AOD (black), OD_{PBL} (blue), and OD_{EL} (green) at 532 nm derived from MULIS measurements in Maisach. Note that OD_{EL} is calculated for the subset of measurements which contain at least one EL. To obtain the mean OD_{EL} over all measurements, either multiply the value with the EL occurrence, or subtract OD_{PBL} from the AOD. Right panel: Monthly probability of EL occurrence. Used are all data from 2007 to 2010.

by a high relative humidity of more than 60%, leading to swollen hydrophilic aerosols. The high values were also confirmed by AERONET measurements. In Fig. 4.5, they lead to a significant increase in the mean AODs in March and in the uncertainty. Also the large difference between the median and mean at the two wavelengths in March indicates that here a single or few events distort the mean values. On this day, however, the 1064 nm channel was not yet operational (see Sect. 3.4.4) so that the mean 1064 nm March AOD is not affected.

The results can be studied further by separating the AOD into the optical depth in the planetary boundary layer (OD_{PBL}) and in elevated layers (OD_{EL}). Note that the latter is calculated for the subset of measurements which contain at least one EL, i.e. measurements not containing ELs will not be considered when e.g. calculating mean values. To obtain the mean OD_{EL} over all measurements, either multiply the value with the respective EL occurrence, or subtractOD_{PBL} from the AOD. The main aerosol load can be found in the PBL, the mean optical depth is much higher than the mean optical depth in the elevated layers ($OD_{\mathrm{PBL}}(1064\ \mathrm{nm}) = 0.042$, $OD_{\mathrm{EL}}(1064\ \mathrm{nm}) = 0.013$, $OD_{\mathrm{PBL}}(532\ \mathrm{nm}) = 0.106$, $OD_{\mathrm{EL}}(532\ \mathrm{nm}) = 0.030$, $OD_{\mathrm{PBL}}(355\ \mathrm{nm}) = 0.198$, $OD_{\mathrm{EL}}(355\ \mathrm{nm}) = 0.047$). Averaged over all measurements including those without EL detection, the optical depth at 532 nm in the EL is even lower (0.017). However, the contribution of the EL on the aerosol amount is still important: Fig. 4.6, left panel, shows the monthly variation at 532 nm for the total mean AOD (black), the OD_{PBL} (blue), and the OD_{EL}(green). In March and from May to August, the difference between AOD and OD_{PBL} is larger than 0.025, which shows a strong contribution of the EL to the AOD. The maximum of the elevated layers is in July:

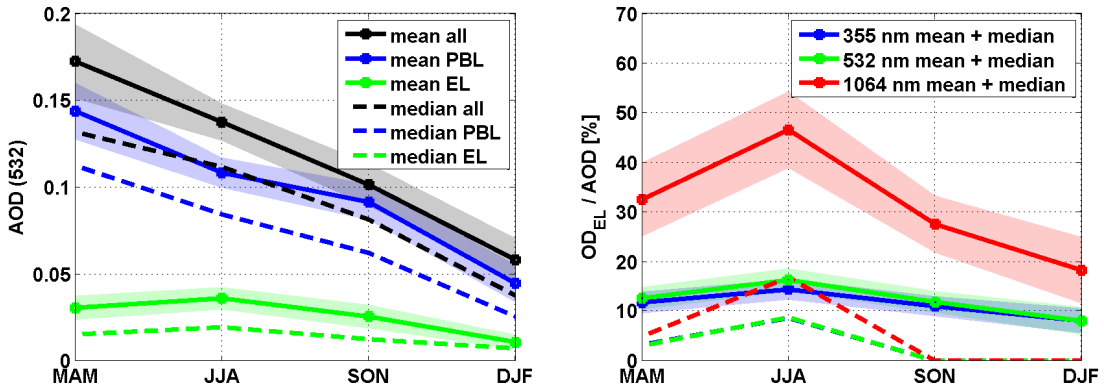

Figure 4.7: Left panel: seasonal mean (solid lines), median (dashed lines), and uncertainty (shaded regions) of of the AOD (black), OD_{PBL} (blue), and OD_{EL} (green) at 532 nm derived from MULIS measurements in Maisach. Right panel: Seasonal variation of the averaged fraction of EL to the AOD at 1064 nm, 532 nm and 355 nm. Used are all data from 2007 to 2010.

OD_{EL}=0.054, the minimum (OD_{EL}=0.004) is in November. For the other wavelengths 1064 nm and 355 nm, the behavior of the monthly variation is similar with total values of . The seasonal behavior of the ODs can be seen in the left panel of Fig. 4.7: Like the total AOD, the OD_{PBL} is decreasing from spring to winter by a factor of 3 with an absolute difference of 0.092. While the seasonal change of the elevated layers is minor in absolute values (OD_{EL}(summer) - OD_{EL}(winter) = 0.020), the ratio between the spring/summer and the winter values is again of the order of 3. In general it can be said that the optical depths in spring/summer are a factor of 4.2 / 3.3 / 2.5 higher than the winter AODs for the wavelengths 1064 nm, 532 nm, and 355 nm respectively. This behavior is reflected in the fact that the fraction of AOD which comes from the EL only varies between 8 % in winter and 16 % in summer for 532 nm and 355 nm (Fig. 4.7, right panel). Thereby all measurements were taken into account: if no elevated layer was detected, the ratio OD_{EL} / AOD is set to zero. As a consequence, in autumn and winter, where less than half of the measurements contain ELs, the median of this ratio is zero. In average, the ELs contribute with about 13 % and 12 % to the total AOD at 532 nm and 355 nm, respectively. Only the contribution of ELs at 1064 nm is clearly higher (34 %) with highest values in summer, maybe correlated with an increased particle size in the elevated layers.

While the optical depths decrease on similar factors for PBL and EL, the geometric depth shows a different behavior for ELs: in Fig. 4.8 the variation of the geometric depth ΔH is shown. While the PBL top (in km a.g.l., equal to PBL depth) is changing from 1.68 km in spring to 0.73 km in winter (factor 2.3), the thickness of the elevated layers is more stable, varying from 1.43 km as maximum in spring to 1.02 km in winter (factor 1.4). Accordingly, if elevated layers occur in autumn or especially in winter, the probability is very high that the geometrical extension of these layers is larger than the one of the PBL.

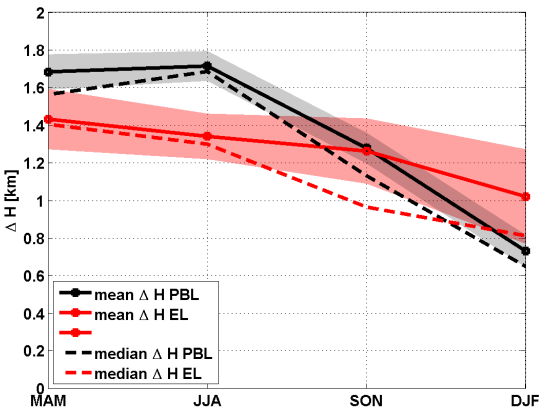

Figure 4.8: Seasonal mean (solid lines), median (dashed lines), and uncertainty (shaded regions) of the geometric depth of PBL (black) and EL (red) derived from MULIS measurements in Maisach 2007-10.

Table 4.3: Layer averaged extinction coefficient $\overline{\alpha_p} = OD/\Delta H$ in units of 1/km for PBL and EL.

		Spring	**Summer**	**Autumn**	**Winter**
$\overline{\alpha_p}(355nm)$ [1/km]	**PBL**	0.1417	0.1247	0.1412	0.1226
$\overline{\alpha_p}(532nm)$ [1/km]	**PBL**	0.0854	0.0631	0.0715	0.0609
$\overline{\alpha_p}(1064nm)$ [1/km]	**PBL**	0.0330	0.0254	0.0309	0.0186
$\overline{\alpha_p}(355nm)$ [1/km]	**EL**	0.0295	0.0445	0.0333	0.0204
$\overline{\alpha_p}(532nm)$ [1/km]	**EL**	0.0213	0.0269	0.0202	0.0106
$\overline{\alpha_p}(1064nm)$ [1/km]	**EL**	0.0094	0.0099	0.0104	0.0029

However, these layers are very rare (see Table 4.2) and –as seen in Fig. 4.7 – optically very thin. Also while on average quite stable, the thickness of the elevated layers has a great variation from 0.06 km up to 4.1 km with an average height of 3.0 km a.s.l..

The ratio between the averaged optical and geometrical depths corresponds to the averaged extinction coefficient of the layer $\overline{\alpha_p}$. Its values indicate that the denseness of the aerosol does not vary very strongly in the PBL: the difference between the spring and winter values (maximum - minimum) is at all wavelengths ∼0.02 / km (see Table 4.3). While $\overline{\alpha_p}(PBL)$ in summer has lower values than in spring and autumn, the elevated layers then show their highest values. Also in the variation do the ELs show a different behavior than the PBL; the average extinction coefficient varies by a factor of more than two, at 1064nm even of 3.6. Yet again, the smallest values occur in winter. Here, 1064nm shows extremely low values, confirming that the EL aerosols are smaller in winter.

4.3.2 Seasonal variation of extinction profiles

While the layer averaged extinction coefficient does not to vary too strongly, we know from the AOD that the total aerosol amount is prone to strong seasonal change. Particularly the profiles separated for the four seasons can illustrate this: in Fig. 4.9 the extinction coefficient profiles α_p of all 233 measurements are shown for the three wavelengths, additionally the respective seasonal averages over all profiles. The averaged profiles are cut below 1 km for spring to autumn and 0.85 km for winter and accordingly higher than some of the single gray profiles, because the overlap of the MULIS profiles differs between the measurements. It is not reasonable to average below a certain height, because measurements with large aerosol content in the PBL lead to strong backscatter signals, which necessitated a high overlap height during the measurement to prevent overloading the detectors. An averaging below this height would produce an artificial bias towards smaller extinction coefficients. In wintertime, very low PBL heights are expected, so the measurements were often performed with a changed detector geometry and data from below 1 km a.s.l. can be derived.

In the profiles of all wavelengths, the change of the aerosol distribution with height can be seen clearly: in spring and summer large extinction coefficients occur frequently up to 3 km a.s.l. ($\sim$2.5 km a.g.l.), so the averaged profiles show values significantly above 0 up to this height. In contrast, the winter profiles mostly show aerosol below 1.2 km; only in a few profiles we observe values much larger values than 0 above this height. The height can also be seen as winter PBL top and matches very well with the PBL depth of Fig. 4.8. In the other seasons, the PBL top can not so easily be estimated from the averaged extinction coefficient profile, since especially in spring and summer elevated layers are detected often. These ELs of course influence the averaged profile; especially in heights from about 1.5 km to 3.5 km, the aerosol information can originate from PBLs which are geometrically thick due to convection as well as from elevated layers.

The occurrence of strong, elevated aerosol layers can best be seen in the spring profiles, where well mixed layers over several kilometers with no strong gradient of α_p with height exist as well as strong, but geometrically thin layers. Two interesting features should be pointed out: The strong elevated layer in spring at 2.5 km to 3 km (best seen at 355 nm) consists of the volcanic ash from Eyjafjallajökull in 2010, and the two measurements with a PBL which reaches up to 4.5 km a.s.l. with an almost constant α_p= 0.2 / km both in 532 nm and 355 nm is the event which explains the large average AOD seen in Fig. 4.5 in March.

4.3.3 Seasonal variation of depolarization ratio and Ångström exponent

The difference of the aerosol situation above Maisach in spring with respect to the other seasons can also be confirmed regarding the particle linear depolarization ratio δ_p at 532 nm and the Ångström exponent $\kappa(1064nm/532nm)$. In the left panel of Fig. 4.10 the variation of the averaged depolarization separated for PBL and EL can be observed. In spring, the depolarization of EL as well as of PBL has its maximum (0.247 and 0.099),

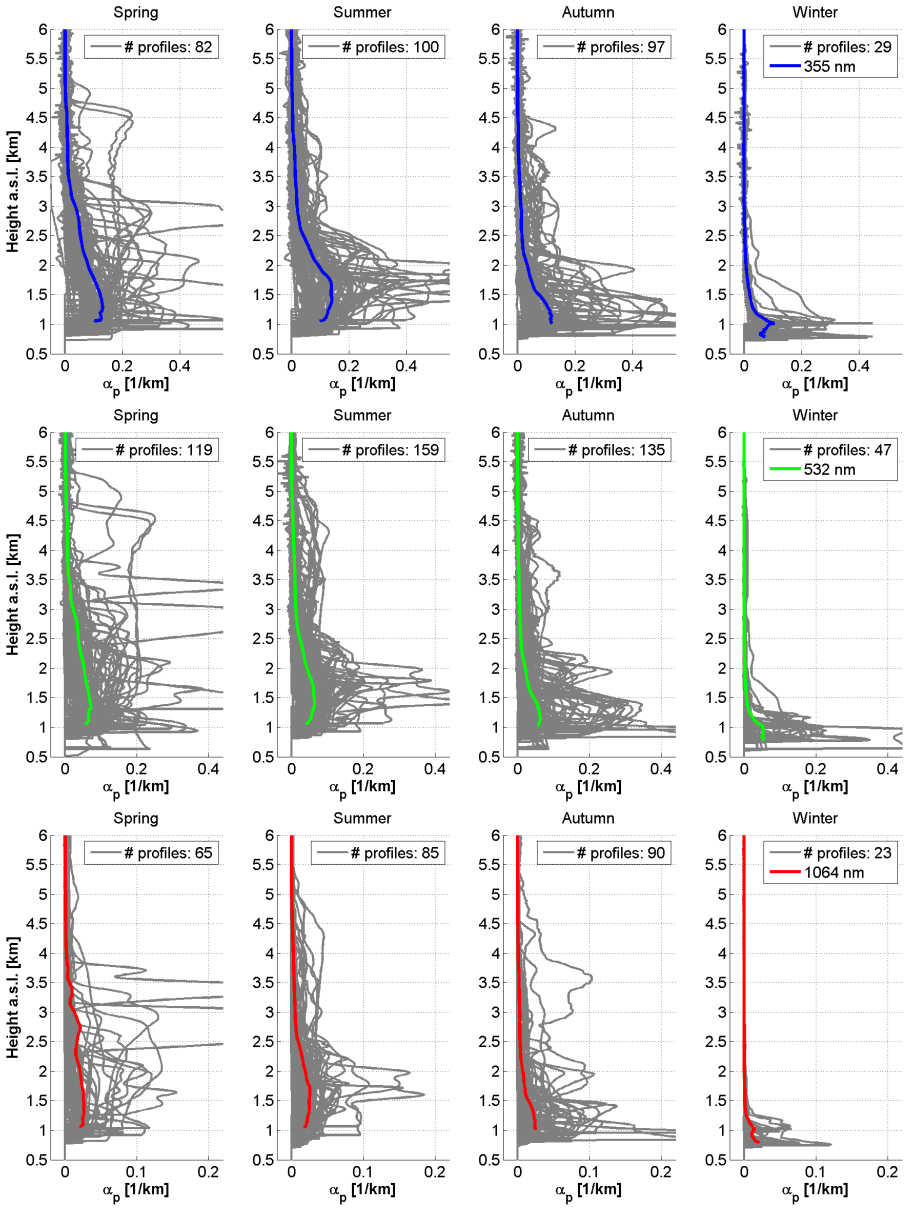

Figure 4.9: Extinction coefficient profiles, grouped into seasons, at 355 nm (upper panel), 532 nm (middle panel), and 1064 nm (lower panel) and mean profiles (blue, green, red), derived from MULIS measurements in Maisach (0.516 km a.s.l.). Used are all data from 2007 to 2010.

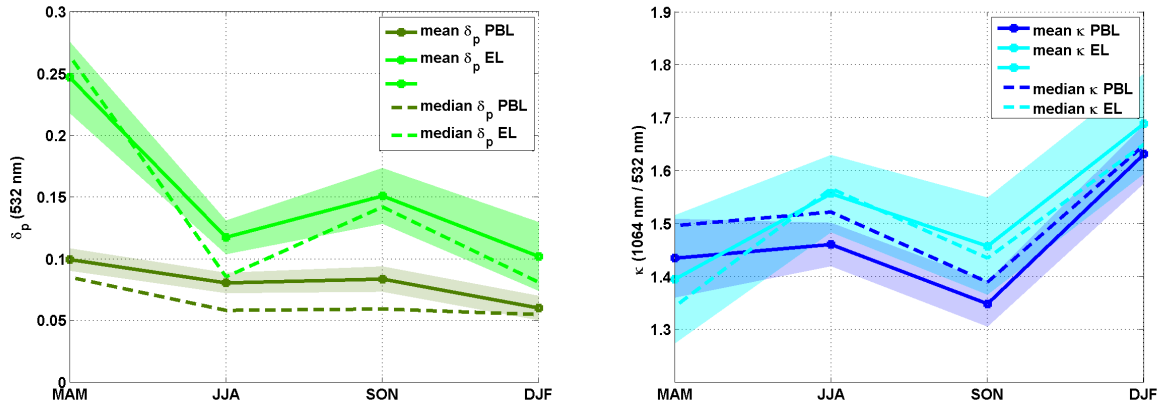

Figure 4.10: Seasonal mean (solid lines), median (dashed lines), and uncertainty (shaded regions) of the particle linear depolarization ratio (left panel) and Ångström exponent (right panel) separated for PBL and EL derived from MULIS measurements in Maisach 2007-10.

both layers have their lowest values in winter (0.102 and 0.060). The values of the ELs are always clearly higher than the ones of the PBL.As the particle linear depolarization ratio is dependent on the shape of the aerosols (see Sect. 2.3.3), it is obvious that aerosols in the PBL must be more spherical than in the EL. In the elevated layers, non-spherical aerosol types like transported Mineral dust or biomass burning ($\delta_p \approx 0.34$ and $\delta_p \approx 0.16$ respectively, from Groß [2011]) occur frequently. The aerosols in the PBL are typically swollen hydrophilic aerosols (see Sect. 4.3.4) and thus more spherical. The increased value in spring is probably due to mixing of elevated layers with high δ_p in the boundary layer.

In the Ångström exponent plots (right panel of Fig. 4.10) the difference between PBL and EL is not as clear as in the depolarization. However, the trend in the elevated layer is inversely proportional to δ_p and confirms the results: the minimum in spring indicates large particles like Mineral dust, while smaller particles large κ) occur in wintertime. For spring, however, the particles in the PBL are larger than in the EL: In elevated layers the particles have often been transported long distances and large particles drop out due to sedimentation. In contrast the aerosols in the boundary layer often originate from local sources, so that the larger particles have not yet been washed out.

4.3.4 Profile of the convective PBL

In most of the measurements, the boundary layer is well mixed; depolarization ratio and Ångström exponent are constant with height. Nevertheless, in about 20 % of the measurements a different behavior can be observed: the range corrected backscatter signal increases within the PBL. This happens especially during daytime, when strong convection occurs. In Fig. 4.11 an example of such a measurement is shown: in the quicklook of the 7th July 2010 at 1064 nm (upper panel) can be seen that the highest values are at 2.5 km a.s.l.

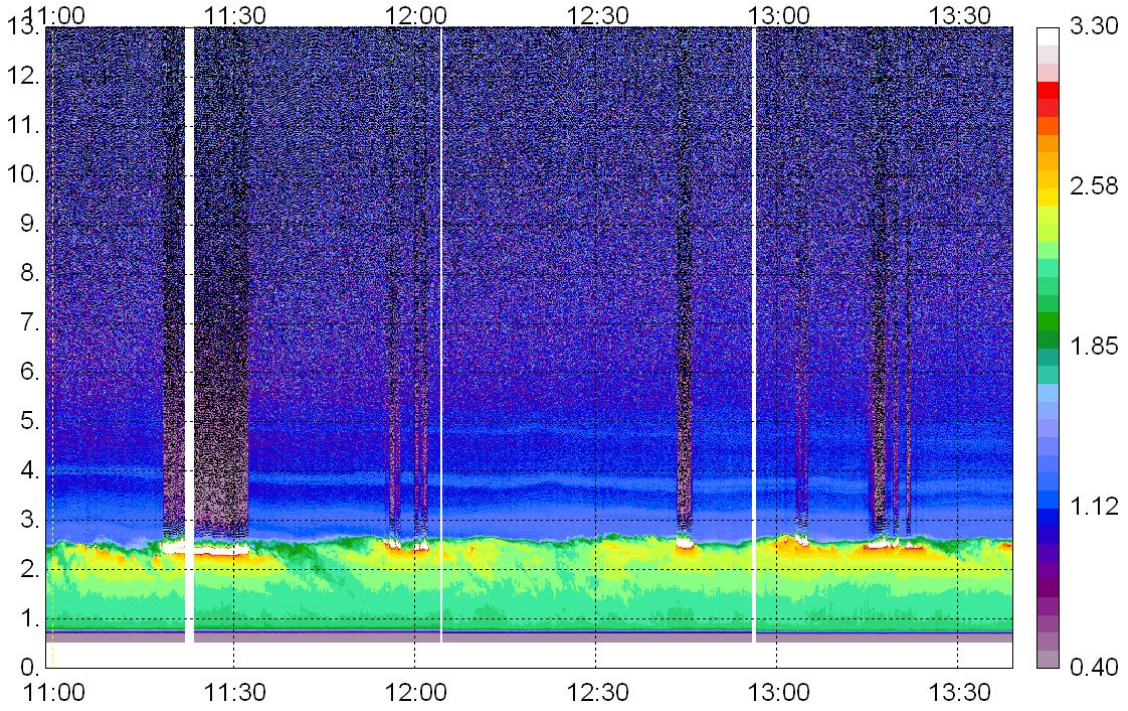

Figure 4.11: Example of typical convective PBL above Maisach on 7. July 2010: MULIS quicklook from 10:58 to 13:57 UTC at 1064 nm. The height is given in km a.s.l. with MULIS at 0.516 km a.s.l..

(=2.0 km a.g.l., red and white areas). For some time (e.g. ∼11:20-11:30), the signal above this height is completely attenuated, only noise is left. These strong signals are clouds on the PBL top.

The analysis of the data (Fig. 4.12) shows an increase in the extinction coefficient at all three wavelengths with maxima near the PBL top at ∼2.5 km a.s.l.. Additionally the particle linear depolarization ratio decreases with height from ∼ 5 % to 2.5 %. The reason for this could be that the relative humidity in the PBL is increasing with height: at a certain level of humidity –dependent on the microphysical properties of the aerosol type– the hydrophilic aerosols act as condensation nuclei and accumulate water. In this manner, the aerosols change their shape; they become more spherical and accordingly the depolarization decreases. This theory is confirmed by the measurements of the nearest radiosonde from Oberschleißheim, started on 12 UTC on the same day (right panel of Fig. 4.12). The air at ground level (0.5 km a.s.l.) is very dry with 33 % rel. humidity. From ground up to 2 km, the rel. humidity increases to 78 %. The top of the PBL can be seen clearly in the inversion of the temperature and the strong minimum of the rel. humidity at 2.6 km to 2.75 km.

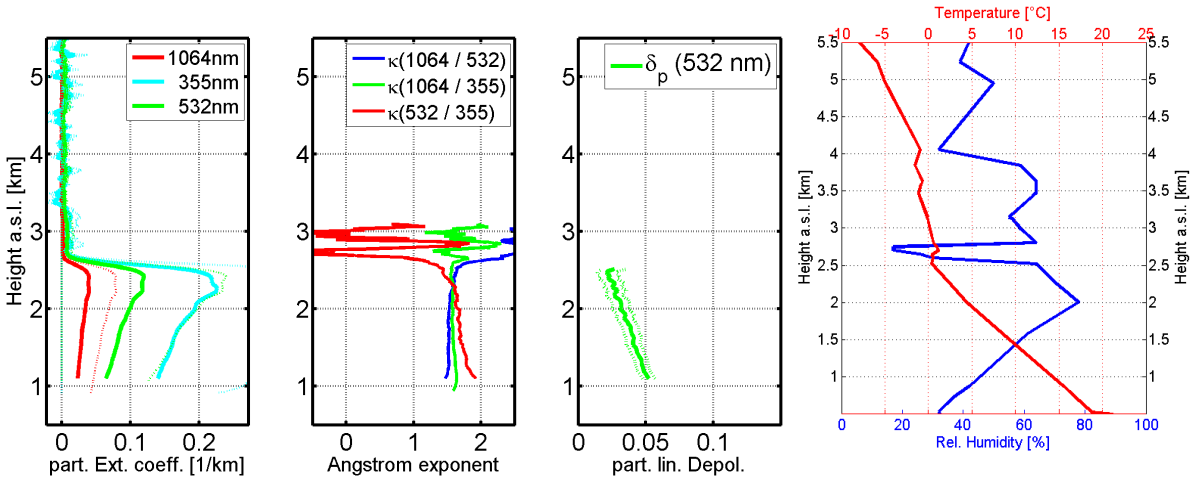

Figure 4.12: Example of typical convective PBL above Maisach on 7th July 2010: Profiles from MULIS analysis (12:04-12:34 UTC) of extinction coefficient at 1064 nm, 532 nm, and 355 nm, Ångström exponent for all three wavelength pairs and particle linear depolarization ratio at 532 nm, and temperature and relative humidity data from radiosonde started at 12 UTC in Oberschleißheim.

Table 4.4: Number of overpass days over the Munich region (3°x3°) (bold) and over MODIS region (1°x1°).

	Number of days with overpasses (**all**/MODIS)	Number of days containing aerosol
Clouds included	**350** / 168	**311** / 121
Only days with cloud free profiles	**206** / 66	**169** / 56

4.4 Distribution derived from CALIPSO

Within the time period from 2007 to 2010, 350 overpasses of CALIPSO can be considered. Due to the information loss below optically thick clouds and often occurring high errors due to signal corrections of overlying layers, only cloud free profiles of CALIPSO are used for this study (see also Sect. 3.5.3). Table 4.4 shows the number of days with overpass data for the Munich and the MODIS region. Of the 350 overpasses over the Munich region, only 206 overpasses contain 5-km-profiles without detected clouds; accordingly 144 overpasses detect clouds in each 5-km-profile within the Munich region. Even if there are no clouds in the profile, it is still possible that there is no aerosol information in the data, mostly because of a too low SNR or too weak aerosol signals. So even in the 206 overpasses with cloud free profiles, 37 days contain no aerosol information at all in the cloud free 5-km-

profiles. These days are for the later statistics assumed to have an AOD amount of 0. Table 4.4 also presents the values with respect to the MODIS region are given which show an even stronger data reduction (the smaller region contains less profiles and therewith a smaller chance of encountering cloud-free profiles.

4.4.1 Variation of the optical depth

The variability of the aerosol optical depth over the Munich region (defined in Sect. 3.1) is shown in Fig. 4.13. The region is split into a 10x10 grid with 0.3° resolution. For each of these grid boxes the mean AOD at 532 nm is calculated. CALIPSO overpasses only 45% of the pixels. The values vary from 0.02 to 0.20 while the lowest values are located at the South East near the Alps. The mean AODs at 532 nm of the three pixels around Munich (pink star) are between 0.064 and 0.090 while the mean of the whole region is at 0.079 with a variability of ± 0.110. For two pixels (49.7°N, 9.8°E and 47.9°N, 10.7°E) significantly higher values occur. These are due to single measurements with very high values of the AOD (1.6 in the northern pixel and 1.5 and 0.8 in the southern pixel).

Considering the monthly variation of the AOD at the two wavelengths 1064 nm and 532 nm in the 3°x3° region (Fig. 4.14), the highest amount of aerosols is measured in the summer months (June, July, August), while the minimum is in December / January. In analogy to the discussion on MULIS in Sect. 4.3.1, the fact that the uncertainties at 532 nm in the months November, January and February are very large indicates that the mean values receive a significant contribution from single overpasses, which is confirmed by the large difference between mean and median. This is also the case at 1064 nm for the months November and February. It is not surprising that this happens mainly during winter, where the PBL often is very low and weak and is easily missed by CALIPSO: The medians in December indicate that at least half the measurements have zero AOD.

The AOD is evidently wavelength dependent; the AOD at 1064 nm is smaller than the one at 532 nm. At the same time, the difference between the two wavelengths varies with the months; especially in January and June the values of 532 nm are more than doubled. As especially the data of 1064 nm has a strong SNR, it is not possible to determine if the strong variability is due to a change in the aerosol type or due to the high noise.

The seasonal variation of the AODs at both wavelengths and their corresponding Ångström exponent $\kappa(1064nm/532nm)$ are shown in Fig. 4.15. As already noted in the monthly variation, the highest values in the AOD appear during summer, the smallest in winter. The median values are clearly lower, which means that the AOD amount is frequently lower and only on single occasions high values were retrieved. The Ångström exponent has an opposing trend: in summer it has its minimum ($\kappa = 0.88$), while in winter the value is doubled ($\kappa = 1.76$), clearly indicating smaller particles than in summer.

4.4.2 Occurrences of aerosol types

But the main aim of CALIPSO is not to gain the AOD, but to determine the types of aerosols and their distribution over height. Therefore the seasonal variation of the aerosol

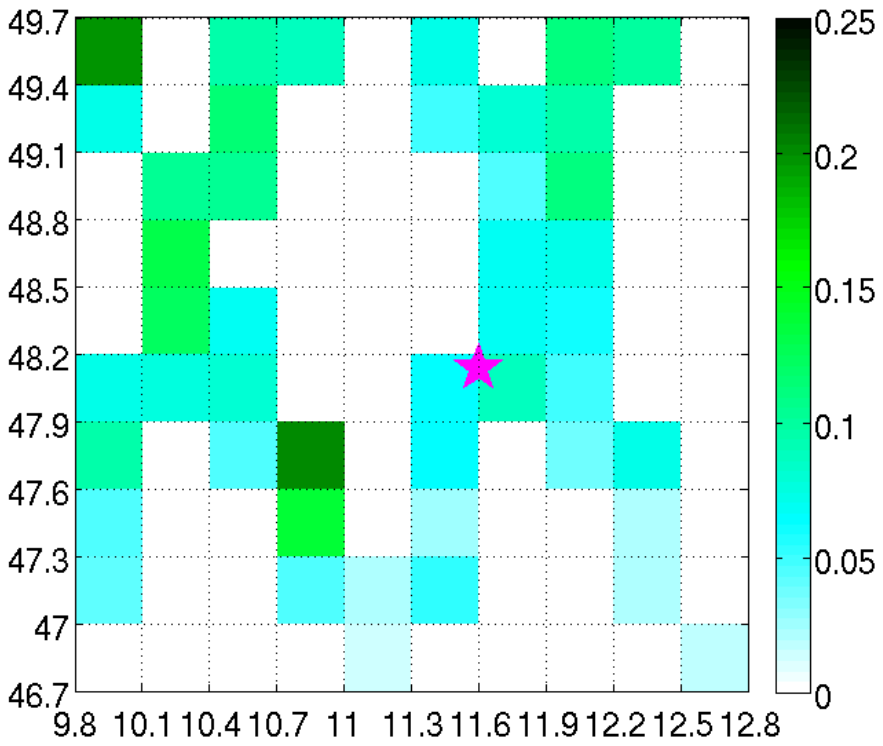

Figure 4.13: Distribution of the aerosol optical depth at 532 nm derived from CALIPSO measurements over the Munich region (46.7-49.7 °N; 9.8-11.6°E). Used are all cloud free overpasses from 2007 to 2010, AOD averaged over 0.3°x0.3°. White boxes mark areas which are not covered by CALIPSO.

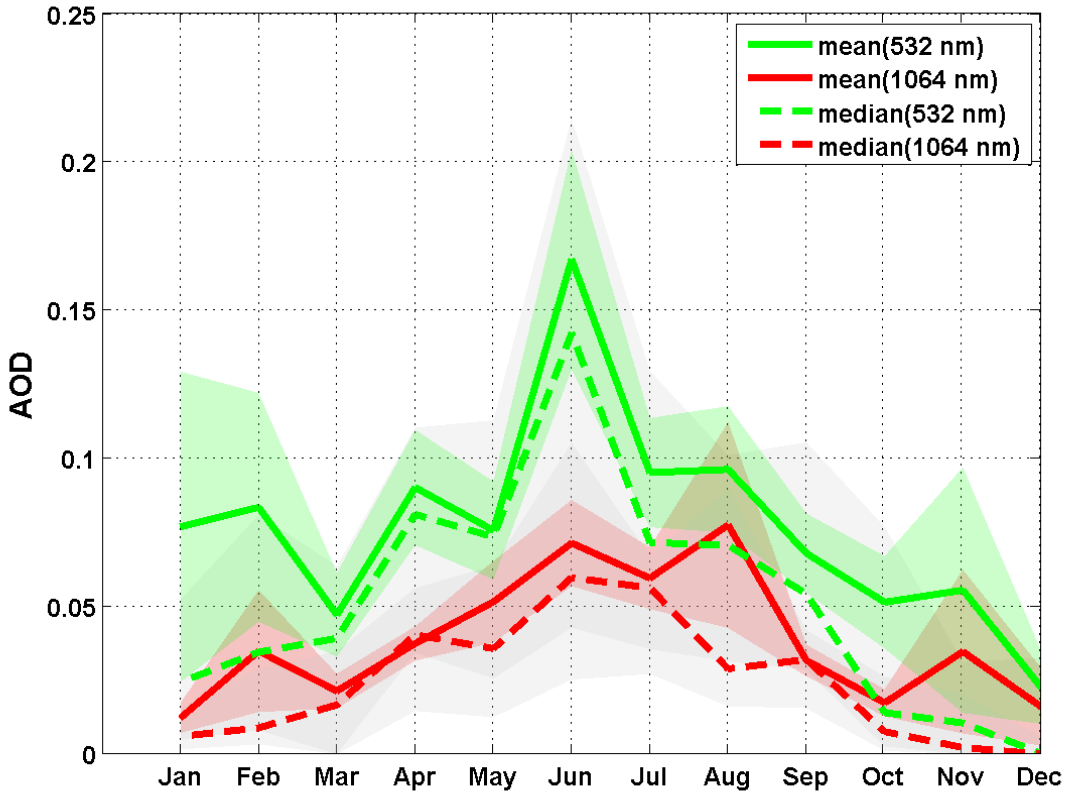

Figure 4.14: Monthly mean (solid lines), median (dashed lines), and uncertainty (shaded regions) of the AOD at 1064 nm and 532 nm derived from CALIPSO measurements over the Munich region. Used are all cloud free overpasses from 2007 to 2010.

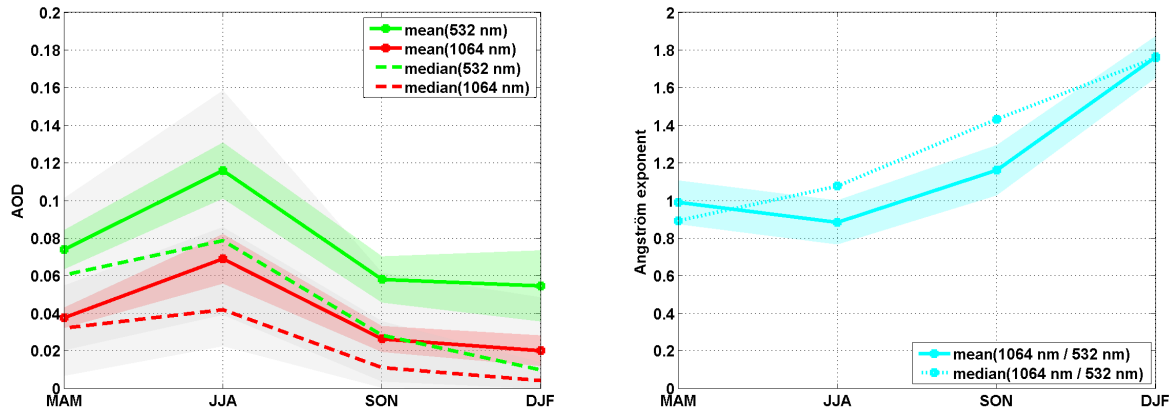

Figure 4.15: Seasonal mean (solid lines), median (dashed lines), and uncertainty (shaded regions) of the AOD at 532 nm and 1064 nm (left panel) and Ångström exponent $\kappa(1064nm/532nm)$ (right) derived from CALIPSO measurements over the Munich region. Used are all cloud free overpasses from 2007 to 2010.

types as well as their height dependency and their optical properties are studied.

Seasonal variation

In Fig. 4.16 the percentaged occurrence of the different aerosol types detected by CALIPSO are shown, separated for the four seasons. Counted are the number of height bins in the 5-km-profiles containing the aerosol type. As can be seen by the total number of bins (below the pie plots), the most aerosols were detected in summer, while in winter only about a quarter of this amount occurs.

The most dominant aerosol is smoke, especially in spring. Only in summertime the polluted dust aerosols are more common. In summer clean dust occurs quite frequently (20%), while the clean and polluted continental aerosols occur more often in autumn and winter. The sixth aerosol type 'marine aerosol' is not detected above the Munich region: in the CALIPSO algorithms for the aerosol type discrimination (see Fig. 3.10), the marine aerosol identification demands ocean as surface type, and accordingly it cannot be selected above land surface. Also, as the Munich region is far away from any coast, its appearance is unlikely.

For a good overview over the aerosol occurrences, however, it is not only necessary to monitor their relative occurrences: their amount is important, as well. Therefore the averaged AOD at 532 nm and the geometric depth is also split into the different aerosol types (see Fig. 4.17). Although the occurrence of clean continental changes between summer and autumn (from 10% to 24%) in the average AOD in case it occurs does not: the aerosol amount keeps stable over the seasons at small values around 0.01; its geometric extent does not change much, either, and is clearly smaller than that of the other types (∼0.3 km). By studying all VFMs it was found that this aerosol type is always present in the

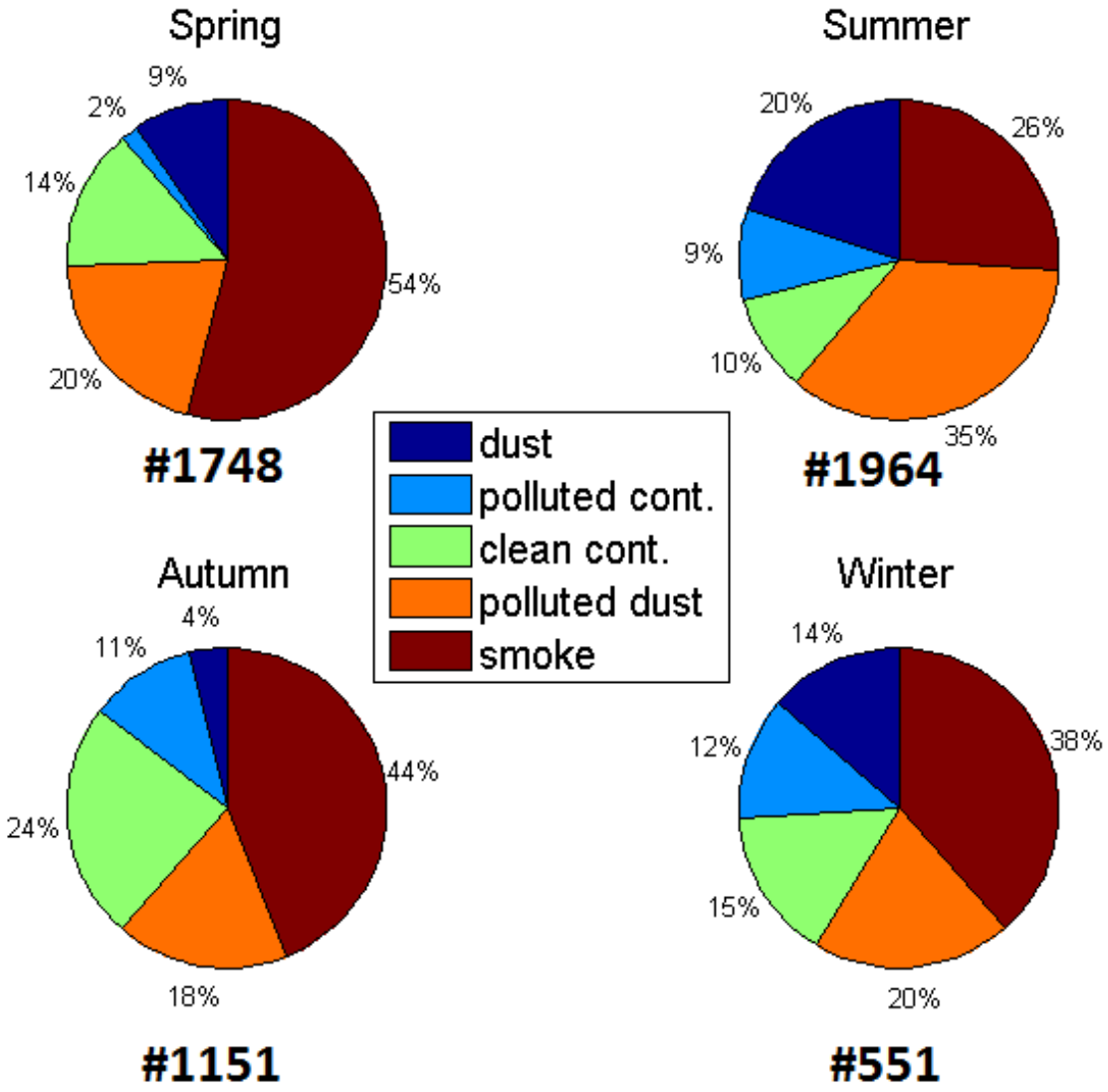

Figure 4.16: Aerosol types over the Munich region as assigned from CALIPSO algorithms. The graphic shows the relative frequency of the different types separated for the four seasons from four years of CALIPSO measurements (2007-2010), i.e. the number of aerosol bins of a given type detected in a given season divided by the total number of aerosol aerosol bins detected in that season (number below the pie plot).

Munich region but contributes little to the total AOD measured by CALIPSO. The other four aerosol types all show a significant dependency on the season: the minimum optical depth is in autumn for all but pure dust. While smoke has the strongest AODs in spring, the maximum of dust, polluted continental and polluted dust is in summer. So even in spring when the smoke is not the most frequent aerosol type, its contribution to the total AOD is still more important than the contribution of polluted dust.

All types except for smoke reach their largest geometric depth in summer and their smallest in winter (Fig. 4.17, right panel). On average, aerosol layers are therefore thinner in cold temperatures. Boundary layer studies have already shown that its extension in wintertime is much less than in summer [Stull, 1988]. Yet the combination of the geometric depth with the AOD also indicates that the layers are denser in winter. For polluted continental, polluted dust, and smoke the AOD increases from autumn to winter, while simultaneously the geometric depth remains stable or even decreases. Regarding the ratio between the AOD and the geometric extent, these three aerosol types have the densest aerosol concentrations in winter. Especially the concentration of polluted continental strongly increases in winter: compared to the other seasons with a relative stable ratio of $\sim$0.13 / km, the winter ratio is more than doubled to 0.28 / km. As polluted continental is only found in ground near layers, it can be assumed that the increase of heating and traffic as sources combined with low PBL tops lead to this strong change.

Height dependency

As already mentioned, the advantage of a lidar system over passive remote sensing is the height resolved information. The separation of the aerosol types can therefore not only be done seasonally resolved, but also height resolved. In Fig. 4.18 the occurrence of the different aerosol types is shown subdivided into 1-km-ranges from 0 km to 7 km a.s.l.. Obviously aerosol is most often measured below 4 km, and smoke aerosols are the dominant type again. The behavior of the types can be divided into two groups: polluted and clean continental aerosols have their maximum near the ground and their occurrence decreases with increasing height. In contrast to this, smoke, dust and polluted dust have their maximum above the ground in 1 to 3 km. The reason for this is that the continental aerosols have local sources while the other three types mainly are transported to Munich from other regions. Especially this can be seen for pure dust: the possibility to occur above 2 km (sum of values from 2 km to 7 km) is clearly larger then below 2 km.

Above 4 km it is not possible to decide which aerosol type dominates as all types but polluted continental appear rarely. Above 7 km, only on single occasions layers were detected, so the representation of the height distribution is only shown up to this height. A smoke layer detected in 11 km to 14 km (not shown) is the result of one strong event; it can not be seen as a typical component in the atmosphere. Considering, however, that the extent of the boundary layer is normally at most at 3 km [Stull, 1988], it can be seen that most occurring elevated layers are smoke or polluted dust aerosol. Pure dust is found much less often than polluted dust, as dust is transported over long distances to reach the Munich region and therefore mixing with other aerosols along the way is very likely.

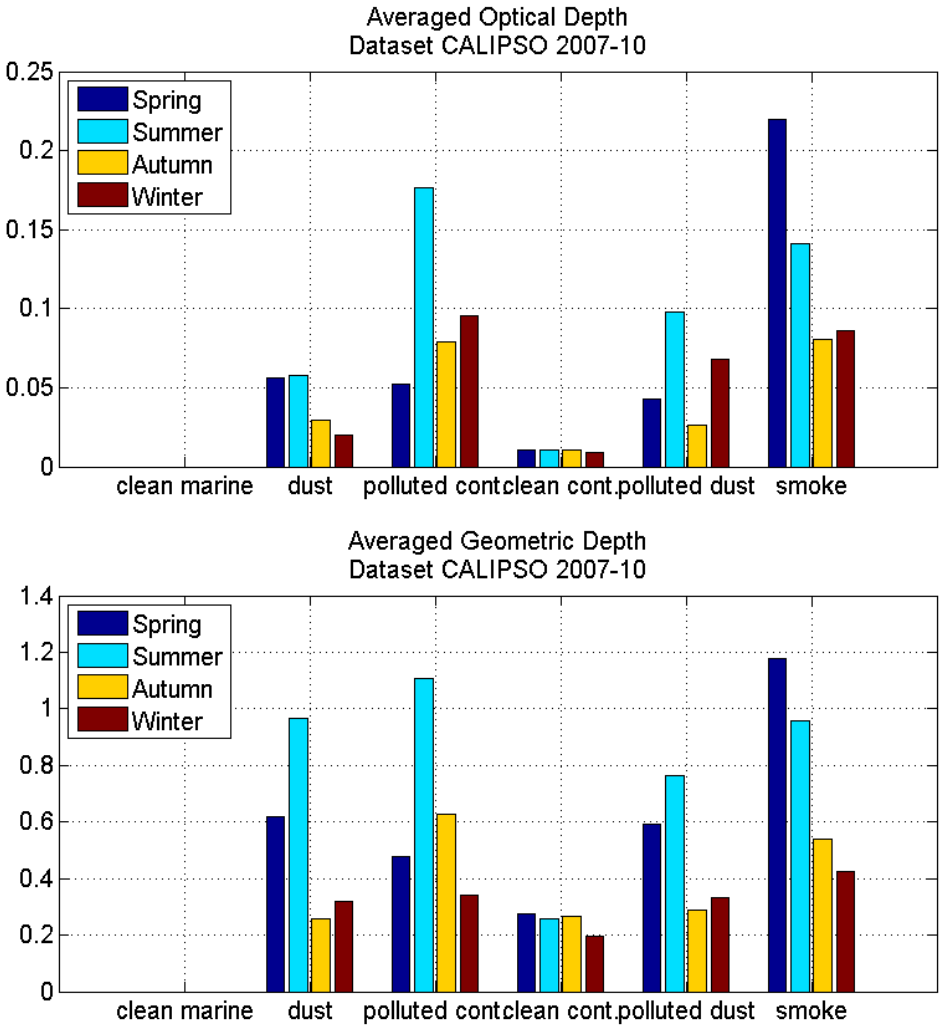

Figure 4.17: Averaged AOD at 532 nm (upper panel) and geometric depth (lower panel) of the different detected aerosol types over Munich region over four years of CALIPSO measurements (2007-2010) separated for seasons, i.e. the average AOD/geometric depth that a detected aerosol layer of a given type has when detected in a given season..

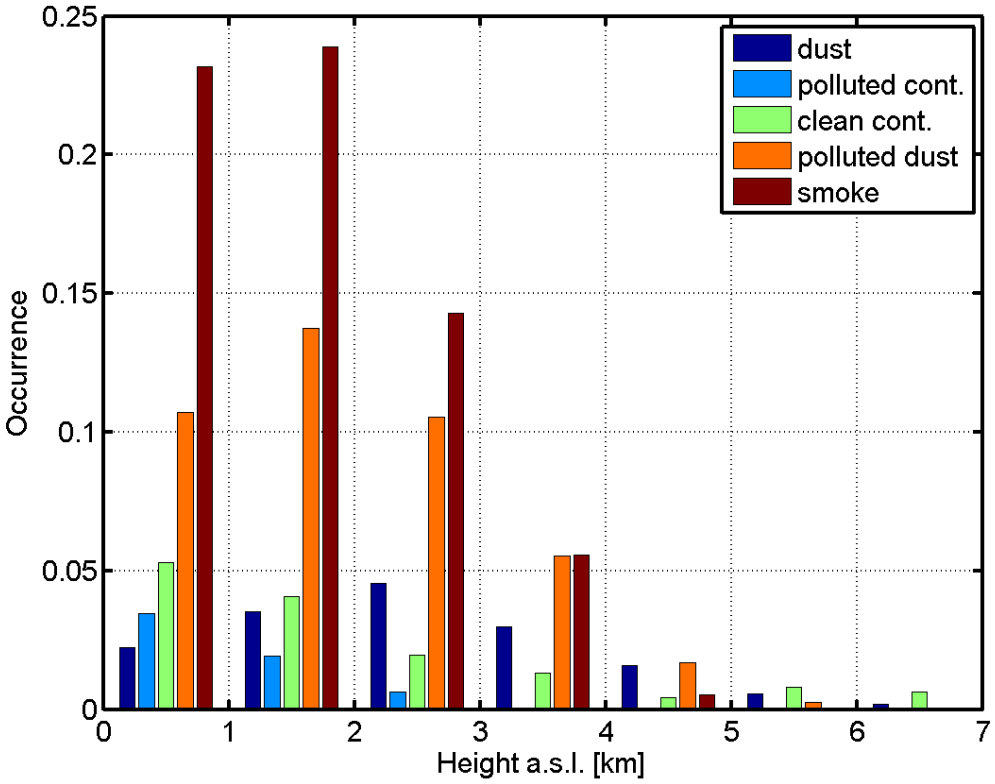

Figure 4.18: Height resolved occurrence of aerosol types in the Munich region over four years of CALIPSO measurements (2007-2010), i.e. the number of overpasses which detect an aerosol of given type in a given height divided by the total number of overpasses.

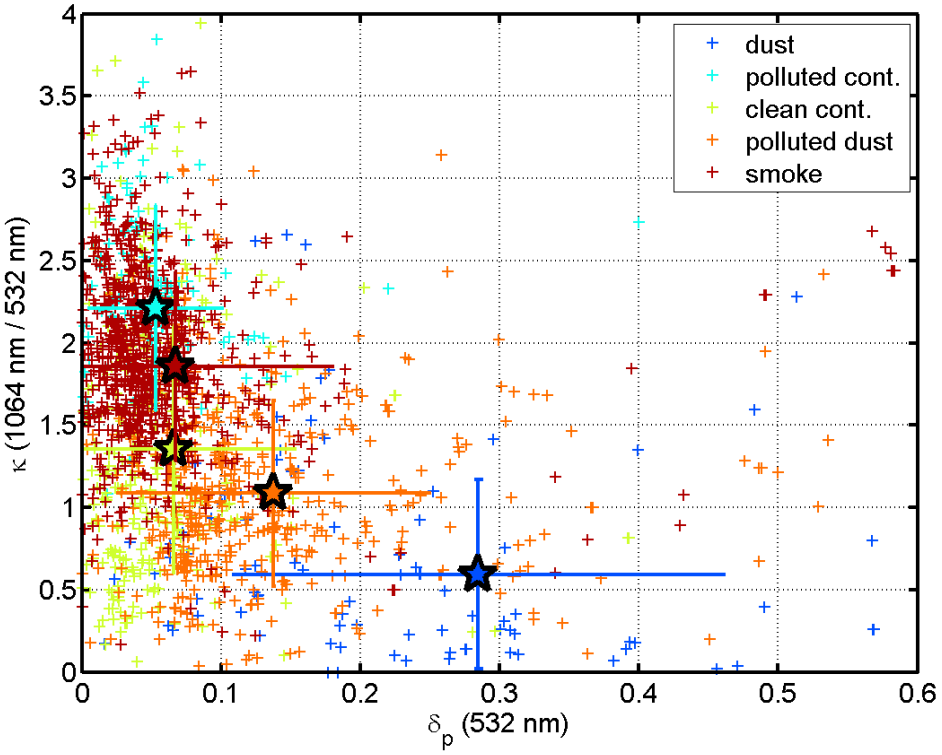

Figure 4.19: Layer means of particle linear depolarization ratio and Ångström coefficient for the different aerosol types. Additionally plotted are the mean values and corresponding variabilities for all five types.

4.4.3 Optical properties of aerosol types

As mentioned earlier, aerosol types differ in their optical properties depending on their microphysical properties. The particle linear depolarization ratio δ_p describes the non-sphericity of the particles while the Ångström coefficient κ is a measure for the averaged size of the aerosols. Both parameters are independent of the amount of aerosols and are therefore very suitable to define aerosol types. Inversely it is possible to sort the aerosol layer data of CALIPSO above the Munich region for the five different aerosol types. In Fig. 4.19, the layer averages of δ_p(532nm) are plotted versus the corresponding κ(1064nm/532nm) with different colors for each aerosol type. On the whole, the Ångström values vary from -4.14 to 5.5, while the particle depolarization varies from -13 to 100. The negative and the extremely high values occur generally coincidentally in both parameters. They are due to retrieval problems or very low SNR and are ignored for further studies. Additionally in Fig. 4.19 the colored stars represent the mean values over all layers of a specific aerosol type, combined with the variability (horizontal and vertical error bars). Dust (blue) has the strongest particle depolarization values of $\delta_p = 0.28$ on average and the lowest average Ångström coefficients of $\kappa = 0.59$, indicating non-spherical particles being

large compared to the other aerosol types. The three aerosol types clean continental, smoke, and polluted continental (yellow, red, cyan) clearly have smaller average depolarization ratios (around 0.06) with large Ångström exponents (increasing from 1.4 to 2.2). The sizes of the Ångström exponent match the size distributions described in Omar et al. [2009, Fig. 1 + Tab. 1], where polluted continental has the higher content in the fine mode compared to the coarse mode, while the clean continental has a high content in the coarse mode. The polluted dust values (orange) are situated between the dust aerosols and the other types: the depolarization is still heightened ($\delta_p = 0.14$) and the Ångström exponent shows a small average value of $\kappa = 1.1$. It can be assumed that this dust has been altered on its way or has mixed with non-dust aerosols.

These results have to be considered carefully: as the volume depolarization is used as one criterion for the subtyping, it is no surprise that the δ_p of pure and polluted dust has the highest values. On the other hand, no wavelength dependency –as a pre-stage for the Ångström exponent – is used in the aerosol subtyping process. As a consequence, this study of depolarization and Ångström coefficient nicely shows that the aerosol subtyping of CALIPSO is self-consistent and the aerosol types in general seem to be well chosen.

4.5 Summary

The results discussed above lead to the conclusion that.the average AOD in the Munich region has values between 0.079 and 0.158 at 532 nm depending on the measuring instrument. The seasonal and mean values of the AOD in the UV, at 532 nm and in the NIR are summarized in Table 4.5. The optical depth of the four independent instruments can be used to qualify the aerosol data by comparing the values. The wavelength dependency can be observed in all four datasets. In general in November the smallest AOD was measured while the highest values occur during spring and summer. Elevated layers were studied using the MULIS lidar: they have an increased particle linear depolarization ratio compared to the PBL and appear most frequently in spring time. From the aerosol type analysis of CALIPSO follows that the most important aerosol type above the Munich region is smoke, and that it occurs not only in elevated layers but in all heights of the troposphere including the boundary layer. The results also confirm the quality of the CALIPSO aerosol type analysis: although the Ångström coefficient is not used in the aerosol subtyping process, the obtained values for κ nicely reproduce the expected behavior.

Clearly, although the instruments in general present qualitatively similar results, there can be large quantitative differences, the most prominent being that the average AOD varies by a factor of two between the difference instruments. The analysis of the their origins will be discussed in the following chapter.

Table 4.5: Average of the AOD over all data 2007 -2010 and separated into seasonal values for the four instruments CALIPSO, MULIS, MODIS, and AERONET.

		Spring	Summer	Autumn	Winter	Total
AERONET	**340 nm**	0.298 ± 0.019	0.328 ± 0.026	0.240 ± 0.029	0.189 ± 0.011	0.269 ± 0.014
MULIS	**355 nm**	0.291 ± 0.026	0.262 ± 0.018	0.194 ± 0.020	0.107 ± 0.018	0.233 ± 0.011
AERONET	**532 nm**	0.174 ± 0.013	0.173 ± 0.018	0.146 ± 0.020	0.117 ± 0.006	0.155 ± 0.008
MODIS	**532 nm**	0.192 ± 0.018	0.185 ± 0.016	0.104 ± 0.018	0.125 ± 0.030	0.158 ± 0.011
MULIS	**532 nm**	0.172 ± 0.021	0.137 ± 0.011	0.101 ± 0.012	0.058 ± 0.012	0.127 ± 0.008
CALIPSO	**532 nm**	0.071 ± 0.023	0.121 ± 0.036	0.064 ± 0.021	0.047 ± 0.066	0.079 ± 0.041
AERONET	**1020 nm**	0.073 ± 0.005	0.063 ± 0.006	0.061 ± 0.008	0.046 ± 0.002	0.062 ± 0.003
MULIS	**1064 nm**	0.068 ± 0.012	0.054 ± 0.005	0.046 ± 0.007	0.016 ± 0.003	0.050 ± 0.004
CALIPSO	**1064 nm**	0.053 ± 0.053	0.059 ± 0.016	0.036 ± 0.037	0.012 ± 0.011	0.040 ± 0.032

Chapter 5

Discussion

In chapter 4 the aerosol distribution above the Munich region data from AERONET, MODIS, MULIS and CALIPSO was presented. In this chapter, the results of the four datasets are now compared with each other to discover accordances and differences which lead to a better estimation of the quality of the data. First, monthly and seasonal means of the column parameters AOD and Ångström exponent are compared to identify deviations. In the second part, a day to day comparison of the two lidar systems is made to verify the reasons for the found underestimation of the AOD by CALIPSO and to investigate the reliability of the CALIPSO data with main focus on the aerosol type. The results are also interpreted in the context of other studies in Europe to get a better survey of the results above Munich. This chapter concludes with estimations on the influence of the AOD underestimation and the aerosol type on radiative forcing.

5.1 Monthly and seasonal comparison of all four datasets

In Chapter 4 independently derived datasets were shown. All four instruments have a different focus of measurement, e.g. the lidar systems obtain optical properties like particle depolarization, while AERONET offers data for the most wavelengths. Therefore not all parameters can be compared. One observable is common for all instruments, however: the AOD at 532 nm, although for MODIS this is a result of interpolating the measurements at 440nm and 670nm. As the AERONET and MODIS instruments are especially designed to measure the AOD, they are established datasets for this comparison. In contrast, the AOD of MULIS and CALIPSO are only a side product. The focus of these instruments is the characterization of the vertical distribution of aerosols. It can therefore be assumed that the AERONET and MODIS datasets are more reliable on the AODs than the lidar instruments.

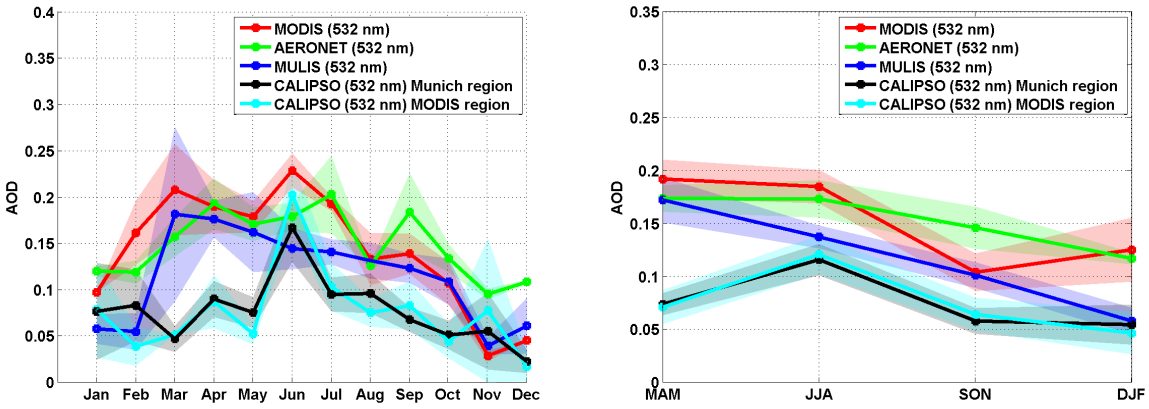

Figure 5.1: Comparison of monthly (left) and seasonal (right) mean and uncertainty of AODs of all four instruments at 532 nm. The CALIPSO means are built from the datasets of Munich (black) and MODIS region (cyan). Note that the five datasets have different measurement bases (see Chap. 3).

5.1.1 Comparison of AODs

For the comparison of the AODs, additionally a second climatology from CALIPSO data is built for the smaller MODIS region (green rectangle in Fig. 3.1). In the left panel of Fig. 5.1, the monthly variation of the mean AOD at the 'green' channel (532 nm) for all four instruments MODIS (red), AERONET-Cimel (green), MULIS (blue), and CALIPSO can be seen. The CALIPSO mean AOD is shown for both the Munich region (black) and MODIS region (cyan). In general, these two curves are in very good agreement, although the data from the Munich region seems to be a bit 'smoother' due to the the larger dataset. The monthly means of the three other instruments match very well with each other, with high values in Spring and Summer, and the minimum AOD of all in November, indicating that these values are credible. However, on a monthly scale some differences can be seen: some, such as that AERONET encounters a local maximum in April while MULIS and MODIS reach it as soon as March, can be explained by the large uncertainties in the latter two instruments in March. This data points to singular high AOD events moving the mean AOD to larger values. More striking is the fact that AERONET obtains much higher AODs in November and December than the other two instruments, and AERONET and MODIS both have higher AODs in January and February than MULIS. These differences probably arise from the different locations of the instruments: AERONET is situated in the center of Munich, while MULIS is positioned in a rural area.

All of the values are clearly higher than the values gained from CALIPSO, with the exception of the months January, June, and November. In seven months this difference is significant. It seems that the CALIPSO AODs are too small. This is also consistent with the mean values over the full time period of four years: there is a very good agreement between MODIS and AERONET (0.158 ± 0.011 and 0.155 ± 0.008) and slightly smaller

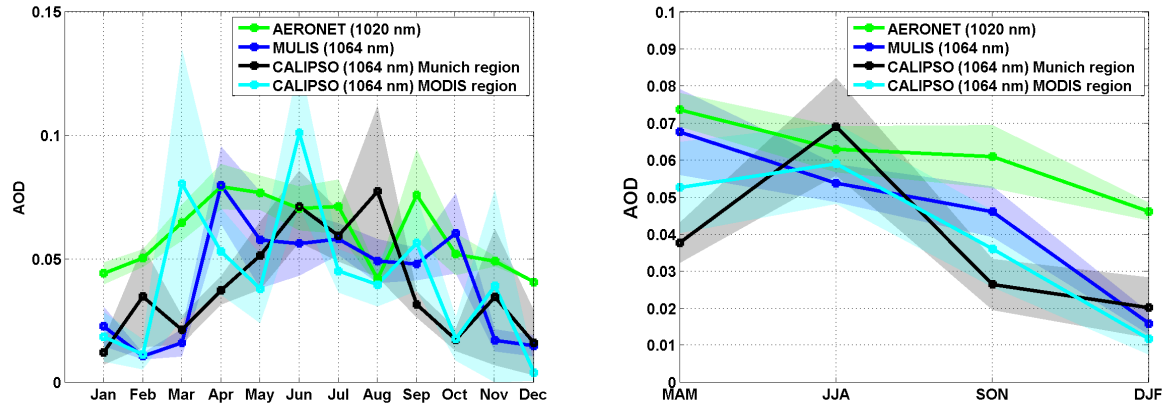

Figure 5.2: Comparison of monthly (left) and seasonal (right) mean and uncertainty of all three instruments at 1064 nm respectively 1020 nm (MODIS delivers no aerosol information for this wavelength). The CALIPSO means are built from the datasets of Munich (black) and MODIS region (cyan). Note that the four datasets have different measurement bases (see Chap. 3).

values of MULIS (0.127 ± 0.008), whereas the CALIPSO values are clearly lower (0.079 ± 0.041) (see Table 4.5). The seasonal variation can be seen in the right panel of Fig. 5.1; here the underestimation of the AOD by CALIPSO can be seen more clearly than in the monthly variation.

The corresponding monthly means as well as the seasonal means of the 'red' channels (1064 nm for MULIS and CALIPSO, 1020 nm for AERONET) show a similar behavior (Fig 5.5). AERONET and MULIS provide similar values from April to October; during other months, MULIS obtains much lower values than AERONET. CALIPSO seems to fit better on average than for the green wavelength, the mean AOD is only slightly lower ($AOD_{CALIPSO} = 0.040 \pm 0.032$, $AOD_{MULIS} = 0.050 \pm 0.004$, $AOD_{AERONET} = 0.062 \pm 0.003$), but the month-to-month variation of CALIPSO is much larger at this wavelength, and the datasets from Munich and MODIS region differ strongly. Due to the small number of data used in the MODIS region, the noise of the 1064 nm channel cannot be balanced.

The correlation study of the monthly values is shown for both wavelengths at Table 5.1 for the four instruments. CALIPSO is listed twice, regarding the whole Munich region ($CALIPSO_{MUNICH}$) and the smaller MODIS region ($CALIPSO_{MODIS}$). The correlation between these two regions is quite well at 532 nm (0.897), but clearly not as strong as at 1064 nm (0.471). In general, the correlation coefficients between MULIS, AERONET, and MODIS at 532 nm are very well (~ 0.8), the values with CALIPSO are much lower (0.3 - 0.65). Surprisingly, there is a stronger correlation of MODIS with $CALIPSO_{MUNICH}$ than with $CALIPSO_{MODIS}$. In the infrared, the correlation between AERONET and MULIS (0.642) is a bit worse than in the green. The correlations with the CALIPSO data sets is below 0.5, even between the two CALIPSO data sets, indicating that these data sets

Table 5.1: Correlation coefficient between the four datasets for the monthly averages of the AOD at 532 nm (green) and at the NIR wavelengths 1064 nm / 1020 nm (red).

	CALIPSO$_{\text{MUNICH}}$	**CALIPSO$_{\text{MODIS}}$**	**MULIS**	**AERONET**
MODIS	**0.641**	**0.500**	**0.804**	**0.798**
AERONET	**0.476**	**0.490**	**0.810**	-
MULIS	**0.326**	**0.300**	-	**0.642**
CALIPSO$_{\text{MODIS}}$	**0.897**	-	**0.467**	**0.625**
CALIPSO$_{\text{MUNICH}}$	-	**0.471**	**0.329**	**0.278**

are too noisy to produce viable results. Merely the correlation between CALIPSO$_{\text{MODIS}}$ and AERONET is large (0.625). Although the better correlation of AERONET with CALIPSO$_{\text{MODIS}}$ than with CALIPSO$_{\text{MUNICH}}$ might be explained by the fact that the MODIS region is smaller and therefore should better represent the AERONET site, it is more likely that the large correlation is coincidence.

5.1.2 Comparison of Ångström exponents

The AOD is not the only column value which can be used for a comparison: the Ångström exponent κ (Eq. 2.8), too, is a convenient parameter to study the reliability of the four instruments and especially of the CALIPSO data. However, as already mentioned for Fig. 4.2, it is only of limited value to compare the different Ångström exponents as they are based on different wavelength pairs. The mean values are summarized in Table 5.2 grouped for most similar wavelength pairs. The values of MULIS ($\kappa = 1.367$) and AERONET ($\kappa = 1.410$) for the wavelength pair NIR to green match very well, while the corresponding CALIPSO value is clearly smaller ($\kappa = 0.949$), indicating bigger particles. Similarly, the comparison of the other data pairs shows considerably stronger differences. The Ångström exponent of MODIS ($\kappa(660nm/470nm) = 0.98$) is much smaller than the one of AERONET ($\kappa(675nm/440nm) = 1.45$). Furthermore, the MULIS Ångström exponent between 532 nm and 355 nm is very large ($\kappa = 1.76$).

Regarding the seasonal behavior of the Ångström exponents (Fig. 5.3), only few consistencies can be observed: like the mean values, the seasonal values of MULIS and AERONET for NIR to green are in good agreement. Also the values from spring to autumn of CALIPSO and MODIS match nearly perfectly; only in winter a large difference can be seen. However, the MODIS values are smaller than found in literature: e.g. Chubarova [2009] found the values to be always between at least 1 and 1.4; the mean from April to September is even larger ($\kappa > 1.4$). Again, a larger amount of data could possibly improve this discrepancy. The very high values of the MULIS Ångström at 532 nm / 355 nm could be due to an overestimation of the extinction coefficient at 355 nm $\alpha_p(355nm)$ or an underestimation of the $\alpha_p(532nm)$. The MULIS data certainly also involves nighttime data, so maybe this influences the results as well.

Table 5.2: Mean Ångström exponents for all instruments for several wavelength pairs.

Wavelength pair	**Instrument**	κ
675 nm / 440 nm	AERONET	1.45
660 nm / 470 nm	MODIS	0.98
532 nm / 340 nm	AERONET	1.23
532 nm / 355 nm	MULIS	1.76
1020 nm / 532 nm	AERONET	1.41
1064 nm / 532 nm	MULIS	1.37
1064 nm / 532 nm	CALIPSO	0.95

It is not possible to explain all differences in the Ångström exponent, as its behavior depends on the aerosol size distribution and the chosen wavelength pair. Especially for CALIPSO it is observed that the AOD differs more strongly at 532 nm from the other datasets than the AOD at 1064 nm (see Sect. 5.1.1). So it is no surprise that $\kappa(1064nm/532nm)$ does not correspond to the MULIS and AERONET values, either. Additionally the error propagation of the extinction coefficients / AODs needs to be taken into account: in Eqs. 2.9 and 2.10 the correlation between the errors of the α_p and κ is shown . For the wavelength pair of CALIPSO (1064 nm, 532 nm) the error enhancement factor at $\kappa = 1$ is f(1064 nm,532 nm) $\simeq 2$. As the relative error of the CALIPSO α_p is at least at 40 % (see Sect. 3.5.3), this leads to a relative error in the Ångström exponent of 80 % or more.

5.2 Direct comparison of AOD from AERONET with MULIS and CALIPSO

While in the previous chapter seasonal and monthly variations based on different datasets were shown, now a direct comparison between two measurement pairs is conducted: first the coincident AODs of AERONET and MULIS are compared, then the same comparison for AERONET and CALIPSO is performed.

For the comparison of the AOD at 532 nm from coincident measurements of MULIS and AERONET, the Sunphotometer measurement nearest in time was searched for a given MULIS measurement. Fig. 5.4 shows all results for which the time difference between the two measurements was less than five hours. The datasets match very well with a correlation coefficient ρ of 0.80. The linear fit (black line) has an inclination near 1 ($m = 0.92$) and a small offset of 0.058. If only the measurements with a time difference of less than one hour are regarded (magenta crosses), the correlation improves even more ($\rho = 0.88$). The properties of the linear fit change only slightly. For the wavelengths 1064 nm and 355 nm the same good agreement can be observed (not shown); the correlation coefficients are 0.86 and 0.87, and again there is a small positive offset (0.032 and 0.105). These offsets are

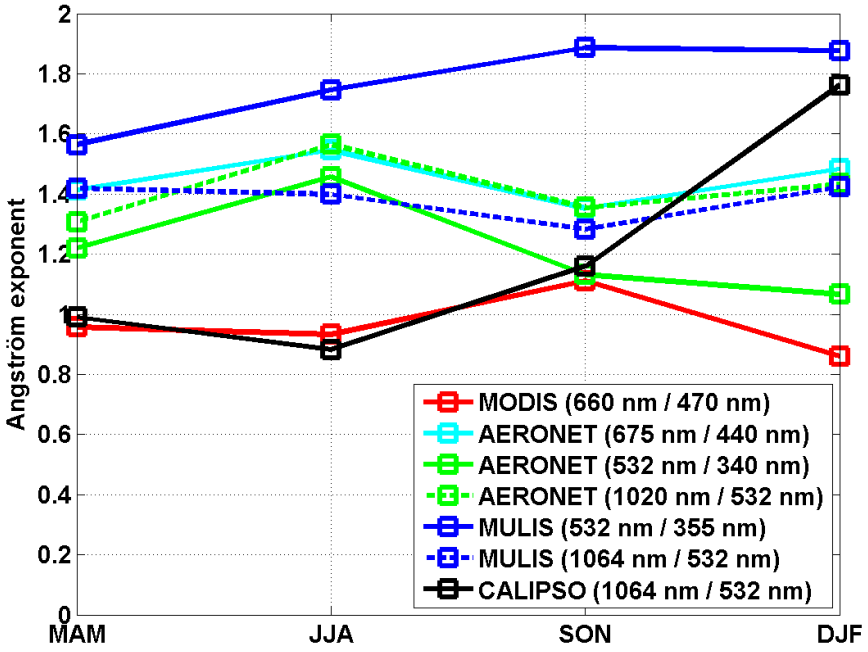

Figure 5.3: Seasonal mean Ångström coefficients for different wavelengths pairs of MODIS, AERONET, MULIS, and CALIPSO measurements within the Munich region. For the sake of clarity only the mean values are shown. For information about uncertainty and median see Ångström-figures in Chap. 4.

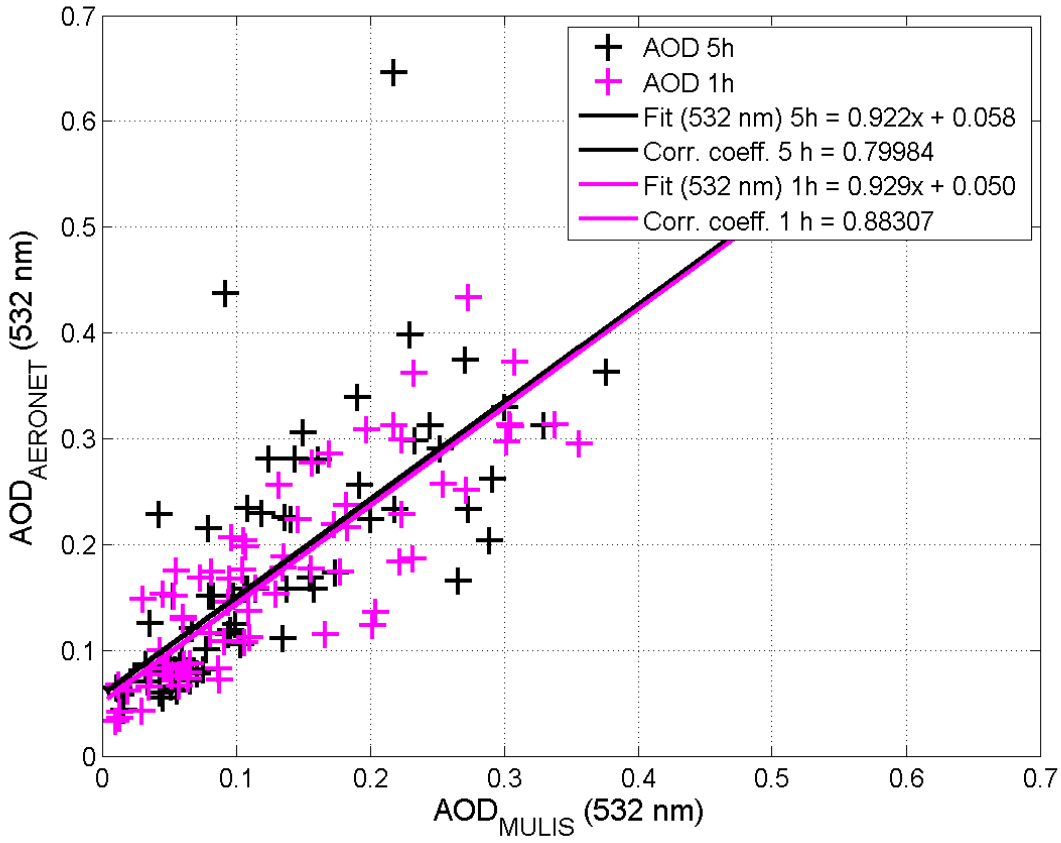

Figure 5.4: Comparison of the AOD(532 nm) from coincident measurements of MULIS and AERONET: all crosses mark measurements coincident within 5 hours, highlighted (magenta) are measurements performed within 1 hour. Additionally the linear fits are shown (the 5h linear fit is fitted to all crosses).

very likely due to differences in the surroundings of the two instruments: while MULIS is located in a rural area 25 km west of Munich, the AERONET-Cimel is operated at the MIM in the center of Munich. Coincident lidar measurements performed by members of the lidar group of the MIM have shown that the PBL top is higher above Munich likely due to the effect of the urban heat island [Arnfield, 2003].

In the same way, the comparison of incident AODs of CALIPSO and AERONET is conducted, except for the fact that the time difference between the measurement is allowed to be 12 h, as half of the CALIPSO overpasses occur in the middle of the night ($\sim$ 01:30 UTC): on the left panel of Fig. 5.5, the AODs at 532 nm of CALIPSO from the whole Munich region are compared to the measurements of the Sunphotometer. No good correlation can be observed ($\rho = 0.22$), while the linear fit shows a very large offset of 0.163. The correlation does not improve by using only measurements with a time difference of less than one hour; rather, the correlation even deteriorates slightly ($\rho = 0.21$), probably

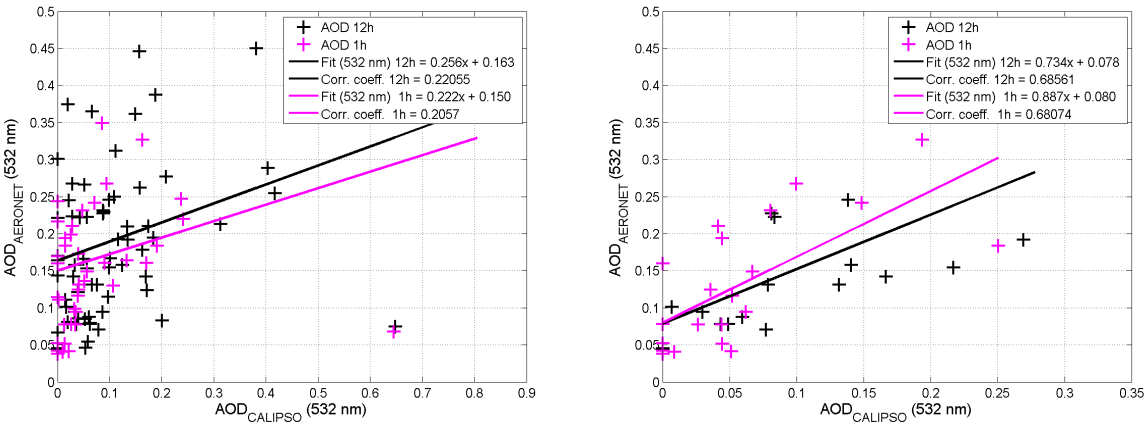

Figure 5.5: Comparison of the AOD at 532 nm from coincident measurements of CALIPSO and AERONET: all crosses mark measurements coincident within 12 hours, highlighted (magenta) are measurements of performed within 1 hour. Additionally the linear fits are shown (the 12 h fit is fitted to all crosses). Left: CALIPSO data taken for the Munich region; Right: CALIPSO data taken for the MODIS region.

because this subset only contains day measurements, where CALIPSO has a much lower SNR. On the other hand, if only data from the MODIS region are used (see right panel of Fig. 5.5), the agreement between the instruments is much better ($\rho = 0.68$, offset of 0.08); CALIPSO and AERONET match quite well. The same behavior can be seen in the AODs at 1064 nm / 1020 nm (not shown). The reason for the better agreement is that the MODIS region is smaller than the Munich region and therefore is a better representation of the location of the AERONET-Sunphotometer. As a consequence, the spatial spatial differences of the CALIPSO and the AERONET measurements are clearly smaller; even some direct overpasses are within this dataset. While the distribution of the aerosol amount in the larger Munich region is very variable (see Fig. 4.13), the values within the MODIS region are more stable. The analysis of the correlation between the monthly mean values confirms the result: from Table 5.1 it can be seen that the correlation between CALIPSO and AERONET is higher for the MODIS region. However, the offset can not be explained due to differences between town and country – as done for MULIS –, because CALIPSO has several overpasses above Munich. Some reasons were identified by comparison of MULIS and CALIPSO profiles in Sect. 3.6.3; their impact on the AOD is discussed in the next section.

Note that the correlation of the monthly means differ strongly from the correlation of the coincident measurements. This is because of two effects: first, the monthly averaging evans out short-term inhomogeneities, second, the monthly means of both instruments sometimes contain measurements which were not available for the other instrument.

Table 5.3: Averaged AODs measured by MULIS and CALIPSO for all coincident data points and split into day and night measurements

	All profiles		**Day**		**Night**	
	MULIS	CALIPSO	MULIS	CALIPSO	MULIS	CALIPSO
AOD(532 nm)	0.116	0.111	0.128	0.117	0.103	0.104
AOD(1064 nm)	0.044	0.059	0.051	0.072	0.038	0.046

Table 5.4: Difference of AODs measured coincidentally by MULIS and CALIPSO (ΔAOD =AOD_{MULIS} - AO$D_{CALIPSO}$); average and variation are shown for all data and split into day and night.

ΔAOD	**All**	**Day**	**Night**
mean(532 nm)	0.005	0.011	-0.001
std(532 nm)	0.075	0.083	0.068
mean(1064 nm)	-0.016	-0.023	-0.009
std(1064 nm)	0.049	0.063	0.030

5.3 Comparison of coincident profiles of MULIS and CALIPSO

The datasets of MULIS and CALIPSO can be compared in more detail, as not only the AOD can be investigated but also height resolved data. As explained in Sect. 3.6.3, 52 coincident measurement from 2007 to 2010 are suited to be used for the comparison. 26 of these were performed during night time around 01:30 UTC, the other half at day time around 12:20 UTC.

5.3.1 Comparison of AODs

A first comparison of the averaged AOD of both instruments shows very good agreement: the mean AOD at 532 nm are 0.116 and 0.111 for MULIS and CALIPSO respectively, while the corresponding value of CALIPSO at 1064 nm is even higher with 0.059 compared to AOD = 0.044 of MULIS (Table 5.3). The division of the measurements into day- and nighttime overpasses (26 profiles each) shows two aspects: first that the AOD is smaller at night than during daytime, and second that the values of MULIS and CALIPSO differ more at daytime when solar background leads to a lower SNR.

The good agreement between the two instruments is somewhat surprising considering the results in Sect. 5.1.1, where it was shown that the monthly and total means of the AOD are strongly underestimated by CALIPSO. A reason why the 52 coincident measurements comparing MULIS with CALIPSO do not show this behavior could not be found, so it must be assumed that it is a statistical fluke due to the low number of events.

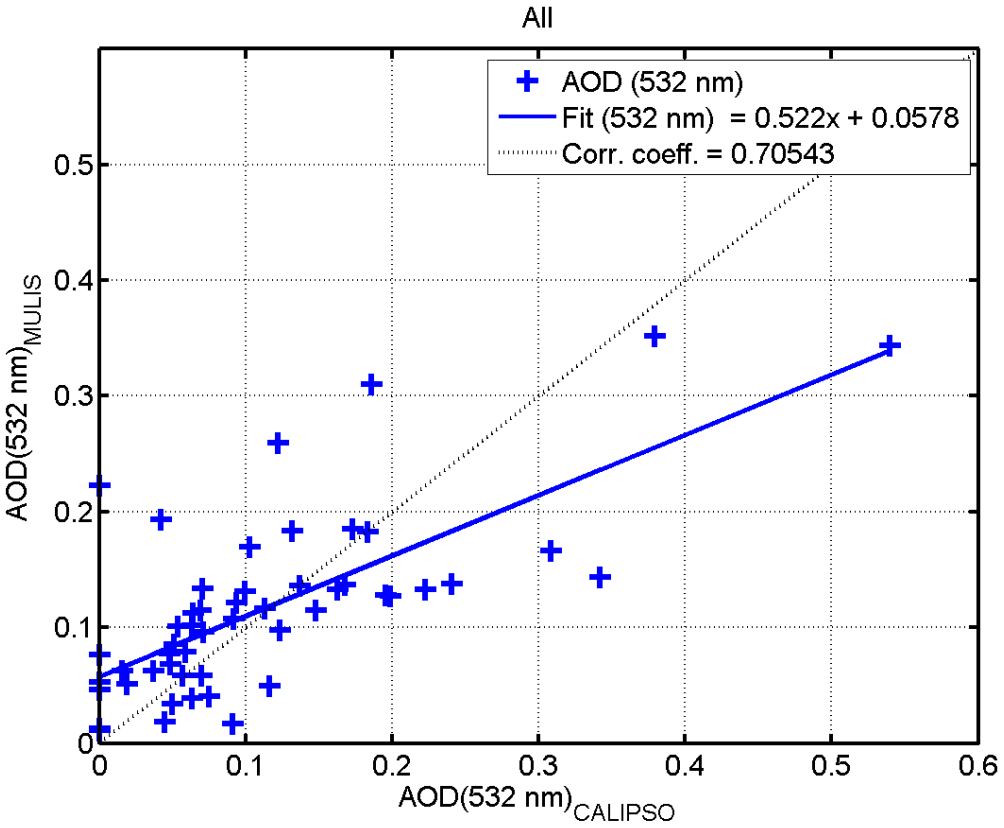

Figure 5.6: Comparison of AOD at 532 nm measured by CALIPSO and MULIS (blue crosses) and linear fit (blue line) between the data.

Nevertheless, a closer look on the comparison of the single AOD measurements at 532 nm, see Fig. 5.6, shows large discrepancies between the two instruments. (The 1064 nm data – not shown – has a similar behavior.) While MULIS always obtains a positive value for the AOD, CALIPSO detected no aerosol at all during several overpasses. In contrast, CALIPSO experiences a stronger spread in AOD values.

In Table 5.4 the averages and standard deviations of the differences $\Delta\mathrm{AOD} = \mathrm{AOD}_{MULIS}$ - $\mathrm{AOD}_{CALIPSO}$ are collected for 1064 nm and 532 nm, also split into day- and night-time: at day time, the differences and their variation are clearly higher than the night time measurements, which is due to the lower SNR at daytime. However, the variation occurring at night is also very large compared to the absolute AOD values. The discrepancies of the AODs of coincident measurements cannot be identified by simply comparing the column value AOD. Instead, the comparison of the extinction coefficient profiles can help to understand the behavior.

Table 5.5: Causes for discrepancies between MULIS and CALIPSO counted for the 52 coincident measurements. The criteria defined in Sect. 3.6.3.4 were used. Note that "Missing PBL" also contains the cases "No aerosol", and "Missing layers" contains both.

Missing layers	**Missing PBL**	**No aerosol**	**cloud influences**	**lidar ratio**
27	12	7	26	7 (of 12)
52%	23%	13%	50%	

5.3.2 Causes for deviation of AOD: comparison of coincident CALIPSO and MULIS profiles

As already explained in Sect. 3.6.3, the comparison of incident extinction coefficient profiles allows the identification of several limitations of the CALIPSO measurements. For the 52 measurement days, these causes for this limitations were studied and are listed in Table 5.5. In more than half of the cases (52%), layers were missing, while the PBL was missed in 23 % of the cases. At 7 days, there was no aerosol data at all available despite cloud free conditions. Also in half of the cases clouds contaminated the results. In 7 of the 12 cases where the lidar ratio could be determined from MULIS, the wrong lidar ratio was identified as a cause of CALIPSO's miscalculation of the AOD. At this point it has to be mentioned that for one profile several causes can apply, an overpass not detecting any aerosol at all will also be counted for missing PBL as well as missing layers, or on a day with a wrong lidar ratio also clouds can influence the results.

5.3.2.1 Missing layers

In 27 cases, the CALIPSO algorithms failed to detect aerosol layers of optical depth > 0.02, sometimes only some thin layer, sometimes whole profiles. Even in unstable meteorological conditions the PBL should be measured. This did not occur on 23% of the days. For all 52 overpass profiles the LOD, i.e. the optical depth of the layers detected by MULIS but missed by CALIPSO, can be determined and is plotted for 532 nm in Fig. 5.7 against the AOD of MULIS: of course the values of the LOD cannot be larger than the total AOD. The mean LOD is 0.035; compared to the total AOD of MULIS (0.13) this is an average underestimation of the optical depth above Munich by 38 %. On more than 50 % of the days, at least a quarter of the optical depth is not noted. At 1064 nm the behavior is similar (not shown): the mean LOD is 0.013 with the median at 0.008, which corresponds to an underestimation of 37.2 % of the total AOD. As no direct correlation between the LOD and the AOD can be found, the chance of overlooking layers – or at least parts of layers – does not depend on the total aerosol amount.

At first glance, the comparison between the LODs and the difference between the total AODs of MULIS and CALIPSO (ΔAOD) shows no correlation, either. In Fig. 5.8 the ΔAOD and the corresponding LODs are plotted. The values scatter strongly and the linear fit (blue line) does not represent the distribution very well. But if only positive values

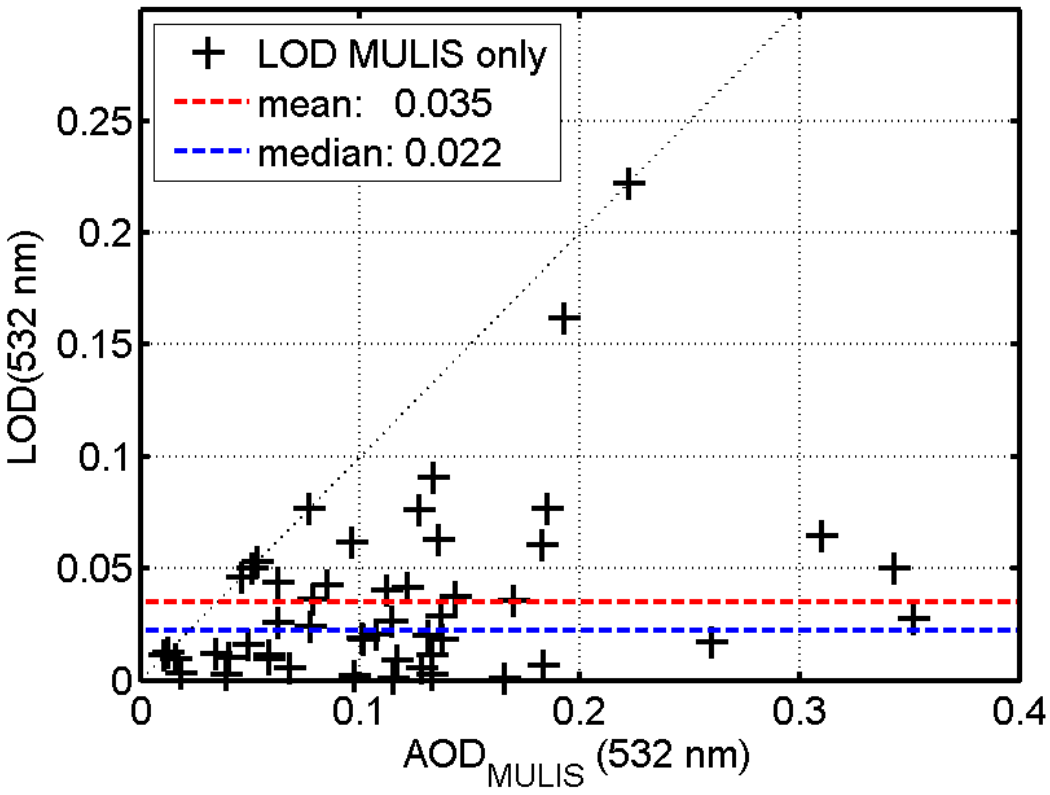

Figure 5.7: Optical depth of layers detected by MULIS layers but missed by CALIPSO (LOD) over the total AOD at 532 nm.

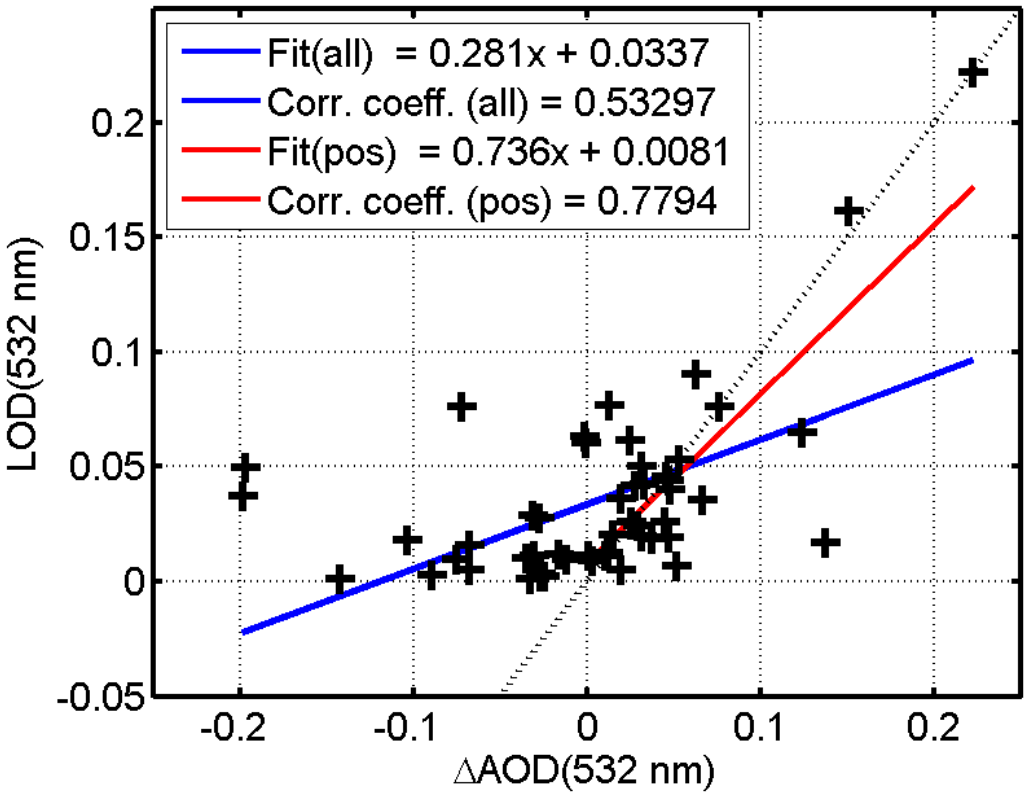

Figure 5.8: Optical depth of layers detected by MULIS layers but missed by CALIPSO (LOD) over ΔAOD at 532 nm. The blue line is the linear fit using all values, the red line only using the values with positive ΔAOD.

of ΔAOD are considered, the correlation between the two properties can be seen clearly (red line). This is also confirmed by the high correlation coefficient of 0.78 (compared to $\rho = 0.53$ when using all values). So if MULIS is measuring larger AODs than CALIPSO, the main cause of the discrepancy lies in the missing of layers.

As can be seen in Table 5.5 as well as in Fig. 5.7, at 7 overpasses no aerosol layers were detected at all (LOD/AOD = 1), although clear sky was reported in the VFM for all cases and therefor no strongly attenuating clouds could disturb the detection algorithm. Analyzing the quicklooks of the attenuated backscatter data (L1B) and the VFM mask, the causes for the detection failure were a too low amount of aerosol on 5 days and extremely high noise on one day. On the seventh day the original AP data as well as the MULIS profiles have a high AOD of around 0.2, but the quality flag of CALIPSO was set to 'unconfident', so this data was removed for the data analysis (see. Sect. 3.5.3).

As the layer detection is particularly dependent on the SNR, it is to be expected that the detection fails more often in daylight condition. This assumption is confirmed by building separately the averages of the LOD for daytime and night time overpasses (see Table 5.6).

Table 5.6: Averaged optical depth of layers missed by CALIPSO but measured by MULIS (LOD) split for day- and nighttime measurements.

	Day	Night	All profiles
LOD(532 nm)	**0.051**	**0.012**	**0.032**
LOD(1064 nm)	**0.014**	**0.005**	**0.010**

The nighttime LODs (0.012 / 0.005) are much smaller than the ones at daytime (0.051/ 0.015) for both wavelengths (532 nm / 1064 nm), which also explains the bad agreement with the MODIS and AERONET data, which need sunlight to work. Nighttime data of CALIPSO is therefore superior to the daytime data.

5.3.2.2 Incorrect lidar ratio

To verify the lidar ratios chosen by the CALIPSO aerosol type classification algorithm, the comparison with the lidar ratio measured by of MULIS is necessary. But due to low SNRs in the 607 nm channel, only 12 days of coincident measurements of MULIS and CALIPSO could be analyzed properly. These values are compared in Tab. 5.7. In order to estimate how strongly the CALIPSO AOD is misestimated due to the wrong lidar ratio, the MULIS AOD was recalculated using the lidar ratios also used by CALIPSO[1].

In four cases the lidar ratio of MULIS was more than 5 sr smaller than the one of CALIPSO which leads to an increase in the newly calculated MULIS AOD and therefore to a positive change. In all other cases the change was negative: on average the AOD is reduced by 0.015 when the CALIPSO S_p is used. For 7 days the difference of the lidar ratios is larger than 10 sr; these days are counted for Tab. 5.5 as days with wrong lidar ratio assumption. The difference of the AOD is also shown in Tab. 5.7. Compared to the absolute AOD values of MULIS, the wrong estimation of the lidar ratio only shows minor influence on the AOD: Fig. 5.9 visualizes the relation between the change in the MULIS AOD using the CALIPSO lidar ratio, $\Delta\mathrm{AOD}(\mathrm{S}_p)$ and the real AOD of MULIS. The use of the wrong lidar ratio leads on average to an underestimation of 5.4% of the total AOD. However, in Fig. 5.9 it can be seen clearly that the effect of a wrong lidar ratio increases for higher AOD.

5.3.2.3 Clouds in scene

Another cause for the mismatch of extinction profiles was found: the presence of clouds within the scene but not in the 5-km-profile. In contrast to the failure of the aerosol layer detection and the misassumption of the lidar ratio, the effect of clouds in the scene can not be quantified directly. However, their influence on the AOD can be seen in Fig. 5.10: the

[1] Although it would be more logical to recalculate the CALIPSO AOD using MULIS lidar ratios, the change in AOD is approximately the same for both methods, so the one was chosen which was easier to perform.

Table 5.7: Lidar ratios at 532 nm of MULIS (including the uncertainty) and CALIPSO, their difference $\Delta S_p = S_p(MULIS) - S_p(CALIPSO)$ and the corresponding change in the AOD of MULIS when using the lidar ratio assumed by CALIPSO instead of the one detected by MULIS: $\Delta AOD(S_p) = AOD_{MULIS}(S_p(CALIPSO)) - AOD_{MULIS}(original)$. On some of the days, one or both instruments detected two aerosol layers with different lidar ratio; on these days both values are shown.

Date	$S_p(MULIS)$	$S_p(CALIPSO)$	$\Delta S_p(MUL-CAL)$	$\Delta AOD(S_p)$
07/04/26	59 ± 2	55	4	-0.006
08/05/05	79 ± 9	55	24	-0.040
08/05/10	43 ± 3	70	-27	+0.020
08/06/27	58 ± 1	55	-3	+0.001
	66 ± 4	70	-4	
09/04/11	65 ± 7	55	10	-0.015
09/08/17	44 ± 4	40	4	-0.009
	49 ± 13		9	
10/04/21	69 ± 5	55	14	-0.049
		40	29	
10/04/30	64 ± 5	55	9	-0.012
10/05/23	73 ± 3	40	33	-0.083
		55	18	
10/06/08	57 ± 5	70	-13	+0.013
	62 ± 11	35	27	
10/06/28	62 ± 16	55	7	+0.002
		70	-8	
10/08/20	66 ± 14	55	11	-0.003
		70	-4	
mean	**61.4**	**52.6**	**7.4**	**-0.015**

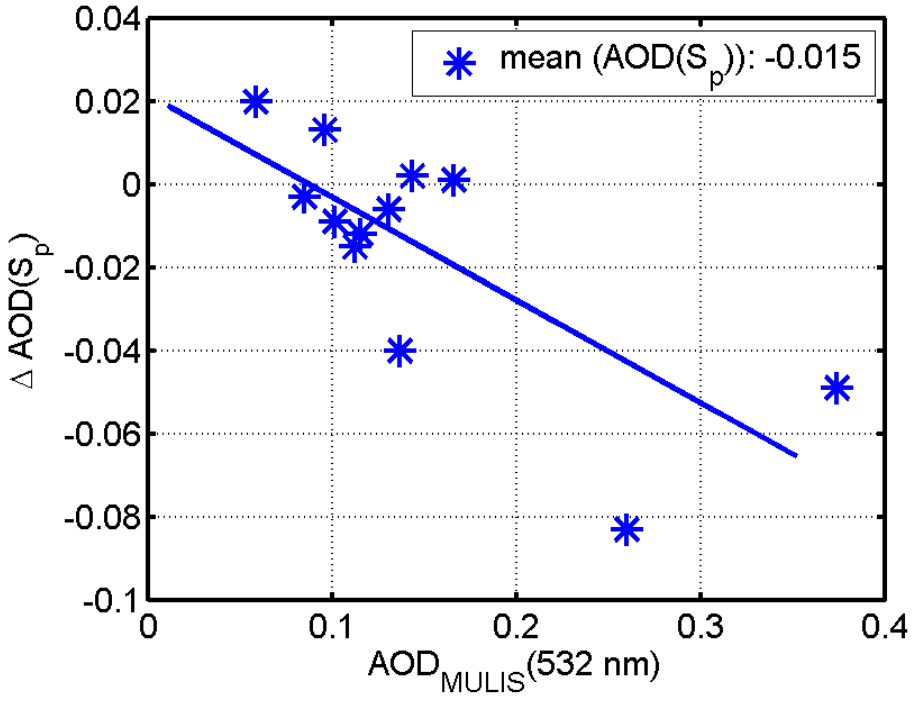

Figure 5.9: Relative change of AOD due to the use of the CALIPSO lidar ratio in the data analysis of the MULIS extinction coefficients for 12 days with Raman lidar measurements.

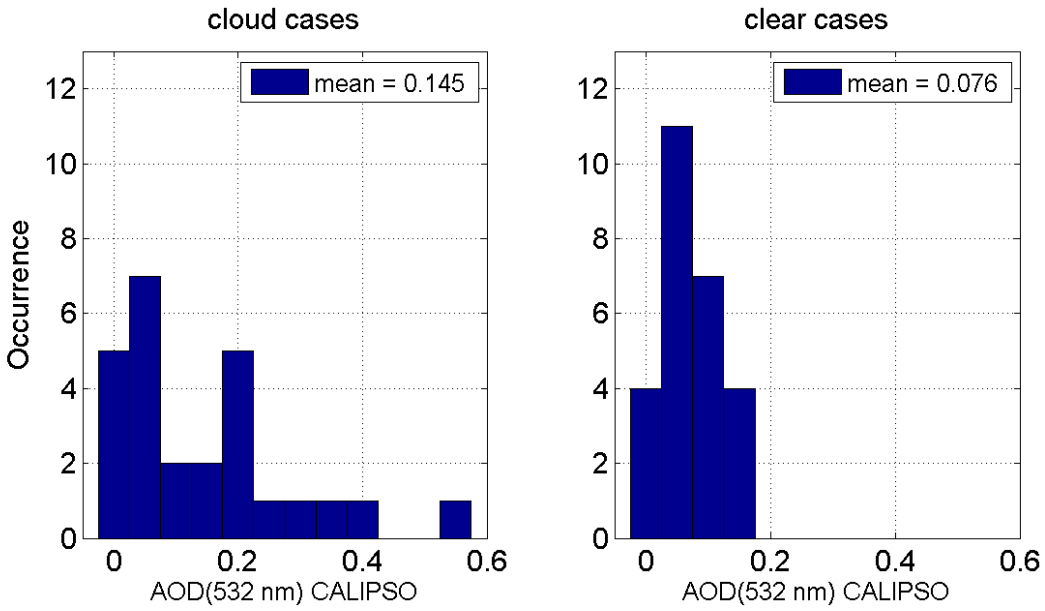

Figure 5.10: Influence of clouds in scene on the AOD distribution: occurrence of AOD values at 532 nm; left: cases in the presence of clouds nearby, right: clear sky cases.

distribution of the AOD dependent on the cloud presence. The left panel shows the AODs at 532 nm found in those overpasses in which clouds were observed. The average over these values is nearly doubled with respect to the average AOD for the clear sky overpasses (right panel) (0.145 and 0.076 respectively). Also the distribution is much broader; in 20 % of the cloudy cases the values are larger than 0.2, while no such large values were detected in the absence of clouds. The near-cloud values are spread over a wide range with a variation of ± 0.135 in contrast to ± 0.049 for clear cases. Also the failure to detect layers occurs more often in cloudy conditions, the mean LOD is 0.045 and 0.026 regarding cloudy and clear case (not shown).

The appearance of high AOD values in the presence of clouds in the scene explains why the negative differences between the AODs are not related to the LOD (see Fig. 5.8). These differences are dominated by the cloud effects, single missed layers have only minor influence.

5.3.2.4 Analysis of the meteorological conditions

As mentioned in Sect. 3.6.4 the meteorological conditions during the measurements of MULIS and CALIPSO can be considered, as well. All in all for 20 days the weather conditions show a straight flow with not much wind shear. Fig. 5.11 shows that the LODs are smaller in case of a straight flow (right panel) than on days with diffuse wind conditions (left panel), while the variation is smaller, as well (0.021 ± 0.017 and 0.044 ± 0.047, respectively). Accordingly, for diffuse wind conditions the assumption of a homogeneous

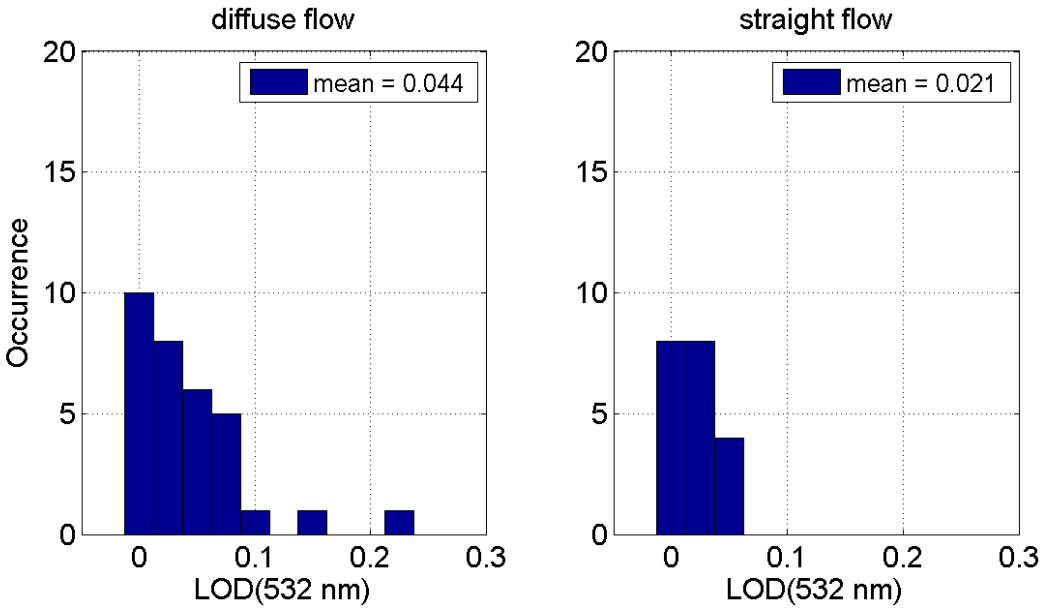

Figure 5.11: Influence of clouds in scene on the LOD. Left: days with diffuse wind conditions; right: days with straight flow.

atmosphere is not always true. Therefore the comparison of MULIS and CALIPSO should be done with great caution as it is not certain that the profiles contain data of the same atmosphere. Note: a lidar site with a direct overpass would make the discussion of this uncertainty unnecessary, but due to the location of the MULIS this could not be arranged for this thesis.

5.3.2.5 Dependency on distance

While the meteorological conditions are relevant for viable comparison, the study of the distance between the overpass and Maisach shows no strong dependency: in Fig. 5.12 the difference of the AOD at 532 nm of MULIS and CALIPSO is plotted depending on the distance of the overpass to the ground lidar. As can be seen on the map of the Munich region (Fig. 3.1), the overpasses are grouped around three distances: the night overpasses occur at ∼35 km east of Maisach and ∼80 km west of Maisach, while the day overpasses take place at a distance of about 55 km. The mean and median values of ΔAOD at 532 nm for overpasses at 35 km and 55 km distance are nearly the same (both 0.005 and 0.013), while only the furthest distance group has a negative mean of ΔAOD = -0.013. However, the median is again positive at 0.003. The variation of the values increases with increasing distance from ±0.05 at 35 km to ±0.09 at 80 km, which is not surprising, as a variation of the atmosphere is more likely at a higher distance.

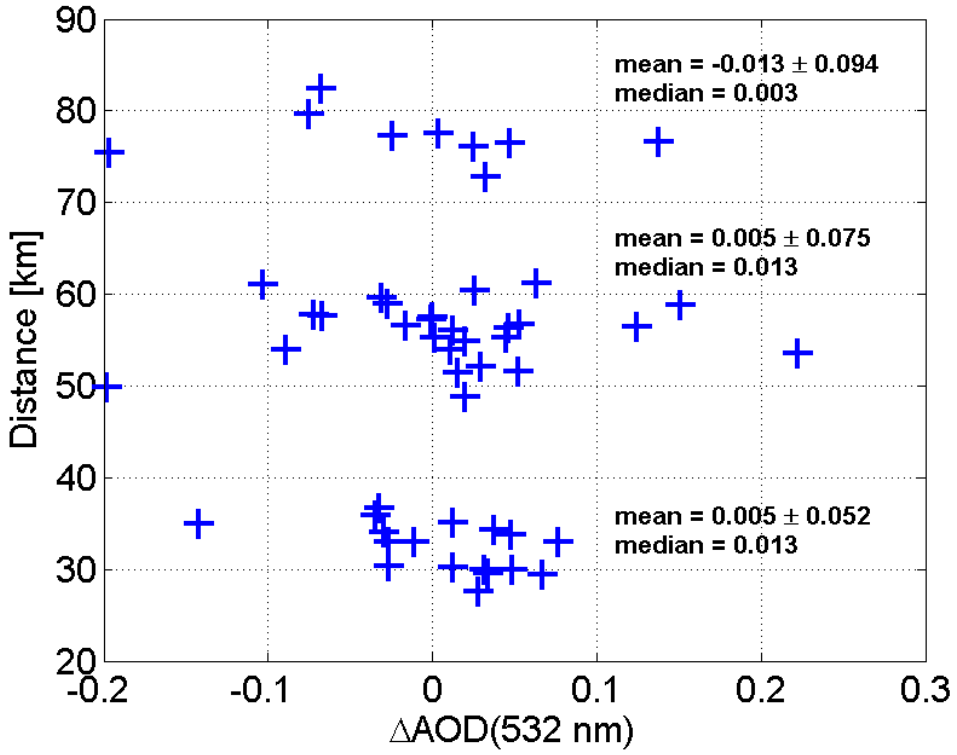

Figure 5.12: Difference of AOD(532 nm) between MULIS and CALIPSO dependent on the distance of the overpass.

5.3.2.6 Summary of CALIPSO - MULIS AOD comparison

The effects mentioned in this section are summarized for all 52 cases separately in Table A.1 in the Appendix. In general it can be said that the underestimation of the AOD by CALIPSO is mainly due to the failure of the layer detection. Its effect on the AOD underestimation is about 36 %. Also the wrong assumption of the lidar ratio contributes to the underestimation, though on a smaller account of ∼5.4%. The influence of clouds on the AOD is not quantifiable, but the analysis shows that clouds lead to an overestimation of the AOD. Since CALIPSO underestimates the AOD in the comparison to the four instruments, the overestimation by clouds seems to play a role only locally. Generally, this effect is surpassed by the detection failure and wrong lidar ratio.

However, the study of the meteorological conditions using HYSPLIT trajectories indicates that not on all coincident measurements sufficiently stable conditions were present. It would be best to use only days with with very stable weather conditions and a straight flow for the comparison of CALIPSO and MULIS. This subset could then be better analyzed with respect to layer detection, choice of lidar ratio, and cloud influence. This was not done in this thesis as the remaining dataset of only 20 overpasses within four years of measurements was considered too small to formulate general statements.

5.3.3 Comparison of layer mean values of MULIS and CALIPSO

The same behavior of well matching averages as in the AODs can be registered with the comparison of layer means of the particle linear depolarization ratio δ_p(532 nm) and the Ångström exponent κ(532 nm/1064 nm), provided that the means are only averaged over layers detected by both instruments. To calculate the means MULIS and CALIPSO must both have detected aerosols in the same heights. Then the height resolved parameters (δ_p, κ) are averaged for both instruments using the same layer tops and bases. Accordingly, only fully coincident measurements are compared. For the particle linear depolarization as well as for the Ångström exponent, the averages show a very good agreement: $\delta_p = 0.078$ / 0.077 and $\kappa = 1.468$ / 1.425 for MULIS / CALIPSO (see Table 5.8), also the data split into day and night values matches well. Only by considering the standard deviation, also listed in Table 5.8, it becomes apparent that the two instruments often measure very different values for single layers. Fig. 5.13 illustrates this for both parameters. The maximum value for the difference of $\delta_p = 0.429$ is accordingly not the result of a particularly high value of MULIS but of a high negative value of CALIPSO. The occurrence of negative values of δ_p in the CALIPSO profiles – which is observed for five layers – is due to very noisy signals: all five overpasses occurred at daytime with small scale clouds within the measurement region. Also the Ångström exponent of CALIPSO has negative values for several cases because the extinction coefficient at 1064 nm surpasses the coefficient at 532 nm. This is meteorologically rather unlikely and probably due to an incorrect calculation of the extinction coefficient either at 532 nm or at 1064 nm.

The direct comparision of the depolarization and the Ångström exponent of CALIPSO and MULIS (Fig. 5.14) shows that while both datasets are strongly dispersed, the corre-

Table 5.8: Layer means and variability of particle linear depolarization ratio δ_p(532 nm) and Ångström exponent κ(1064 nm/532 nm) from MULIS and CALIPSO data; average and standard deviation are shown for all data and split into day and night.

	All	**Day**	**Night**
Mean δ_p**(MULIS)**	0.078 ± 0.055	0.069 ± 0.051	0.087 ± 0.058
Mean δ_p**(CALIPSO)**	0.077 ± 0.105	0.060 ± 0.133	0 090 ± 0.077
Mean κ**(MULIS)**	1.468 ± 0.386	1.498 ± 0.387	1.444 ± 0.389
Mean κ**(CALIPSO)**	1.425 ± 0.695	1.409 ± 0.542	1.437 ± 0.805

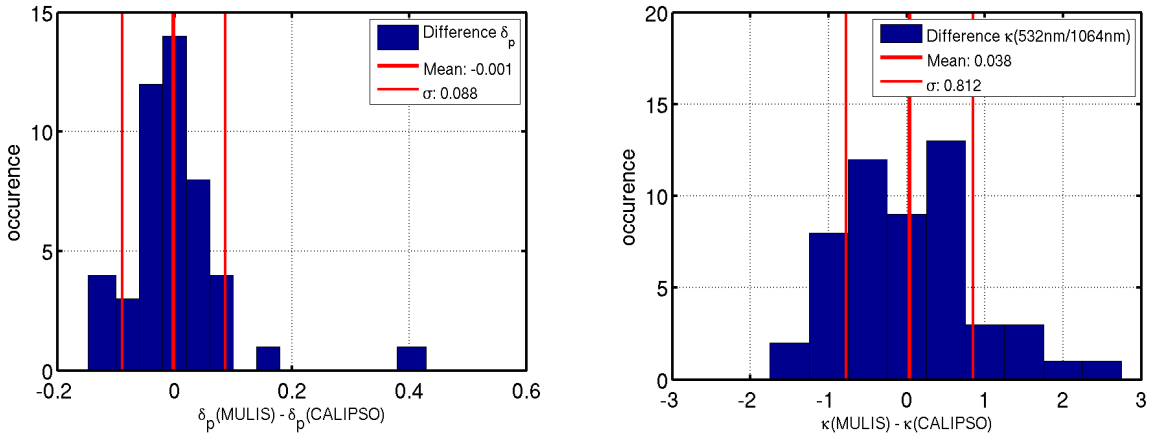

Figure 5.13: Occurrence, mean and standard deviation (variability) of the difference between MULIS and CALIPSO values; left: for the particle linear depolarization ratio δ_p(532 nm), right: for the Ångström exponent κ(532 nm/1064 nm).

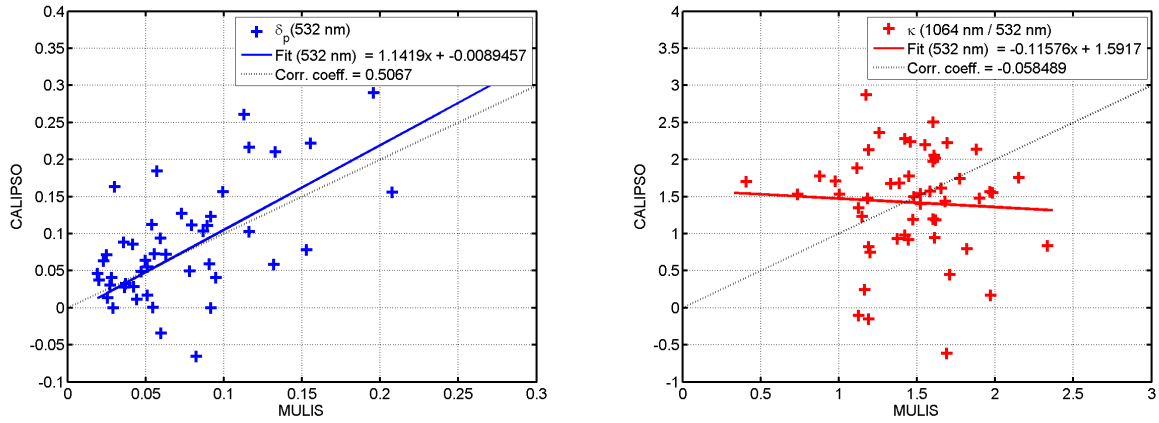

Figure 5.14: Coincident measurements of CALIPSO and MULIS of the particle linear depolarization ratio $\delta_p(532\text{ nm})$ (left) and for the Ångström exponent $\kappa(532\text{ nm}/1064\text{ nm})$ (right).

lation for δ_p is quite well, the slope of the linear fit is nearly 1. In contrast no relation between the Ångström exponents of the two instruments can be determined. As already discussed in Sect. 5.1.2 κ depends strongly on the correct extinction coefficients at both wavelengths which are itself dependent on the correct selection of the lidar ratio.

5.3.4 Calculation of extinction coefficients from CALIPSO L1B data

As the comparison of the attenuated backscatter signals (Sect. 3.6.2) shows, the raw data of MULIS and CALIPSO often matches very well. Differences in the extinction profiles must then be due to limitations of the analysis algorithms of CALIPSO. In case more accurate aerosol information is needed from CALIPSO than provided by the L2 data, it is possible to calculate the extinction coefficients from CALIPSO raw data manually. In this way, it is possible to detect layers missed by the SIBYL algorithm, to clear the profiles from clouds, or to vary the lidar ratio directly. Also days where no aerosol data is given in the L2 dataset can be analyzed.

The analysis of the data is done using the Newton Raphson method (Eq. 2.20) to calculate the particle extinction coefficient α_p from the attenuated backscatter signals β^* of the CALIPSO L1B data. This data also contains height resolved the molecular number density from which the molecular extinction and backscatter coefficients (α_m, β_m) can be derived. As lidar ratio input one measured from MULIS is used.

In Fig. 5.15 these newly calculated profiles are compared with the original CALIPSO L2 profiles and the corresponding MULIS profiles for four examples: for failed layer detection (top left), for the wrong assumption of the lidar ratio (top right), for failed cloud clearing (bottom left), and for completely missed aerosol layers (bottom right).

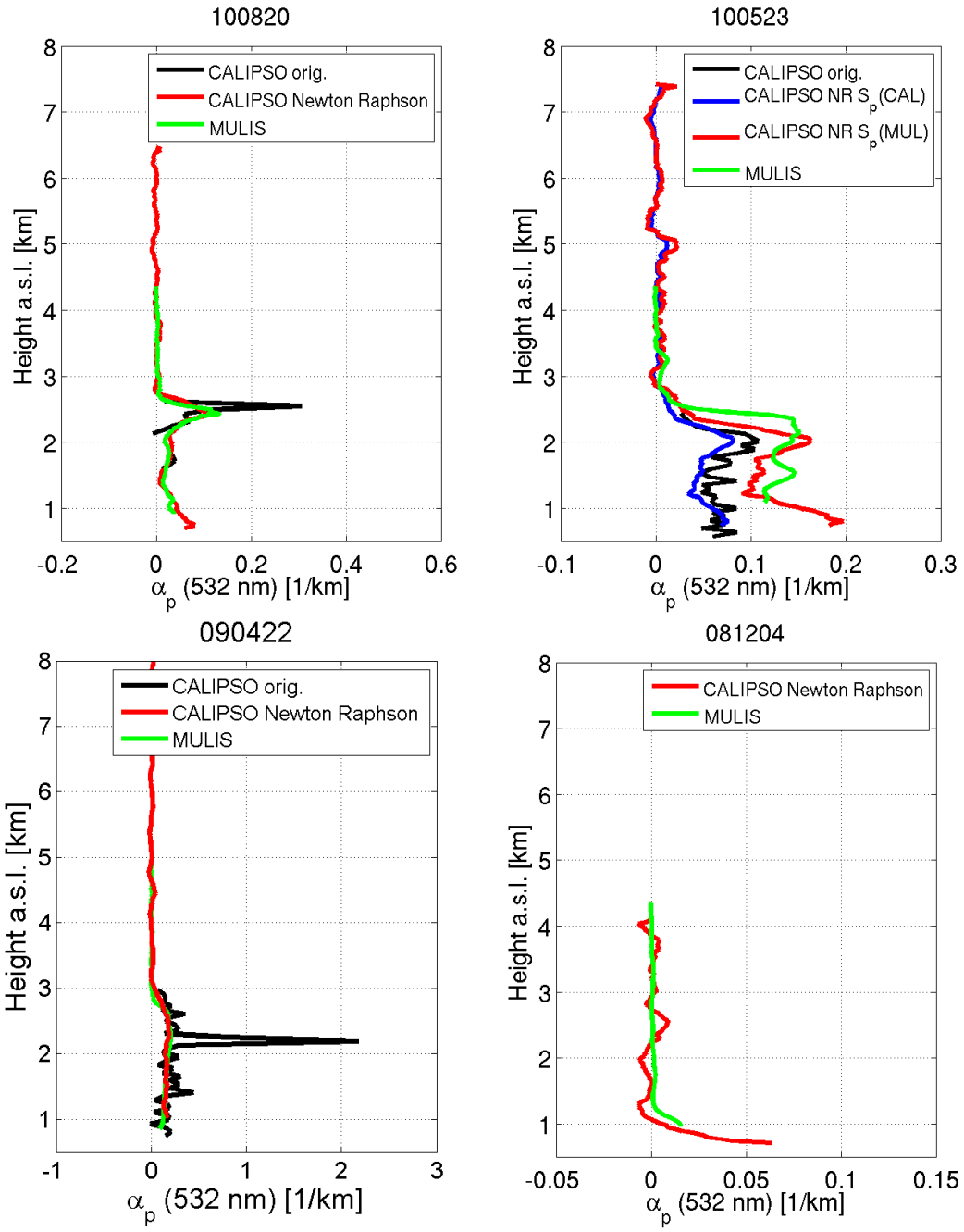

Figure 5.15: Extinction coefficients of MULIS (green), from CALIPSO L2 AP data (black), and calculated from CALIPSO L1B data (red) for an example of failed layer detection (20th August 2010, see Fig. 3.14), for a wrong assumption of the lidar ratio (23th May 2010, see Fig. 3.15), for failed cloud clearing (22th April 2009, see Fig. 3.16), and for completely missed aerosol layers (4th December 2008).

In the upper left panel (20th August 2010), in contrast to the original AP profile (black), the Newton Raphson profile (red) matches very well with the MULIS profile (green). Additionally, the small aerosol amounts from 1.8 km - 2.0 km and above 2.5 km are detected. The PBL even has values in lower heights than MULIS due to the overlap of the ground based instrument. The upper right panel (23th May 2010) shows in addition to the last mentioned three profiles the Newton Raphson profile with the lidar ratio of the CALIPSO AP data (blue) given as 40 sr and 55 sr (two layer of different aerosol type). This profile is in good agreement with the original AP profile, while the one calculated with the MULIS lidar ratio S_p= 73 sr agrees better with the measured MULIS extinction coefficient. The cloud clearing of the attenuated backscatter signals before the analysis (on 22nd April 2009) leads to a peak free CALIPSO profile which thus matches again well with the MULIS profile as shown in the lower left panel. The fourth example of Fig. 5.15 (4th December 2008) confirms the assumption that on this day the aerosol amount was too low to be well detected by the SYBIL algorithm. Down to 0.5 km above ground, the atmosphere is nearly free of aerosols; neither MULIS nor CALIPSO could detect any layers. Only in the lowest part of the profiles low extinction values exist. The CALIPSO AOD of 532 nm is hereby 0.008, the one of the MULIS profile 0.005 respectively 0.013 after adding the overlap correction (see Sect. 3.4.4).

So with the Newton Raphson method it is possible to calculate extinction profiles from CALIPSO data. However, this analysis is complex and needs experience as well as time. The huge dataset generated by CALIPSO with about 100,000 5-km-profiles for each day can not be analyzed in such an expensive way. It is therefore mostly useful for case studies, e.g. on field campaigns when single profiles are needed for detailed analysis.

5.4 Identification of aerosol type

The previous section gave a survey of the causes for the underestimation of the AOD. Another important question is how reliable the classification of the aerosol type by CALIPSO is.

A wrong classification of the aerosol type is linked to a wrong assumption of the lidar ratio (Sect. 3.6.3.2). Accordingly, the identification of the type by ground based lidar systems can help to review the confidentiality of the CALIPSO algorithms. The best method to classify the type is to use of intensive parameters like the particle linear depolarization ratio δ_p, the lidar ratio S_p, and the Ångström exponent κ. Unfortunately, these parameters are not available for most of the MULIS measurements. Especially the lidar ratio can only be determined on 12 overpasses (as explained in Sect. 3.6.3.2). Also the Ångström exponent at 1064 nm / 532 nm derived from MULIS data is always dependent on the assumption of the lidar ratio at the NIR wavelength, so it is not a very a reliable parameter for the classification.

On account of this, additional resources like the HYSPLIT trajectories need to be used to identify the possible sources of the aerosols detected by MULIS and CALIPSO.

In the context of this study, only case studies of three aerosol types are discussed: Pure

Table 5.9: Cases with dust classified by CALIPSO: layer averages of the particle linear depolarization ratio δ_p(532 nm) and Ångström exponent κ(1064nm/532nm) for CALIPSO and MULIS. Additionally the wind direction is shown as well as a flag whether dust was forecasted the Central Europe by DREAM.

	CALIPSO		**MULIS**		**Wind direction**	**DREAM**
date	δ_p	κ	δ_p	κ		
27.7.2007	0.26	0.17	0.11	1.97	W	No
30.3.2008	0.29	0.24	0.20	1.17	W	No
14.5.2008	0.37	-0.11	-	1.13	SO	Yes
17.8.2009	0.21	-0.16	0.13	1.19	W	No
23.5.2010	0.22	0.79	0.12	1.82	N	No

Saharan dust, which can be classified by high depolarization values, smoke as the most common aerosol type, and marine aerosol which CALIPSO only classifies above ocean (see Fig. 3.10) and therefore never above the Munich region. All further analysis is beyond the scope of this thesis; the interested reader is referred to an ongoing ESA study dedicated to this challenge [Hiebsch et al., 2010].

5.4.1 Saharan dust

Saharan dust is an aerosol type which occurs only occasionally – mainly in spring and summer – above Munich after long term transportation from the Saharan desert. The crystalline structure of its minerals leads to strong depolarization so that dust can be identified quite well through a high particle linear depolarization ratio with values of about 30 %. The condition for CALIPSO classifying dust is a high mean volume depolarization of the detected layer with $\delta_v > 0.2$. On five days of the coincident measurements, CALIPSO detected dust (see Table 5.9).

In the CALIPSO data, all five days have high particle depolarization values between 0.21 and 0.37, while the Ångström exponent κ(1064nm/532nm) is very low, between -0.16 and 0.79, indicating large particles. A first impression suggests that these aerosols seems to be Saharan dust. However, the coincident measurements with MULIS do not verify all of these measurements. The δ_p is lower than measured by CALIPSO (0.11 to 0.20) but still larger than the average over all MULIS measurements (0.08), which leads to the assumption that the detected aerosol was not pure but maybe polluted dust. For three days, the Ångström exponents are smaller than average (1.47), but on the other two days – which are also those measuring the smallest depolarizations – κ is clearly higher, indicating small particles.

The verification of Saharan dust can also be done using additional data like the dust forecast calculated with the BSC-DREAM8b model [Basart et al., 2012, Perez et al., 2006]. The aerosol source can be examined by calculation of backward trajectories with HYSPLIT.

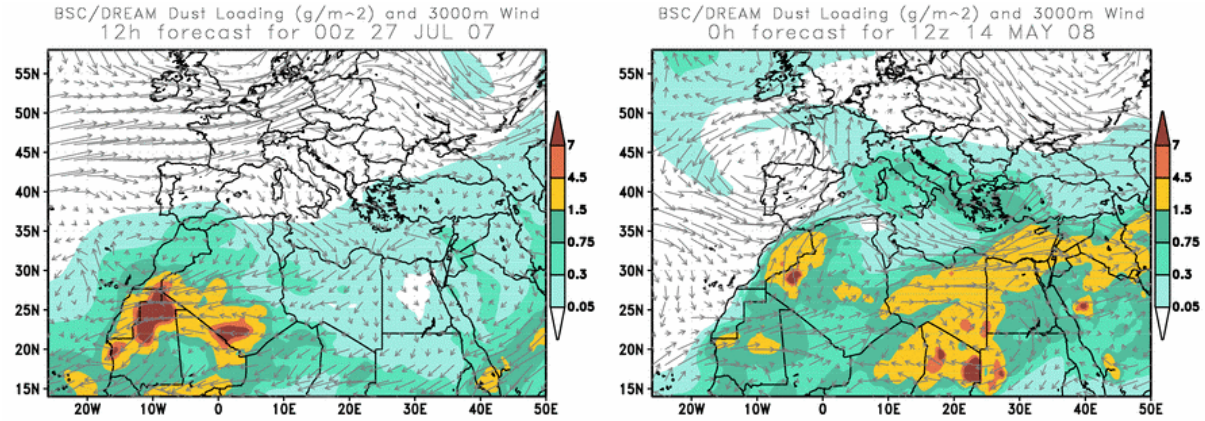

Figure 5.16: Forecast of the Saharan dust distribution above North Africa and Europe by the DREAM model for 27th July 2007, 00 UTC (left) and for 14th May 2008, 12 UTC (right). The dust concentration is color coded, white areas mean dust free regions. Additionally also the wind flow at 3 km a.s.l. is shown. Source: http://www.bsc.es/projects/earthscience/DREAM.

The DREAM model predicts the atmospheric life cycle of eroded desert dust. In Fig. 5.16 the forecasts of the Saharan dust distribution above North Africa and Europe are shown for the 27th July 2007, 00 UTC and for the 14th May 2008, 12 UTC. In the first example DREAM forecasts Saharan dust mainly above North Africa, while Europe is free of dust with the exception of Greece and South Spain. The HYSPLIT trajectories of this day (top panel of Fig. 5.17) show that air masses come mainly from the west so the aerosol type tagged by CALIPSO as dust may be biomass burning from the USA which also has increased depolarization. For the second example on 14th May 2008, small amounts of Saharan dust are expected in large parts of Europe (turquoise blue colors of right panel in Fig. 5.16). While there is no direct dust forecast above South Germany, the corresponding HYSPLIT trajectories confirm that air from South-East Europe –where higher concentrations of dust are expected– was transported to Munich. For the other 3 days the CALIPSO dust detection could not be confirmed.

So with the combined analysis of MULIS, the DREAM forecast, and the HYSPLIT trajectories the CALIPSO identification of Saharan Dust can only be verified for one of the five days – the 14th May 2008. On the 23rd May 2010 the trajectory analysis shows that the air masses are coming from the North. It is very probable that the detected aerosol is not Saharan dust but volcanic ash from Eyjafjallajökull. As the aerosol type volcanic ash is not included in the CALIPSO typing scheme but also has an increased particle linear depolarization ratio, the classification of this aerosol layer as dust is a good assumption.

The consequence of a wrong aerosol typing is a wrong assignment of the lidar ratio S_p. The lidar ratio for dust is very low at 532 nm ($S_p(532\text{ nm}) = 40$ sr) compared to smoke, polluted continental and polluted dust (55 sr - 70 sr), while it is the highest for dust at 1064 nm with $S_p(1064\text{ nm}) = 55$ sr (Table 3.5). Accordingly, a wrong identification will

Table 5.10: Cases with smoke classified by CALIPSO and coincident MULIS lidar ratio measurement (all at night): layer averages of the particle linear depolarization ratio δ_p(532 nm) and the lidar ratio S_p(532 nm) for CALIPSO and MULIS. In two cases CALIPSO lists two different lidar ratios (from different aerosol types in two layers). Additionally the wind direction derived from HYSPLIT trajectories is shown as well as a flag, that is, whether fires were detected in the source region of the trajectories.

	CALIPSO		**MULIS**		**Wind direction**	**MODIS fires**
date	δ_p	S_p	δ_p	S_p		in source region
10.5.2008	0.11	63/43	0.09	42±3	NE	No
27.6.2008	0.06	70	0.05	66±4	W	low
21.4.2010	0.08	62/44	0.15	69±5	WNW	high
8.6.2010	0.02	70	0.05	62±11	W / E	low
20.8.2010	0.01	70	0.03	66±14	W	high

lead to an underestimation of the extinction coefficient at 532 nm and an overestimation of α_p at 1064 nm which results in too small or even negative Ångström exponents.

5.4.2 Smoke

Smoke / biomass burning aerosol does not have such as strong a depolarization as dust, so δ_p cannot be used as main indicator for the classification. Instead a combination of the lidar ratio and δ_p has to be used. Therefore the 52 coincident measurements of MULIS and CALIPSO were screened for cases of smoke detection by CALIPSO with coincident lidar ratio measurements by MULIS. Five cases could be found, which are listed in Table 5.10. An analysis by Groß [2011] describes the properties of biomass burning as follows: S_p(532 nm) ranges from 60 sr to 90 sr and δ_p(532 nm) from 0.12 to 0.20. Compared to the values of Groß, the MULIS lidar ratios on four days match very well; only on the 10th May 2008 the value is clearly smaller (S_p= 42 sr). On the other hand, considering also the range of δ_p given by Groß et al. for smoke (0.12 - 0.20), only on one day – the 21st April 2010 – the δ_p measured by MULIS is within this range, indicating that the aerosol above Munich was indeed biomass burning.

However, a study of biomass burning over South-East Europe [Amiridis et al., 2009] showed huge differences in the aerosol properties of biomass burning which depend both on the transportation time of the smoke aerosols as well as on their source. The measured lidar ratios vary from 39 sr to 94 sr and the Ångström exponent has a variation from κ= 0.7 to 2.2, indicating strong changes of the microphysical properties (e.g. the size distribution) of the different observed smoke plumes. Accordingly, lidar measurements alone do not suffice to identify biomass burning aerosols. As additive again the HYSPLIT trajectories are used together with the MODIS fire maps [Giglio et al., 2003] to locate possible sources of biomass burning. Consequently the used fire maps refer to a time period of 10 days

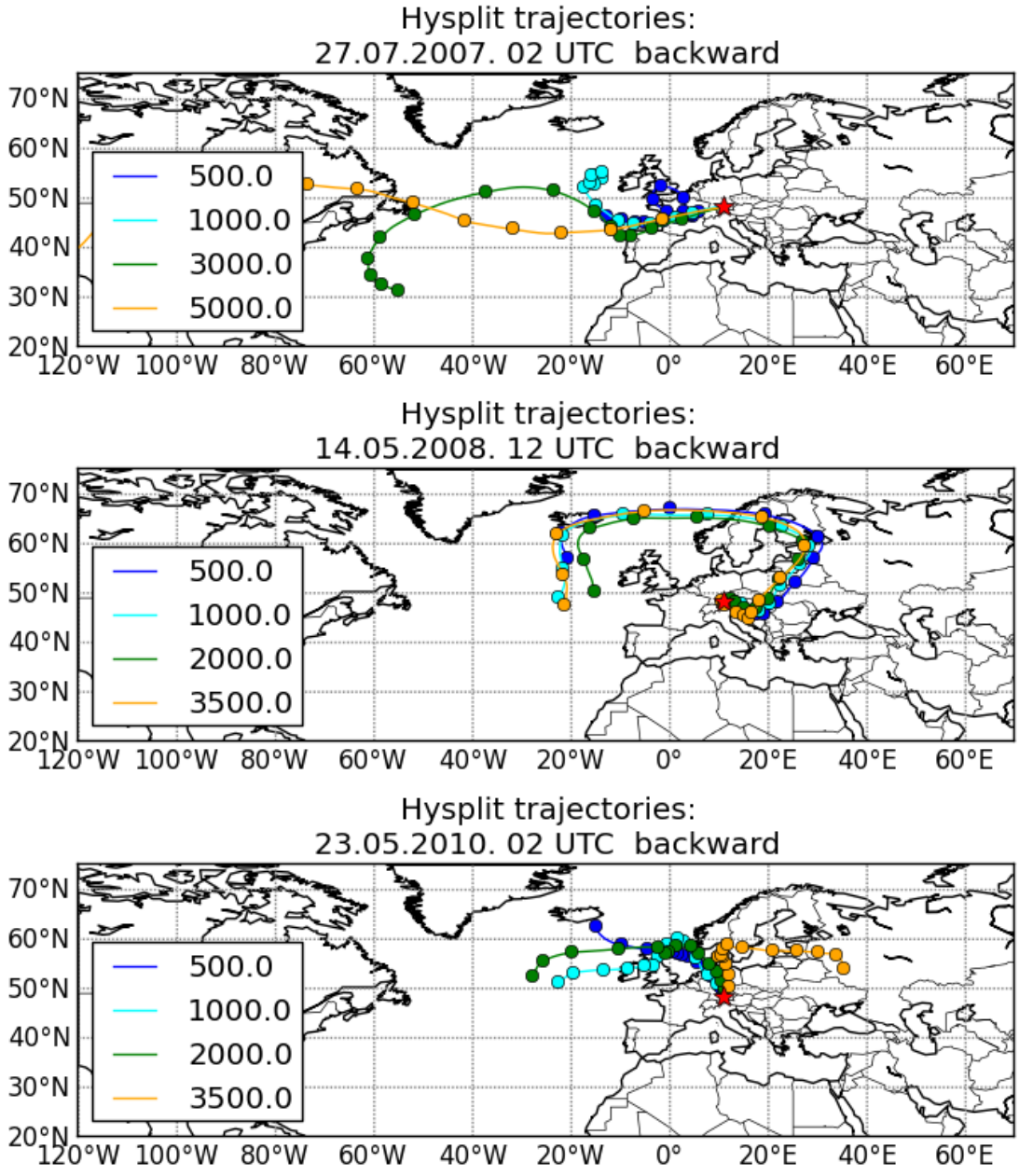

Figure 5.17: Backward trajectories from HYSPLIT analysis for 27th July 2007 (top), for 14th May 2008 (middle), and for 23rd May 2010 (base). The lines show the trajectories for air masses ending over Maisach on the date of interest, the color marks the altitude a.s.l. at which it ends. The distance between the circles is 12 h.

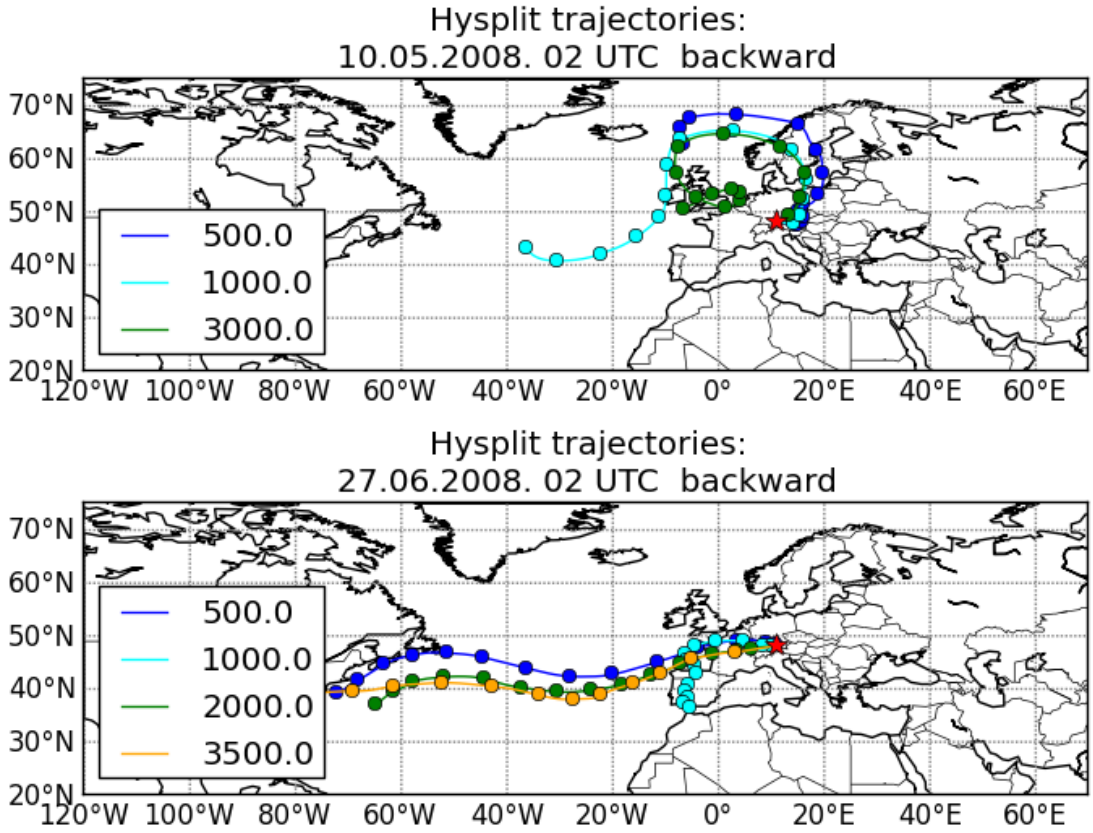

Figure 5.18: Backward trajectories from HYSPLIT analysis for 10th May 2008 (top) and 27th June 2008 (base). The lines show the trajectories for air masses ending over Maisach on the date of interest; the color marks the altitude a.s.l. at which it ends. The distance between the circles is 12 h.

and are chosen not for the overpass date but with consideration of the transportation time given by HYSPLIT.

As examples the trajectories and fire maps of two days are shown in Figs. 5.18 and 5.19. On the 10th May 2008 the trajectories do not show a straight flow. The air masses originate from Great Britain but circle over Scandinavia so that they arrive in Munich from the north-east. The corresponding fire map only detects few small fires, while no real source for smoke can be verified. Consistent with the complex flow pattern, for this day CALIPSO detected both smoke and clean continental aerosols and therefore lists two different lidar ratios. As the depolarization is at the same time increased it is very likely that on this day a mixture of aerosol types occurred. On 27th June 2008, in contrast, the wind pattern shows a strong westerly flow; the air masses originate from North America where several fires were detected. As a consequence, on this day the classification of smoke is very likely to be correct.

All in all it seems that smoke is correctly classified by CALIPSO at least in three out of

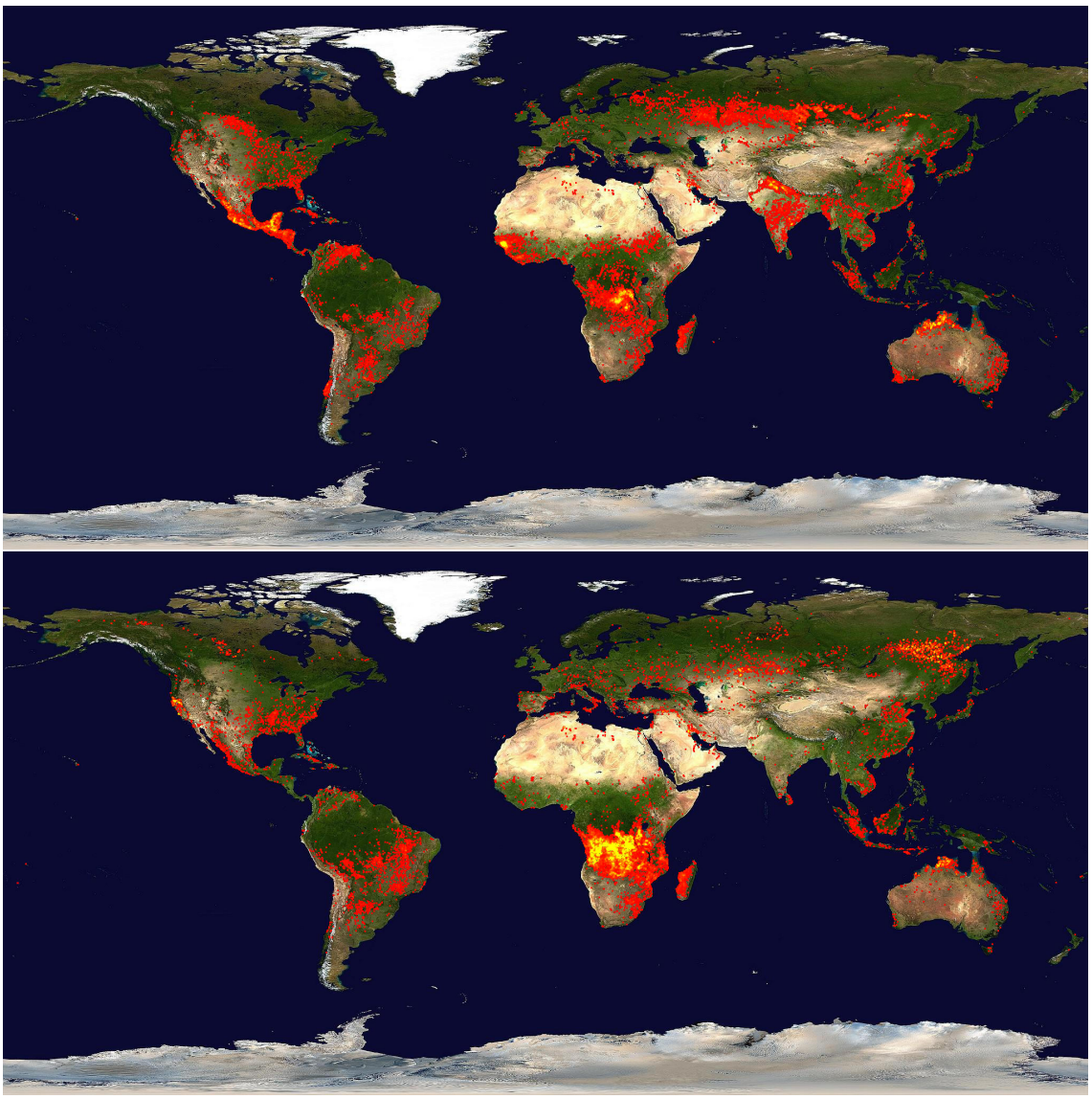

Figure 5.19: Locations of the fires detected by MODIS on board the Terra and Aqua satellites over a 10-day period. Each colored dot indicates a location where MODIS detected at least one fire during the compositing period. Maps are shown corresponding to 10th May 2008 (top, period from 30.4.-9.5.2008) and to 27th June 2008 (base, period from 19.-28.6.2008). Source: http://rapidfire.sci.gsfc.nasa.gov/firemaps/.

the five cases. On one day – 10th May 2008 – the classification is very likely incorrect and on the 20th August 2010 it is not possible with the additives used here to decide whether or not a correct classification was conducted.

The analysis of the five cases is a confirmation of the range of lidar ratios given by Groß et al. for smoke, while the variation observed by Amiridis et al. could not be confirmed. However, the sample is very small and the location in South Germany in contrast to South-East Europe may also account for the differences. For the particle linear depolarization ratio, however, the findings of Groß et al. could not be confirmed; two of the three cases which definitely measure smoke have significantly smaller values of δ_p. A possible explanation may be that the source of the smoke aerosol was quite different: Groß studied biomass burning from Africa; the examples shown here have their origin in North America. Alternatively, alteration or mixing along the transportation may have influenced the microphysical properties of the smoke aerosols.

5.4.3 Marine aerosol

The Munich region in the middle of the European continent does not provide the best opportunity to study marine aerosol. But on rare occasions – especially when strong northerly flows occur – it is possible that marine aerosol can be transported as far as Munich [Gosewisch, 2013]. For example on the 10th May 2008 trajectories show that air from the Baltic Sea was transported to Munich, see Fig. 5.17. The lidar ratio measured by MULIS (Table 5.10) is also very low (42sr), only consistent with dust – which can be excluded by the trajectories – and clean continental, but could also indicate marine aerosol mixed with other aerosols. Such a strong limitation as used by CALIPSO – marine aerosol is only identified if the measurement was performed above ocean – cannot take such transportation into account. In any case, in coastal regions this regulation can lead to grave errors in the AOD at 532 nm as for marine aerosol a clearly smaller lidar ratio is used than for all other aerosol types (see Table 3.5).

5.5 Aerosol studies in Central Europe

One of the main results of Chap. 4 is the determination of the aerosol optical depth in the Munich region. According to the AERONET instrument – which is best fit to measure the AOD – the mean value for the AOD is about 0.16 at 532 nm. Now this value is set into context: from the MODIS data it is possible not only to calculate the mean values above Munich, but to get large-scale information about aerosols. So Fig. 5.20 shows the mean AOD at 532 nm of all data from 2007 to 2010 for Central Europe. An exact identification is possible of the strong aerosol sources at the Po Valley in Italy, the densely populated area around Belgium and the Netherlands, and the industrial South of Poland – also identified e.g. by Chubarova [2009] – with values of over 0.2 (reddish colors), while in the North, the Scandinavian countries show very low values smaller than 0.1 (bluish colors). At Munich/Maisach (magenta dot), the AOD has a mean value of 0.158 ± 0.011 which fits

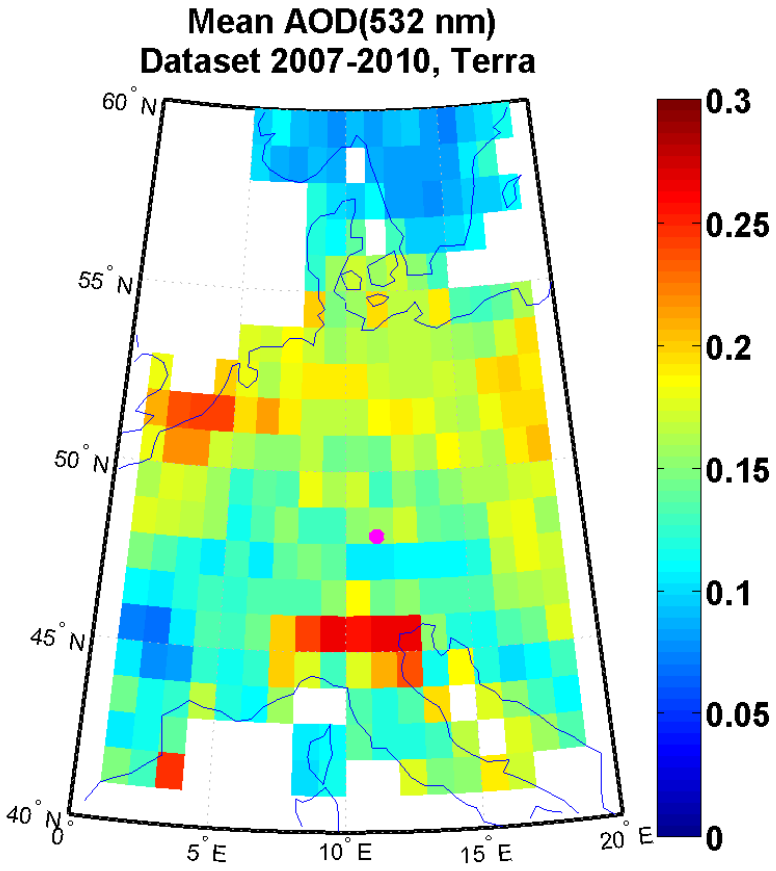

Figure 5.20: MODIS AOD at 532 nm for Central Europe: mean over all data from 2007 to 2010. Maisach/Munich is marked with a dot (magenta).

well with the AERONET value. Compared to the whole region it can be said that Munich has a medium amount of aerosol. This is due to the absence of nearby strong aerosol sources like the big industrial regions mentioned above as well as due to the geographical position just north of the Alps, which block large scale transportation of polluted air from Italy. It is possible that smaller mountain chains in the middle of Germany, too, block part of the polluted air masses from the Benelux region.

The seasonal variation of the AOD can be seen in Fig. 5.21: clearly the AOD has higher values above Europe in spring and summer; the reddish colors are dominant (AOD > 0.2). In contrast in autumn and winter the values are much lower, with dark blue regions with the AOD smaller than 0.1. In all four seasons, the above mentioned regions with strong aerosol amount are visible, additionally mainly in spring and summer, the East of Central Europe has high values probably due to biomass burning from Eastern Europe. This is for example confirmed by Barnaba et al. [2011] or Arola et al. [2007], who identify wildfires in Eastern Europe and Russia and describe the transportation of the biomass burning aerosol across Europe during spring and summer.

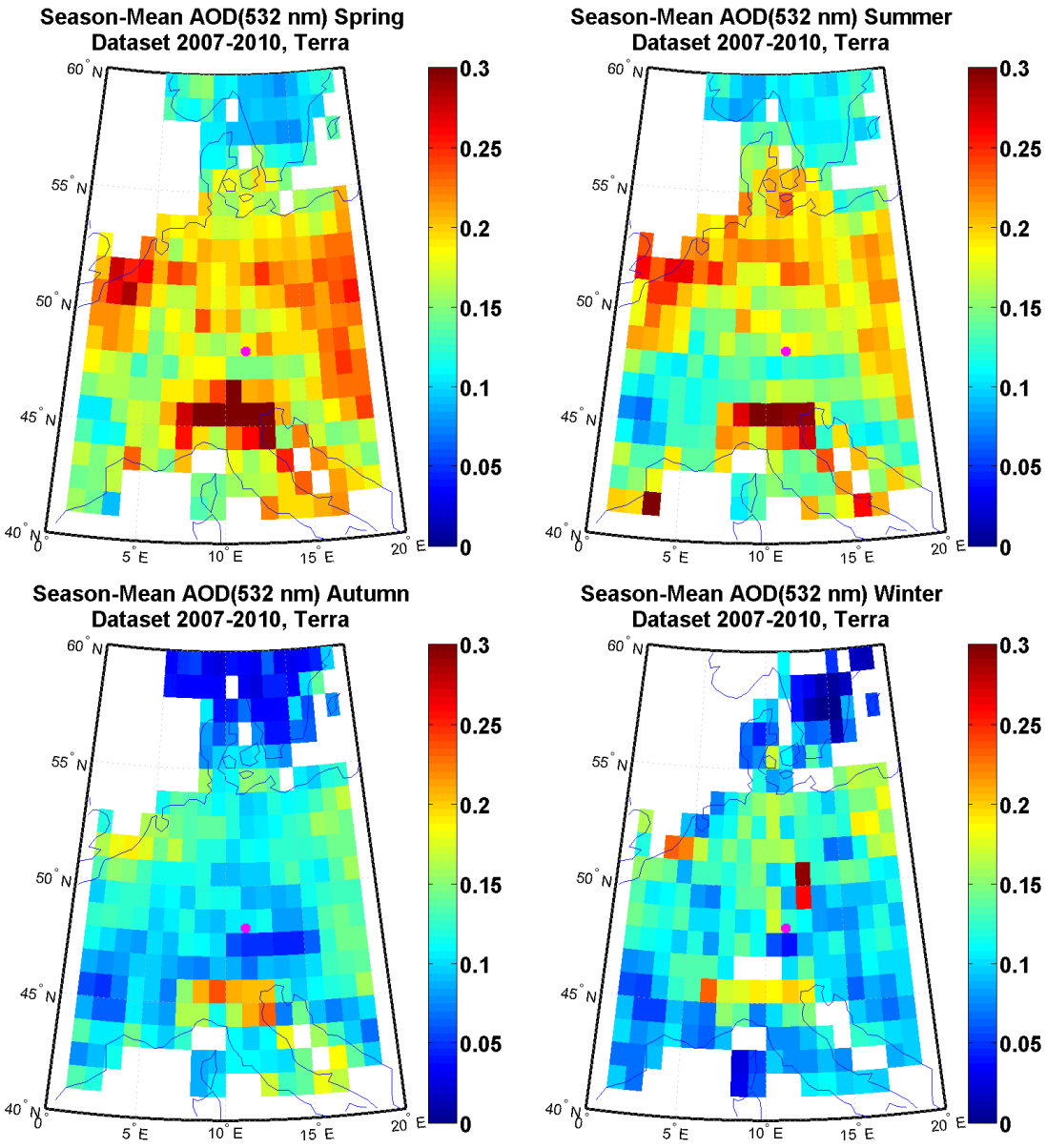

Figure 5.21: MODIS seasonal variation of AOD at 532 nm over Central Europe from all data from 2007 to 2010. Maisach/Munich is marked with a dot (magenta)

The study of Barnaba et al. [2011] also explains the maximum AOD in spring for smoke aerosols, as found by CALIPSO (Fig. 4.17). However, the monthly variation of the AOD from this study differs from the results shown here: Barnaba et al. [2011] receive a monthly bimodal distribution of the aerosol optical depth with maxima in April and August (AOD = 0.2), and an absolute minimum in December (AOD = 0.08). Chubarova [2009], too, report this distribution with its maxima in April and August. While the extremal values can be confirmed roughly by the datasets shown in this thesis, in none of the instruments a bimodal is observed (see Fig. 5.1). Although the minimum in November/December is very pronounced, the two maxima are perceivable only in few of the datasets, shifted in time, and partly adjoined by a third maximum in September: The first maximum appears as early as March for MODIS and MULIS and only distinctive in the latter; the second maximum already appears in June, but only in the spaceborne datasets, and with smaller amplitude in the AERONET data in July, and a third maximum is detected by the passive instruments in September. Both these instruments detect a *miminum* in August. It is not possible to assign one month to have the highest aerosol load, as the four instruments have different results on whether March or June/July wins the contest. The reason for the discrepancies between the mentioned papers and the results in this thesis is that the studies of Chubarova and Barnaba are based on a longer time period of nine years (2000-2008) and six years (2002-2007), respectively, instead of the four year analysis done in this thesis which in addition covers different years: for example, the Eyjafjallajökull event in 2010 clearly has an effect on the four years of this study. Also the AOD distribution of the Barnaba study refers to a larger region over Central Europe (46° to 56°N, 7° to 25° E), so small scale variations specific to the Munich region can be smoothed out by the average over the large region. In contrast the EARLINET study based on lidar measurements at 10 sites in Europe within two years [Matthias et al., 2004] also delivers very noisy distributions; a binomial distribution can only be observed in four out of ten sites.

The seasonal distribution of the aerosol types done by CALIPSO (Sect. 4.4.2) can be improved by analyzing the origin of the air masses above Munich. A study on the major trajectory directions was recently done at the MIM by Gosewisch [2013]. In this study, daily HYSPLIT trajectories were calculated for the time period of two years (March 2011 to February 2013), backwards for 5 days, starting at 11 UTC in Munich (48.148° N, 11.573° E) at the boundary layer top. On these trajectories a cluster analysis was conducted to identify the major trajectory directions. Fig. 5.22 shows the cluster analysis according to season. Different air flow patterns can be identified: only in spring and autumn, southerly air masses are transported, while occasionally air comes from Eastern Europe. Long range transportation over the Atlantic ocean bringing biomass burning from North America can be observed during the entire year, while the trajectories in autumn and winter originate from directions further north than in spring and summer. In general, for no season a single dominant trajectory direction can be identified. Accordingly, a large quantityof different aerosol types can be expected above Munich, which is very likely to also have been mixed during its transportation.

The extent of the PBL top measured by Mattis et al. [2004] above Leipzig varies from about 2.35 km in summer to 1.30 km in winter with AOD values of 0.18 ± 0.11 and $0.38 \pm$

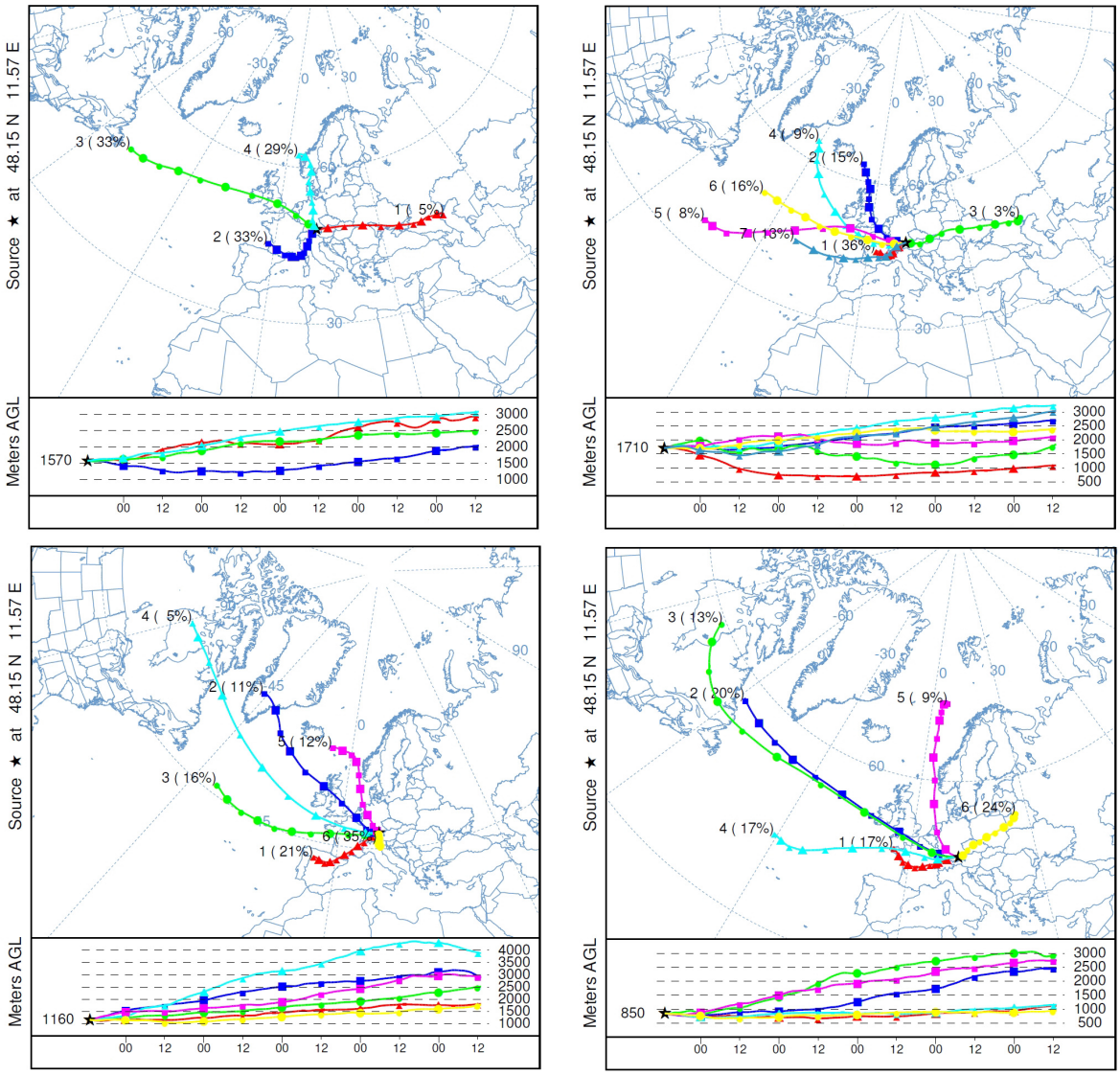

Figure 5.22: Seasonal cluster analysis of HYSPLIT trajectories for spring (upper left), summer (upper right), autumn (lower left) and winter (lower right): Next to each trajectory number the occurrence is given in percent. The distance between two markers on a trajectory is 12 hours. Source: A. Gosewisch, MIM.

0.23 at 532 nm and 355 nm, respectively. The extent in Munich is less, changing from 1.68 km in spring to 0.73 km in winter. However, the change between the seasons is stronger (factor 2.3 in Munich in contrast to 1.8 in Leipzig). Also the AODs are lower with values of about 0.12 to 0.17 at 532 nm and about 0.22 to 0.28 at 355 nm. As both, the PBL height and the optical depth differ, it is best to compare additionally the averaged extinction coefficient of the $\overline{\alpha_p}$ to get information about the aerosol concentration. In Leipzig, $\overline{\alpha_p}$ in the PBL is nearly the same for winter (0.10 / km) and summer (0.09 / km). While the values in Munich are a bit lower for the four season (0.085 / km, 0.063 / km, 0.072 / km, 0.061 / km), also here no strong variation can be observed. In general it can be said that in Leipzig a higher amount of aerosols occurs coupled with a thicker PBL height.

Comparing the optical depth of the PBL at 355 nm with the values collected from several EARLINET lidar stations by Matthias et al. [2004], the Munich value of $OD_{PBL}(355\ nm) = 0.20$ is at the lower side, especially the southern stations measure higher values up to 0.45 in Thessaloniki. Also in Hamburg and Leipzig higher values occur (0.26 and 0.30, respectively). This confirms the finding of the MODIS observations (Fig. 5.20) that the Munich region has lower values than the surrounding in Central Europe.

5.6 Consequence of wrong estimation of AOD and aerosol type on radiative forcing

One of the main findings of the comparison of the four instruments is the underestimation of the AOD by CALIPSO. Hence using CALIPSO data as input for a climate model would lead to a wrong aerosol-induced radiative forcing merely through the direct aerosol effect. In the following a rough estimate of the order of magnitude of this error is made; a sophisticated analysis could fill a complete new thesis on its own. The estimate is done using the software package libRadtran [Mayer and Kylling, 2005], which can be used to simulate radiative transfer in the Earth's atmosphere. The influence on the radiative forcing is estimated by modeling the difference of the outgoing top-of-atmosphere irradiances for the same scenario but altered AOD for different aerosol types.

For the calculations the following pre-adjustments are defined: The sun zenith angle is set to 63° to characterize an average situation for the Munich region, e.g. 8:15 UTC on the 21st March. A surface albedo of 0.05 can be assumed as a suitable value around Munich [Hausmann, 2012]. The altitude of the surface is set to 0.518 km. As correct AOD the mean value of AERONET ($AOD_{true} = 0.15$) is used, while as incorrect optical depth the CALIPSO mean AOD ($AOD_{false} = 0.08$) is set. The aerosol type is varied to study their influence on the radiative change, while the used aerosol types are taken from the OPAC (Optical Properties of Aerosols and Clouds) software package which provides optical properties of clouds and aerosol components [Hess et al., 1998]. The calculations are done for the predefined OPAC profiles desert, urban, continental averaged, and for pure soot, the PBL height is at approximately 1.5km. The aerosol concentrations are scaled to obtain the desired AOD at 550nm. The radiative forcing is defined as the difference between the

Table 5.11: Calculation of outgoing irradiances at the top-of-atmosphere for the aerosol types desert, urban, continental averaged and pure soot at AOD = 0.08 and AOD = 0.15, and their difference (radiative forcing). The following input parameters were used: a surface albedo of 0.05 and sun zenith angle = 63°, corresponding to an incoming irradiance of 621 W/m².

Aerosol type	**AOD(532 nm)**	**E(outgoing) [W/m²]**	**Difference [W/m²]**
desert	0.08	73.3	+ 7.9 (+ 9.7%)
desert	0.15	81.2	
continental averaged	0.08	70.6	+ 5.8 (+ 7.6%)
continental averaged	0.15	76.4	
urban	0.08	68.5	+ 3.6 (+ 5.0%)
urban	0.15	72.1	
soot	0.08	61.2	- 1.8 (- 3.0%)
soot	0.15	59.4	

outgoing top-of-atmosphere irradiance for AOD_{true} and the one for AOD_{false}.

For thermal radiation the radiative forcing is negligible (< 0.1 W/m²). It is only for large particles (coarse mode of Mineral dust) in highly elevated layers that a contribution of of 1 W/m² can occur. In the solar part of the spectrum several effects are visible: In Table 5.11 the outgoing irradiance at top-of-atmosphere and the radiative forcing induced by the change in AOD are listed. The irradiance depends on the aerosol type: desert aerosol has the strongest effect while soot has the smallest influence on the outgoing radiation (the outgoing irradiance for AOD = 0 is 63.5 W/m²). The effect of the underestimation of the AOD – calculation with AOD_{false} instead of AOD_{true} – leads for desert, continental averaged, and urban aerosol to an underestimation of the outgoing irradiance, that is a positive radiative forcing. E.g. for urban aerosol, the calculation of E(outgoing) results in 68.5 W/m² while the true value would be 72.1 W/m², resulting in a difference of 3.6 W/m² = 5.0%. The relative change is different for the three aerosol types with a contribution between 5.0% and 9.7% of the total radiation. In contrast pure soot which is highly absorbing leads to a negative change of -1.8 W/m².

On a yearly average, the radiative forcing is, of course, somewhat smaller since the effect completely disappears at night and almost disappears in the presence of clouds (calculations not shown). Nevertheless, this basic calculation already shows how important the use of the right AOD in combination with the right aerosol type is to determine the radiative influence of aerosols.

Chapter 6

Summary and Outlook

The aim of this study was to determine the aerosol distribution above Munich by using remote sensing techniques. To this end, data from the Sunphotometer Cimel of the network AERONET, the spectroradiometer MODIS onboard the TERRA satellite, the space lidar onboard CALIPSO, and the MULIS lidar system of the Meteorological Institute Munich was analyzed for a time period of four years (2007-2010). An additional focus was set on the estimation of the reliability of the CALIPSO data, taking into account the known limitations of the instrument. Especially the direct comparison of extinction coefficient profiles from coincident measurements of CALIPSO and the ground based Raman lidar MULIS could quantify these limitations.

6.1 Summary of results

The aerosols distribution was determined for a region around Munich from 46.7° to 49.7°N and 9.8° to 12.8°E. It was analyzed regarding the monthly and seasonal variation of several properties. Especially the AOD at 532 nm was studied in detail as this parameter can be derived from all four datasets. The studies with the lidar systems MULIS and CALIPSO additionally provided height resolved information, such as a discrimination between EL and PBL, aerosol layer specific results, e.g. optical depth, particle linear depolarization ratio, and Ångström exponent, and profiles of extinction coefficients.

Typical values of the AOD for Munich (Sect. 5.1.1)

Not taking the results from CALIPSO into account (see below for reason), on average the AOD above the Munich region is at 1064 nm about 0.05 to 0.06, at 532 nm about 0.12 to 0.17, and at 355 nm about 0.22 to 0.28. The values vary with season; in spring and summer the highest values occur (average spring AOD(532 nm) = 0.19 from MODIS) while in winter only low amounts of aerosol can be measured (average winter AOD(532 nm) = 0.06 from MULIS). The month with the highest AOD varies for the four instruments; maxima can be observed in March/April as well as in June/July. However, all four instruments detect the smallest AOD in November/December.

Structure of the atmosphere (Sect. 4.3)

The structure of the atmosphere can be best observed with MULIS. Using the entire set of data gained in the four years, seasonally averaged profiles of the extinction coefficients at 1064 nm, 532 nm and 355 nm were calculated. Additionally the optical properties of the boundary and elevated layers were studied. The occurrence of ELs is highest in spring, when in about three quarters of the measurements elevated layers are detected, while in winter only a third of the profiles contains layers above the PBL. The average geometric depth of the PBL decreases from 1.68 km in spring to 0.73 km in winter (factor 2.3), while the thickness of the elevated layers is more stable, varying from 1.43 km as maximum in spring to 1.02 km in winter (factor 1.4). Measurements of the particle linear depolarization ratio show that the aerosols in the elevated layers clearly differ from the aerosols in the PBL. Especially in spring the average EL depolarization is large (25 %), indicating transportation of strongly depolarizing aerosols like Saharan dust in the free troposphere.

Typical aerosol type (Sect. 4.4)

The analysis of the CALIPSO aerosol data from 2007 to 2010 shows that the dominant aerosol type in the Munich region is smoke (also called biomass burning). Polluted and clean continental aerosols were observed less frequently. However, while clean continental aerosol does not play a significant role (very low AOD), polluted continental can occur in high concentrations especially during summer time. The occurrence of dust – which contributes quite strongly to the atmosphere above Italy, Greece, or Spain – is low; generally the dust is already altered or mixed and classified as polluted dust. In any case, most events classified as pure dust were shown to be misclassifications by CALIPSO (Sect. 5.4). The aerosol type volcanic ash is not known to CALIPSO, so part of the aerosols classified as dust or polluted dust in April and May 2010 is probably volcanic ash.

Comparison of the four datasets (Sects. 5.1.1, 5.2)

All in all the datasets of MODIS and AERONET match very well, while for MULIS slightly smaller values are obtained. A comparison between coincident measurements of MULIS and AERONET shows an excellent agreement. The offset between the two datasets is due to the instruments being at different locations: MULIS is located at the rural site Maisach, while the AERONET Sunphotometer resides in the city of Munich which acts as an urban heat island.

CALIPSO's AOD at 532 nm is clearly smaller and, although to a smaller extent, also its AOD at 1064 nm. This difference between CALIPSO and the other instruments can not be explained by the difference in the location. It can be concluded, therefore, that CALIPSO underestimates the AOD.

Underestimation of the AOD by CALIPSO (Sect. 5.3.2)

The AOD values of CALIPSO scatter very strongly; in general the AOD is underestimated. A thorough comparison of coincident profile data between CALIPSO and MULIS was performed to find viable explanations for this phenomenon. While the raw data of CALIPSO and MULIS, the so called attenuated backscatter, matches very well, the comparison between the profile data like extinction coefficient and particle linear depolarization ratio often show strong discrepancies. This may be explained by the following causes: failure of aerosol layer detection, assumption of an incorrect lidar ratio, and influence of clouds in the surroundings of the analyzed profile.

In general it can be said that the underestimation of the AOD above Munich by CALIPSO is mainly due to the failure of the layer detection. Its effect on the AOD underestimation is about 36 %. Also the wrong assumption of the lidar ratio contributes to the underestimation, though on a smaller account of $\sim$5 %. The influence of clouds on the AOD is not quantifiable, but the analysis shows that clouds lead to an overestimation of the AOD. Since CALIPSO underestimates the AOD in comparison to the other three instruments, the overestimation by clouds seems to play a role only locally. In general, this effect is surpassed by the layer detection failure and incorrect lidar ratio.

Note that the contribution strengths of the different effects refer to the measurements above Munich with typical AODs of order 0.15 at 532 nm. For regions with higher aerosol load (e.g. Saharan desert) the use of a wrong lidar ratio will contribute much more strongly than the missing of thin layers. In contrast, in regions with less aerosol than Munich (e.g. Scandinavia) the percentaged effect of layer detection failure is expected to be even higher.

Usefulness of CALIPSO data

The study of the limitations of CALIPSO leads to the result that the CALIPSO data should only be taken as a lower bound when describing the aerosol load of a region, at least under the condition that the amount of aerosol is equal to or smaller than that of the Munich region (under these conditions aerosol layer detection failure is significant). However, the CALIPSO data has the great advantage of providing data in night time conditions, when passive aerosol instruments like MODIS and the AERONET-Cimel can not measure. This data has less limitations than the daytime data of CALIPSO, as the SNR is much higher and so the detection success rate of aerosol layers is also much better. Therefore the CALIPSO data is an immensely valuable source for aerosol studies at night time, especially for the polar and subpolar regions during the arctic winter.

Improving CALIPSO results for case studies (Sect. 5.3.4)

If more accurate data from CALIPSO are needed, it is possible to calculate the extinction coefficients from CALIPSO raw data (L1B) manually using for example the Newton Raphson method. A case study was performed on four profiles to show how the quality of the data can be improved: layers missed by the CALIPSO algorithm can be found, the correct lidar ratio, if obtainable from other sources, can be used and small scale clouds

can be better filtered. However, this analysis is complex and needs experience as well as time. The huge dataset of CALIPSO with about 100,000 5-km-profiles each day can not be analyzed in such an expensive way. This method is therefore mostly useful for case studies, e.g. on field campaigns when single profiles are needed for detailed analysis.

6.2 Open scientific questions and outlook

Since height resolved studies above Central Europe are quite rare – especially regarding typical optical properties in the PBL and elevated layers –, this thesis can be used to fill this gap. As a consequence, the Munich region is particularly interesting and challenging because it is a region experiencing a multitude of aerosol types which occur dependent on the wind flow. Also, it is a region with rather low AOD compared to most other locations at which aerosol studies have been performed.

The aerosol distribution obtained in this thesis – e.g. seasonally averaged extinction profiles, occurrence and average optical depths of elevated layers, most common aerosol type – is valuable information for several other scientific groups. As an example, it can be used to improve the aerosol parametrizations in atmospheric and climate models.

The methodology used in this thesis, both for obtaining the aerosol distribution as well as for evaluating the CALIPSO aerosol retrieval, can also be transferred onto other regions. Especially the combination of MODIS and CALIPSO has the opportunity to deliver aerosol distributions in any region on Earth.

Finally the analysis of the influence of the different CALIPSO limitations will help to improve aerosol studies based on CALIPSO data as well as the CALIPSO algorithms themselves. Particularly the evaluation of the CALIPSO AOD for moderate to low aerosol amounts as shown in this study can be very useful for other satellite missions. For example for a spaceborn methane lidar as discussed by Kiemle et al. [2011], knowing the exact amount of AOD in the region being overpassed is essential. The horizontal resolution on which methane can be retrieved correlates with the amount of aerosol, while only for small values of the AOD (< 0.1 at 1.65 μm) the precision is good. Accordingly, correct information on the AOD will clearly result in a better retrieval of the global distribution of methane in the atmosphere. Knowing how much CALIPSO underestimates the AOD is therefore important for the retrieval development of this satellite.

However, CALIPSO also has the potential to improve ground based instruments: Since 2010 a ceilometer network with 52 instruments distributed in all of Germany was established by the DWD performing continuous measurements of the backscatter signal at 1064 nm [Flentje et al., 2010]. While the ceilometer's ability to detect aerosol in the free troposphere is limited, the height and extinction coefficient of the boundary layer can often be determined. So for Germany a three dimensional distribution of the PBL can be determined with interpolations between the ceilometer sites. The intersection of the distribution with overpasses of CALIPSO can provide valuable information about the correctness of the interpolation.

This being the first extensive study of aerosol distributions in the Munich region, there

is, of course, room for improvement. The distribution shown here is based on only four years of measurements from 2007 to 2010. Since then all four instruments have continued to collect data. The data from 2011 to 2013 can help to strengthen the results shown here by increasing the days of useable measurements; by doing this, the influence of the interannual variation of the datasets would be further smoothed out.

Such an extended study could also append further instruments. Here the research aircraft FALCON would be of great value, which performed in-situ measurements onboard during departure and landing flights at Oberpfaffenhofen near Maisach on several days. Coincident lidar measurements with MULIS were arranged. The comparison between the in-situ data and the optical properties derived from the MULIS measurements would provide additional information on the aerosol composition above Maisach.

Also the valuation of the CALIPSO algorithms, done in this thesis for a limited number of days, can be augmented. By using additives like HYSPLIT or Flexpart the sources of the aerosols can be estimated and, combined with Raman and depolarization measurements, an aerosol classification similar to the one done by Groß et al. [2011] could be performed with the MULIS data. This would also directly lead to a further validation of the aerosol type classification of CALIPSO. Extending this validation method to other stations of the EARLINET network which are performing coincident measurements with CALIPSO will allow a four dimensional analysis of CALIPSOs aerosol detection skills. For better comparability, the aerosol type classification of CALIPSO could be applied to the measurements of the ground based lidars.

It should be noted that the validity of the lidar ratios used by CALIPSO for given aerosol types was not questioned in this thesis, e.g. the lidar ratio for dust at 532 nm is assumed to be 40 sr while several field campaigns discovered higher values. Consequently, long term studies of the lidar ratio for different aerosol types should also help to improve these values in the CALIPSO algorithms.

One large drawback in the comparison of MULIS and CALIPSO is the fact that the overpass of CALIPSO is not directly above the ground lidar but at least 30 km away. The thus required homogeneity is only an assumption which needs affirmation, e.g. by using trajectory models, and can lead to errors if not affirmed. This can be avoided by measurements directly below the overpass, as could be performed with another lidar system of the MIM, POLIS, which is located at the institute in the city of Munich. Until now this instrument has not been used for regular measurements of EARLINET. Since June 2009 a ceilometer is located at the MIM which performs continuous measurements at 1064 nm. Also this data can be used for comparison.

But also the CALIPSO data has deficits which make a comparison with other instruments difficult: since the start of the mission, several new versions of data have been published. As the CALIPSO extinction coefficient profiles are in the present version only available for heights in which aerosols are detected, they are not continuous; also their noise is quite high. Therefore it was not possible to study the behavior of the extinction profiles very well. This situation will improve when in a future data version the extinction profiles of CALIPSO also take into account the spaces between the detected layers.

For the next years two new spaceborn lidar systems are planned, the ADM Aeolus

[Endemann et al., 2004] and the ATLID as part of the EarthCARE mission [Heliere et al., 2007]. The HSRL lidar ATLID emits at 355 nm and has the advantage that it does not need the complex aerosol classification but can gain the lidar ratio directly. Also the smaller wavelength has generally higher extinction; this combined with the lower orbit of about 393 km leads to higher SNR compared to that of CALIPSO so that the detection of aerosol layers is likely to be enhanced.

These new satellites will also help to improve further the knowledge about the aerosol distribution above Munich. As CALIPSO measures at the two wavelengths 1064 nm and 532 nm and several ground based lidars like MULIS use the same wavelengths and the additional 355 nm, the validation measurements of the ground based instruments can also be seen as a bond between the data of the CALIPSO lidar and those of ATLID and ADM Aeolus. If CALIPSO is still operating when the new lidar systems are started, 'triple' measurements – longtime measurements at ground until both satellites have overpassed – could be advantageous to both satellite retrievals.

All in all, a lot of interesting work remains to be done.

Appendix A

Overview about the measurement differences of MULIS and CALIPSO

For each date of the 52 coincindent measurements of MULIS and CALIPSO following parameters are listed in Table A.1: the date, the day/night (DN) flag, the AOD measured by MULIS, the absolute difference of the AODs (ΔAOD = $\mathrm{AOD_{MULIS}}$ - $\mathrm{AOD_{CALIPSO}}$), the optical depth of layers missed by CALIPSO but detected by MULIS (LOD), the change in the AOD of MULIS when using the lidar ratio of CALIPSO (ΔS_p), the flag of clouds in the 80 km scene around the measurement, the HYSPLIT flag indicating straight (flag = 0) and diffuse (1) flow, as well as the distance of the nearest overpass of CALIPSO to Maisach.

Note that two day measurements have ΔS_p, there the lidar ratios were obtained uring evening measurements on the same day.

Table A.1: Overview of the discrepancies at 532 nm of MULIS and CALIPSO: absolute difference in AOD (ΔAOD = AOD_{MULIS}-$AOD_{CALIPSO}$), optical depth of missed layers (LOD), change in the AOD with different lidar ratio (ΔS_p), flag of cloud in scene (= 1, if clouds present in scene), Hysplit flag (=1, if trajectories are unfavorable), and distance of CALIPSO overpass footprint to Maisach.

	Date	**DN flag**	**AOD MULIS**	**ΔAOD**	**LOD**	**ΔS_p**	**Cloud flag**	**Hysplit flag**	**Distance [km]**
01	070401	**D**	0.136	-0.001	0.063		0	1	57.2
02	070410	**D**	0.133	-0.089	0.003		1	0	53.99
03	070417	**D**	0.053	0.053	0.053		0	0	56.7
04	070426	**D**	0.115	0.045	0.026		0	1	55.2
05	070519	**D**	0.068	0.020	0.005		0	0	54.9
06	070524	**N**	0.131	0.032	0.020	-0.006	0	0	30.0
07	070620	**D**	0.186	0.012	0.077		0	1	56.0
08	070727	**N**	0.170	0.067	0.036		1	0	29.4
09	070823	**D**	0.049	-0.067	0.016		1	0	57.7
10	070913	**N**	0.122	0.028	0.042		0	1	27.6
11	071015	**D**	0.101	0.048	0.019		0	1	33.8
12	080330	**N**	0.063	0.047	0.044		1	1	76.5
13	080408	**N**	0.077	0.077	0.077		0	1	33.0
14	080505	**D**	0.137	-0.031	0.029	-0.040	1	0	59.6
15	080510	**N**	0.059	-0.011	0.010	0.020	0	0	33.0
16	080514	**D**	0.077	0.029	0.024		1	1	52.1
17	080627	**N**	0.166	-0.142	0.001	0.001	1	0	34.9
18	080724	**D**	0.138	-0.103	0.018		1	0	61.1
19	080818	**D**	0.079	0.019	0.036		0	0	48.8
20	080919	**D**	0.107	0.015	0.020		0	1	51.4
21	081008	**N**	0.051	0.032	0.050		1	1	72.8
22	081204	**N**	0.013	0.013	0.013		0	0	35.1
23	081231	**D**	0.034	-0.016	0.012		1	1	56.6
24	090406	**D**	0.183	-0.000	0.060		1	1	57.5
25	090411	**N**	0.112	0.048	0.040	-0.015	0	1	30.0
26	090415	**D**	0.183	0.052	0.007		0	1	51.6
27	090422	**D**	0.276	-0.027	0.028		1	1	59.0
28	090427	**N**	0.012	0.012	0.012		1	1	30.2
29	090707	**N**	0.128	-0.068	0.005		1	0	82.4
30	090801	**N**	0.097	-0.026	0.002		0	1	33.0
31	090805	**D**	0.134	0.063	0.091		1	1	61.2
32	090817	**N**	0.102	0.038	0.018	-0.009	0	0	34.3
33	090824	**N**	0.117	0.003	0.009		0	1	77.5
34	090906	**D**	0.127	-0.072	0.076		1	1	57.8
35	090909	**N**	0.016	-0.075	0.010		0	0	79.7
36	090922	**D**	0.310	0.124	0.065		1	1	56.4
37	091004	**N**	0.018	-0.026	0.003		0	0	30.4
38	091218	**D**	0.058	0.001	0.012		0	1	55.2
39	100119	**D**	0.011	0.011	0.011		1	1	54.0
40	100421	**N**	0.374	-0.197	0.050	-0.049	1	0	75.4
41	100430	**N**	0.115	-0.032	0.001	-0.012	1	0	36.7
42	100523	**N**	0.260	0.139	0.017	-0.083	0	1	76.6
43	100605	**D**	0.063	0.026	0.026		0	1	60.4
44	100608	**N**	0.096	0.025	0.062	0.013	1	1	76.1
45	100628	**D**	0.144	-0.198	0.037	0.002	1	1	49.9
46	100703	**N**	0.133	-0.030	0.011		0	1	34.1
47	100707	**D**	0.193	0.151	0.162		1	1	58.8
48	100714	**D**	0.222	0.222	0.222		1	1	53.5
49	100820	**N**	0.085	0.034	0.042	-0.003	1	0	29.5
50	100912	**N**	0.039	-0.024	0.002		0	1	77.3
51	100921	**N**	0.041	-0.034	0.010		1	1	35.9
52	101011	**D**	0.046	0.046	0.046		0	0	56.3

Appendix B

Monthly and seasonal values

Tables of monthly and seasonal mean values of AOD and Ångström exponents as shown in Chapter 4 are listed for the following instruments:

- AERONET: Table B.1 and B.2
- MODIS: Table B.3
- MULIS: Table B.4
- CALIPSO: Table B.5.

Table B.1: AERONET: monthly and seasonal mean values of AOD for all seven wavelengths.

AOD	**1020 nm**	**870 nm**	**675 nm**	**532 nm**	**440 nm**	**380 nm**	**340 nm**
January	0.044	0.056	0.080	0.120	0.153	0.175	0.193
February	0.050	0.061	0.082	0.119	0.152	0.176	0.195
March	0.065	0.079	0.108	0.157	0.202	0.238	0.267
April	0.079	0.099	0.136	0.193	0.248	0.292	0.323
May	0.077	0.093	0.123	0.171	0.222	0.269	0.304
June	0.070	0.089	0.125	0.179	0.236	0.291	0.333
July	0.071	0.093	0.139	0.202	0.268	0.330	0.379
August	0.042	0.056	0.085	0.126	0.170	0.214	0.252
September	0.076	0.095	0.132	0.184	0.235	0.276	0.309
October	0.052	0.067	0.095	0.134	0.171	0.197	0.219
November	0.049	0.058	0.071	0.095	0.117	0.130	0.142
December	0.041	0.051	0.072	0.108	0.137	0.156	0.172
Spring	0.073	0.090	0.122	0.174	0.224	0.266	0.298
Summer	0.063	0.081	0.119	0.173	0.230	0.284	0.328
Autumn	0.061	0.077	0.105	0.146	0.186	0.215	0.240
Winter	0.046	0.057	0.079	0.117	0.149	0.171	0.189
All	**0.062**	**0.078**	**0.108**	**0.155**	**0.200**	**0.238**	**0.269**

Table B.2: AERONET: monthly and seasonal mean values of Ångström exponents.

	κ(**532 nm / 340 nm**)	κ(**1020 nm / 532 nm**)	κ(**675 nm / 440 nm**)
January	1.052	1.550	1.523
February	1.092	1.310	1.435
March	1.192	1.351	1.461
April	1.166	1.350	1.402
May	1.302	1.221	1.377
June	1.382	1.455	1.488
July	1.468	1.572	1.548
August	1.546	1.701	1.619
September	1.258	1.391	1.393
October	1.126	1.485	1.400
November	0.887	1.021	1.172
December	1.036	1.508	1.517
Spring	1.220	1.307	1.413
Summer	1.458	1.565	1.546
Autumn	1.131	1.355	1.352
Winter	1.066	1.434	1.483
All	**1.228**	**1.413**	**1.448**

Table B.3: MODIS: monthly and seasonal mean values of AOD and Ångström exponent.

	AOD(660 nm)	**AOD(532 nm)**	**AOD(480 nm)**	**κ(660 nm / 480 nm)**
January	0.080	0.097	0.109	0.911
February	0.133	0.161	0.180	0.860
March	0.173	0.208	0.231	0.811
April	0.150	0.189	0.217	1.058
May	0.144	0.179	0.202	1.000
June	0.188	0.229	0.256	0.928
July	0.162	0.193	0.213	0.813
August	0.107	0.133	0.151	1.058
September	0.108	0.139	0.161	1.198
October	0.084	0.107	0.122	1.149
November	0.016	0.029	0.022	0.860
December	0.038	0.045	0.050	0.808
Spring	0.156	0.192	0.217	0.957
Summer	0.152	0.185	0.207	0.933
Autumn	0.074	0.104	0.109	1.111
Winter	0.103	0.125	0.140	0.860
All	**0.126**	**0.159**	**0.174**	**0.976**

Table B.4: MULIS: monthly and seasonal mean values of AOD and Ångström exponents; κ(1064 nm / 532 nm) = κ(R / G), κ(532 nm / 355 nm) = κ(G / B).

	AOD(1064nm)	**AOD(532nm)**	**AOD(355nm)**	κ**(R / G)**	κ**(G / B)**
January	0.023	0.058	0.102	1.309	1.535
February	0.011	0.055	0.125	1.360	2.250
March	0.016	0.181	0.293	1.699	1.648
April	0.080	0.176	0.323	1.408	1.664
May	0.058	0.162	0.240	1.338	1.370
June	0.056	0.144	0.271	1.387	1.716
July	0.058	0.141	0.265	1.322	1.674
August	0.049	0.131	0.256	1.470	1.811
September	0.048	0.123	0.241	1.386	1.783
October	0.060	0.109	0.200	1.131	1.838
November	0.017	0.040	0.080	1.336	2.195
December	0.015	0.061	0.093	1.548	1.845
Spring	0.068	0.172	0.291	1.420	1.564
Summer	0.054	0.137	0.262	1.399	1.746
Autumn	0.046	0.101	0.194	1.283	1.886
Winter	0.016	0.058	0.106	1.422	1.876
All	**0.051**	**0.127**	**0.233**	**1.367**	**1.755**

Table B.5: CALIPSO: monthly and seasonal mean values of AOD and Ångström exponents.

	AOD(1064 nm)	**AOD(532 nm)**	κ**(1064 nm / 532 nm)**
January	0.012	0.077	1.934
February	0.035	0.083	1.649
March	0.021	0.047	1.114
April	0.037	0.090	1.143
May	0.051	0.075	0.691
June	0.071	0.167	1.188
July	0.059	0.095	0.611
August	0.077	0.096	0.908
September	0.032	0.068	0.909
October	0.017	0.051	1.341
November	0.035	0.055	1.298
December	0.016	0.023	1.731
Spring	0.038	0.074	0.989
Summer	0.069	0.116	0.883
Autumn	0.026	0.058	1.159
Winter	0.020	0.055	1.762
All	**0.041**	**0.079**	**1.131**

Appendix C

Error calculation of Ångström exponent

The error of the Ångström exponent is directly related to the errors of the corresponding extinction coefficients. Here the derivation of the relation between the errors is shown.

From Eq. 2.8 the Ångström exponent κ of wavelenghts λ_1 and λ_2 can be written as:

$$\kappa = c \cdot \ln \frac{\alpha_1}{\alpha_2};\ c \equiv -\frac{1}{ln\frac{\lambda_1}{\lambda_2}} \tag{C.1}$$

According to the Gaussian propagation of uncertainties, the error σ_κ of the Ångström exponent κ can be calculated from the the extinction coefficients α_1 and α_2 and their corresponding errors σ_α.

$$\sigma_\kappa = \sqrt{\left(\frac{\partial \kappa}{\partial \alpha_1}\right)^2 \sigma_{\alpha_1}^2 + \left(\frac{\partial \kappa}{\partial \alpha_2}\right)^2 \sigma_{\alpha_2}^2}$$

Using the derivations from Eq. C.1

$$\frac{\partial \kappa}{\partial \alpha_1} = -c\frac{1}{\alpha_1} \text{ and } \frac{\partial \kappa}{\partial \alpha_2} = -c\frac{1}{\alpha_2}$$

which leads to:

$$\Rightarrow \sigma_\kappa = |c| \sqrt{\left(\frac{\sigma_{\alpha_1}}{\alpha_1}\right)^2 + \left(\frac{\sigma_{\alpha_2}}{\alpha_2}\right)^2}$$

Assuming that the relative errors of the two extinction coefficients are of the same order of size $\frac{\sigma_{\alpha_1}}{\alpha_1} \simeq \frac{\sigma_{\alpha_2}}{\alpha_2}$, the relative error of the Ångström exponent $\frac{\sigma_\kappa}{\kappa}$ can be expressed by relative error of the extinction coefficient multiplied by a factor f:

$$\frac{\sigma_\kappa}{\kappa} = \frac{\sqrt{2}\,|c|}{\kappa}\frac{\sigma_\alpha}{\alpha} = f\frac{\sigma_\alpha}{\alpha}$$

So the error of the Ångström exponent κ depends not only on the error in the extinction but also on the factor f, in which the dependency on the wavelengths as well as on the absolute value of κ is noted:

Table C.1: Factor f for three different wavelength pairs and three different Ångström exponents.

	$f(\frac{1064nm}{532nm})$	$f(\frac{675nm}{440nm})$	$f(\frac{660nm}{470nm})$
$\kappa = 1.4$	1.4	2.4	3.0
$\kappa = 1.0$	2	3.3	4.2
$\kappa = 0.5$	4.1	6.6	8.3

$$f \equiv \frac{\sqrt{2}\,|c|}{\kappa} = \left| \frac{\sqrt{2}}{\kappa \ln \frac{\lambda_1}{\lambda_2}} \right|.$$

In Table C.1 some examples are listed to show the influence of factor f: obviously the factor – and therefor the error of κ – is increasing with decreasing Ångström exponents. Also, the smaller the difference between the both wavelengths, the stronger is the error of the Ångström exponent.

List of Abbreviations

AERONET	Aerosol Robotic Network
AL	Aerosol Layer data
AP	Aerosol Profile data
AOD	Aeorosol Optical Depth
AT	Aerosol Type
BLB	Beer's law = Lambert-Beer law or law of Beer-Lambert-Bouguer
CALIOP	Cloud-Aerosol Lidar with Orthogonal Polarization
CALIPSO	Cloud-Aerosol Lidar and Infrared Pathfinder Satellite Observation
CP	Cloud Profile data
EARLINET	European Aerosol Research Lidar Network
EL	Elevated layer
EM	Electromagnetic
FOD	Feature Optical Depth (used in CALIPSO algorithms)
FT	Feature Type
GMAO	Global Modeling and Assimilation Office
HERA	Hybrid Extinction Retrieval Algorithms
L1B	Level 1B data
L2	Level 2 data
LIDAR	Light Detection and Ranging
LOD	'Lost' Optical Depth: optical depth of layers detected by MULIS but missed by CALIPSO

MIM	Meteorological Institute Munich
MODIS	MODerate resolution Imaging Spectroradiometer
MULIS	Multiple wavelength Lidar System
NASA	National Aeronautics and Space Administration
Nd:YAG	Neodym-doped Yttrium Aluminium Garnet
OPAC	Optical Properties of Aerosols and Clouds
PBL	Planetary Boundary Layer
SCA	Scene Classification Algorithms
SIBYL	Selective Iterated Boundary Locator
SNR	Signal-to-Noise Ratio
UTC	Universal Time Coordinated
VFM	Vertical Feature Mask

Bibliography

V. Amiridis, D. S. Balis, E. Giannakaki, A. Stohl, S. Kazadzis, M. E. Koukouli, and P. Zanis. Optical characteristics of biomass burning aerosols over southeastern europe determined from uv-raman lidar measurements. *Atmospheric Chemistry and Physics*, 9(7): 2431–2440, 2009. doi: 10.5194/acp-9-2431-2009. URL `http://www.atmos-chem-phys.net/9/2431/2009/`.

A. Ansmann, U. Wandinger, M. Riebesell, C. Weitkamp, and W. Michaelis. Independent measurement of extinction and backscatter profiles in cirrus clouds by using a combined raman elastic-backscatter lidar. *Applied Optics*, 31(33):7113–7113, Nov 1992. doi: 10.1364/AO.31.007113. URL `http://ao.osa.org/abstract.cfm?URI=ao-31-33-7113`.

A. Ansmann, H. Baars, M. Tesche, D. Müller, D. Althausen, R. Engelmann, T. Pauliquevis, and P. Artaxo. Dust and smoke transport from africa to south america: Lidar profiling over cape verde and the amazon rainforest. *Geophysical Research Letters*, 36:L11802, 2009. doi: 10.1029/2009GL037923.

A. Ansmann, M. Tesche, V. Groß, S. Freudenthaler, P. Seifert, A. Hiebsch, J. Schmidt, U. Wandinger, I. Mattis, D. Müller, and M. Wiegner. The 16 april 2010 major volcanic ash plume over central europe: Earlinet lidar and aeronet photometer observations at leipzig and munich, germany. *Geophysical Research Letters*, 37:5, 2010. doi: 10.1029/2010GL043809.

R. Arimoto, Y.J. Kim, Y.P. Kim, P.K. Quinn, T.S. Bates, T.L. Anderson, S. Gong, I. Uno, M. Chin, B.J. Huebert, A.D. Clarke, Y. Shinozuka, R.J. Weber, J.R. Anderson, S.A. Guazzotti, and Sodeman D.A. Sullivan, R.C., K.A. Prather, and I.N. Sokolik. Characterization of asian dust during ace-asia. *Global and Planetary Change*, 52:23–56, 2006.

A. John Arnfield. Two decades of urban climate research: a review of turbulence, exchanges of energy and water, and the urban heat island. *International Journal of Climatology*, 23(1):1–26, 2003. ISSN 1097-0088. doi: 10.1002/joc.859. URL `http://dx.doi.org/10.1002/joc.859`.

A. Arola, A. Lindfors, A. Natunen, and K. E. J. Lehtinen. A case study on biomass burning aerosols: effects on aerosol optical properties and surface radiation levels. *Atmospheric Chemistry and Physics*, 7(16):4257–4266, 2007. doi: 10.5194/acp-7-4257-2007. URL `http://www.atmos-chem-phys.net/7/4257/2007/`.

D. S. Balis, V. Amiridis, S. Nickovic, A. Papayannis, and C. Zerefos. Optical properties of saharan dust layers as detected by a raman lidar at thessaloniki, greece. *Geophysical Research Letters*, 31:L13104, 2004. doi: 10.1029/2004GL019881.

D.S. Balis, V. Amiridis, C. Zerefos, E. Gerasopoulos, M. Andreae, P. Zanis, A. Kazantzidis, S. Kazadzis, and A. Papayannis. Raman lidar and sunphotometric measurements of aerosol optical properties over thessaloniki, greece during a biomass burning episode. *Atmospheric Environment*, 37(32):4529 – 4538, 2003. ISSN 1352-2310. doi: http://dx.doi.org/10.1016/S1352-2310(03)00581-8. URL http://www.sciencedirect.com/science/article/pii/S1352231003005818.

F. Barnaba, F. Angelini, G. Curci, and G. P. Gobbi. An important fingerprint of wildfires on the european aerosol load. *Atmospheric Chemistry and Physics*, 11(20):10487–10501, 2011. doi: 10.5194/acp-11-10487-2011. URL http://www.atmos-chem-phys.net/11/10487/2011/.

S. Basart, C. Pérez, S. Nickovic, E. Cuevas, and J. Baldasano. Development and evaluation of the bsc-dream8b dust regional model over northern africa, the mediterranean and the middle east. *Tellus B*, 64, 2012.

A. Behrendt and T. Nakamura. Calculation of the calibration constant of polarization lidar and its dependency on atmospheric temperature. *Opt. Express*, 10(16):805–817, Aug 2002. URL http://www.opticsexpress.org/abstract.cfm?URI=oe-10-16-805.

J. Biele, G. Beyerle, and G. Baumgarten. Polarization lidar: Correction of instrumental effects. *Opt. Express*, 7(12):427–435, Dec 2000. doi: 10.1364/OE.7.000427. URL http://www.opticsexpress.org/abstract.cfm?URI=oe-7-12-427.

J. Boesenberg. Earlinet : a european aerosol research lidar network to establish an aerosol climatology. *Max-Planck-Institut fuer Meteorologie, Hamburg*, Report 248, 2003.

A. Bovchaliuk, G. Milinevsky, V. Danylevsky, P. Goloub, O. Dubovik, A. Holdak, F. Ducos, and M. Sosonkin. Variability of aerosol properties over eastern europe observed from ground and satellites in the period from 2003 to 2011. *Atmospheric Chemistry and Physics Discussions*, 13(1):2641–2670, 2013. doi: 10.5194/acpd-13-2641-2013. URL http://www.atmos-chem-phys-discuss.net/13/2641/2013/.

Arika Bridhikitti. Atmospheric aerosol layers over bangkok metropolitan region from {CALIPSO} observations. *Atmospheric Research*, 127(0):1 – 7, 2013. ISSN 0169-8095. doi: http://dx.doi.org/10.1016/j.atmosres.2013.02.008. URL http://www.sciencedirect.com/science/article/pii/S0169809513000690.

B. Brunekreef and S. Holgate. Air pollution and health. *The lancet*, 360(9341):1233–1242, 2002.

E. Buijsman and F. De Leeuw. Pm10 measurement results and correction factors in airbase. Technical report, European Topic Centre on Air and Climate Change, Bilthoven, 2004.

P. Chazette, J.-C. Raut, F. Dulac, S. Berthier, S.-W. Kim, P. Royer, J. Sanak, S. Loaëc, and H. Grigaut-Desbrosses. Simultaneous observations of lower tropospheric continental aerosols with a ground-based, an airborne, and the spaceborne caliop lidar system. *Journal of Geophysical Research: Atmospheres*, 115(D4):n/a–n/a, 2010. ISSN 2156-2202. doi: 10.1029/2009JD012341. URL `http://dx.doi.org/10.1029/2009JD012341`.

M. Chin, P. Ginoux, S. Kinne, B. N. Holben, B. N. Duncan, R. V. Martin, J. A. Logan, A. Higurashi, and T. Nakajima. Tropospheric aerosol optical thickness from the gocart model and comparisons with satellite and sunphotometer measurements. *Journal of Atmospheric Sience*, 59:461–483, 2002.

N. Y. Chubarova. Seasonal distribution of aerosol properties over europe and their impact on uv irradiance. *Atmospheric Measurement Techniques Discussions*, 2(4):1863–1899, 2009. doi: 10.5194/amtd-2-1863-2009. URL `http://www.atmos-meas-tech-discuss.net/2/1863/2009/`.

L. Costantino and F.-M. Bréon. Aerosol indirect effect on warm clouds over south-east atlantic, from co-located modis and calipso observations. *Atmospheric Chemistry and Physics*, 13(1):69–88, 2013. doi: 10.5194/acp-13-69-2013. URL `http://www.atmos-chem-phys.net/13/69/2013/`.

P.-Y. Deschamps, F.-M. Breon, M. Leroy, A. Podaire, A. Bricaud, J.-C. Buriez, and G. Seze. The polder mission: instrument characteristics and scientific objectives. *Geoscience and Remote Sensing, IEEE Transactions on*, 32(3):598–615, 1994. ISSN 0196-2892. doi: 10.1109/36.297978.

M. Di Pierro, L. Jaeglé, E. W. Eloranta, and S. Sharma. Spatial and seasonal distribution of arctic aerosols observed by the caliop satellite instrument (2006-2012). *Atmospheric Chemistry and Physics*, 13(14):7075–7095, 2013. doi: 10.5194/acp-13-7075-2013. URL `http://www.atmos-chem-phys.net/13/7075/2013/`.

D.J. Diner, J.C. Beckert, T.H. Reilly, C.J. Bruegge, J.E. Conel, R.A. Kahn, J.V. Martonchik, T.P. Ackerman, R. Davies, S.A.W. Gerstl, H.R. Gordon, J.-P. Muller, R.B. Myneni, P.J. Sellers, B. Pinty, and M.M. Verstraete. Multi-angle imaging spectroradiometer (misr) instrument description and experiment overview. *Geoscience and Remote Sensing, IEEE Transactions on*, 36(4):1072 –1087, jul 1998. ISSN 0196-2892. doi: 10.1109/36.700992.

R. R. Draxler and G. D. Rolph. Hysplit (hybrid single particle lagrangian integrated trajectory) model. *NOAA Air Resources Laboratory, Silver Spring, MD*, 2012. URL `http://ready.arl.noaa.gov/HYSPLIT.php`.

M. Endemann, P. Dubock, P. Ingmann, R. Wimmer, D. Morancais, and D. Demuth. The adm-aeolus mission-the first wind-lidar in space. In *22nd Internation Laser Radar Conference (ILRC 2004)*, volume 561, page 953, 2004.

H. Flentje, B. Heese, J. Reichardt, and W. Thomas. Aerosol profiling using the ceilometer network of the german meteorological service. *Atmospheric Measurement Techniques Discussions*, 3(4):3643–3673, 2010. doi: 10.5194/amtd-3-3643-2010. URL `http://www.atmos-meas-tech-discuss.net/3/3643/2010/`.

V. Freudenthaler, M. Esselborn, M. Wiegner, B. Heese, M. Tesche, A. Ansmann, D. Müller, D. Althause, M. Wirth, A. Fix, G. Ehret, P. Knippertz, C. Toledano, J. Gasteiger, M. Garhammer, and M. Seefeldner. Depolarization ratio profiling at several wavelengths in pure saharan dust during samum 2006. *Tellus B*, 61:165–179, 2009.

J. Gasteiger, S. Groß, V. Freudenthaler, and M. Wiegner. Volcanic ash from iceland over munich: mass concentration retrieved from ground-based remote sensing measurements. *Atmospheric Chemistry and Physics*, 11(5):2209–2223, 2011. doi: 10.5194/acp-11-2209-2011. URL `http://www.atmos-chem-phys.net/11/2209/2011/`.

L. Giglio, J. Descloitres, J.O. Justice, and Y.J. Kaufman. An enhanced contextual fire detection algorithm for modis. *Remote Sensing of Environment*, 87(2-3):273 – 282, 2003. ISSN 0034-4257. doi: 10.1016/S0034-4257(03)00184-6. URL `http://www.sciencedirect.com/science/article/B6V6V-49S6Y33-1/2/976f699aa7ebeb9b867cda782a0816d1`.

A. Gosewisch. Beitrag zu einer aerosolklimatologie für münchen auf basis von aeronet-daten und hysplit-clusteranalyse. Master's thesis, Meteorological Institute Munich, LMU, 2013.

S. Groß. *Aerosol characterization by multi-wavelength Raman- and depolarization lidar observations*. PhD thesis, Ludwig-Maximilians-Universität München, 2011.

S. Groß, J. Gasteiger, V. Freudenthaler, F. Schnell, and M. Wiegner. Characterization of the eyjafjallajökull ash-plume by means of lidar measurements over the munich earlinet-site. *Proc. of SPIE Vol. 7832-20, Toulouse, France, 20-23 September 2010*, 2010.

S. Groß, M. Tesche, V. Freudenthaler, C. Toledano, M. Wiegner, A. Ansmann, D. Althausen, and M. Seefeldner. Characterization of saharan dust, marine aerosols and mixtures of biomass burning aerosols and dust by means of multi-wavelength depolarization- and raman-measurments during samum-2. *Tellus*, B63:706 – 724, 2011. doi: 10.1111/j.1600-0889.2011.00556.x. Tellus B63.

P. Hausmann. Ground-based remote sensing of optically thin ice clouds. Master's thesis, Meteorological Institute Munich, LMU, 2012.

J. Haywood and O. Boucher. Estimates of the direct and indirect radiative forcing due to tropospheric aerosols: a review. *Rev. of Geophysics*, 38:513–543, 2000.

J. Heintzenberg. The samum–1 experiment over southern morocco: overview and introduction. *Tellus*, B 61, 2009. doi: 10.1111/j.1600-0889.2008.00403.x.

A. Heliere, A. Lefebvre, T. Wehr, J. Bezy, and Yannig Durand. The earthcare mission: Mission concept and lidar instrument pre-development. In *Geoscience and Remote Sensing Symposium, 2007. IGARSS 2007. IEEE International*, pages 4975–4978, July 2007. doi: 10.1109/IGARSS.2007.4423978.

M. Hess, P. Köpke, and I. Schult. Optical properties of aerosols and clouds: The software package opac. *Bulletin of American Meteorological Society*, 1998.

A. Hiebsch, U. Wandinger, I. Mattis, A. Ansmann, G. Pappalardo, L. Mona, F. Madonna, G. D'Amico, A. Giunta, H. Linné, et al. Long-term aerosol and cloud database from correlative earlinet-calipso observations. In *Proceedings of the 25th International Laser Radar Conference, this volume*, 2010.

B.N. Holben, T.F. Eck, I. Slutsker, D. Tanré, J.P. Buis, A. Setzer, E. Vermote, J.A. Reagan, Y.J. Kaufman, T. Nakajima, F. Lavenu, I. Jankowiak, and A. Smirnov. Aeronet–a federated instrument network and data archive for aerosol characterization. *Remote Sensing of Environment*, 66(1):1 – 16, 1998. ISSN 0034-4257. doi: 10.1016/S0034-4257(98)00031-5. URL `http://www.sciencedirect.com/science/article/B6V6V-3V7SF8D-1D/2/7452854b09ed6f6d885f0aa14ac67ed6`.

C. Hostetler, John Reagan Liu, Z., M. Vaughan, M. Osborn, W. H. Hunt, K. A. Powell, and C. Trepte. Caliop algorithm theoretical basis document: Calibration and level 1 data products; pc-sci-201. Technical report, NASA, 2006.

N.C. Hsu, Si-Chee Tsay, M.D. King, and J.R. Herman. Aerosol properties over bright-reflecting source regions. *Geoscience and Remote Sensing, IEEE Transactions on*, 42 (3):557–569, 2004. ISSN 0196-2892. doi: 10.1109/TGRS.2004.824067.

L. Huang, J. H. Jiang, J. L. Tackett, H. Su, and R. Fu. Seasonal and diurnal variations of aerosol extinction profile and type distribution from calipso 5-year observations. *Journal of Geophysical Research: Atmospheres*, 118(10):4572–4596, 2013. ISSN 2169-8996. doi: 10.1002/jgrd.50407. URL `http://dx.doi.org/10.1002/jgrd.50407`.

M. Kacenelenbogen, M. A. Vaughan, J. Redemann, R. M. Hoff, R. R. Rogers, R. A. Ferrare, P. B. Russell, C. A. Hostetler, J. W. Hair, and B. N. Holben. An accuracy assessment of the caliop/calipso version 2/version 3 daytime aerosol extinction product based on a detailed multi-sensor, multi-platform case study. *Atmospheric Chemistry and Physics*, 11(8):3981–4000, 2011. doi: 10.5194/acp-11-3981-2011. URL `http://www.atmos-chem-phys.net/11/3981/2011/`.

C. Kiemle, M. Quatrevalet, G. Ehret, A. Amediek, A. Fix, and M. Wirth. Sensitivity studies for a space-based methane lidar mission. *Atmospheric Measurement Techniques*

Discussions, 4(3):3545–3592, 2011. doi: 10.5194/amtd-4-3545-2011. URL http://www.atmos-meas-tech-discuss.net/4/3545/2011/.

S. Kinne, U. Lohmann, J. Feichter, M. Schulz, C. Timmreck, S. Ghan, R. Easter, M. Chin, P. Ginoux, T. Takemura, I. Tegen, D. Koch, M. Herzog, J. Penner, G. Pitari, B. Holben, T. Eck, A. Smirnov, O. Dubovik, I. Slutsker, D. Tanre, O. Torres, M. Mishchenko, I. Geogdzhayev, D. A. Chu, and Y. Kaufman. Monthly averages of aerosol properties: A global comparison among models, satellite data, and aeronet ground data. *Journal of Geophysical Research: Atmospheres*, 108(D20):n/a–n/a, 2003. ISSN 2156-2202. doi: 10.1029/2001JD001253. URL http://dx.doi.org/10.1029/2001JD001253.

James D. Klett. Lidar inversion with variable backscatter/extinction ratios. *Applied Optics*, 24(11):1638–1643, Jun 1985. doi: 10.1364/AO.24.001638. URL http://ao.osa.org/abstract.cfm?URI=ao-24-11-1638.

R.B.A. Koelemeijer, C.D. Homan, and J. Matthijsen. Comparison of spatial and temporal variations of aerosol optical thickness and particulate matter over europe. *Atmospheric Environment*, 40(27):5304 – 5315, 2006. ISSN 1352-2310. doi: http://dx.doi.org/10.1016/j.atmosenv.2006.04.044. URL http://www.sciencedirect.com/science/article/pii/S1352231006004183.

A. Kokhanovsky and G. de Leeuw. *Satellite Aerosol Remote Sensing Over Land*. Springer, 2009.

P Kollias, E.E. Clothiaux, M.A. Miller, B.A. Albrecht, G.L. Stephens, and T.P. Ackerman. Millimeter-wavelength radars: New frontier in atmospheric cloud and precipitation research. *Bulletin of the American Meteorological Society*, 88(10):1608–1624, 2007.

P. Köpke and M. Sachweh. *Satellitenmeteorologie*. UTB GmbH, 2012.

P.F. Levelt, G. H. J. Van den Oord, M.R. Dobber, A. Malkki, H. Visser, J. de Vries, P. Stammes, J.O.V. Lundell, and H. Saari. The ozone monitoring instrument. *Geoscience and Remote Sensing, IEEE Transactions on*, 44(5):1093–1101, 2006. ISSN 0196-2892. doi: 10.1109/TGRS.2006.872333.

T. Lillesand, R.W. Kiefer, and J. Chipman. *Remote Sensing and Image Interpretation*. Wiley, 2007.

U. Lohmann and J. Feichter. Global indirect aerosol effects: a review. *Atmospheric Chemistry and Physics*, 5(3):715–737, 2005. doi: 10.5194/acp-5-715-2005. URL http://www.atmos-chem-phys.net/5/715/2005/.

V. Matthias, D. Balis, J. Bösenberg, R. Eixmann, M. Iarlori, L. Komguem, I. Mattis, A. Papayannis, G. Pappalardo, M. R. Perrone, and X. Wang. Vertical aerosol distribution over europe: Statistical analysis of raman lidar data from 10 european aerosol research lidar network (earlinet) stations. *Journal of Geophysical Research: Atmospheres (1984–2012)*, 109(D18), 2004.

I. Mattis, A. Ansmann, D. Müller, U. Wandinger, and D. Althausen. Multiyear aerosol observations with dualwavelength raman lidar in the framework of earlinet. *Journal of Geophysical Research*, 109:D13203, 2004. doi: 10.1029/2004JD004600.

I. Mattis, L. Mona, D. Müller, G. Pappalardo, L. Alados-Arboledas, G. D'Amico, A. Amodeo, A. Apituley, J. Baldasano, C. Böckmann, J. Bösenberg, A. Chaikovsky, A. Comeron, E. Giannakaki, I. Grigorov, Guerrero R., O. Gustafsson, M. Iarlori, H. Linne, V. Mitev, F. Molero Menendez, D. Nicolae, A. Papayannis, C. Garcia-Pando, M. Perrone, A. Pietruczuk, J. Putaud, F. Ravetta, A. Rodríguez, P. Seifert, M. Sicard, V. Simeonov, P. Sobolewski, N. Spinelli, K. Stebel, A. Stohl, M. Tesche, T. Trickl, X. Wang, and M. Wiegner. Earlinet correlative measurements for calipso. volume 6750, pages 67500Z–67500Z–12, 2007. doi: 10.1117/12.738090. URL `http://dx.doi.org/10.1117/12.738090`.

I. Mattis, D. Müller, A. Ansmann, U. Wandinger, J. Preißler, P. Seifert, and M. Tesche. Ten years of multiwavelength raman lidar observations of free-tropospheric aerosol layers over central europe: Geometrical properties and annual cycle. *Journal of Geophysical Research: Atmospheres*, 113(D20), 2008. ISSN 2156-2202. doi: 10.1029/2007JD009636. URL `http://dx.doi.org/10.1029/2007JD009636`.

I. Mattis, P. Seifert, D. Müller, M. Tesche., A. Hiebsch, T. Kanitz, J. Schmidt, F. Finger, U. Wandinger, and A. Ansmann. Volcanic aerosol layers observed with multiwavelength raman lidar over central europe in 2008-2009. *Journal of Geophysical Research*, 115: D00L04, 2010.

B. Mayer and A. Kylling. Technical note: The libradtran software package for radiative transfer calculations - description and examples of use. *Atmospheric Chemistry and Physics*, 5(7):1855–1877, 2005. doi: 10.5194/acp-5-1855-2005. URL `http://www.atmos-chem-phys.net/5/1855/2005/`.

R. A. McCormick and J. H. Ludwig. Climate modification by atmospheric aerosols. *Science*, 156(3780):1358–1359, 1967. doi: 10.1126/science.156.3780.1358. URL `http://www.sciencemag.org/content/156/3780/1358.abstract`.

E. L. McGrath-Spangler and A. S. Denning. Global seasonal variations of midday planetary boundary layer depth from calipso space-borne lidar. *Journal of Geophysical Research: Atmospheres*, 118(3):1226–1233, 2013. ISSN 2169-8996. doi: 10.1002/jgrd.50198. URL `http://dx.doi.org/10.1002/jgrd.50198`.

A. Molod, L. Takacs, M. Suarez, J. Bacmeister, I. Song, and A. Eichmann. The geos-5 atmospheric general circulation model: Mean climate and development from merra to fortuna. *Technical Report Series on Global Modeling and Data Assimilation*, 28, 2012.

L. Mona, G. Pappalardo, A. Amodeo, G. D'Amico, F. Madonna, A. Boselli, A. Giunta, F. Russo, and V. Cuomo. One year of cnr-imaa multi-wavelength raman lidar measurements in coincidence with calipso overpasses: Level 1 products comparison. *Atmospheric*

Chemistry and Physics, 9(18):7213–7228, 2009. doi: 10.5194/acp-9-7213-2009. URL http://www.atmos-chem-phys.net/9/7213/2009/.

A. H. Omar, D. M. Winker, J. L. Tackett, D. M. Giles, J. Kar, Z. Liu, M. A. Vaughan, K. A. Powell, and C. R. Trepte. Caliop and aeronet aerosol optical depth comparisons: One size fits none. *Journal of Geophysical Research: Atmospheres*, 118(10):4748–4766, 2013. ISSN 2169-8996. doi: 10.1002/jgrd.50330. URL http://dx.doi.org/10.1002/jgrd.50330.

A.H. Omar, D.M. Winker, C. Kittaka, M.A. Vaughan, Z. Liu, Y. Hu, C.R. Trepte, R.R. Rogers, R.A. Ferrare, K.P. Lee, R.E. Kuehn, and C.A. Hostetler. The calipso automated aerosol classification and lidar ratio selection algorithm. *Journal of Atmospheric Oceanic Technologie*, 26:1994–2014, 2009. doi: http://dx.doi.org/10.1175/2009JTECHA1231.1.

A. Papayannis, V. Amiridis, L. Mona, and G. Tsaknakis et al. Systematic lidar observations of saharan dust over europe in the frame of earlinet (2000-2002). *Geophysical Research Letters*, 113:D10204, 2008.

G. Pappalardo. European aerosol research lidar network-advanced sustainable observation system (earlinet-asos). In *14th International School on Quantum Electronics: Laser Physics and Applications*, pages 66041Y–66041Y. International Society for Optics and Photonics, 2007.

G. Pappalardo, L. Mona, G. D'Amico, U. Wandinger, M. Adam, A. Amodeo, A. Ansmann, A. Apituley, Alados Arboledas, L., D. Balis, et al. Four-dimensional distribution of the 2010 eyjafjallajökull volcanic cloud over europe observed by earlinet. *Atmospheric Chemistry & Physics*, 13(8), 2013.

C. Perez, S. Nickovic, J. M. Baldasano, M. Sicard, F. Rocadenbosch, and V. E. Cachorro. A long saharan dust event over the western mediterranean: Lidar, sun photometer observations, and regional dust modeling. *Journal of Geophysical Research: Atmospheres*, 111(D15), 2006. ISSN 2156-2202. doi: 10.1029/2005JD006579. URL http://dx.doi.org/10.1029/2005JD006579.

G. W. Petty. *A First Course in Atmospheric Radiation*. Sundog Publishing, 2006.

K. Powell, Lee K.P. Mark Vaughan, David Winker, M. Pitts, C. Trepte, P. Detweiler, W. Hunt, J. Lambeth, P. Lucker, T. Murray, O. Hagolle, A. Lifermann, M. Faivre, A. Garnier, and J. Pelon. Data management systems data products catalog. Technical report, Document No: PC-SCI-503, 2013.

J. Preißler, F. Wagner, Pereira S. N., and J. L. Guerrero-Rascado. Multi-instrumental observation of an exceptionally strong saharan dust outbreak over portugal. *Journal of Geophysical Research*, 116:D24204, 2011. doi: 10.1029/2011JD016527.

J. Preißler, F. Wagner, J. L. Guerrero-Rascado, and A. M. Silva. Two years of free-tropospheric aerosol layers observed over portugal by lidar. *Journal of Geophysical Research: Atmospheres*, 118(9):3676–3686, 2013. ISSN 2169-8996. doi: 10.1002/jgrd.50350. URL `http://dx.doi.org/10.1002/jgrd.50350`.

J. Redemann, M. A. Vaughan, Q. Zhang, Y. Shinozuka, P. B. Russell, J. M. Livingston, M. Kacenelenbogen, and L. A. Remer. The comparison of modis-aqua (c5) and caliop (v2 & v3) aerosol optical depth. *Atmospheric Chemistry and Physics*, 12(6):3025–3043, 2012. doi: 10.5194/acp-12-3025-2012. URL `http://www.atmos-chem-phys.net/12/3025/2012/`.

L. A. Remer, Y. J. Kaufman, D. Tanré, S. Mattoo, D. A. Chu, J. V. Martins, R.-R. Li, C. Ichoku, R. C. Levy, R. G. Kleidman, T. F. Eck, E. Vermote, and B. N. Holben. The modis aerosol algorithm, products, and validation. *J. Atmos. Sci.*, 62(4):947–973, April 2005. ISSN 0022-4928. doi: 10.1175/JAS3385.1. URL `http://dx.doi.org/10.1175/JAS3385.1`.

E. Roeckner. *The atmospheric general circulation model ECHAM-4: Model description and simulation of present-day climate*. Max-Planck-Institut fürr Meteorologie, 1996.

V.V. Salomonson, W. Barnes, P.W. Maymon, H.E. Montgomery, and H. Ostrow. Modis: advanced facility instrument for studies of the earth as a system. *Geoscience and Remote Sensing, IEEE Transactions on*, 27(2):145–153, 1989. ISSN 0196-2892. doi: 10.1109/36.20292.

S.K. Satheesh and K. Krishna Moorthy. Radiative effects of natural aerosols: A review. *Atmospheric Environment*, 39(11):2089 – 2110, 2005. ISSN 1352-2310. doi: 10.1016/j.atmosenv.2004.12.029. URL `http://www.sciencedirect.com/science/article/B6VH3-4FJGWDS-3/2/82028899d671058f9a9e50dbd991a0fc`.

F. Schnell, M. Wiegner, and V. Freudenthaler. Calipso validation measurements with the raman lidar mulis in maisach, germany. In *Proceedings of the 25th International Laser Radar Conference, 5-9 July 2010, St.-Petersburg, Russia*, 2010.

P. J. Sheridan, E. Andrews, J. A. Ogren, J. L. Tackett, and D. M. Winker. Vertical profiles of aerosol optical properties over central illinois and comparison with surface and satellite measurements. *Atmospheric Chemistry and Physics*, 12(23):11695–11721, 2012. doi: 10.5194/acp-12-11695-2012. URL `http://www.atmos-chem-phys.net/12/11695/2012/`.

T.F. Stocker, D. Qin, G.-K. Plattner, M. Tignor, S. K. Allen, J. Boschung, A. Nauels, Y. Xia, V. Bex, and P.M. Midgley, editors. *IPCC, 2013: Summary for Policymakers. In: Climate Change 2013: The Physical Science Basis. Contribution of Working Group I to the Fifth Assessment Report of the Intergovernmental Panel on Climate Change*. Cambridge University Press, Cambridge, United Kingdom and New York, NY, USA, 2013.

A. Stohl, C. Forster, A. Frank, P. Seibert, and G. Wotawa. Technical note : The lagrangian particle dispersion model flexpart version 6.2. *Atmopheric Chemistry and Physics*, 5: 2461–2474, 2005.

R. B. Stull. *An Introduction to Boundary Layer Meteorology*. Springer, 1988.

T Takamura and T Nakajima. Skynet community group, 2004. overview of skynet and its activities. In *Proceedings of AERONET workshop, El Arenosillo. Optica Pura y Aplicada*, volume 37, pages 3303–3308, 2004.

S. Twomey. Aerosols, clouds and radiation. *Atmospheric Environment. Part A. General Topics*, 25(11):2435 – 2442, 1991. ISSN 0960-1686. doi: 10.1016/0960-1686(91)90159-5. URL http://www.sciencedirect.com/science/article/B757D-48CGBBT-PV/2/ed9ec503fffde5334b71dc9b59c7988b. Symposium on Global Climatic Effects of Aerosols.

T. Várnai and A. Marshak. Analysis of co-located modis and calipso observations near clouds. *Atmospheric Measurement Techniques Discussions*, 4(6):6861–6881, 2011. doi: 10.5194/amtd-4-6861-2011. URL http://www.atmos-meas-tech-discuss.net/4/6861/2011/.

M. Vaughan. Tilt mode geometry. Technical report, Atmospheric Science Data Center, 2008. URL https://eosweb.larc.nasa.gov/sites/default/files/project/calipso/TiltModeGeometry.pdf.

M. A. Vaughan, K. A. Powell, D. M. Winker, C. A. Hostetler, R. E. Kuehn, W. H. Hunt, B. J. Getzewich, S. A. Young, Z. Liu, and M. J. McGill. Fully automated detection of cloud and aerosol layers in the calipso lidar measurements. *J. Atmos. Oceanic Technol.*, 26(10):2034–2050, October 2009. ISSN 0739-0572. doi: 10.1175/2009JTECHA1228.1. URL http://dx.doi.org/10.1175/2009JTECHA1228.1.

G. Verver, F. Raes, D. Vogelezang, and D. Johnson. The 2nd aerosol characterization experiment (ace-2): meteorological and chemical context. *Tellus*, 52B:126–140, 2000.

J. Wallace and P. Hobbs. *Atmospheric Science: An Introductory Survey*. Academic Press, 2006.

U. Wandinger, D. Müller, C. Böckmann, D. Althausen, V. Matthias, J. Bösenberg, V. Weiß, M. Fiebig, M. Wendisch, A. Stohl, and A. Ansmann. Optical and microphysical characterization of biomass–burning and industrial–pollution aerosols from multiwavelength lidar and aircraft measurements. *Journal of Geophysical Research*, 117(D21):8125, 2002.

Claus Weitkamp. *Lidar: Range-Resolved Optical Remote Sensing of the Atmosphere*. Springer, 2005.

E. J. Welton, J. R. Campbell, T. A. Berkoff, S. Valencia, J. D. Spinhirne, B. Holben, S. Tsay, and B. Schmid. The nasa micro-pulse lidar network (mplnet): an overview and recent results. *Opt. Pur. Apl*, 39:67–74, 2006.

M. Wiegner, S. Groß, V. Freudenthaler, and J. Gasteiger. Saharan dust event over europe. *Journal of Geophysical Research*, 116:D23213, 2011. doi: 10.1029/2011JD016619. Journal of Geophysical Research - submitted.

M. Wiegner, J. Gasteiger, S. Groß, F. Schnell, V. Freudenthaler, and R. Forkel. Characterization of the eyjafjallajökull ash-plume: Potential of lidar remote sensing. *Physics and Chemistry of the Earth, Parts A/B/C*, 45 / 46:79 – 86, 2012. ISSN 1474-7065. doi: 10.1016/j.pce.2011.01.006. URL `http://www.sciencedirect.com/science/article/B6X1W-521M6DC-1/2/df4c65196c7fbabc1221a92d6f6f10ae`.

D. M. Winker, W. H. Hunt, and M. J. McGill. Initial performance assessment of caliop. *Geophysical Research Letters*, 34:L19803, 2007.

D. M. Winker, M. A. Vaughan, A. Omar, Y. Hu, K. A. Powell, Z. Liu, W. H. Hunt, and S. A. Young. Overview of the calipso mission and caliop data processing algorithms. *J. Atmos. Oceanic Technol.*, 26(11):2310–2323, November 2009. ISSN 0739-0572. doi: 10.1175/2009JTECHA1281.1. URL `http://dx.doi.org/10.1175/2009JTECHA1281.1`.

D. M. Winker, Z. Liu, A. Omar, J. Tackett, and D. Fairlie. Caliop observations of the transport of ash from the eyjafjallajökull volcano in april 2010. *Journal of Geophysical Research: Atmospheres*, 117(D20):n/a–n/a, 2012. ISSN 2156-2202. doi: 10.1029/2011JD016499. URL `http://dx.doi.org/10.1029/2011JD016499`.

D. Wu, Z. Wang, B. Wang, J. Zhou, and Y. Wang. Calipso validation using ground-based lidar in hefei (31.9Â°n, 117.2Â°e), china. *Applied Physics B*, 102(1):185–195, 2011. ISSN 0946-2171. doi: 10.1007/s00340-010-4243-z. URL `http://dx.doi.org/10.1007/s00340-010-4243-z`.

S. A. Young, D. M. Winker, M. A. Vaughan, Y. Hu, and R. E. Kuehn. Caliop algorithm theoretical basis document: Part 4: Extinction retrieval algorithms; pc-sci-202 part 4. Technical report, NASA, 2008.

Stuart A. Young and Mark A. Vaughan. The retrieval of profiles of particulate extinction from cloud-aerosol lidar infrared pathfinder satellite observations (calipso) data: Algorithm description. *J. Atmos. Oceanic Technol.*, 26(6):1105–1119, June 2009. ISSN 0739-0572. doi: 10.1175/2008JTECHA1221.1. URL `http://dx.doi.org/10.1175/2008JTECHA1221.1`.

Acknowledgments

This thesis is the result of a research work at the Meteorological Institute of the Ludwig-Maximilians-Universität, Munich. During my work at the institute I was accompanied and supported by many people. Therefore I want to take the opportunity to thank those numerous people.

First of all, I like to thank Dr. Matthias Wiegner for giving me the opportunity to work in this interesting research field and for his guidance during the last years. Also many thanks to my supervisor Prof. Dr. Bernadett Weinzierl who helped me to improve this thesis in several very constructive discussions. Furthermore, I want to thank my co-supervisor Prof. Dr. Markus Rapp for his interest and support. Many thanks to the measurement team of the MIM lidar group, especially Dr. Volker Freudenthaler, without whom no measurements would have been possible. A special thank goes to Tobias Sirch, who analyzed part of the MULIS data and to Astrid Gosewisch who provided some valuable trajectory calculations. Thanks to Dr. Josef Gasteiger for the fruitful discussions about microphysical properties. I also want to thank my former collegue Dr. Silke Groß for many helpful suggestions and creative tea breaks.

Natürlich möchte ich besonders meinen Eltern Christine und Richard danken, für ihre Unterstützung und Ermutigung während meiner gesamten Zeit an der Universität. Danke auch an Gurli und Andrzej für die ruhige Zuflucht in den letzten Wochen der Arbeit. Vor allem möchte ich mich bei Robert bedanken, der immer viel Verständnis und Geduld für mich und diese Arbeit hatte und der das Beste ist, das ich aus der Uni mitgenommen habe.

The research leading to these results has received funding by the European Commission under grant RICA-025991, from the European Union Seventh Framework Programme (FP7/2007-2013) and grant agreement n° 262254.